Automotive Three-Way Exhaust Aftertreatment under Transient Conditions – Measurements, Modeling and Simulation

von der Faktultät Maschinenbau
der Universität Stuttgart zur Erlangung der Würde
eines Doktor-Ingenieurs (Dr.-Ing.)
genehmigte Abhandlung

vorgelegt von
Clemens Brinkmeier
aus Freising

Hauptberichter: Prof. Dr.-Ing. Gerhart Eigenberger
Mitberichter: Prof. Dr.-Ing. Miloš A. Marek

Tag der mündlichen Prüfung: 23. Februar 2006

Institut für Chemische Verfahrenstechnik

2006

Acknowledgements

This thesis summarizes some of the work carried out within a well established co-operation between research and development departments at Volkswagen AG, Wolfsburg and the Institute of Chemical Process Engineering at University of Stuttgart.

First, I would like to express my gratitude to my doctoral advisor Professor Gerhart Eigenberger. His benevolent guidance and support over the years made this work possible. I am impressed by his academic independence: Professor Eigenberger's enormous efforts in extending engineering knowledge and developing technical solutions seem to be devoted to the common good.

Special thanks go to Professor Miloš A. Marek, Center for Nonlinear Dynamics at the University of Prague for valuable discussions, writing the co-principal report on this thesis and finally serving on my doctoral committee.

Generous financial support by Volkswagen AG is gratefully acknowledged. Many thanks to Stefan Büchner, Achim Donnerstag, Wolfgang Held, Gerald Herding and Axel König at Volkswagen AG for fruitful discussions, the open interchange of information and ideas, the gathering of valuable engine bench and vehicle data and all the administrative work.

I owe great thanks to many students and colleagues who supported this work. I would like to thank particularly Timo Deuschle, Jörg Frauhammer, Henner Kerskes, Gregor Kolios, Frank Meier, Christian Schiller and Hongben Zhou for their contributions. I also appreciate the way Carsten Becker, Jürgen Hildinger and Frank Opferkuch introduced me to data acquisition, system automation and electrical installation. The hardware systems were ingenuously designed by Gerhard Friedrich. Thanks to all the internal and external workshops.

I appreciate the interesting conversations I had with Professor James C. Peyton Jones, Electrical and Computer Engineering, Villanova University: Part of our work seems to complement one another. Many thanks to Shuigen Huang and Professor Lin Li, Material Science and Engineering, University of Shanghai and Professor Jef Vleugels, Metallurgy and Materials Engineering, Katholieke Universiteit Leuven for our discussions on thermodynamic properties of mixed oxides.

Since this thesis was not just a technical challenge I am indebted to those, who found me frequently unavailable: my friends, my family and particularly my loving wife Zahra. My next thesis will be on husbandship.

Contents

Notation

Latin Symbols

A	m^2	crosssectional area
A/F	-	weight based air to fuel ratio
a	m^2/m^3	volume specific surface area
c_p	kJ/(kg K)	mass specific heat capacity
D	kg/(m s)	dispersion coefficient
d	m	diameter
E	kJ/kmol	activation energy
EQ	-	equilibrium coefficient
f	Hz	frequency
f_{subs}	-	fraction of the face area occupied by the substrate
f_{wc}	-	fraction of the face area occupied by the washcoat
f_{P}	-	polarity factor (section I.2)
f_{Q}	-	quantum factor (section I.2)
G_z	kg/(m^2 s)	specific mass flow
h	m	length of catalyst unit cell
$\Delta h_{\text{R},i}$	kJ/kmol	heat of reaction i
I	-	inhibition coefficient
k_i	kmol/(m^2 s)	reaction rate constant of reaction i
K_i	-	chemical equilibrium constant of reaction i

K_j^{inh}	-	adsorption constant of species j
L	m	total brick length
m	kg	mass
$\dot{m}$	kg/s	mass flux
MW_j	kg/kmol	molar weight of species j
$\dot{N}_j$	kmol/s	molar flux of species j
p	N/m^2	pressure
R_i	kmol/(m^2 s)	rate of reaction number i
$R_{j,k}$	kmol/(m^2 s)	rate of reaction of species j with species k
s	m	substrate wall thickness
s_{wc}	m	washcoat thickness
SV	h^{-1}	space velocity at standard conditions
t	s	time
T	K	temperature
U	V	voltage
V	m^3	volume
v	m/s	velocity
v_j	cm^3/mol	diffusion volume of species j (eqn. I.4)
w_j	-	weight fraction of gas species j
x	-	molar fuel H/C-ratio
x_j	-	weight fraction of solid species j
X	-	oxidation extent of oxygen storage
y_j	-	molar fraction of gas species j
z	m	axial coordinate

Greek Symbols

α	kW/(m^2 K)	heat transfer coefficient
β_j	kmol/m^3/s	mass transfer coefficient of species j

γ	-	porosity
ε	-	void fraction
ζ	-	cerium cation ratio $Ce^{+4}/(Ce^{+4}+Zr^{+4})$
η	(N s)/m^2	viscosity
λ	-	amount of air relative to stoichiometric amount
λ_c	kW/(m K)	thermal conductivity
μ	debyes	dipole moment (section I.2)
$\nu_{i,j}$	-	stoichiometric coefficient of species j in reaction i
ψ	kg/m^3	effective density (loading) based on total volume
Ω	kg/m^3	oxygen storage capacity complete (OSCC)
ρ	kg/m^3	density
ξ_i	kmol/s	molar flux (extent) of reaction i

Indices

0	standard conditions ($p^0 = 1.013\,\text{bar}$, $T^0 = 273\,\text{K}$)
ad	adiabatic
app	apparent
c	critical
cal	calculated
cor	corrected
db	diffusion barrier
down	downstream
eff	effective
eq	equilibrium
exh	exhaust
f	feed
g	gas phase
geo	geometric

h	hydraulic
hom	homogeneous
i	reaction index
inh	inhibition
I	total number of reactions
j	species index
J	total number of species
k	index of species different from j
l	lean
meas	measured
mix	mixture
or	oxygen release
os	oxygen storage
osr	oxygen storage and release
pm	precious metal
r	rich or reduced in section I.2, depending on context
raw	raw data
s	solid phase or stoichiometric, depending on context
smp	sample
sp	setpoint
subs	substrate
tot	total
up	upstream
wc	washcoat
$+$	engine in

Dimensionless Groups

Nu	$= \frac{\alpha z}{\lambda_c}$	Nusselt number
Pr	$= \frac{\eta c_p}{\lambda_c}$	Prandtl number
Re	$= \frac{v d_h \rho_g}{\eta}$	Reynolds number
Sc_j	$= \frac{\eta}{\rho D_j}$	Schmidt number species j
Sh	$= \frac{\beta_j d_h}{D_j}$	Sherwood number

Constants

$N_A = 6.023\ 10^{26}$	$kmol^{-1}$	Avogadro constant
R = 8.314	kJ/(kmol K)	universal gas constant
F = 96.485	J/(mol V)	Faraday constant

Abbreviations

AFR	Air to Fuel Ratio
CARB	California Air Resources Board
EU98	European Union Emission Certification Cycle
FTP75	Federal Test Procedure
HEGO	Heated Exhaust Gas Oxygen Sensor
MVEG	Motor Vehicle Emissions Group, advisory expert committee to the European Commission
OBD	OnBoard Diagnosis

OSC	Oxygen Storage Capacity – to be utilized in actual operation, may characterize the dynamic behavior of the system [181, 37]
OSCC	Oxygen Storage Capacity Complete – reflects the overall reducibility of the system [181, 37]
PWM	Pulse Width Modulation
PZEV	Partial Zero Emission Vehicle
SPC	Stored Program Control
SULEV	Super Ultra Low Emission Vehicle
TPR	Temperature Programmed Reduction
TPR-O_2	limiting amount of transferable oxygen attained by prolonged TPR with pure hydrogen at temperatures attainable in automotive exhaust [181]
TWC	Three-Way Catalytic Converter
UEGO	Universal Exhaust Gas Oxygen Sensor
ULEV	Ultra Low Emission Vehicle

Zusammenfassung

In dieser Arbeit wird ein mathematisches Modell des thermischen Verhaltens und der makrokinetischen Stoffumwandlungsvorgänge eines kommerziellen Drei-Wege Autoabgaskatalysators entwickelt und mittels unabhängiger Messungen parametriert. Trotz seiner relativen Einfachheit ist das Modell umfassend genug, um die für die Konvertierung in der Kaltstartphase und im betriebswarmen Zustand wesentlichen Phänomene zu berücksichtigen.

Das eindimensionale Zweiphasen-Modell berücksichtigt neben den drei gesetzlich limitierten Schadstoffen bzw. Schadstoffgruppen Kohlenmonoxid, Kohlenwasserstoffe (welche im Rahmen dieser Arbeit in Form von Propen und Propan repräsentiert werden) und Stickoxiden auch Sauerstoff und den für den Kaltstart wichtigen Wasserstoff.

Die Reaktionsgeschwindigkeitsparameter werden durch Anpassung der Modellrechnungen an stationäre Kinetikmessungen in isothermen Flachbettreaktoren gewonnen. Bei diesen Messungen wird der λ-geregelte Drei-Wege Betrieb durch überlagerte Schwingungen der Luftzahl λ mit der Frequenz 1 Hz nachgebildet. Repräsentative fette (λ = 0.98) und magere (λ = 1.02) Abgaszusammensetzungen werden abgeleitet aus Abgas-Zertifizierungszyklen nach Europäischer und US-Amerikanischer Gesetzgebung (EU98 und FTP75). Ausgehend von diesen Basis-Zusammensetzungen werden einzelne Schadstoffkonzentrationen gezielt im Temperaturbereich $100 \leq T \leq 700\,^{\circ}\mathrm{C}$ variiert. Die Messungen umfassen folglich nicht nur den katalytisch dominierten Temperaturbereich bis ca. 450 °C, sondern reichen hinein in den Hochtemperaturbereich, in welchem Geschwindigkeiten von Homogenreaktionen jene der heterogen katalysierten übertreffen können. Tatsächlich würde die starke Zunahme der Abbrandgeschwindigkeiten von Wasserstoff, Propen und Propan mit steigender Temperatur jenseits von 600 °C unterbewertet bei alleiniger Anpassung der Reaktionsgeschwindigkeiten an Messungen im Temperaturbereich des katalytischen Zündens. Es wird daher ein zweiter Verbrennungsmechanismus eingeführt, welcher als heterogen-homogen gekoppelt bezeichnet wird. Dieser für die Modellierung der Autoabgasreinigung neue Ansatz steht in Einklang mit Erkenntnissen der Verbrennungsforschung. Es wird gezeigt, daß mit einem einzigen Parametersatz alle relevanten Gas-Gas Reaktionen, welche in einem Autoabgaskatalysator zwischen 100 und 700 °C unter fetten und mageren Bedingungen ablaufen, zutreffend beschrieben werden können (Tabelle 5.1).

Eine für die Abgasreinigung eines λ-geregelten 3-Wege Katalysators zentrale Eigenschaft ist dessen Fähigkeit, unter mageren Abgasbedingungen (Luftüberschuß) Sauer-

stoff einzuspeichern und diesen unter fetten Bedingungen (Luftmangel) wieder freizusetzen. Mit Sauerstoff angereicherte Speichermaterialien (wie Cer-Zirkon Mischoxid Feststofflösungen) setzen Sauerstoff frei, wenn der Sauerstoffpartialdruck des im Kontakt mit diesen Materialien stehenden Abgases unter den Sauerstoffpartialdruck des jeweiligen Materials im thermodynamischen Gleichgewicht fällt. Da Sauerstoffpartialdrücke von einer Größenordnung $y_{O_2} = 1 \cdot 10^{-30} \ldots 1 \cdot 10^{-10}$ notwendig für die Reduktion der Speichermaterialien sind, würde eine direkte modellmäßige Berücksichtigung des Gleichgewichts (für einige Materialen finden sich Beschreibungen in der Literatur) höchste Anforderungen an die Genauigkeit der numerischen Lösung stellen. Statt dessen wird in dieser Arbeit ein einfacher Sorptionsansatz für die Beschreibung der Einspeicher- und Freisetzungsgeschwindigkeiten gewählt, welcher neben dem Füllgrad X des Sauerstoffspeichers die Gemischabweichung von der stöchiometrischen Zusammensetzung $(\lambda - 1)$ berücksichtigt. Sauerstoffspeicherkapazitäten Ω und -geschwindigkeitskonstanten werden durch fett-mager und mager-fett Sprungversuche in Flachbett-Reaktoren unter isothermen Bedingungen vermessen. Es wird gezeigt, daß sowohl die Speicherkapazität Ω als auch die Reaktionsgeschwindigkeitskonstante der Sauerstoffeinspeicherung k_{os} mit steigender Temperatur zunimmt. Für die Reaktionsgeschwindigkeitskonstante der Sauerstofffreisetzung k_{or} wird ein temperaturunabhängiger Wert gefunden.

Das erstellte mathematische Modell wird validiert durch Vergleich der Simulationsergebnisse mit den zeitlich aufgelösten Verläufen der Katalysatortemperatur, der Abgasemissionen und des Luftverhältnisses in einem Abgas-Zertifizierungszyklus. Das gemessene Verhalten wird durch die Simulationsrechnung gut wiedergegeben. Dies ist beachtenswert, da – abgesehen von der Wärmetönung der Sauerstoffspeicherreaktion $\Delta h_{R,os}$ – alle Modellparameter den Lieferpapieren des Katalysatorherstellers, der Literatur oder aber den in dieser Arbeit dargestellten unabhängigen Messungen in isothermen Flachbettreaktoren entstammen. Die bestmögliche instationäre Beschreibung der Katalysatortemperaturen wird für eine Wärmetönung der Sauerstoffspeicherreaktion von $\Delta h_{R,os} = -200$ kJ/(mol O_2) erzielt – in Übereinstimmung mit Literaturwerten für kalorimetrische Messungen an einem Serienkatalysator. Über die validierbaren Größen hinaus gibt die Modellrechnung Aufschluß über den zeitlichen Verlauf des ortsaufgelösten Beladungsgrades mit Sauerstoff X, welcher sich bislang einer direkten Messung entzieht. Er ist von besonderem Interesse für die motorische Applikation im Kraftfahrzeug.

Ein weiterer für den automobilen Einsatz wesentlicher Aspekt der Abgasreinigung mittels λ-geregelter Drei-Wege Katalysatoren ist die insbesondere unter fetten Abgasbedingungen auftretende reversible Deaktivierung des Autoabgaskatalysators. In dieser Arbeit kann gezeigt werden, daß diese vorrangig durch Vergiftung mit Schwefel verursacht wird. Schwefelhaltige Komponenten, welche dem Katalysator entweder unmittelbar zugeführt werden und/oder nach vorangegangener Speicherung im Washcoat des Katalysators aus diesem freigesetzt werden, deaktivieren den Katalysator. Neben der Konvertierung der Brenngase verschlechtert sich auch die Konvertierung der Stickoxide, für welche man unter fetten Bedingungen hohe Umsätze erwarten darf. Die Deaktivierung ist langsam unterhalb von 450 °C und schnell oberhalb von 550 °C

und reversibel beim Wechsel auf magere Atmosphäre. Im Katalysator gespeicherter Schwefel kann jedoch nur bei hohen Temperaturen vollständig ausgetragen werden. Der in dieser Arbeit untersuchte Serienkatalysator wurde vor den experimentellen Untersuchungen jeweils in stark reduzierender Atmosphäre bei 700 °C entschwefelt.

Bei Beaufschlagung mit schwefelfreiem Abgas fetter Zusammensetzung wird bei Temperaturen unterhalb von 350 °C ebenso eine Deaktivierung der Wassergas-Shift und Steam-Reforming Aktivität festgestellt. In Übereinstimmung mit dem Gleichgewicht der Boudouard Reaktion (Abbildung 3.4) wird diese Niedertemperatur-Deaktivierung in schwefelfreier Atmossphäre auf die Bildung von kohlenstoffhaltigen Ablagerungen auf dem Katalysator zurückgeführt.

Werden Autoabgaskatalysatoren für längere Zeit oder aber wiederholt kurzzeitig (z.B. infolge von Fahrzeugverzögerungsvorgängen mit Kraftstoffabschaltung im Schubbetrieb) hohen Temperaturen ausgesetzt, so vermindert sich sowohl die katalytische Aktivität, als auch die Fähigkeit zur Sauerstoffeinspeicherung. Nach dem Stand der Technik messen Verfahren zur gesetzlich vorgeschriebenen Überwachung der Katalysatoraktivität im Fahrbetrieb (OnBoard Diagnose = OBD) die alterungsabhängige Sauerstoffspeicherfähigkeit und korrelieren diese mit der Katalysatoraktivität.

Die Speicherkapazität Ω des untersuchten Katalysators bricht von einem Wert von 1.5 g/l_{cat} im (konditionierten) Frischzustand auf einen Wert von 0.05 g/l_{cat} nach vierstündiger Alterung in magerer Atmosphäre bei 1300 °C ein (Abbildung B.3). Der Rückgang ist auf eine Segregation der im sauerstoffspeichernden Zustand ineinander gelösten Mischoxide zurückzuführen. Die entstehenden (reinen) Phasen können unter Autoabgasbedingungen nicht – oder nur unwesentlich – reduziert werden und stehen daher für eine Speicherung nicht zur Verfügung (Sauerstoffpartialdrücke im Gleichgewicht mit reinen Ceroxiden siehe Abb. 3.7). Der alterungsbedingte Anstieg der Zündtemperaturen für Kohlenmonoxid und Kohlenwasserstoffe mit abnehmender Sauerstoffspeicherkapazität kann beispielhaft Abbildung B.2 entnommen werden.

Eine für diese Arbeit entwickelte mit einem Flüssig-Kraftstoff-Brenner befeuerte Hochtemperatur-Alterungsanlage erlaubt es, den Katalysator hohen stationären und transienten Bauteiltemperaturen (bis zu 1300 °C) auszusetzen. Alterungsversuche mit simulierten periodisch eingeleiteten Schubschaltungen bestätigen die mit gewöhnlichen Temperaturfühlern meßbare Bauteiltemperatur als wesentlichen Alterungsparameter: Wird dabei die Reaktionswärme erst im Katalysator freigesetzt – der unmittelbare Katalysatoreintritt ist dann kälter verglichen mit dem Fall bei dem dieselbe Wärmemenge mit dem heißen Abgas zugeführt wird – so ist dieser weniger stark gealtert, als der genannte Referenzfall mit entsprechend höheren Zulauftemperaturen (Abbildung B.4).

Schließlich wird in Anhang D für lineare λ-Sonden, die im Rahmen dieser Arbeit u.a. zur Vermessung der Sauerstoffspeicherfähigkeit Anwendung finden, die Signalempfindlichkeit bezüglich der verschiedenen Abgaskomponenten vermessen und ein Literatur-Modell der so genannten Sensor-Blendung validiert. Darüber hinaus umfasst der Anhang eine gründliche Beschreibung der experimentellen Anla-

gen, physikalischer Eigenschaften der untersuchten Katalysatoren, physikalische und thermodynamische Eigenschaften von Gasen, Feststoffen und deren Reaktionen und Wärme- und Stofftransportkorrelationen.

Abstract

In this work a mathematical model for the dynamic thermal and the macrokinetic conversion behavior of a commercial automotive three-way exhaust catalytic converter is developed and parameterized with independent measurements. In spite of its relative simplicity the developed model is comprehensive enough to cover the major phenomena relevant for catalyst conversion under light-off conditions and – in particular – under warmed-up closed-loop conditions.

A one-dimensional, two-phase model, incorporating all major reactions is set up. The model considers in addition to the three legislated pollutants carbon monoxide, hydrocarbons (which are represented by propene and propane) and nitrogen oxide the species hydrogen and oxygen. Between these species combustion, nitrogen oxide reduction, water gas shift and steam reforming reactions are considered.

The respective species conversion rate parameters are adjusted to steady state experiments in isothermal flat bed reactors with a superimposed air to fuel ratio modulation of 1 Hz – simulating closed-loop engine control. Representative rich (λ = 0.98) and lean (λ = 1.02) exhaust compositions are retrieved from several emission certification driving cycles (both the European EU98 and the US-American FTP75). Starting with these base compositions individual species' concentrations are varied within a wide temperature range of $100 \leq T \leq 700\,^{\circ}\mathrm{C}$. Thus kinetic experiments do not just cover the catalytic light-off temperature range (up to 450 °C catalyst temperature) but immerse into the high temperature range where homogeneous reaction rates overtake the catalytic reaction rates. Indeed catalytic combustion rates of hydrogen, propene and propane adjusted in the catalytic light-off regime would fail to describe the temperature activation of the combustion reactions at temperatures beyond 600 °C. A second combustion mechanism, referred to as heterogeneous-homogeneous coupled, is thus introduced. This novel approach is in good agreement with combustion research. It is shown that all relevant gas-gas reactions proceeding in a catalytic converter at temperatures between 100 and 700 °C at rich and lean conditions can be covered with one single set of reaction rate parameters (table 5.1).

One main feature in λ-controlled three-way catalytic exhaust conversion is the catalyst's ability to store oxygen under fuel lean (oxygen surplus) conditions and to release oxygen under fuel rich (oxygen deficient) conditions. Oxygen saturated oxygen storage materials (such as ceria-zirconia solid solutions) decompose once the exhaust oxygen partial pressure falls below the respective material's equilibrium oxygen partial pressure. Decomposition is accompanied by oxygen release – and thus reduc-

tion of the oxygen storage material. Since oxygen partial pressures in the order of $y_{O_2} = 1 \cdot 10^{-30} \ldots 1 \cdot 10^{-10}$ are necessary for reduction, the consideration of an exact thermodynamic description (which is available for certain relevant materials) would lead to excessive demands on the numerical solution's precision. Instead a simple sorption type rate expression depending on the richness/leanness – expressed in the mixture's deviation from stoichiometry ($\lambda - 1$) and the oxidation extent of the oxygen storage X – is applied for oxygen storage and release. Oxygen storage capacity and kinetics are measured by lean/rich-step experiments in flat-bed reactors under isothermal conditions. It turns out that the respective storage capacity and the rate constant of oxygen uptake are increasing with temperature whereas the rate constant of oxygen release is found to be temperature independent.

The resulting model is validated by comparing simulation results with a set of detailed emission certification test results and is able to represent the measured temperature and conversion behavior with good accuracy. This is in particular remarkable since all parameters – except the heat of oxygen storage – are retrieved from catalyst shipping papers, literature and independent, isothermal measurements presented in this work. For a good match of simulated and measured catalyst bed temperatures the heat of oxygen storage was adjusted to $\Delta h_{R,os}$ = - 200 kJ/(mol O_2) which is in good agreement with calorimetric measurements reported in literature. Furthermore the model provides information not directly accessible by measurements like the spatial evolution of the oxidation extent of the oxygen storage material which is a most valuable information for engine control and calibration engineers.

Under fuel rich conditions reversible catalyst deactivation is a major issue in exhaust emission control. In this work sulfur poisoning is shown to be of particular importance. Sulfur species – either instantaneously fed to the catalyst or previously stored under lean conditions and subsequent released under rich conditions – deactivate the catalyst. Not just combustion efficiency is affected by sulfur poisoning but also nitrogen oxide reduction, which is expected to be high under fuel rich conditions. The deactivation is slow below 450 °C and fast above 550 °C and turns out to be reversible by exposure to lean exhaust conditions. However sulfur stored within the catalyst can only be purged at elevated temperatures. The catalyst investigated in this work is purged at 700 °C under strong reducing conditions prior to kinetic measurements. A deactivation of water gas shift and steam reforming reactions with rich exhaust is also observed for sulfur free feed at temperatures below 350 °C. In accordance with equilibrium conversion of the Boudouard reaction (figure 3.4) this is attributed to the formation of carbonaceous deposits at the active catalyst sites.

High temperature deactivation either by extended periods of constant high temperature or of frequent, short, high temperature spikes (e.g. due to deceleration with fuel-cut) cause both a decrease in catalyst activity and oxygen storage capacity. Current on board diagnostics (OBD) of catalyst activity rely on this correlation and measure the aging state dependent oxygen storage capacity. It is shown that the investigated catalyst's oxygen storage capacity Ω drops from a value of 1.5 g/l_{cat} in its fresh/conditioned state to a value of 0.05 g/l_{cat} after four hours of lean aging at 1300 °C (figure B.3). This decrease is due to segregation of active oxygen storage components (such as ceria-

zirconia solid solutions) into e.g. pure phases of cerium and zirconium oxide, both unable to release – and thus to store – oxygen (equilibrium partial pressures above pure cerium oxide see figure 3.7). A relation between the decrease in oxygen storage capacity due to thermal aging and increasing ignition temperatures of carbon monoxide and hydrocarbons is derived (figure B.2).

A high temperature burner-fired experimental set-up, which allows to subject the catalyst to high steady state and transient catalyst temperatures (up to 1300 °C) at typical exhaust conditions, is developed in this work. Aging with simulated fuel cut decelerations confirm the dominant impact of catalyst temperature (measurable with standard equipment) on catalyst aging: If the exothermic potential is released within the catalyst – and thus the very first section of the catalyst is at a colder temperature compared to the case with the same amount of heat supplied by the hot exhaust – it is less aged than the respective section submitted to higher inlet temperatures (figure B.4).

The sensitivity of the linear oxygen sensor (applied for oxygen storage measurements in this work) towards different exhaust constituents is measured and a literature model of the so-called sensor distortion is validated in appendix D. Furthermore the appendix comprises a thorough description of the experimental facilities, physical catalyst data, physical and thermochemical properties of gases, solids and reactions and heat and mass transfer correlations applied in this work.

Chapter 1

Introduction

Since the introduction of automotive emission control, the California Air Resources Board (CARB) drives the process of defining increasingly tighter emission standards (figure 1.1) [175].

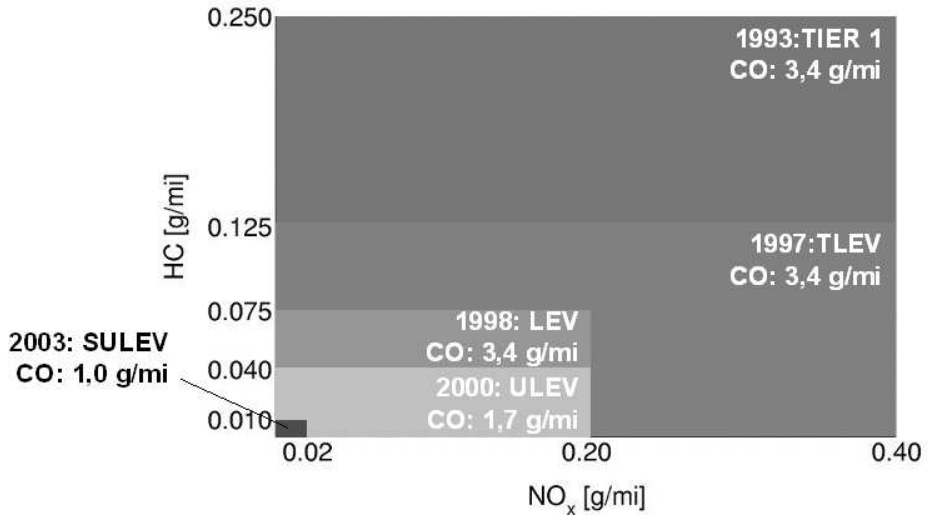

Figure 1.1: Emission standards California Air Resources Board (CARB)

With model year 2003 legislation in California, New York, Vermont, Maine and Massachusetts, which represent approximately 40% of the US market, became much stricter: Up to 10% of the fleet has to be sold as Zero Emission Vehicle (ZEV). Alternatively, a higher percentage of Partial Zero Emission Vehicles (PZEV) can be sold. Volkswagen meets this legislation with the concepts SULEV and Zero Evaporation Fuel Handling [178].

SULEV emission thresholds are significantly lower than ULEV thresholds (figure 1.1). They demand rapid catalytic converter light-off and excellent conversion in the warmed-up catalyst. The warmed-up performance depends on the engine exhaust air to fuel ratio and the converter's ability to compensate deviations from stoichiometric

composition due to oxygen storage [6]. A thorough description of recently developed oxygen storage materials and their characteristic properties is given in [161].

The development of catalytic converter systems is significantly supported by numerical simulation [24]. Especially for the low SULEV emission levels the catalyst definition (location, volume, cell density, precious metal, aged conversion efficiency, etc.) at early exhaust aftertreatment system design stages (with target exhaust systems, engines and vehicles not yet available) requires a reliable numerical simulation tool. With the model described in this work the exhaust system's conversion performance can be simulated in the transient phases of emission certification driving cycles.

1.1 Automotive Three-Way Exhaust Aftertreatment

With increased performance of air to fuel ratio control the importance of catalyst dynamics on tailpipe emissions and control strategy became increasingly apparent [82].

Up to the mid 1990s the dynamic behavior of the catalytic converter has been largely neglected in engine control systems. Due to tougher emission standards and mandatory on-board diagnosis systems of exhaust emission relevant parts, a closer look at the three-way catalytic converter and the lambda sensor became inevitable [45, 7].

Rather general reviews of catalytic air pollution control and three-way catalytic systems in particular can be found elsewhere, e.g. [175, 97, 38, 145, 63]. A review of the development and application of mathematical models for three-way catalytic converter systems is provided by [96].

1.2 Objectives and Thesis Structure

Objectives A mathematical model of the three-way catalytic converter capable of describing the conversion of the three legislated pollutants (pollutant groups) carbon monoxide, nitrogen oxides and hydrocarbons at real exhaust conditions is the major objective of this thesis. The three-way catalytic converter model should be physically and chemically sound, although no attempt is made to take all elementary adsorptive, dissociative, diffusive and reaction processes into account.

The model dealing with heat and mass transfer phenomena, reactive species conversion and heat and species storage and release under transient conditions shall be based upon information retrieved from proper measurements.

Numerical simulation with this model should support the development process of automotive exhaust aftertreatment systems. For a given time-resolved engine exhaust (engine out temperature, exhaust composition, mass flow) the exhaust system can be optimized to fulfill certain emission thresholds at reasonable costs. In particular the effect of the location of the catalytic converter bricks (close coupled or underfloor or

both) their respective volume, the diameter/length ratio, the material (coiled corrugated metal foil monoliths or extruded ceramic monoliths), cell density, wall thickness, catalytic activity, oxygen storage capacity can be studied without extensive experimental testing.

Furthermore the effect of engine out conditions (e.g. temperature ramp under cold start conditions, lambda setpoint, air to fuel ratio control, catalyst purge) on the emission performance of a certain exhaust aftertreatment system can be evaluated. With the available hardware a proper engine control strategy can be developed.

Thesis Structure Since the model has to deal with engine out exhaust conditions likely to be encountered during emission certification driving cycles, a variety of engine out emission measurements for these cycles is analyzed and discussed along with the corresponding air to fuel ratio control in chapter 2.

Exhaust aftertreatment based upon gas-gas and gas-solid reactions within state of the art three-way catalysts is discussed from a thermodynamic point of view in chapter 3.

The governing mathematical equations of the three-way catalytic converter model describing temperature and species composition changes within the considered phases are discussed in chapter 4.

It is generally agreed that most models published suffer from a lack of reliable kinetic data [148, 96]. Thus a major focus of this work is on gaining reaction kinetics for both oxygen storage/release and species conversion. Model parameters are gained by several consecutive suitable laboratory scale measurements. Measurements performed to obtain the species conversion kinetics are described in chapter 5 whereas experiments targeting for oxygen storage capacities and kinetics are presented in chapter 6. Obtained model parameters and a comparison of measurements and simulations are included in the respective chapters to check for the model and parameter fit quality.

Validation of the parameterized model is performed by independent full scale measurements on a Volkswagen SULEV emission concept vehicle performing an FTP75 emission driving cycle on a vehicle roll dynamometer (chapter 7).

Slow catalyst deactivation under rich operation is addressed in chapter 8. Suggestions for future work on reaction engineering aspects to support automotive three-way catalytic aftertreatment development are summarized in chapter 9. Amongst a thorough compendium of relationships and data applied/retrieved in this work the appendix comprises a description of the experimental facilities developed and applied in this work (appendix A), experimental results and a discussion of catalyst aging (appendix B) and a description of commercial oxygen sensor operation and sensitivity towards different exhaust constituents (appendix D).

Chapter 2

Engine Exhaust

The catalytic converter is fed with the gas being discharged from the engine's cylinders after homogeneous combustion. Further homogeneous reactions in manifold and take-down pipe can be significant. Additionally induced homogeneous combustion in the takedown pipe e.g. ensures rapid catalytic converter light-off as discussed in chapter 7.

The driving schedules for emission certification are well defined. Today the most frequently applied test cycles are the US-American FTP75 and the European MVEG-B (figure 2.1 and table 2.1). Most other countries have adopted one of these cycles. The extra urban portion of the MVEG-B considers vehicle speed up to 120 km/h. The maximum speed encountered during other emission certification driving cycles is even lower.

	FTP75	MVEG-B
duration	1877 s	1180 s
length	17.8 km	11.0 km
average speed	34 km/h	34 km/h
maximum speed	91 km/h	120 km/h

Table 2.1: Emission test cycles: US-American FTP75 and European MVEG-B (Effective for Euro 3 onwards with modified start-up phase compared to MVEG-A: Deletion of the 40 seconds idle period prior to bag sampling start.).

It is common practice to go to oxygen deficient (fuel rich) combustion when exceeding the respective cycles speed limit in order to protect parts located in the exhaust system (exhaust manifold, turbocharger (if applied), sensors, catalysts) from overheating. Conditions encountered beyond the cycle's speed limits are important in terms of aging (appendix B) but irrelevant for emission certification. The operating range of the three-way catalytic converter model is described exemplarily in section 2.2 by analyzing engine out emissions during FTP75 and MVEG-A/B driving cycles for engines with different cubic capacities. Furthermore representative gas compositions are defined for experimental investigations of the catalyst (chapters 5, 6 and appendix B).

Due to the stoichiometry of fuel combustion with air, exhaust species concentrations are closely related to each other. In section 2.1 an important measure in engine control

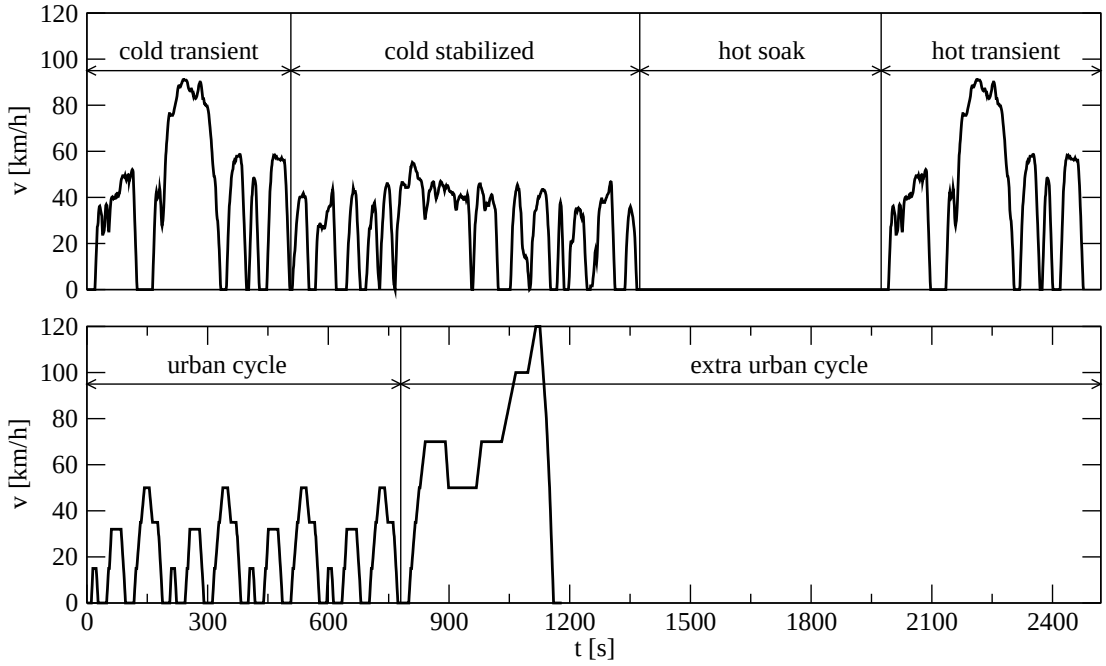

Figure 2.1: Emission certification driving schedules: US-American FTP75 (top) and European MVEG-B (bottom).

– the relative air to fuel ratio – is calculated from exhaust species concentrations. It is also illustrated how certain exhaust species concentrations (e.g. water or oxygen) can be calculated from the remaining exhaust species concentrations and the lambda value - if available.

2.1 Air to Fuel Ratio

The ideal combustion reaction of fuel with air leads to the products of total oxidation, water and carbon dioxide:

$$\mathrm{CH}_x + (1 + \frac{x}{4})\,\mathrm{O}_2 \longrightarrow \mathrm{CO}_2 + \frac{x}{2}\,\mathrm{H}_2\mathrm{O} \tag{2.1}$$

Here gasoline will – independent of its actual composition – only be represented by its molar hydrogen to carbon ratio x, where CH_x has the formal molecular weight of $\mathrm{MW}_{\mathrm{CH}_x} = (12 + x)$ kg/kmol. If 1 kg gasoline ($x = 1.85$) is burned with fresh air ($y_{\mathrm{O}_2,\mathrm{air}} = 0.2093$) 14.6 kg air are necessary for complete combustion. In this case an air to fuel ratio of $A/F = 14.6$ marks stoichiometric, a greater value lean (with oxygen excess) and a lower value rich (oxygen deficient) composition. Another popular measure for exhaust gas composition is the lambda value which is specified independently from the fuels H/C-ratio and the oxygen content in the combustion air:

$$\lambda = \frac{\text{amount of air provided for fuel oxidation}}{\text{amount of air necessary for total fuel oxidation}}$$

It is important to realize that the lambda value refers to *fuel* combustion[1]. A value of $\lambda = 1$ addresses just the necessary (stoichiometric) air supply. Again values greater one represent lean, values lower one rich compositions. In state of the art three-way catalytic aftertreatment systems the lambda value is measured by means of a lambda sensor (e.g. the model applied in this work: Bosch Lambda Sensor Universal LSU, described in appendix A).

In the following it will be shown how the lambda value can be calculated from available exhaust concentrations and which concentrations are necessary or linearly dependent. To do so, it will be assumed that incomplete fuel combustion and nitrogen oxidation results in an exhaust which contains hydrogen, carbon monoxide, propene, propane and nitrogen monoxide in addition to the products of complete combustion, carbon dioxide and water.

A synthetic exhaust gas containing the above species is generally considered to well represent the actual exhaust of λ-controlled combustion engines with three-way catalysts [120, 40, 89, 1, 80, 153]. In the following the actual exhaust composition will be approximated through the above components while all kinetic measurements will be based upon a synthetic exhaust containing the above species. Then the following reaction equation needs to be considered:

$$\begin{aligned} \mathrm{CH}_x + \nu_{\mathrm{O}_2}\,\mathrm{O}_2 + \nu_{\mathrm{N}_2}\,\mathrm{N}_2 \quad &\longrightarrow \quad \nu_{\mathrm{CO}_2}\,\mathrm{CO}_2 + \nu_{\mathrm{H}_2\mathrm{O}}\,\mathrm{H}_2\mathrm{O} + \nu_{\mathrm{H}_2}\,\mathrm{H}_2 + \nu_{\mathrm{CO}}\,\mathrm{CO} + \\ &+ \quad \nu_{\mathrm{C}_3\mathrm{H}_6}\,\mathrm{C}_3\mathrm{H}_6 + \nu_{\mathrm{C}_3\mathrm{H}_8}\,\mathrm{C}_3\mathrm{H}_8 + \nu_{\mathrm{NO}}\,\mathrm{NO} \end{aligned} \tag{2.2}$$

The stoichiometric coefficients do obey the C-, H-, O- and N-atom balances:

$$\begin{aligned} &\text{C-balance:} && -1 + \nu_{\mathrm{CO}_2} + \nu_{\mathrm{CO}} + 3\,\nu_{\mathrm{C}_3\mathrm{H}_6} + 3\,\nu_{\mathrm{C}_3\mathrm{H}_8} = 0 \\ &&\rightsquigarrow\ & \nu_{\mathrm{CO}_2} = 1 - \nu_{\mathrm{CO}} - 3\,\nu_{\mathrm{C}_3\mathrm{H}_6} - 3\,\nu_{\mathrm{C}_3\mathrm{H}_8} && (2.3) \\ &\text{H-balance:} && -x + 2\,\nu_{\mathrm{H}_2\mathrm{O}} + 2\,\nu_{\mathrm{H}_2} + 6\,\nu_{\mathrm{C}_3\mathrm{H}_6} + 8\,\nu_{\mathrm{C}_3\mathrm{H}_8} = 0 \\ &&\rightsquigarrow\ & \nu_{\mathrm{H}_2\mathrm{O}} = \frac{x}{2} - \nu_{\mathrm{H}_2} - 3\,\nu_{\mathrm{C}_3\mathrm{H}_6} - 4\,\nu_{\mathrm{C}_3\mathrm{H}_8} && (2.4) \\ &\text{O-balance:} && 2\,\nu_{\mathrm{O}_2} + 2\,\nu_{\mathrm{CO}_2} + \nu_{\mathrm{H}_2\mathrm{O}} + \nu_{\mathrm{CO}} + \nu_{\mathrm{NO}} = 0 \\ &&\rightsquigarrow\ & 0 = 2 + \frac{x}{2} - \nu_{\mathrm{H}_2} - \nu_{\mathrm{CO}} - 9\,\nu_{\mathrm{C}_3\mathrm{H}_6} - 10\,\nu_{\mathrm{C}_3\mathrm{H}_8} + 2\,\nu_{\mathrm{O}_2} + \nu_{\mathrm{NO}} && (2.5) \\ &\text{N-balance:} && 2\,\nu_{\mathrm{N}_2} + \nu_{\mathrm{NO}} = 0 \\ &&\rightsquigarrow\ & \nu_{\mathrm{N}_2} = -\frac{\nu_{\mathrm{NO}}}{2} && (2.6) \end{aligned}$$

Hence four linear relations apply for the nine stoichiometric coefficients of equation 2.2, which means that only five stoichiometric coefficients are linearly indepen-

[1] Redefinitions – such as relating to engine out emissions – cause confusion: e.g. the lambda value of a virtually clean exhaust consisting of nitrogen, carbon dioxide, water, 4 ppm carbon monoxide and 1 ppm oxygen is $\lambda = 0.999995$. Related to engine out concentrations the corresponding value would be 0.5 – an air-fuel-mixture of $\lambda = 0.5$ would be well below the engine's lower ignition limit.

dent. Furthermore the stoichiometric coefficients are accessible from the engine's inlet conditions N_j^+, the extent of combustion ξ and the exhaust species mole fractions y_j:

$$y_j = \frac{\dot{N}_j^+ + \nu_j \xi}{\sum_{j=1}^{J} (\dot{N}_j^+ + \nu_j \xi)} \tag{2.7}$$

For a given feed with $\lambda = \frac{\dot{N}_{O_2}^+}{\left(1+\frac{x}{4}\right)\dot{N}_{CH_x}^+}$ it follows:

$$\dot{N}_{O_2}^+ = \lambda \left(1+\frac{x}{4}\right)\dot{N}_{CH_x}^+,\ \dot{N}_{N_2}^+ = \lambda \left(1+\frac{x}{4}\right)\left(\frac{1-y_{O_2,air}}{y_{O_2,air}}\right)\dot{N}_{CH_x}^+,\ \dot{N}_{j\neq CH_x,O_2,N_2}^+ = 0$$

With equation 2.7 complete fuel conversion ($\xi = \dot{N}_{CH_x}^+$) leads to:

$$y_{H_2} = \frac{\nu_{H_2}\dot{N}_{CH_x}^+}{\sum_{j=1}^{J} (\dot{N}_j^+ + \nu_j \xi)} \tag{2.8}$$

$$y_{CO} = \frac{\nu_{CO}\dot{N}_{CH_x}^+}{\sum_{j=1}^{J} (\dot{N}_j^+ + \nu_j \xi)} \tag{2.9}$$

$$y_{C_3H_6} = \frac{\nu_{C_3H_6}\dot{N}_{CH_x}^+}{\sum_{j=1}^{J} (\dot{N}_j^+ + \nu_j \xi)} \tag{2.10}$$

$$y_{C_3H_8} = \frac{\nu_{C_3H_8}\dot{N}_{CH_x}^+}{\sum_{j=1}^{J} (\dot{N}_j^+ + \nu_j \xi)} \tag{2.11}$$

$$y_{O2} = \frac{\left(\lambda\left(1+\frac{x}{4}\right)+\nu_{O_2}\right)\dot{N}_{CH_x}^+}{\sum_{j=1}^{J} (\dot{N}_j^+ + \nu_j \xi)} \tag{2.12}$$

$$y_{NO} = \frac{\nu_{NO}\dot{N}_{CH_x}^+}{\sum_{j=1}^{J} (\dot{N}_j^+ + \nu_j \xi)} \tag{2.13}$$

with the common denominator:

$$\sum_{j=1}^{J} (\dot{N}_j^+ + \nu_j \xi) = \dot{N}_{CH_x}^+ \Bigg(\overbrace{\lambda\left(1+\frac{x}{4}\right)}^{\dot{N}_{O_2}^+/\dot{N}_{CH_x}^+} + \nu_{O_2} + \overbrace{\lambda\left(1+\frac{x}{4}\right)\frac{1-y_{O_2,air}}{y_{O_2,air}}}^{\dot{N}_{N_2}^+/\dot{N}_{CH_x}^+} + \nu_{N_2} +$$

$$
\begin{aligned}
&+ \quad \nu_{CO_2} + \nu_{H_2O} + \nu_{H_2} + \nu_{CO} + \nu_{C_3H_6} + \nu_{C_3H_8} + \nu_{NO} \Big) = \\
= \dot{N}^{+}_{CH_x} \Big(1 \quad &+ \quad \frac{x}{2} + \lambda \left(1 + \frac{x}{4}\right) \frac{1}{y_{O_2,air}} - 5\,\nu_{C_3H_6} - 6\,\nu_{C_3H_8} + \nu_{O_2} + \frac{\nu_{NO}}{2} \Big)
\end{aligned}
$$

The system of seven linear equations 2.5, 2.8–2.13 solved for the unknowns λ, ν_{H_2}, ν_{CO}, $\nu_{C_3H_6}$, $\nu_{C_3H_8}$, ν_{O_2}, ν_{NO} leads to the following expression for λ, dependent on mid range gas species concentrations:

$$
\lambda = \frac{y_{O_2,air}}{4+x} \frac{4Y + x\left(2 - 2y_{H_2} - 2y_{CO} - 8y_{C_3H_6} - 8y_{C_3H_8} + 2y_{O_2} + y_{NO}\right)}{y_{H_2} + y_{CO} + 9y_{C_3H_6} + 10y_{C_3H_8} - 2y_{O_2} - y_{NO} + y_{O_2,air} Y} \tag{2.14}
$$

with $\quad Y = \left(2 - y_{H_2} - y_{CO} + y_{C_3H_6} + 2y_{C_3H_8}\right)$

Furthermore the concentrations of water and carbon dioxide can be calculated from the remaining exhaust species concentrations:

$$
\begin{aligned}
y_{CO_2} \;=\; & \frac{1}{4 + x(1 + y_{O_2,air})} \Big(2y_{H_2} - 2y_{CO} + 6y_{C_3H_6} + 8y_{C_3H_8} - 4y_{O_2} - 2y_{NO} + \\
+ \; & 2y_{O_2,air} \left(2 - y_{H_2} - y_{CO} + y_{C_3H_6} + 2y_{C_3H_8}\right) - \\
- \; & x(1 + y_{O_2,air})(y_{CO} + 3y_{C_3H_6} + 3y_{C_3H_8}) \Big) \qquad (2.15) \\
y_{H_2O} \;=\; & \frac{1}{4 + x(1 + y_{O_2,air})} \Big(-4(y_{H_2} + 3y_{C_3H_6} + 4y_{C_3H_8}) + \\
+ \; & x(y_{CO} + 6y_{C_3H_6} + 6y_{C_3H_8} - 2y_{O_2} - y_{NO}) + \\
+ \; & x\, y_{O_2,air}(2 - 2y_{H_2} - y_{CO} - 2y_{C_3H_6} - 2y_{C_3H_8}) \Big) \qquad (2.16)
\end{aligned}
$$

In case of stoichiometric ($\lambda = 1$) complete combustion ($y_{j \neq N_2,H_2O,CO_2} = 0$) of gasoline ($x = 1.85$) with dry fresh air ($y_{O_2,air} = 0.2093$) the product concentrations are $y_{H_2O} = 12.4\%$ and $y_{CO_2} = 13.4\%$. Equations 2.15 and 2.16 can e.g. be applied to check a complete set of exhaust concentrations for consistency.

In state of the art three-way catalytic converter systems the lambda value is available by means of a linear lambda sensor. If a lambda signal is available with a higher accuracy than the oxygen signal, the oxygen concentration may be calculated by rearranging equation 2.14:

$$
\begin{aligned}
y_{O_2} \;=\; & \frac{\lambda(4+x)(y_{H_2} + y_{CO} + 9y_{C_3H_6} + 10y_{C_3H_8} - y_{NO})}{2\left(\lambda(4+x) + x\, y_{O_2,air}\right)} + \\
+ \; & \frac{y_{O_2,air}\left(\lambda(4+x) - 4\right)\left(2 - y_{H_2} - y_{CO} + y_{C_3H_6} + 2y_{C_3H_8}\right)}{2\left(\lambda(4+x) + x\, y_{O_2,air}\right)} - \\
- \; & \frac{x\, y_{O_2,air}\left(2 - 2y_{H_2} - 2y_{CO} - 8y_{C_3H_6} - 8y_{C_3H_8} + y_{NO}\right)}{2\left(\lambda(4+x) + x\, y_{O_2,air}\right)}
\end{aligned} \tag{2.17}
$$

This approach is applied in chapter 7.

2.2 Engine Out Concentrations

In this section a collection of typical average and maximum exhaust species concentrations is given. The data are derived from modal engine exhaust measurements during both FTP75 and MVEG-A/B test runs with engines ranging from 1.4 to 2.8 l cubic capacities throughout the years 1993 - 2002 (table 2.2). Some of the test runs were performed during engine application, thus not all of them do meet the emission thresholds they target for.

time averaged values [vol%]

test run	H_2O	CO	NO	O_2	C_3H_y	CO_2
930310	12	0.83	0.067	n.a.	0.074	12
950214	11	0.70	0.059	1.6	0.091	12
950315	11	0.83	0.119	1.2	0.091	12
950703	11	0.78	0.108	1.4	0.142	12
950705	11	0.71	0.102	1.7	0.131	12
981026	11	0.58	0.098	n.a.	0.125	12
000119	11	0.74	0.090	1.6	0.085	11
020802	12	0.63	0.064	1.7	0.041	12

maximum values [vol%]

test run	H_2O	CO	NO	O_2	C_3H_y	CO_2
930310	15	4.1	0.220	n.a.	0.540	13
950214	41	2.9	0.220	21	0.530	14
950315	40	3.5	0.350	16	0.725	14
950703	25	3.3	0.300	20	1.000	14
950705	19	6.0	0.340	13	1.370	13
981026	16	2.5	0.280	n.a.	0.330	14
000119	14	4.7	0.320	22	0.320	13
020802	17	2.2	0.325	21	0.330	13

Table 2.2: Measured time averaged and maximum engine exhaust species concentrations in vol% during European and US emission certification driving cycles for 1.4 to 2.8 l engines - arbitrary selection of tests performed during the last decade.

Volkswagen's System for Emission Sampling And Measurement (SESAM) provides time resolved concentration analysis of the polar exhaust species by means of Fourier Transform Infrared Spectroscopy (FTIR) with a sampling rate of 1 Hz [8]. The non-polar oxygen is analyzed after condensation of water with a paramagnetic analyzer. No hydrogen analysis is available. For the variety of engines evaluated, the time averaged engine exhaust concentrations agree quite well. Water and carbon dioxide with average values of 11 % and 12 % respectively are approximately 1.5 % below the corresponding values for complete fuel combustion combined with stoichiometric air supply (section 2.1). The data basis with just a few engines developed to a different degree in different driving cycles is too weak for a sound review of engine out concentrations.

But it is clear from table 2.2 that the improvements in legislated tailpipe emissions achieved during the recent decade (chapter 1) are to a higher degree due to more efficient exhaust aftertreatment and to a lesser due to "cleaner" engines. The engine with the lowest average emissions is Volkswagen's low-end torque 2.0l-2V-85kW engine (model EA113) with e.g. average hydrocarbon emissions of 400 ppm C_3H_y (test run 020802 in table 2.2). In combination with a sophisticated exhaust aftertreatment strategy it fulfills the SULEV thresholds and is sold in California from summer 2002 on. In this work it is chosen for model validation (chapter 7).

The maximum carbon dioxide concentrations are consistent with the calculated value of 13.4 % for complete stoichiometric combustion, whereas the maximum water concentrations are for some test runs way above their respective value of 12.4 %: This is due to water condensation during cold start, followed by a more or less immediate evaporation which leads to such significant water overshoot. Time resolved engine exhaust concentrations during the cold start phase of test run 020802 with relatively moderate overshoot of approximately 5 % demonstrate this phenomenon (figure 2.2). It can be seen how water concentration gradually increases to a value of 11 - 12 % during the first 90 sec while a peak of water evaporated from the exhaust line appears at about 210 sec. Nitrogen oxides are formed in the engine during regular driving under high load. It can be seen from figures 2.2 and 2.3 that nitrogen oxide formation is closely coupled to engine load. The maximum nitrogen oxide concentrations for the different test runs agree with each other.

Maximum carbon monoxide and hydrocarbon emissions however exhibit significant differences. They depend on the respective engine application. This can be illustrated with the example of hydrocarbon emissions and test run 000119 (figure 2.3). Fuel cut during deceleration is consistently applied: In figure 2.3 the vehicle goes twice into deceleration during the first four minutes of the FTP75 test cycle (at $t = 115$ s and $t = 183$ s). For the sake of fuel economy the fuel injection is interrupted for some seconds, as can be seen from the lambda signal that goes to lean values far away from stoichiometry. At the same time the carbon dioxide concentration drops down to values close to zero[2] indicating that combustion has stopped. Likewise the water signal should drop down, but due to saturation with previously condensed water the response is noticeable damped. During fuel cut the engine out hydrocarbon emissions increase significantly: High boiling gasoline fractions condensed during high load on the intake manifold walls are sucked away by the engine which rather acts as a vacuum pump - trying to evacuate the space between almost closed throttle and intake ports. Immediate after fuel cut the hydrocarbon emissions further increase until the air-fuel-mixture - which is lead back to slightly rich conditions - catches fire again.

As mentioned before, fuel cut was previously applied under the aspect of driveability and fuel economy. In chapter 7 fuel cut is discussed in terms of oxygen storage management and in appendix B in terms of aging.

[2]the signal probably would be zero if dispersion within the one liter optical chamber of the FTIR analyzer (mean residence time $\tau > 3s$) could be neglected.

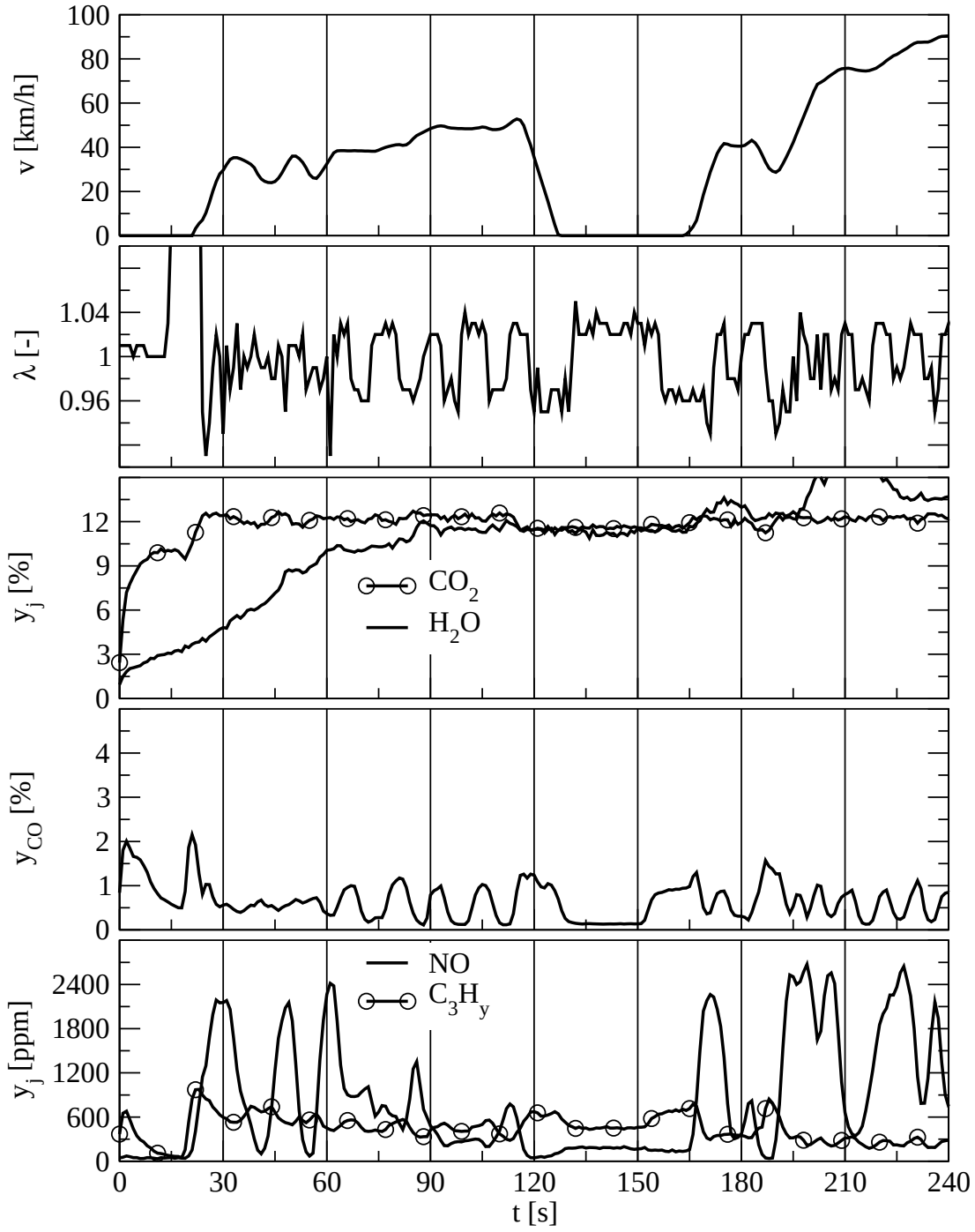

Figure 2.2: Modal raw engine out exhaust measurements during the first four minutes of an FTP75 emission certification driving cycle - Volkswagen Jetta equipped with a 2.0l-2V-85kW engine and four gear automatic transmission (test run 020802).

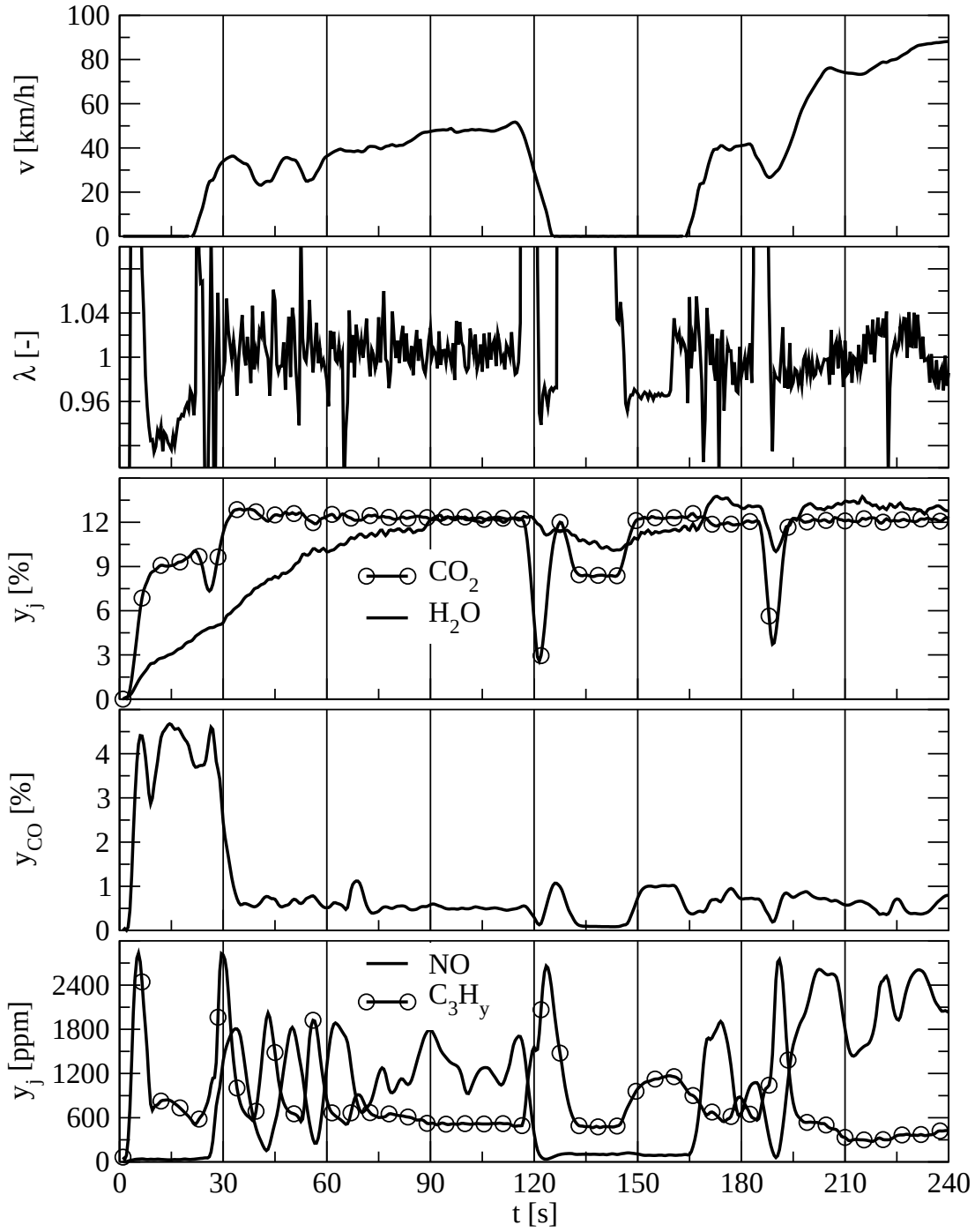

Figure 2.3: Modal raw engine out exhaust measurements during the first four minutes of an FTP75 emission certification driving cycle - Volkswagen New Beetle equipped with a 2.0l-2V-85kW engine and five gear manual transmission (test run 000119 - development status).

Chapter 3

Thermodynamic Equilibria in Exhaust Aftertreatment

The state of the art exhaust aftertreatment device for regular (non stratified charge) spark ignition engines is the so called Three-Way Catalytic (TWC) converter. The term is derived from the three legislated pollutants (pollutant groups) which primarily need to be converted: carbon monoxide, nitrogen oxides and hydrocarbons.

The converter is build up from monolithic structures coated with high surface ceramic washcoats which contain - amongst other substances - at least one of the precious metals platinum, palladium and rhodium.

Either coiled corrugated metal foil monoliths (supplier: Emitec) or extruded ceramic monoliths (suppliers: Corning, Denso, NGK) are commercialized. Extruded cordierite ($2\,MgO \cdot 2\,Al_2O_3 \cdot 5\,SiO_2$) monoliths are most common today.

The precise composition and construction of the washcoat is regarded as the coaters proprietary information. Two palladium rich series three-way catalytic converters are investigated in this work. The basic available information provided by the coater (Umicore) is listed in table 3.1. Further information is gathered in appendix F.

	converter A	converter B
Washcoat	MLKX5	MLKV150
PM	100 g/ft^3 Pd/Rh 14/1	100 g/ft^3 Pd/Rh 14/1
Substrate	CG 600 cpsi 4* mil	CG 400 cpsi 8 mil
Dimensions	$4.66'' \times 6''$	$4.66'' \times 6''$
Lot	90803	AS 093/2

Table 3.1: Series Pd-rich three-way catalytic converters – information provided on shipping papers (*the average wall thickness is rather $s = 4.3$ mil $= 0.11$ mm according to the substrate supplier Corning).

Although palladium was rarely used in first generation three-way catalysts in the 1980s it emerged in three-way catalytic applications in the 1990s for economical and tech-

nical reasons: Palladium was significantly less expensive and exhibited a lower light-off temperature for hydrocarbons under net-oxidizing atmosphere. Based on equal masses palladium is in particular more effective in oxidation of unburned paraffins and aromatic hydrocarbons [113]. While providing a higher resistance towards sintering under high temperature lean conditions [33, 38] palladium is prone towards sulfur poisoning. Improved fuel quality and a tight air to fuel control allowed the introduction of palladium based catalysts [23, 113].

3.1 Gas-Gas Reactions

Two out of three restricted emissions can be reduced by further oxidation with oxygen: carbon monoxide and hydrocarbons. Throughout this work the group of hydrocarbons is represented by propane and propene, a simplification which is quite common [120, 40, 89, 1, 80, 153]. Hydrogen is a combustible exhaust gas species which is not legislated but very important in terms of catalyst light-off (chapter 5), warmed-up conversion with slightly rich bias (chapter 7) and oxygen sensor distortion (chapter 6).

During cold start the combustion with oxygen plays a major role:

$$H_2 + 0.5\,O_2 \rightleftharpoons H_2O \tag{3.1}$$
$$CO + 0.5\,O_2 \rightleftharpoons CO_2 \tag{3.2}$$
$$C_3H_6 + 4.5\,O_2 \rightleftharpoons 3\,CO_2 + 3\,H_2O \tag{3.3}$$
$$C_3H_8 + 5\,O_2 \rightleftharpoons 3\,CO_2 + 4\,H_2O \tag{3.4}$$

Nitrogen oxide reduction is an additional/competing route for the conversion of combustible species:

$$H_2 + NO \rightleftharpoons H_2O + 0.5\,N_2 \tag{3.5}$$
$$CO + NO \rightleftharpoons CO_2 + 0.5\,N_2 \tag{3.6}$$
$$C_3H_6 + 9\,NO \rightleftharpoons 3\,CO_2 + 3\,H_2O + 4.5\,N_2 \tag{3.7}$$
$$C_3H_8 + 10\,NO \rightleftharpoons 3\,CO_2 + 4\,H_2O + 5\,N_2 \tag{3.8}$$

Under rich conditions the water gas shift reaction (reaction 3.9) and reforming reactions (reactions 3.10, 3.11) may become important:

$$CO + H_2O \rightleftharpoons CO_2 + H_2 \tag{3.9}$$
$$C_3H_6 + 3\,H_2O \rightleftharpoons 3\,CO + 6\,H_2 \tag{3.10}$$
$$C_3H_8 + 3\,H_2O \rightleftharpoons 3\,CO + 7\,H_2 \tag{3.11}$$

Chemical equilibrium calculations show that under moderately lean conditions technically relevant concentrations of nitrogen dioxide (1 ppm and above) are neither formed

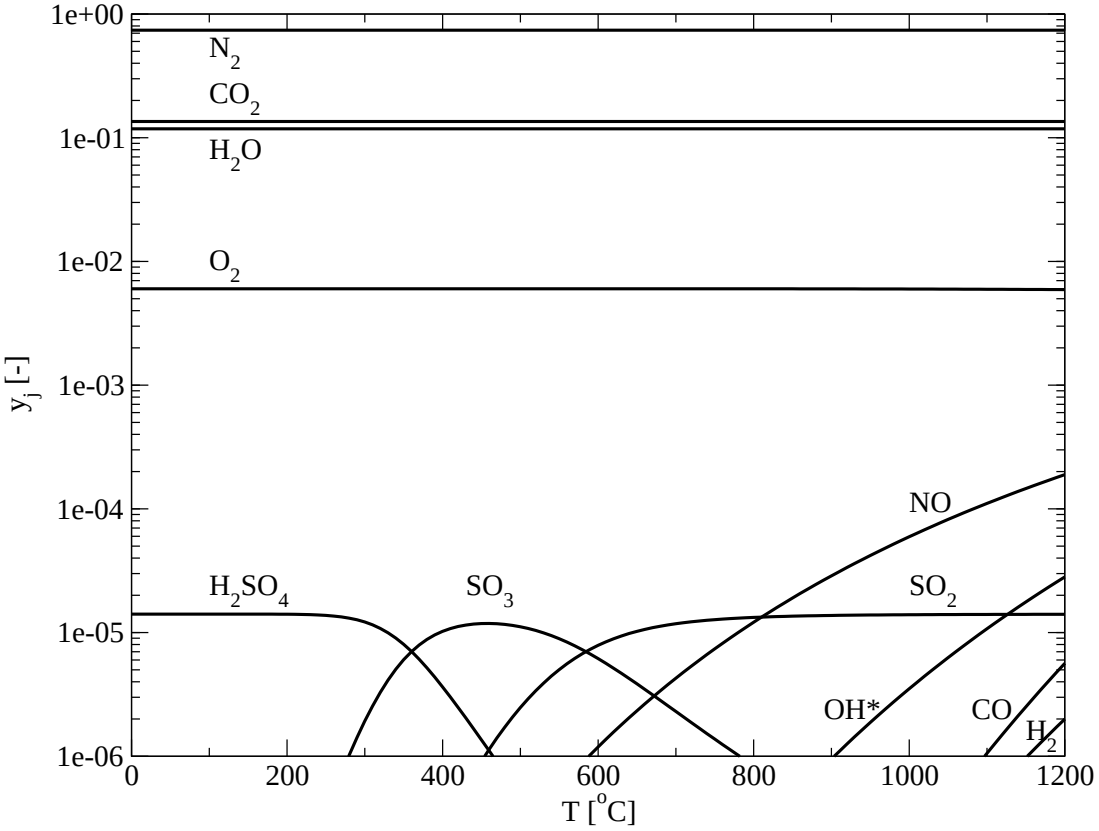

Figure 3.1: Equilibrium exhaust gas composition of technical interest (above 1 ppm) for a gasoline engine operated moderately lean ($\lambda = 1.03$, $p = 1.1$ bar), calculated with the open source NASA CEA package [51, 52] based on NIST-JANAF Thermochemical Tables [84], omitting condensed species, considering a total of 183 relevant species.

during homogeneous combustion within the engine nor within the exhaust system (figure 3.1). Thus nitrogen dioxide is not considered throughout this work.

At higher temperatures nitrogen oxide decomposition is thermodynamically limited. Engine operation at leaner conditions does not give a completely different picture since equilibrium oxygen concentration does not change by several orders of magnitude as it does upon transition of stoichiometric composition. At much leaner conditions the occurrence of nitrogen oxide emissions higher than 1 ppm is shifted towards lower temperatures. Under these lean conditions nitrogen dioxide becomes the dominant nitrogen oxide species at lower temperatures [50]. This is the case for lean burn Otto and Diesel engines.

Sulfur from fuel and lubricants is leaving the engine as sulfur dioxide but is likely to be further oxidized in the exhaust system below 700 °C [163, 36]. Below 500 °C sulfuric acid (H_2SO_4) is formed. The conversion of the combustible species hydrogen, carbon monoxide and hydrocarbons by catalytic aftertreatment can be considered practically irreversible within the temperature-range encountered ($T < 1000$ °C).

Under rich conditions however not all combustible species can be combusted with either oxygen or nitrogen oxide (figure 3.2). While the water gas shift reaction strongly

reaction	$\Delta h_{R,i}(25\,^{\circ}C)$	$\Delta h_{R,i}(500\,^{\circ}C)$	$K_i(25\,^{\circ}C)$	$K_i(500\,^{\circ}C)$
	kJ/mol	kJ/mol	-	-
3.1	-242	-246	$1.2\,10^{040}$	$7.3\,10^{013}$
3.2	-283	-284	$1.2\,10^{045}$	$3.5\,10^{014}$
3.3	-1926	-1926	$4.8\,10^{338}$	$2.3\,10^{131}$
3.4	-2044	-2044	$4.5\,10^{363}$	$5.5\,10^{143}$
3.5	-332	-337	$1.9\,10^{055}$	$2.1\,10^{019}$
3.6	-374	-374	$1.9\,10^{060}$	$1.0\,10^{020}$
3.7	-2742	-2742	$3.0\,10^{475}$	$3.0\,10^{180}$
3.8	-2950	-2950	$4.4\,10^{515}$	$2.1\,10^{198}$
3.9	-41	-37	$9.9\,10^{004}$	$4.8\,10^{000}$
3.10	374	403	$9.3\,10^{-38}$	$3.3\,10^{004}$
3.11	498	532	$7.3\,10^{-53}$	$1.1\,10^{003}$

Table 3.2: Standard heat of reactions 3.1 to 3.11 and corresponding equilibrium constants at 25 and 500 °C, calculated from pure gaseous species standard heats and entropies of formation are summarized in appendix G, heat capacities in appendix I.

favors the formation of hydrogen at low temperatures (high equilibrium constant $K_i(T)$ in table 3.2) it equilibrates a carbon monoxide rich mixture at high temperatures (figure 3.2). Since hydrogen requires non-standard, high-maintenance gas analysis systems like soft ionization mass spectrometry – or careful cross sensitivity corrections as discussed in section A.1 – it is common to assume its concentrations to be one third of the corresponding carbon monoxide concentrations [175, 123, 20, 97, 80, 153]. This value is established due to equilibration of the water gas shift reaction at approx. 1250 °C - a temperature likely to be encountered in the exhaust port region (figure 3.3).

Even at moderate temperatures the endothermic steam reforming reactions allow practically complete hydrocarbon conversion. The formation of ammonia (NH_3) is favored at temperatures below 600 °C. Therefore early dual brick concepts with mid brick secondary air (rich engine out exhaust nitrogen oxide conversion in the first brick followed by secondary air assisted oxidation reactions in the second brick) failed due to significant ammonia formation under rich conditions [175, 38]. Sulfur dioxide is likely to be converted to hydrogen sulfide which strongly poisons metal surfaces and in particular lowers the activity for hydrocarbon conversion of palladium supported on cerium-zirconium rich washcoats [138] (chapter 8). Equilibrium conversion of SO_2 towards H_2S is practically complete below 800 °C [36]. The amount of hydrogen stored during rich engine operation as hydrogen sulfide sticking to the catalytic surface under rich conditions is reported to be that high, that it may contribute significantly to the delay time (and thus to the so-called oxygen storage capacity – see chapter 6) measured on a standard engine test bench [138]. Furthermore the formation of hydrogen sulfide is particularly objectionable because of its strong odor [64].

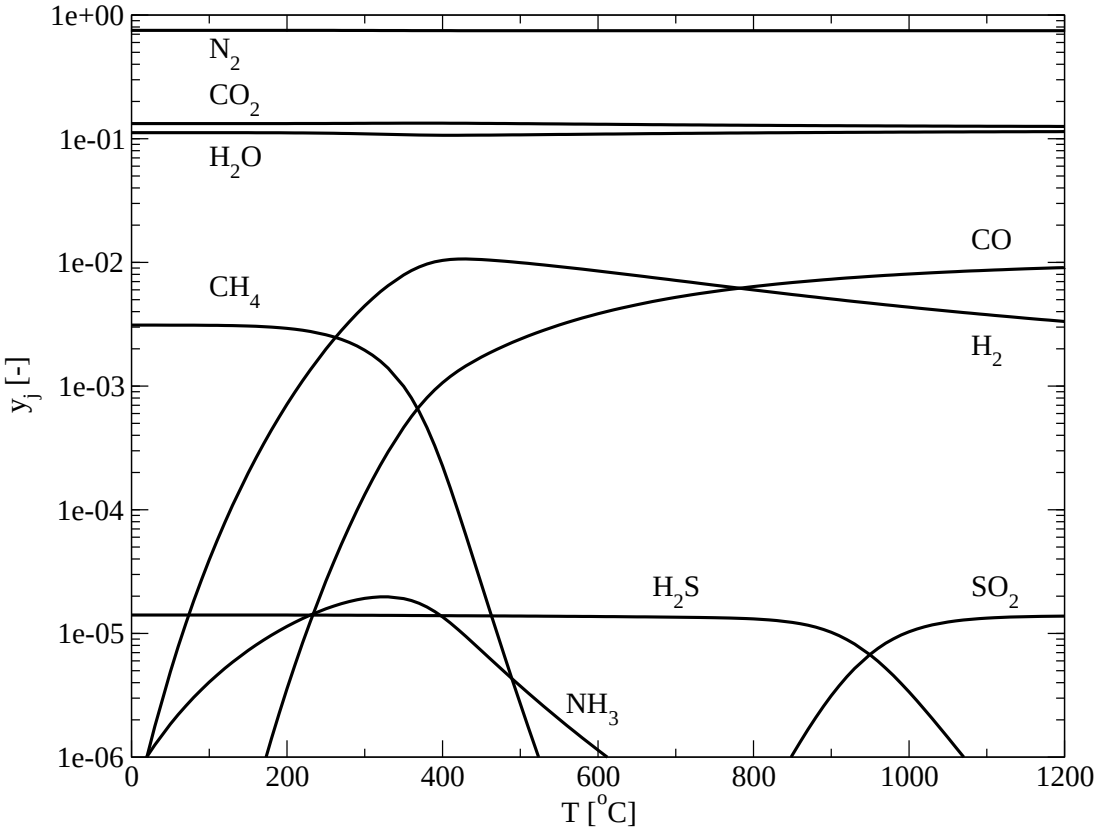

Figure 3.2: Equilibrium exhaust gas composition of technical interest (above 1 ppm) for a gasoline engine operated moderately rich ($\lambda = 0.97$, $p = 1.1\,\mathrm{bar}$), calculated with the open source NASA CEA package [51, 52] based on NIST-JANAF Thermochemical Tables [84], omitting condensed species, considering a total of 183 relevant species.

3.2 Gas-Solid Reactions

3.2.1 Soot Formation

The formation of soot is not considered in the reaction equilibria of the rich gas phase discussed (figure 3.2). An oxygen deficient, carbon monoxide rich atmosphere might lead to soot formation. If soot is represented by carbon, which is a save simplification since e.g. aromatic species are even less favored, the formation of soot can be described by the Boudouard reaction:

$$2\,\mathrm{CO} \rightleftharpoons \mathrm{C} + \mathrm{CO_2}\,, \qquad \Delta h_\mathrm{R}(25^\circ\mathrm{C}) = -172\,\mathrm{kJ/kmol} \tag{3.12}$$

Since the carbon phase is – if existent – a pure phase and thus the chemical potential of this phase is that of pure carbon, the equilibrium carbon monoxide concentration can be expressed by (e.g. [105]):

$$y_\mathrm{CO}^\mathrm{eq} = \sqrt{\frac{y_\mathrm{CO_2}^\mathrm{eq}}{K_i(T)}}\sqrt{\frac{p^0}{p}} \qquad \text{with:} \quad K_i(T) = \mathrm{e}^{-\dfrac{\Delta g_R(T)}{RT}} \tag{3.13}$$

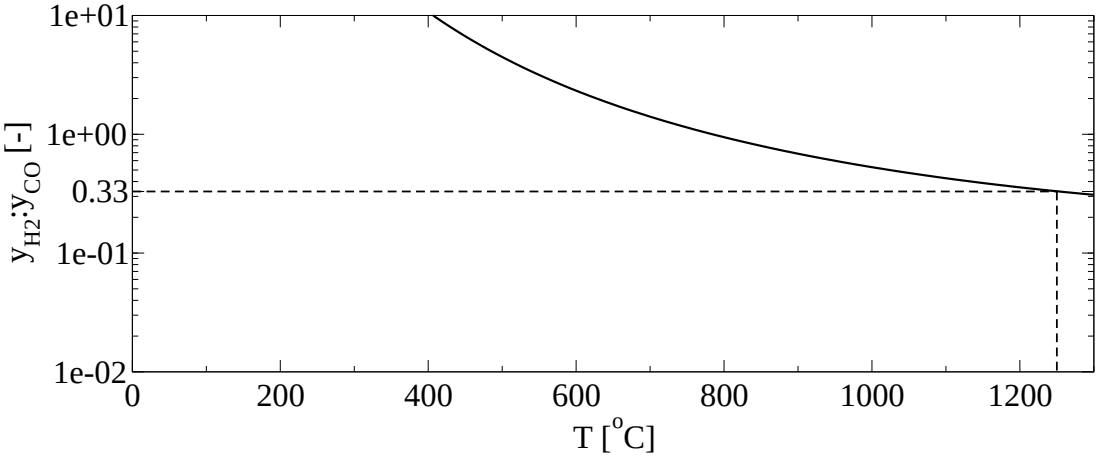

Figure 3.3: Hydrogen to carbon monoxide ratio - equilibration of water gas shift reaction no. 3.9. The commonly assumed ratio of 0.33 corresponds to a gas temperature of approx. 1250 °C - a reasonable value within the exhaust valve region.

For temperatures above 330 °C the Boudouard carbon monoxide equilibrium concentrations are higher than the respective carbon monoxide concentrations in the gas phase without Boudouard reaction (figure 3.4). Thus the Boudouard reaction favors in this temperature range the formation of carbon monoxide from carbon dioxide and carbon already in the system. By the time that the carbon is consumed the solid phase disappears and the carbon monoxide concentration labeled *without Boudouard reaction* will establish in chemical equilibrium.

In the colder temperature range below 330 °C the carbon formation is favored by thermodynamics. Reaction systems with pure condensed phases have an ”all-or-nothing”-character [35]: thermodynamics would not limit the carbon build up in an open system like the exhaust system.

Since the Boudouard reaction is known to be very slow – especially in the low temperature range where it might play a role – and since the three-way catalytic converter is not fed with rich exhaust in that low temperature range (chapter 2) the formation of soot is not considered in the mathematical model of the catalytic converter (chapter 4).

3.2.2 Oxide Formation

A common way of evaluating the stability of metal oxides is to plot the standard free energies of metal oxide formation reactions versus temperature [105, 102].

Precious Metal Oxides Precious metal oxides might be stable under lean conditions. Thermodynamic calculations indicate that Rh_2O_3 has a higher stability compared to PdO (figure 3.5): for oxygen partial pressures above the metal oxide lines the metals are oxidized in equilibrium, below the metallic state is favored.

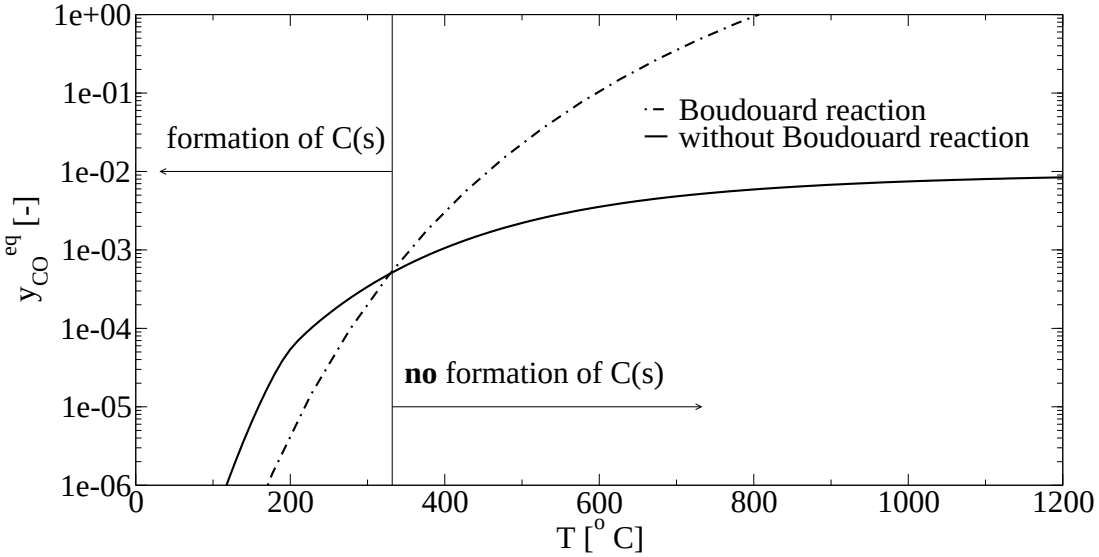

Figure 3.4: Equilibrium carbon monoxide concentration calculated for moderately rich gasoline combustion (λ = 0.95, x = 1.85, p = 1.0 bar, omitting soot and methane formation) along with the carbon monoxide concentration resulting from Boudouard reaction equilibrium with a carbon dioxide concentration fixed to y_{CO_2} = 13%

In contact to moderate lean exhaust (λ = 1.03) pure palladium oxide is likely to decompose at temperatures above approx. 660 °C. Above approx. 870 °C pure Rh_2O_3 decomposes as well and both metals will prevail in their metallic state, as they do for all temperatures in contact with rich exhaust. Thus the pure precious metals palladium and rhodium are likely to undergo oxidation/reduction cycles when the exhaust composition changes from rich to lean and vice versa under low- and mid-temperature operating conditions [14]. Palladium oxide has been addressed as a major source of oxygen storage [109]. Since e.g. palladium oxide is recognized to be the catalytically active phase [136, 141] this is not just important in terms of oxygen storage (especially for catalysts with high precious metal loadings as discussed in chapter 6) but also in terms of catalytic activity (chapter 5 and 7).

Another source of oxygen storage is the formation of washcoat constituents oxides. This contribution is generally attributed to cerium containing oxides.

Cerium Oxides Cerium oxides are reported to be present in high quantities in automotive three-way catalytic washcoats (28 weight% [115], e.g. 1000 g/ft^3 [166]). Cerium oxides are capable of undergoing a change in oxidation state depending on the redox potential of the exhaust. In particular the IV-valent cerium dioxide CeO_2 can be transformed to the III-valent cerium sesquioxide Ce_2O_3 while keeping the same cubic fluorite type crystal structure and thus having a very small volume change (high mechanical stability) compared to early oxygen storage materials as copper or ferrous oxides [152]:

$$2\,CeO_2 \rightleftharpoons Ce_2O_3 + 0.5\,O_2\,, \qquad \Delta h_R(25^\circ C) = 380\,kJ/kmol \tag{3.14}$$

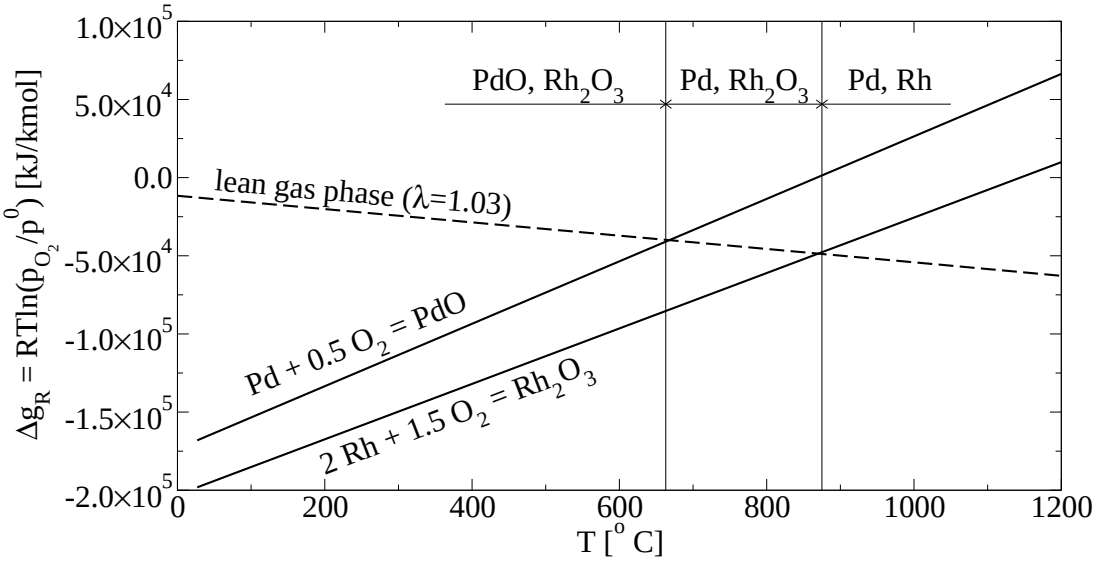

Figure 3.5: Ellingham diagram for pure palladium and rhodium and their stable oxides along with a slope representing the equilibrium oxygen potential in a moderate lean exhaust. Gibbs energies of formation are listed in table G.1.

If one would plot the Gibbs free energies of reactions for cerium oxides into the Ellingham diagram 3.5 they would be far below the precious metal oxides[1] indicating that cerium oxides are much more stable and thus much harder to reduce [160].

It can be seen from the – still incomplete – Ce-O phase diagram (figure 3.6) that cerium oxide reduced at elevated temperatures forms a seeming continuum of oxygen-deficient non-stoichiometric oxides, whereas at lower temperatures superstructures with complex stoichiometries build up.

Thus the formation reaction of oxygen deficient cerium oxide under reducing conditions reads:

$$CeO_2 \rightleftharpoons CeO_{2-y} + \frac{y}{2} O_2, \quad 0 \leq y \leq 0.5 \tag{3.15}$$

Bulky cerium oxide exposed to moderately rich exhaust ($\lambda = 0.97$) can not be reduced to higher oxygen deficiencies than $CeO_{1.99}$ below 1000 °C (see figure 3.7). In support of this finding it has been reported that the reduction of bulk ceria by hydrogen is thermodynamically not favored at the typical H_2O concentrations and temperatures present in automotive exhaust [129].

Even in flowing de-oxidized, dehumidified hydrogen, unsupported cerium oxide needs temperatures as high as 900 °C for complete reduction, whereas full re-oxidation is facile at 200 °C [181] or even at 25 °C [14, 2]. Thus reduction is the limiting step in pure cerium oxygen storage [72].

Ultra fine ceria poly-crystals of less than 50 nm grain size have an enhanced reducibility compared to bulk cerium oxides [30, 160, 164, 31]. Nanostructured 30 nm

[1] with the current axis settings they would not even appear on the plots

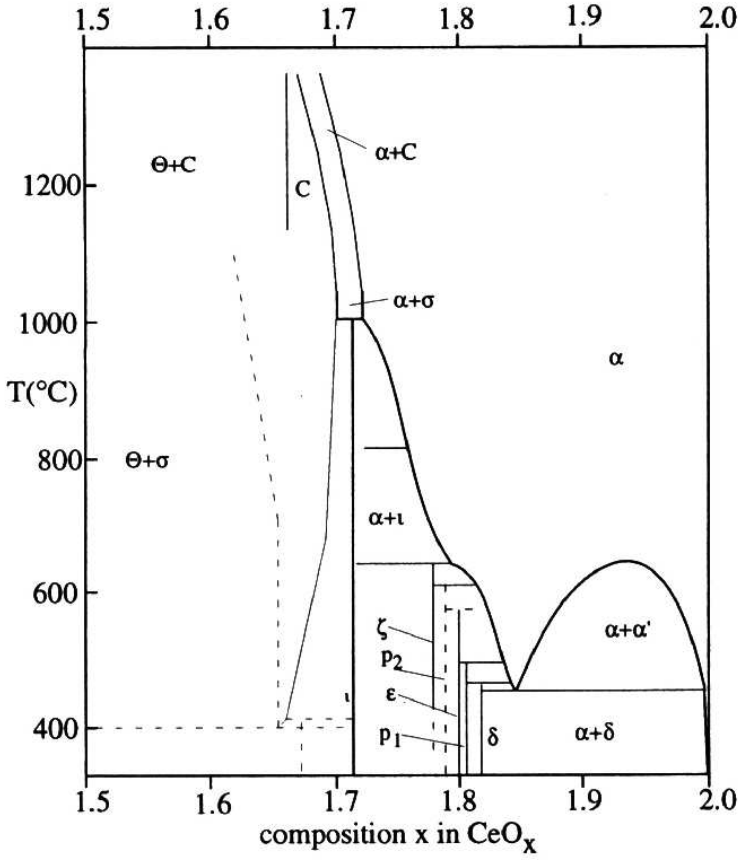

Figure 3.6: Ce-O phase diagram: x = 2 refers to cerium oxide in its completely oxidized state, x = 1.5 to the completely reduced state [160].

cerium oxide however does not exhibit a significantly improved oxygen reducibility (figure 3.7). After calcination in air at 800 °C ceria particles supported on aluminum oxide can have particle sizes as low as 55 to 67 Å which means that roughly every second cerium oxide offers a surface site. However oxygen storage capacities (OSCC) of these highly dispersed materials measured under more realistic conditions is still two orders of magnitude below the values obtained by temperature programmed reduction with high purity hydrogen [181]. Unsatisfactory oxygen storage capacities for practical use with deficiency values lower than y = 0.005 are reported [152]. Pure Ce_2O_3 is probably not formed during the redox cycles in automotive exhaust [59, 34].

Due to its negligible oxygen storage capacity under real exhaust conditions and the poor thermal stability with sintering temperatures as low as 800 °C pure cerium oxide is not a major component in modern three-way catalysts [34, 33].

Ceria-Zirconia Materials Ceria-zirconia mixed oxides are major washcoat components in state of the art three-way catalytic converters [15, 171]. The incorporation of ZrO_2 into the CeO_2-lattice strongly modifies the reduction behavior compared to pure cerium oxide [42]. Ceria-zirconia solid solutions with less than 20 mol% Zr^{+4}

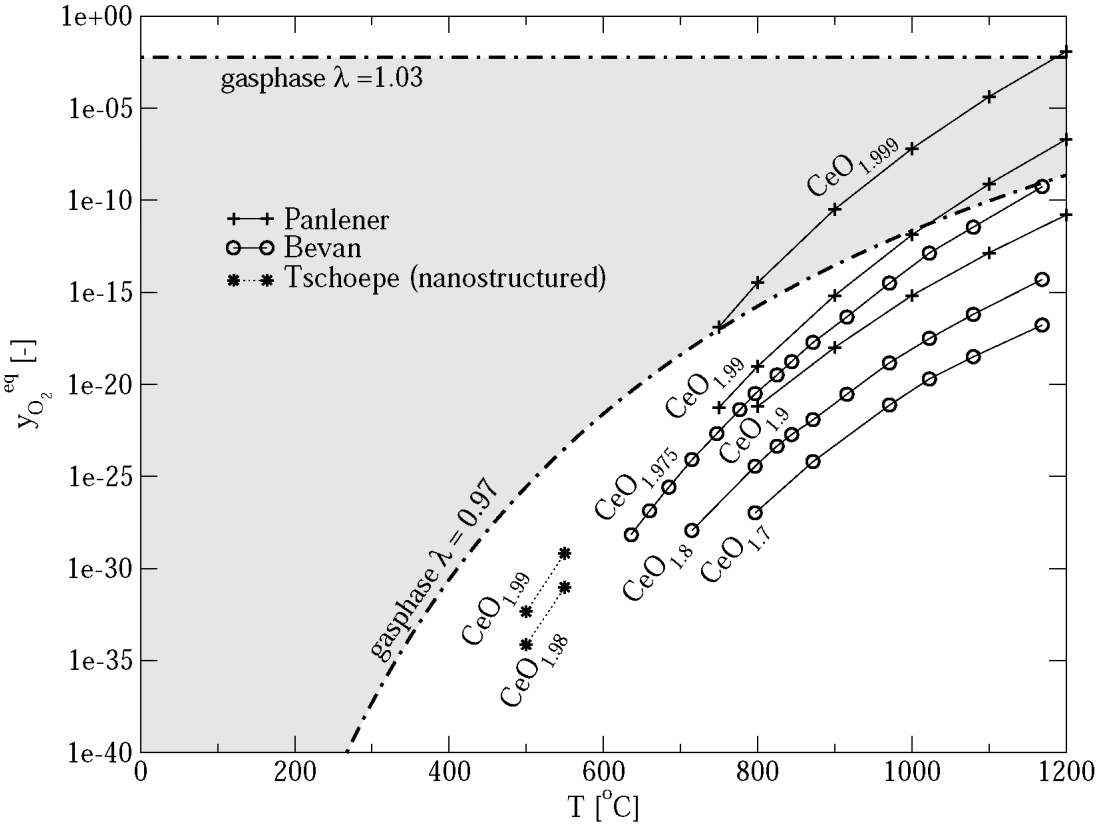

Figure 3.7: Oxygen decomposition pressures in equilibrium with oxygen deficient phases CeO_{2-y} along with the equilibrium oxygen partial pressures in moderate rich and lean exhaust [130, 16, 164].

dissolved in the CeO_2 lattice were developed as excellent oxygen storage materials in 1987 [150]. In 1996 a new technology was developed to dissolve more than 20 mol% Zr^{+4} [152]. The complete oxygen storage capacity (OSCC) based on cerium oxide mass of catalysts containing zirconium rich oxygen storage components is reported to be one order of magnitude higher compared to catalysts containing pure high surface area cerium dioxide[2]. Thus a catalyst with zirconium rich oxygen storage components exhibited a better oxygen storage/release behavior with 85% less ceria loading compared to a catalyst with pure cerium dioxide [113].

Even though the oxidation state of ZrO_2 remains unchanged, its presence in the mixed oxide crystal facilitates the oxidation state change of its neighboring cerium atoms [152]. The incorporation of undersized Zr^{+4} with an effective ionic radius of 0.84 Å into the cerium oxide framework might mitigate the mechanical stress induced upon reduction from Ce^{+4} (ionic radius 0.97 Å) to Ce^{+3} (ionic radius 1.14 Å) and thus ease reduction [114].

Zirconium also adds thermal stability to the precious metals and washcoat oxides [152]. A perfect ceria-zirconia solid solution with a Ce/(Ce + Zr) cation ratio of $\zeta = 0.5$

[2]catalyst samples are loaded with 60 g/ft^3 Pd, measured OSCC for samples containing highly dispersed pure CeO_2 is lower than the value which can be attributed to the formation of PdO.

will build the κ-phase $CeZrO_4$ under lean and the pyrochlore $Ce_2Zr_2O_7$ under sufficing rich conditions [152]. The equilibrium ZrO_2-CeO_2 phase diagram reveals that at quite high temperatures the mixed oxide prevails as a homogeneous solid solution. Upon cooling the cubic phase solid solution transforms into a tetragonal t-phase. The transition temperature of approximately 2350 °C for virtually pure zirconium dioxide (cerium content $\zeta \approx 0$) is shifted towards lower temperatures with increasing cerium content: the respective transition temperature for a cerium-zirconium oxide solid solution with a cerium content of e.g. $\zeta = 0.8$ is as low as $\sim$ 1220 °C) [156].

Hydrothermal treatment at sufficiently high temperatures leads to (stable) oxygen deficient pyrochlore. Upon re-oxidation at temperatures as low as 600 °C the metastable cubic κ-phase is obtained [128].

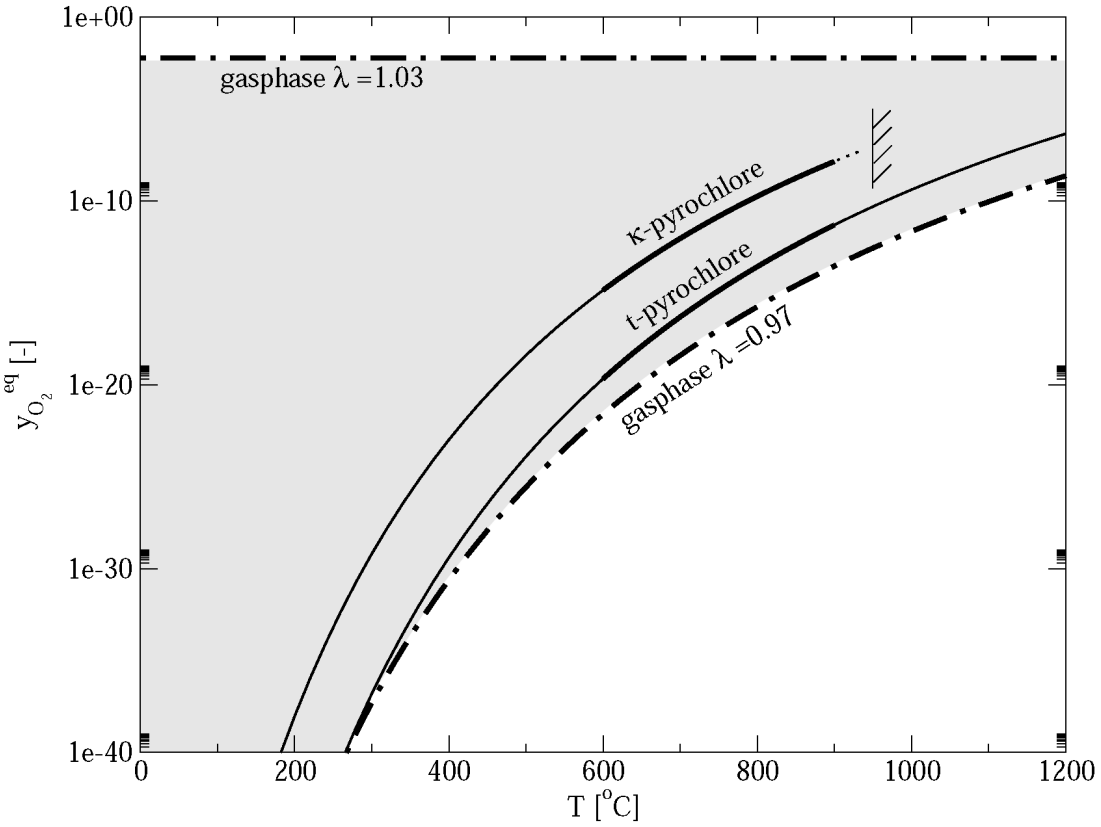

Figure 3.8: Temperature dependence of oxygen pressures over cubic and tetragonal phase $CeZrO_2$ decomposing to oxygen deficient pyrochlore $CeZrO_{1.75}$ (thin lines extrapolated) along with the equilibrium oxygen partial pressures in moderate rich and lean exhaust [128].

Reduction of the κ-phase is more facile compared to the t-phase (figure 3.8). With increasing temperatures the equilibrium partial pressures increase as well, indicating that the fully oxidized materials become thermodynamically less stable. Below 250 °C the tetragonal phase can not be reduced in moderate rich exhaust atmosphere, wheres the cubic phase has still the potential to be reduced. The thermodynamically unstable (metastable) κ-phase does exist up to 900 °C where it transforms into the tetragonal phase [128].

Since the zirconium content can vary between 0 and 100 % and intermediate oxygen deficient oxides can be formed on the cerium oxide sub-lattice the general reaction equation reads:

$$Zr_{1-\zeta}Ce_{\zeta}O_2 \rightleftharpoons Zr_{1-\zeta}Ce_{\zeta}O_{2-\zeta y} + \frac{\zeta y}{2}O_2, \quad 0 \leq y \leq 0.5, \quad 0 \leq \zeta \leq 1 \tag{3.16}$$

Thermodynamic models predict that the oxygen decomposition pressures corresponding to the same oxygen deficiency y on the cerium oxide sub-lattice strongly increase with increasing zirconium content (decreasing cerium content ζ) [75, 74, 76]. Temperature programmed reduction experiments show significantly lower reduction peak temperatures. Most facile reduction is observed at a zirconium content of 50 % [117, 118]. Zirconia rich regular ordered ceria-zirconia solid solutions with cerium contents $0.2 \leq \zeta \leq 0.5$ can be reduced to oxygen deficiencies on the cerium oxide sub-lattice close to the theoretical maximum value of $y = 0.5$ [152]. In this composition range the oxygen mobility within the solid solution crystal is approximately two orders of magnitude higher compared to pure cerium oxide [19, 161]. It increases significantly with increasing temperature (figure J.2).

Temperature programmed reduction by hydrogen of samples aged at 1000 °C is reported to be not yet complete at 950 °C with pure CeO_2 whereas it is complete below 680 °C with $Ce_{0.5}Zr_{0.5}O_2$ [42]. After aging in air at 1000 °C for 5 h ceria-zirconia solid solutions doped with Al_2O_3 developed in 1998 provide an even higher oxygen storage capacity compared to undoped ceria-zirconia solid solutions [152]. According to the diffusion barrier concept a layer of aluminum inhibits the coagulation of cerium-zirconium solid solution and aluminum at higher temperature [150].

Nevertheless, segregation of the mixed oxide solid solution storage component at high temperature seems to be the major cause for loss of oxygen storage capacity in aged catalysts. Since the loss of oxygen storage capacity is correlated with the loss of catalytic activity (see appendix B, figure B.2) it can be exploited for on board diagnosis (OBD) of the state of an exhaust catalyst.

3.2.3 Sulfate Formation

Gasoline market fuels in Europe contain up to 50 ppm on a weight basis of elementary sulfur at present [131]. Sulfates of washcoat components may be formed if sulfur is present as SO_2 or SO_3 in the exhaust. Whereas sulfates with aluminum are likely to be formed in moderate lean exhaust up to temperatures of 400 °C sulfates from pure ceria are stable at temperatures up to 500 °C (figure 3.9). These temperatures give an indication for the temperature regime sulfur storage on washcoat oxides occurs. For a complete picture other washcoat constituents as e.g. barium oxide and ceria-zirconia solid solution oxides need to be considered.

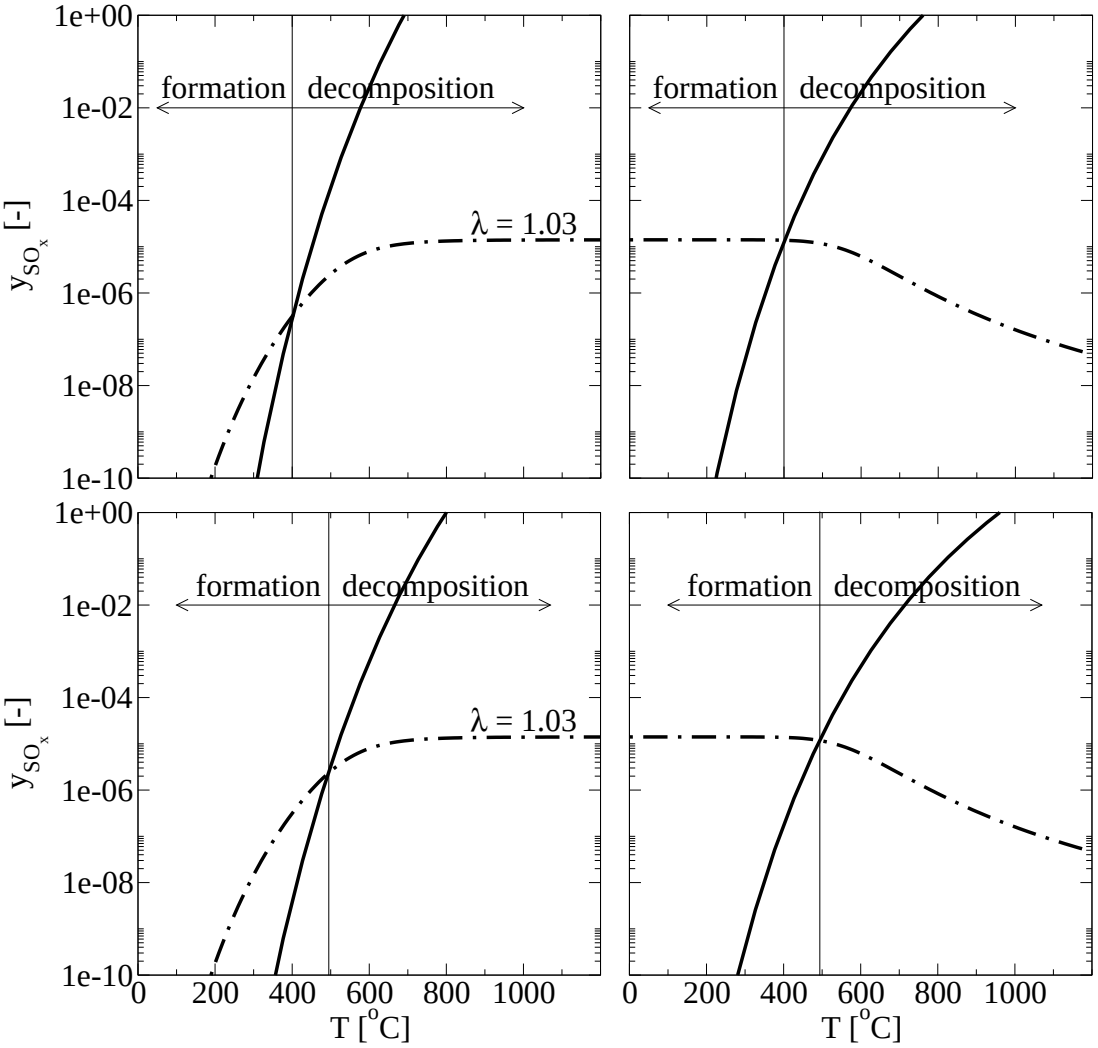

Figure 3.9: Aluminum sulfate formation (above) and cerium sulfate formation (below) with SO_2 (left) and SO_3 (right): Equilibrium SO_x pressures for sulfate formation from pure oxides along with equilibrium partial pressures in moderate lean exhaust (λ = 1.03, y_{SO_x} = 14 ppm).

Decomposition of washcoat component sulfates under rich conditions leads to the formation of H_2S, a powerful poison for metal surfaces [138]. Thus upon transition from

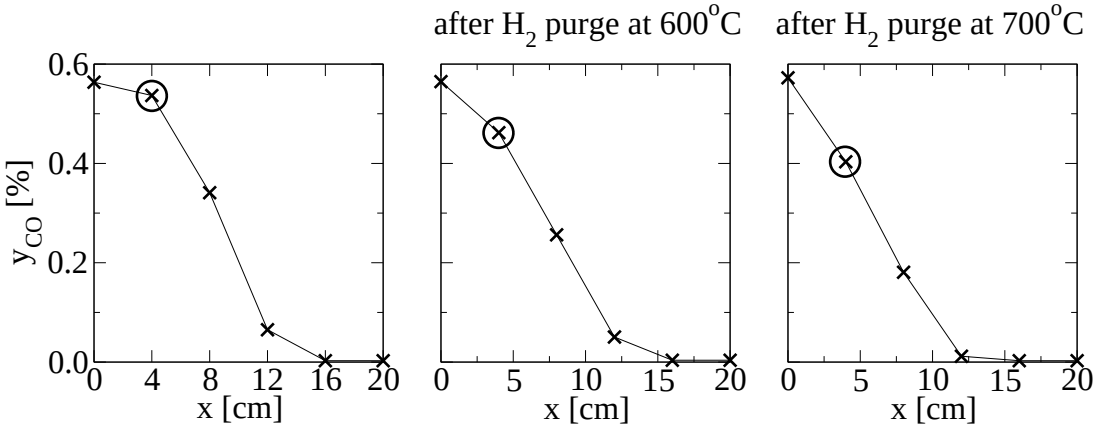

Figure 3.10: Carbon monoxide concentration profile along a monolith catalyst at 275 °C (feed composition $y^{\mathrm{f}}_{\mathrm{H_2}} = 0.19\,\%$, $y^{\mathrm{f}}_{\mathrm{CO}} = 0.57\,\%$, $y^{\mathrm{f}}_{\mathrm{C_3H_6}} = 0.08\,\%$, $y^{\mathrm{f}}_{\mathrm{C_3H_8}} = 0.065\,\%$, $y^{\mathrm{f}}_{\mathrm{O_2}} = 1.0\,\%$, $y^{\mathrm{f}}_{\mathrm{NO}} = 0.12\,\%$, $y^{\mathrm{f}}_{\mathrm{SO_2}} = 11$ ppm, $y^{\mathrm{f}}_{\mathrm{H_2O}} = 11\,\%$, balance nitrogen, $SV = 16500$ 1/h): after 22h on stream at $T = 175 \ldots 450$ °C with intermediate hydrogen purges (left), after purging with pure hydrogen for 4 h at 600 °C (center) and 700 °C (right).

lean to rich engine operation the H_2S concentration can overshoot its respective rich operation steady state value by several orders of magnitude. This phenomenon is certainly most pronounced when fresh catalysts with high oxygen storage material contents deal with exhaust of high sulfur level fuel combustion [36, 64, 59, 138].

Desulfurization temperatures of 600 °C for a full reactivation of a model platinum-rhodium catalyst are reported in literature [120]. However the fully formulated commercial three-way catalytic converter investigated in this work requires temperatures up to 750 °C for a complete sulfur purge (figure 3.10).

3.2.4 Sulfide Formation

Palladium is prone to sulfur poisoning under stoichiometric and rich conditions by strong adsorption of elementary sulfur. The formation of $Pd(S)_{ad}$ species results in significant loss in catalyst performance due to a combination of physical blockage and electronic effects inhibiting the adsorption of reactants [163].

In the late 1980's nickel – which was used before as an oxygen storage component – was used as an "H_2S scavenger" to prevent precious metal poisoning by the formation of stable nickel sulfides [64]. The automotive industry drives the process of lowering fuel sulfur contents [122], one of the causes being the prohibition of nickel use in automotive catalysts in Europe. Palladium rich formulations are known to be more sensitive to the effects of sulfur than Pt/Rh formulations [163]. Rhodium sulfides are reported to form at temperatures up to 500 °C [36]. Poisoned Pd surface can be regenerated under lean conditions by oxidation at mild temperatures [138].

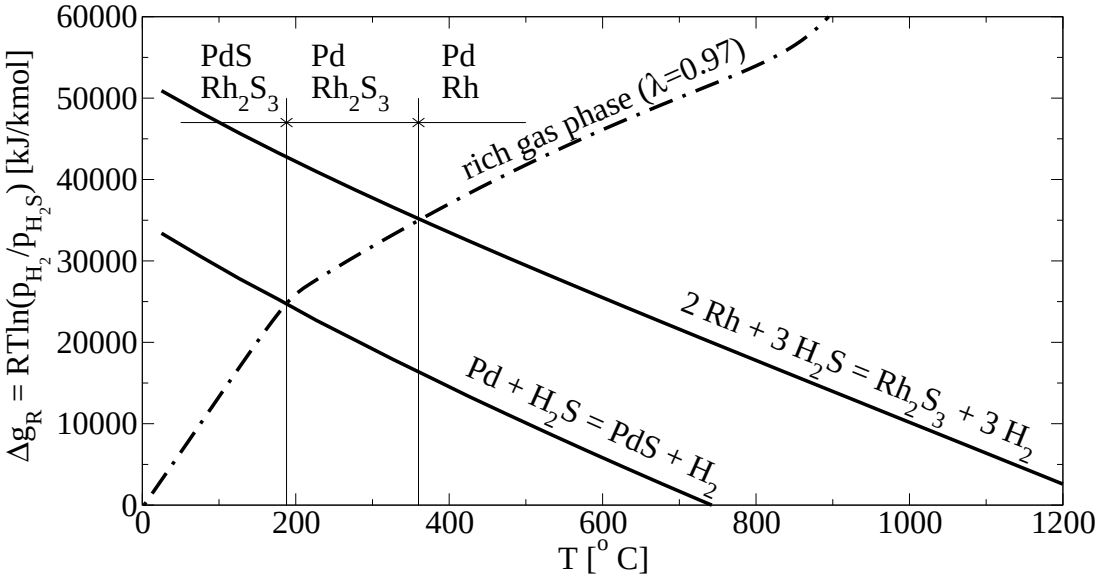

Figure 3.11: Ellingham diagram for pure palladium and rhodium and their stable sulfides along with a slope representing the equilibrium $p_{\mathrm{H_2}}/p_{\mathrm{H_2S}}$ potential in a moderate rich exhaust ($\lambda = 0.97$). Gibbs energies of formation are listed in table G.2.

Chapter 4

Mathematical Model

To cover the major phenomena occurring in a three-way catalytic converter the mathematical model described in this chapter extends an oxidation catalyst model [88, 89] with the description of nitrogen monoxide conversion reactions, water gas shift reaction, steam reforming reactions and – in particular – oxygen storage and release in the catalyst washcoat. A sound description of oxygen storage is necessary to correctly describe the competition between hydrogen, carbon monoxide and hydrocarbon oxidation on the one hand and nitrogen oxide reduction on the other hand under both rich and lean three-way catalytic operation [126].

It is assumed that the emission behavior of the catalytic converter can be described by one representative channel [62]. It has been reported that one-dimensional modeling does not significantly lack valuable emission relevant information compared to a three-dimensional model [29]. Within this single-passage channel the gas species hydrogen, carbon monoxide, propene, propane, nitrogen oxide and oxygen in the gas phase and at the catalytic surface, the oxidation extent of the available oxygen storage material, the enthalpy of the gas phase, and the enthalpy of the solid phase are balanced.

The mass flow is assumed to be laminar within the monolith's channels and evenly distributed over the monolith cross-section. Axial thermal conduction and mass dispersion are considered in both the gas bulk phase and at the catalytic surface. Oxygen diffusion within the oxygen storage material is modeled as well. Radial heat exchange between the converter and its canning has been considered to be negligible due to efficient insulation [124, 89, 126, 101, 11, 6] and is therefore omitted in the description of the mathematical model below. Enhanced heat and mass transfer between gas phase and solid phase close to the converter inlet due to boundary layer buildup is accounted for.

In contrast to elementary step models (e.g. [66, 115, 72, 70, 21, 28, 151, 57, 171, 3, 137, 61, 91, 94, 93, 92]) all mechanisms involved in the conversion of gas species (pore diffusion, adsorption, desorption, catalytic reaction) except external (gas-catalyst) mass- and heat transfer are lumped into overall reaction rate expressions.

The dynamic behavior of a three-way catalytic converter is dominated by changes in the enthalpy of the converter itself [123, 101] and the oxidation extent of the oxygen

storage material. Therefore quasi-steady state is assumed for all balances except for the solid phase enthalpy balance and the oxygen storage balance [22].

The governing equations described below are quite similar to the ones early reported except that those do not account for species storage within the solid phase and neglect thermal and mass dispersion [175, 62, 147]. Axial heat conduction in the solid phase is emphasized to have an important effect on the wall temperature profile within the catalytic converter and is thus included in more recent models [123, 132, 107, 46, 126, 26, 80, 81, 7, 1, 101, 27, 6].

4.1 Enthalpy Balances

The enthalpy of the gas phase is transported along the channel axis by convection and thermal conduction (figure 4.1). Heat is transferred through the boundary layer to the solid phase. The enthalpy of reaction released at the catalytic surface is also considered in the solid phase. In the solid phase axial thermal conduction is considered.

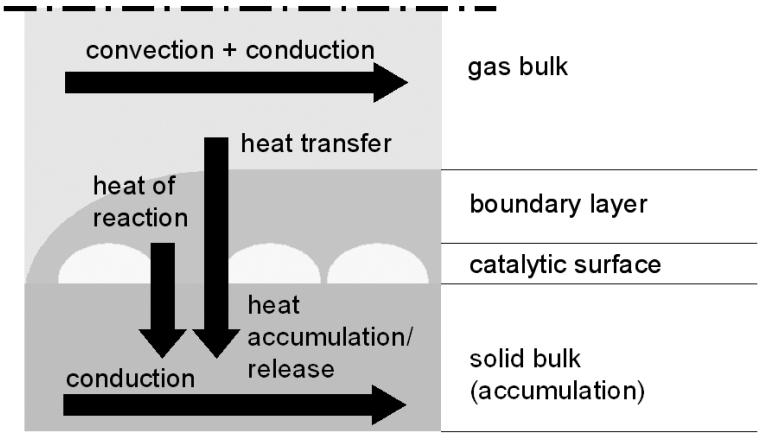

Figure 4.1: Mechanisms accounted for in the enthalpy balances.

Gas Bulk Phase The enthalpy balance in the gas phase reads:

$$0 = \underbrace{-\frac{\dot{m}}{A} c_{p,\mathrm{g}} \frac{\partial T_\mathrm{g}}{\partial z}}_{\text{convection}} + \underbrace{\varepsilon \lambda_{\mathrm{c,g}} \frac{\partial^2 T_\mathrm{g}}{\partial z^2}}_{\text{heat conduction}} + \underbrace{a_\mathrm{geo}\, \alpha\, (T_\mathrm{s} - T_\mathrm{g})}_{\text{heat transfer}} \tag{4.1}$$

with boundary conditions at the catalyst front and back respectively:

$$\left.\frac{\dot{m}}{A} c_{p,\mathrm{g}} T_\mathrm{g}\right|_\mathrm{f} = \left.\frac{\dot{m}}{A} c_{p,\mathrm{g}} T_\mathrm{g}\right|_{z=0} - \varepsilon \lambda_{\mathrm{c,g}} \left.\frac{\partial T_\mathrm{g}}{\partial z}\right|_{z=0} \quad \text{and} \quad \left.\frac{\partial T_\mathrm{g}}{\partial z}\right|_{z=L} = 0. \tag{4.2}$$

Converter specific properties such as geometric surface area and void fraction are listed in appendix F. In appendix H the heat transfer correlation applied is discussed. Gas phase properties such as heat capacity and thermal conductivity are gathered in appendix I.

Solid Phase The enthalpy balance in the solid phase with respective boundary conditions is:

$$\underbrace{(1-\varepsilon)\,\rho_{\mathrm{s}}\,c_{p,\mathrm{s}}\frac{\partial T_{\mathrm{s}}}{\partial t}}_{\text{heat accumulation}} = \underbrace{(1-\varepsilon)\,\lambda_{c,\mathrm{s}}\frac{\partial^2 T_{\mathrm{s}}}{\partial z^2}}_{\text{heat conduction}} \underbrace{-a_{\mathrm{geo}}\,\alpha\,(T_{\mathrm{s}}-T_{\mathrm{g}})}_{\text{heat transfer}} \underbrace{+a_{\mathrm{geo}}\sum_{i=1}^{I} R_i\,(-\Delta h_{\mathrm{R},i})}_{\text{heat of reaction}} \tag{4.3}$$

$$\left.\frac{\partial T_{\mathrm{s}}}{\partial z}\right|_{z=0} = \left.\frac{\partial T_{\mathrm{s}}}{\partial z}\right|_{z=L} = 0 \tag{4.4}$$

Since the solid phase consists of both substrate and washcoat it is described by averaged solid properties such as density, heat capacity and thermal conductivity (appendix J). The assumption of isothermal conditions across the washcoat thickness is reported to be reasonable [60]. Reaction rates are discussed in the following section 4.2. Respective heats of reaction are listed in table 3.2.

The precious metal dispersion in the catalytic washcoat – the number of catalytic active sites – can not be determined by means of H_2- or CO-chemisorption since ceria and related mixed oxides can be reduced by these species and hydrogen and carbon monoxide can also adsorb on the CeO_2 surface [182, 72, 15]. Thus the reaction rates are related to the geometric (outer) surface area of the catalytic converter.

4.2 Species Balances

The considered species are transported in the gas phase by convection and diffusion in flow direction. They reach the the washcoat surface by mass transfer through the boundary layer where they are converted. Oxygen arriving at the catalytic surface can in addition be stored in the solid bulk phase (figure 4.2).

Gas Bulk Phase The gas bulk species balance reads:

$$0 = \underbrace{-\frac{\dot{m}}{A}\frac{\partial w_{j,\mathrm{g}}}{\partial z}}_{\text{convection}} + \underbrace{\varepsilon\,D_j\frac{\partial^2 w_{j,\mathrm{g}}}{\partial z^2}}_{\text{diffusion}} \underbrace{-a_{\mathrm{geo}}\,\rho_{\mathrm{g}}\,\beta_j\,(w_{j,\mathrm{g}}-w_{j,\mathrm{s}})}_{\text{mass transfer}} \tag{4.5}$$

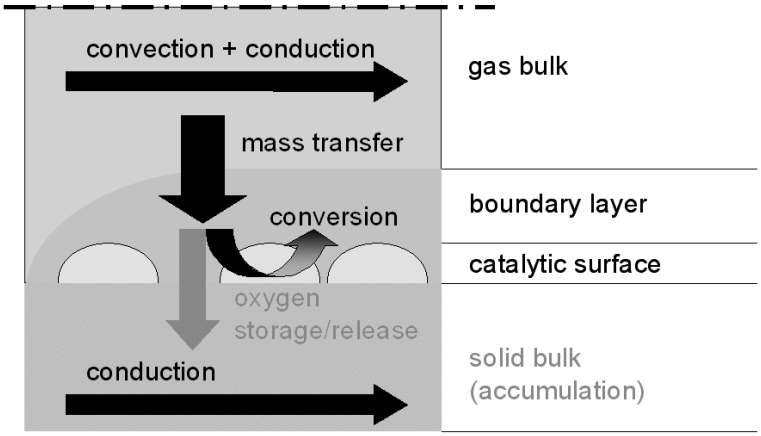

Figure 4.2: Mechanisms accounted for in the species balances.

with boundary conditions

$$\left.\frac{\dot{m}}{A} w_{j,\mathrm{g}}\right|_f = \frac{\dot{m}}{A}\, w_{j,\mathrm{g}}\big|_{z=0} - \varepsilon D_j \left.\frac{\partial w_{j,\mathrm{g}}}{\partial z}\right|_{z=0}, \left.\frac{\partial w_{j,\mathrm{g}}}{\partial z}\right|_{z=L} = 0 \tag{4.6}$$

Diffusivities are calculated according to equation I.6. The mass transfer correlation applied is discussed in section H.2.

Catalyst Surface The balance of all species except oxygen in the vicinity of the washcoat surface is described by:

$$0 = \underbrace{\rho_{\mathrm{g}} \beta_j a_{\mathrm{geo}} \left(w_{j,\mathrm{g}} - w_{j,\mathrm{s}}\right)}_{\text{mass transfer}} + \underbrace{a_{\mathrm{geo}} MW_j \sum_{i=1}^{I} \nu_{ij} R_i}_{\text{reaction}} \tag{4.7}$$

Oxygen at the washcoat surface can in addition be supplied/consumed by the storage (reaction rate R_{osr}):

$$0 = \underbrace{a_{\mathrm{geo}} \rho_{\mathrm{g}} \beta_{\mathrm{O_2}} \left(w_{\mathrm{O_2,g}} - w_{\mathrm{O_2,s}}\right)}_{\text{mass transfer}} + \underbrace{a_{\mathrm{geo}} MW_{\mathrm{O_2}} \left(\sum_{i=1}^{I} \nu_{\mathrm{i,O_2}} R_i + \nu_{\mathrm{osr,O_2}} R_{\mathrm{osr}}\right)}_{\text{conversion and storage reactions}} \tag{4.8}$$

At the catalyst surface no distinction is therefore made between oxygen transferred from the gas bulk phase and oxygen set free from the oxygen storage. Thus oxygen storage/release and species conversion kinetics are coupled at the catalyst surface.

The change of the oxygen content of the storage material is described by:

$$\underbrace{\Omega \frac{\partial X}{\partial t}}_{\text{oxygen storage}} = \underbrace{(\varepsilon_{\text{subs}} - \varepsilon)\, D_{\text{O}_2,\text{s}}\, \rho_{\text{O}_2}\, \frac{\partial^2 X}{\partial z^2}}_{\text{oxygen diffusion}} - \underbrace{a_{\text{geo}}\, MW_{\text{O}_2}\, \nu_{\text{osr,O}_2}\, R_{\text{osr}}}_{\text{reaction}} \tag{4.9}$$

$$\left.\frac{\partial X}{\partial z}\right|_{z=0} = \left.\frac{\partial X}{\partial z}\right|_{z=L} = 0 \tag{4.10}$$

Temperature dependent available oxygen storage capacity (OSCC) Ω and oxygen mobility $D_{\text{O}_2,\text{s}}$ within the cerium-zirconium lattice are calculated from equation 6.2 and J.1 respectively.

4.3 Reaction Rates

Species Conversion Rates Heterogeneous-homogeneous coupled combustion rates are assumed to be first order in both reactant concentrations:

$$R^{\text{hom}}_{\text{H}_2,\text{O}_2} = k^{\text{hom}}_{\text{H}_2,\text{O}_2}\, y_{\text{H}_2}\, y_{\text{O}_2} \left(1 - \frac{y_{\text{H}_2\text{O}}}{y_{\text{H}_2}\sqrt{y_{\text{O}_2}}\, K^{\text{eq}}_{\text{H}_2,\text{O}_2}}\right) \tag{4.11}$$

$$R^{\text{hom}}_{\text{CO},\text{O}_2} = k^{\text{hom}}_{\text{CO},\text{O}_2}\, y_{\text{CO}}\, y_{\text{O}_2} \left(1 - \frac{y_{\text{CO}_2}}{y_{\text{CO}}\sqrt{y_{\text{O}_2}}\, K^{\text{eq}}_{\text{CO},\text{O}_2}}\right) \tag{4.12}$$

$$R^{\text{hom}}_{\text{C}_3\text{H}_6,\text{O}_2} = k^{\text{hom}}_{\text{C}_3\text{H}_6,\text{O}_2}\, y_{\text{C}_3\text{H}_6}\, y_{\text{O}_2} \left(1 - \frac{y^3_{\text{H}_2\text{O}}\, y^3_{\text{CO}_2}}{y_{\text{C}_3\text{H}_6}\, y^{4.5}_{\text{O}_2}\, K^{\text{eq}}_{\text{C}_3\text{H}_6,\text{O}_2}}\right) \tag{4.13}$$

$$R^{\text{hom}}_{\text{C}_3\text{H}_8,\text{O}_2} = k^{\text{hom}}_{\text{C}_3\text{H}_8,\text{O}_2}\, y_{\text{C}_3\text{H}_8}\, y_{\text{O}_2} \left(1 - \frac{y^4_{\text{H}_2\text{O}}\, y^3_{\text{CO}_2}}{y_{\text{C}_3\text{H}_8}\, y^{5}_{\text{O}_2}\, K^{\text{eq}}_{\text{C}_3\text{H}_8,\text{O}_2}}\right) \tag{4.14}$$

All catalytic reaction rates are described by Langmuir-Hinshelwood type rate equations which account for promoting and inhibiting effects of certain species. The rates of oxygen consuming combustion reactions are:

$$R_{\text{H}_2,\text{O}_2} = \frac{k_{\text{H}_2,\text{O}_2}\, y_{\text{H}_2}\, y_{\text{O}_2}}{I^2} \left(1 - \frac{y_{\text{H}_2\text{O}}}{y_{\text{H}_2}\sqrt{y_{\text{O}_2}}\, K^{\text{eq}}_{\text{H}_2,\text{O}_2}}\right) \tag{4.15}$$

$$R_{\text{CO},\text{O}_2} = \frac{k_{\text{CO},\text{O}_2}\, y_{\text{CO}}\, y_{\text{O}_2}}{I^2} \left(1 - \frac{y_{\text{CO}_2}}{y_{\text{CO}}\sqrt{y_{\text{O}_2}}\, K^{\text{eq}}_{\text{CO},\text{O}_2}}\right) \tag{4.16}$$

$$R_{\text{C}_3\text{H}_6,\text{O}_2} = \frac{k_{\text{C}_3\text{H}_6,\text{O}_2}\, y_{\text{C}_3\text{H}_6}\, y_{\text{O}_2}}{I^2} \left(1 - \frac{y^3_{\text{H}_2\text{O}}\, y^3_{\text{CO}_2}}{y_{\text{C}_3\text{H}_6}\, y^{4.5}_{\text{O2}}\, K^{\text{eq}}_{\text{C}_3\text{H}_6,\text{O}_2}}\right) \tag{4.17}$$

$$R_{\text{C}_3\text{H}_8,\text{O}_2} = \frac{k_{\text{C}_3\text{H}_8,\text{O}_2}\, y_{\text{C}_3\text{H}_8}\, y_{\text{O}_2}}{I^2} \left(1 - \frac{y^4_{\text{H}_2\text{O}}\, y^3_{\text{CO}_2}}{y_{\text{C}_3\text{H}_8}\, y^{5}_{\text{O}_2}\, K^{\text{eq}}_{\text{C}_3\text{H}_8,\text{O}_2}}\right) \tag{4.18}$$

Rates of competing combustion reactions involving nitrogen monoxide:

$$R_{\mathrm{H_2,NO}} = \frac{k_{\mathrm{H_2,NO}}\, y_{\mathrm{H_2}}\, y_{\mathrm{NO}}}{I^2}\left(1-\frac{y_{\mathrm{H_2O}}\sqrt{y_{\mathrm{N_2}}}}{y_{\mathrm{H_2}}\, y_{\mathrm{NO}}\, K^{\mathrm{eq}}_{\mathrm{H_2,NO}}}\right) \tag{4.19}$$

$$R_{\mathrm{CO,NO}} = \frac{k_{\mathrm{CO,NO}}\, y_{\mathrm{CO}}\, y_{\mathrm{NO}}}{I^2}\left(1-\frac{y_{\mathrm{CO_2}}\sqrt{y_{\mathrm{N_2}}}}{y_{\mathrm{CO}}\, y_{\mathrm{NO}}\, K^{\mathrm{eq}}_{\mathrm{CO,NO}}}\right) \tag{4.20}$$

$$R_{\mathrm{C_3H_6,NO}} = \frac{k_{\mathrm{C_3H_6,NO}}\, y_{\mathrm{C_3H_6}}\, y_{\mathrm{NO}}}{I^2}\left(1-\frac{y^3_{\mathrm{CO_2}}\, y^3_{\mathrm{H_2O}}\, y^{4.5}_{\mathrm{N_2}}}{y_{\mathrm{C_3H_6}}\, y^9_{\mathrm{NO}}\, K^{\mathrm{eq}}_{\mathrm{C_3H_6,NO}}}\right) \tag{4.21}$$

$$R_{\mathrm{C_3H_8,NO}} = \frac{k_{\mathrm{C_3H_8,NO}}\, y_{\mathrm{C_3H_8}}\, y_{\mathrm{NO}}}{I^2}\left(1-\frac{y^3_{\mathrm{CO_2}}\, y^4_{\mathrm{H_2O}}\, y^5_{\mathrm{N_2}}}{y_{\mathrm{C_3H_8}}\, y^{10}_{\mathrm{NO}}\, K^{\mathrm{eq}}_{\mathrm{C_3H_8,NO}}}\right) \tag{4.22}$$

Water gas shift and reforming reaction rates:

$$R_{\mathrm{CO,H_2O}} = \frac{k_{\mathrm{CO,H_2O}}\, y_{\mathrm{CO}}}{I}\left(1-\frac{y_{\mathrm{CO_2}}\, y_{\mathrm{H_2}}}{y_{\mathrm{CO}}\, y_{\mathrm{H_2O}}\, K^{\mathrm{eq}}_{\mathrm{CO,H_2O}}}\right) \tag{4.23}$$

$$R_{\mathrm{C_3H_6,H_2O}} = \frac{k_{\mathrm{C_3H_6,H_2O}}\, y_{\mathrm{C_3H_6}}}{I}\left(1-\frac{y^3_{\mathrm{CO}}\, y^6_{\mathrm{H_2}}}{y_{\mathrm{C_3H_6}}\, y^3_{\mathrm{H_2O}}\, K^{\mathrm{eq}}_{\mathrm{C_3H_6,H_2O}}}\right) \tag{4.24}$$

$$R_{\mathrm{C_3H_8,H_2O}} = \frac{k_{\mathrm{C_3H_8,H_2O}}\, y_{\mathrm{C_3H_8}}}{I}\left(1-\frac{y^3_{\mathrm{CO}}\, y^7_{\mathrm{H_2}}}{y_{\mathrm{C_3H_8}}\, y^3_{\mathrm{H_2O}}\, K^{\mathrm{eq}}_{\mathrm{C_3H_8,H_2O}}}\right) \tag{4.25}$$

Combustion reactions 4.15 through 4.22 are practically not equilibrium limited from an emission point of view over the full operating range. However e.g. equilibrium oxygen concentration under rich conditions are important in terms of oxygen storage (chapter 3) and oxygen sensor operation (appendix D). Thus equilibrium limitation is considered with all rate equations even though it has no impact on the simulation results presented in chapter 7.

An Arrhenius type equation describes the temperature dependence of the reaction rate constants:

$$k^{(\mathrm{hom})}_{j,k}(T) = k^{300\,^\circ\mathrm{C}(,\mathrm{hom})}_{j,k}\, \mathrm{e}^{-\frac{E_{j,k}}{\mathrm{R}}\left(\frac{1}{T}-\frac{1}{573.15\,\mathrm{K}}\right)} \tag{4.26}$$

All catalytic rate expressions share the common denominator which represents the inhibition of adsorbed species:

$$I = 1 + K^{\mathrm{inh}}_{\mathrm{C_3H_6}}\, y_{\mathrm{C_3H_6}} + K^{\mathrm{inh}}_{\mathrm{CO}}\, y_{\mathrm{CO}} + K^{\mathrm{inh}}_{\mathrm{O_2}}\, y_{\mathrm{O_2}} \tag{4.27}$$

$$\text{with} \quad K^{\mathrm{inh}}_j(T) = K^{300\,^\circ\mathrm{C,inh}}_j\, \mathrm{e}^{\frac{E^{\mathrm{inh}}_{j,k}}{\mathrm{R}}\left(\frac{1}{T}-\frac{1}{573.15\,\mathrm{K}}\right)} \tag{4.28}$$

The expression accounts for competitive adsorption of the species propene, carbon monoxide and oxygen. The Langmuir-Hinshelwood type reaction rate expressions 4.15 through 4.22 represent collision reactions between two reactants adsorbed on physically equivalent catalytic sites where the catalytic sites are (more or less) occupied by strongly adsorbing species. Water gas shift and reforming reactions 4.23 through 4.25 – involving the abundant water as a reactant – represent collision between one species adsorbed on the indifferent catalytic site and non-adsorbed excess water. No attempt is made to connect the rate equations with the availability of specific active sites (e.g. Pt, Pd or Rh) since the detailed surface composition of the catalyst used has not been disclosed. Compared to the pioneering work of Volts [170], which has been used in many subsequent publications (e.g. [123, 140, 124, 148, 147, 98, 46, 26, 172, 80, 85, 135, 108, 110, 165]) the inhibition term in the denominator is less complex. But as in Voltz' work the rate equations provide a reasonable global kinetics fit to the experimental results.

Equilibrium limitations are considered by the factor $EQ_{\mathrm{j,k}}$ which is zero at equilibrium conditions (suggested by [98]), e.g.

$$EQ_{\mathrm{CO,H_2O}} = \left(1 - \frac{y_{\mathrm{CO_2}}\, y_{\mathrm{H_2}}}{y_{\mathrm{CO}}\, y_{\mathrm{H_2O}}\, K^{\mathrm{eq}}_{\mathrm{CO,H_2O}}}\right) \tag{4.29}$$

The reaction rate constants obey an Arrhenius-type temperature dependence having activation energies in the order of 50 kJ/mol (catalytic reactions) and 170 kJ/mol (homogeneous reactions). The adsorption constants obey a similar type of temperature dependence with (negative) adsorption enthalpies in the order of 10 kJ/mol.

Oxygen Uptake and Release Transient catalyst behavior is dominated by a process of oxygen storage and release [82]. The rate of oxygen uptake is modeled to be proportional to the unoxidized extent of oxygen storage material, $1 - X$. Based upon experimental observations discussed below, the oxygen uptake rate is set to be also proportional to the stoichiometric oxygen excess ("leanness"), $(\lambda_{\mathrm{s}} - 1)$, of the gas at the washcoat surface. The opposite is true for oxygen release.

The oxygen uptake/release rate can thus be described by

$$\lambda_{\mathrm{s}} \geq 1: \quad R_{\mathrm{osr}} = k_{\mathrm{os}}\,(1 - X)\,(\lambda_{\mathrm{s}} - 1) \tag{4.30}$$

$$\lambda_{\mathrm{s}} < 1: \quad R_{\mathrm{osr}} = -k_{\mathrm{or}}\, X\,(1 - \lambda_{\mathrm{s}}) \tag{4.31}$$

The formulation of the oxygen storage and release rates is also quite phenomenological. The rates of oxygen diffusing out of the oxygen storage bulk phase back to the oxygen storage material surface and the spill over rate back to the precious metal surface – where the oxygen might participate in a catalytic oxidation reaction – are lumped into the above rate expression.

In addition to reaction 3.15 several reduction equations directly including combustible species as e.g. carbon monoxide and hydrocarbons [98, 99] are considered in literature. Apart from being not any more likely to occur on pure cerium oxide from a thermodynamic point of view, they tend to fail under phenomenological aspects: if a certain combustible species (e.g. hydrogen) is neglected, cerium reduction via this route is not described. Pretty much every measure which is suitable to reduce the oxygen partial pressure in the gas phase below its respective equilibrium value favors oxide reduction (see section 3.2).

4.4 Numerical Solution

The set of highly nonlinear partial differential and algebraic equations is solved by the method of lines solver PDEXPACK [119]. Second order finite differences are applied for axial discretization. The resulting system of ordinary differential and algebraic equations is solved with LIMEX. A semi-implicit Euler method is applied for time integration combining the advantages arising from implicit methods (stability) and explicit methods (without iteration).

Both the grid density and the time step size are fully adaptive – ensuring a solution with the requested accuracy at reasonable computation times. The advantages of a fully adaptive solver for the mathematical simulation of automotive emission control with steep moving concentration and temperature gradients have also been acknowledged by other groups [125].

Chapter 5

Reaction Kinetics

Species conversion rates are most important under cold start conditions with catalytic rates controlling overall conversion.

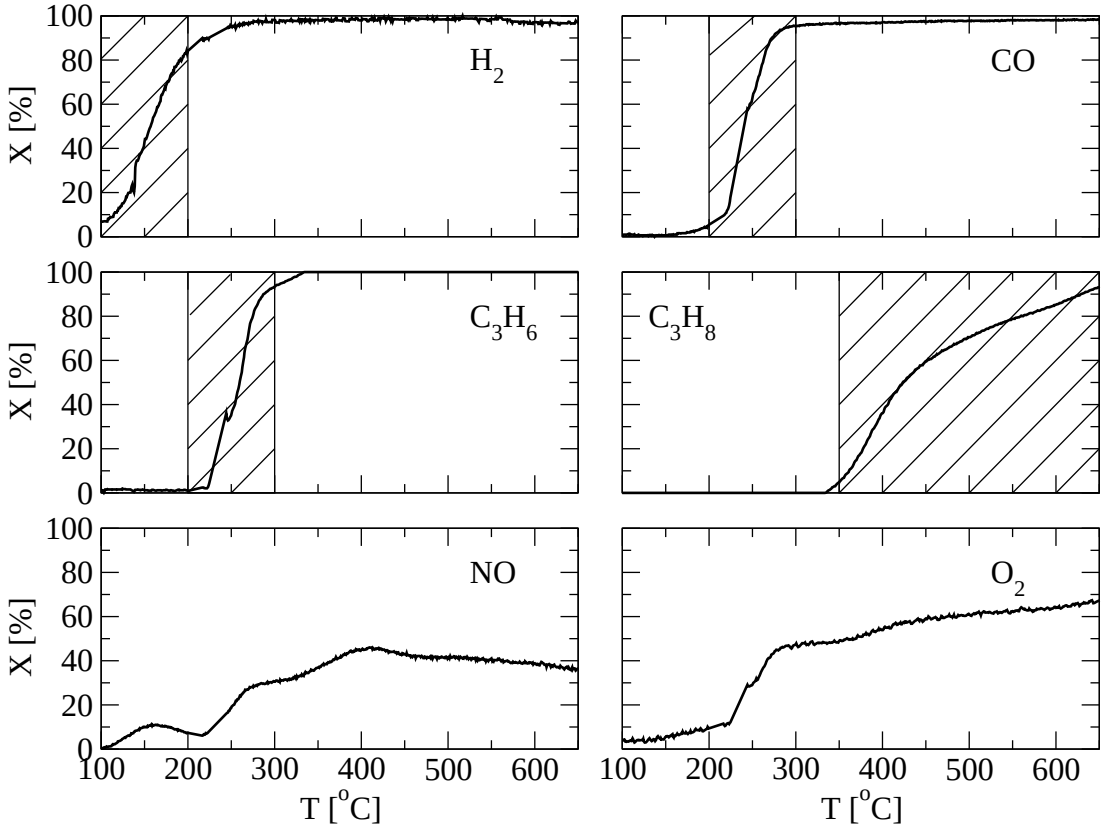

Figure 5.1: Conversion of different combustible exhaust species ("light-off" curves) for lean exhaust composition G7 in table 5.2, $SV = 77000\ \mathrm{h}^{-1}$, $\lambda = 1.02 \pm 0.03$ at a frequency of $f = 1$ Hz.

The exhaust composition is set to either lean or rich conditions since air to fuel-ratio readings are not available immediately after cranking the engine until the oxygen sensor's dew point is exceeded. Hydrogen contributes significantly to catalyst converter

light-off: close to stoichiometry light-off occurs at temperatures well below 200 °C (figure 5.1). Carbon monoxide and propene exhibit similar light-off temperatures between 200 and 300 °C. Significant propane combustion however does not occur at temperatures below 350 °C. Under lean conditions nitrogen oxide and oxygen compete over the full temperature range for the oxidation of the combustible species.

Hydrogen, propane and nitrogen monoxide light-off suffer from increasing oxygen partial pressures (figure 5.2). Inhibiting effects of these species are considered to be negligible compared to carbon monoxide, oxygen and propene and are therefore not considered in the common denominator I (equation 4.27). On the other hand increased oxygen concentrations enhance carbon monoxide light-off. Even under lean conditions carbon monoxide oxidation seams to be self-inhibited by mainly carbon monoxide covered precious metal surfaces.

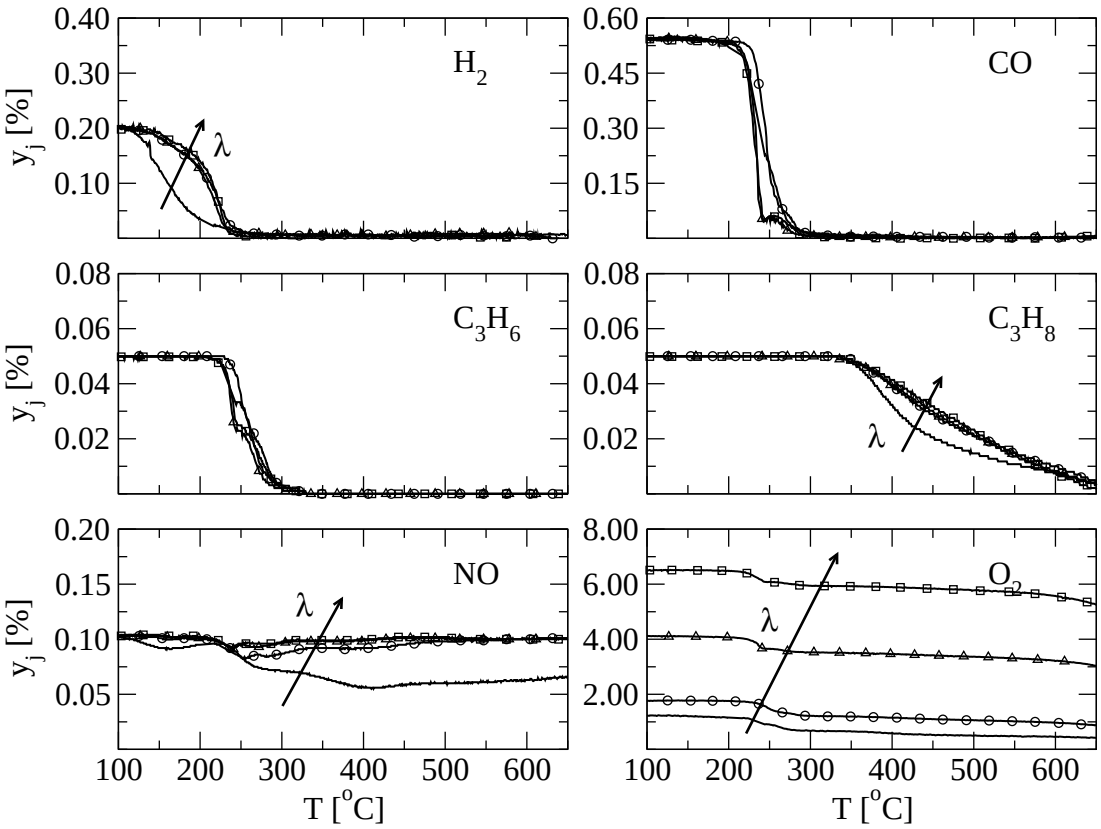

Figure 5.2: Conversion of different combustible exhaust species (light-off curves) for lean exhaust composition G7 in table 5.2 with stepwise increased oxygen fraction, $SV = 77000\ \mathrm{h}^{-1}$, average air to fuel ratio $\lambda = 1.02$ (no symbol), $\lambda = 1.05$ (circle), $\lambda = 1.20$ (triangle) and $\lambda = 1.50$ (square) perturbed with ± 0.03 at a frequency of $f = 1$ Hz.

5.1 General Approach

In real exhaust aftertreatment a complex interaction of different oxidizing and reducing reactions results in the overall three-way catalytic activity. As discussed in chapter 2 the exhaust composition fluctuates within certain domains – defined by air to fuel ratio control and combustion stoichiometry. From emission certification cycle raw emission measurements (figures 2.3 and 2.2) two typical exhaust base compositions representing lean and rich engine out exhaust compositions are derived. Starting from the lean base composition hydrogen, carbon monoxide, propene, propane and nitrogen oxide concentrations are varied in order to determine the respective species influence on reaction kinetics (exhaust compositions see table 5.2). Subsequently, similar concentration variations are performed for the rich base composition (table 5.3). In both cases the average air to fuel ratio is superimposed by 1 Hz fluctuations to simulate characteristic engine out air to fuel ratio excursions due to λ-control (see figure 5.3 and 5.14). Thus the influence of the fast λ-cycling by air to fuel ratio feedback control is considered implicitly in the reaction kinetic parameters obtained from measurements under fuel lean (oxygen storage completely filled) and fuel rich (oxygen storage completely empty) conditions (table 5.1). It is well known that these kinetics may differ substantially from kinetics measured under fully steady-state ($\lambda = \text{const}$) conditions [143].

5.2 Experimental Implementation

In order to decouple the influence of temperature and species concentrations on reaction rates, a flat bed reactor is chosen which allows to operate under almost isothermal conditions (appendix A.1). The multiple slice reactor applied for steady state reaction kinetics experiments discussed in this chapter contains five catalyst slices in a row. Behind each slice the exhaust concentrations are analyzed. Thus isothermal concentration profiles along the catalyst length are obtained. Frequently a reference gas mixture is passed through the reactor at 275 °C to check for repeatability (gas composition see figure 3.10). A thorough description of the reactor itself, the whole experimental setup and its operation is given in appendix A.1.

5.3 Reaction Rate Parameters

Reaction rate parameters are determined from steady state isothermal conversion profiles. Since the typical imposed air to fuel ratio modulation is much faster than the respective analyzers time resolution, the impact of air to fuel ratio modulation is already included in the time averaged steady state concentration profiles. The catalyst is either considered to be filled with oxygen (lean conditions) or oxygen depleted (rich conditions). Short term oxygen storage and release is not considered when simulating these profiles. Furthermore diffusive transport is considered to be much smaller

than convective transport and thus neglected. The resulting linear-implicit differential-algebra system is efficiently solved with the Euler integrator Excels. A Simplex-Box optimization algorithm estimates the reaction rate parameters such that the deviations between measured and simulated concentration profiles are below a predefined threshold.

The rate constants, activation energies, inhibition constants and adsorption energies of species conversion reactions 4.11 through 4.25, found to well describe the isothermal experiments under both lean and rich conditions are gathered in table 5.1. Conversion profiles simulated with these parameters are discussed in section 5.4 along with the respective measured profiles.

heterogeneous reactions							
$k^{300\,^\circ\mathrm{C}}_{\mathrm{H_2,O_2}}$	=	92	kmol/($\mathrm{m^2_{geo}}$ s)	$E_{\mathrm{H_2,O_2}}/\mathrm{R}$	=	4760	K
$k^{300\,^\circ\mathrm{C}}_{\mathrm{CO,O_2}}$	=	33	kmol/($\mathrm{m^2_{geo}}$ s)	$E_{\mathrm{CO,O_2}}/\mathrm{R}$	=	8800	K
$k^{300\,^\circ\mathrm{C}}_{\mathrm{C_3H_6,O_2}}$	=	14	kmol/($\mathrm{m^2_{geo}}$ s)	$E_{\mathrm{C_3H_6,O_2}}/\mathrm{R}$	=	9365	K
$k^{300\,^\circ\mathrm{C}}_{\mathrm{C_3H_8,O_2}}$	=	0.075	kmol/($\mathrm{m^2_{geo}}$ s)	$E_{\mathrm{C_3H_8,O_2}}/\mathrm{R}$	=	6200	K
$k^{300\,^\circ\mathrm{C}}_{\mathrm{H_2,NO}}$	=	9.7	kmol/($\mathrm{m^2_{geo}}$ s)	$E_{\mathrm{H_2,NO}}/\mathrm{R}$	=	2790	K
$k^{300\,^\circ\mathrm{C}}_{\mathrm{CO,NO}}$	=	18	kmol/($\mathrm{m^2_{geo}}$ s)	$E_{\mathrm{CO,NO}}/\mathrm{R}$	=	8330	K
$k^{300\,^\circ\mathrm{C}}_{\mathrm{C_3H_6,NO}}$	=	3.3	kmol/($\mathrm{m^2_{geo}}$ s)	$E_{\mathrm{C_3H_6,NO}}/\mathrm{R}$	=	10980	K
$k^{300\,^\circ\mathrm{C}}_{\mathrm{C_3H_8,NO}}$	=	0	kmol/($\mathrm{m^2_{geo}}$ s)				
$k^{300\,^\circ\mathrm{C}}_{\mathrm{CO,H_2O}}$	=	$1.8\,10^{-6}$	kmol/($\mathrm{m^2_{geo}}$ s)	$E_{\mathrm{CO,H_2O}}/\mathrm{R}$	=	8880	K
$k^{300\,^\circ\mathrm{C}}_{\mathrm{C_3H_6,H_2O}}$	=	$1.8\,10^{-9}$	kmol/($\mathrm{m^2_{geo}}$ s)	$E_{\mathrm{C_3H_6,H_2O}}/\mathrm{R}$	=	19900	K
$k^{300\,^\circ\mathrm{C}}_{\mathrm{C_3H_8,H_2O}}$	=	$4.3\,10^{-11}$	kmol/($\mathrm{m^2_{geo}}$ s)	$E_{\mathrm{C_3H_8,H_2O}}/\mathrm{R}$	=	22000	K
$K^{300\,^\circ\mathrm{C}}_{\mathrm{inh,C_3H_6}}$	=	2900	-	$E_{\mathrm{inh,C_3H_6}}/\mathrm{R}$	=	90	K
$K^{300\,^\circ\mathrm{C}}_{\mathrm{inh,CO}}$	=	1385	-	$E_{\mathrm{inh,CO}}/\mathrm{R}$	=	82	K
$K^{300\,^\circ\mathrm{C}}_{\mathrm{inh,O_2}}$	=	950	-	$E_{\mathrm{inh,O_2}}/\mathrm{R}$	=	255	K
homogeneous-heterogeneous coupled reactions							
$k^{300\,^\circ\mathrm{C,hom}}_{\mathrm{H_2,O_2}}$	=	$5.9\,10^{-3}$	kmol/($\mathrm{m^2_{geo}}$ s)	$E_{\mathrm{H_2,O_2}}/\mathrm{R}$	=	20000	K
$k^{300\,^\circ\mathrm{C,hom}}_{\mathrm{CO,O_2}}$	=	0	kmol/($\mathrm{m^2_{geo}}$ s)				
$k^{300\,^\circ\mathrm{C,hom}}_{\mathrm{C_3H_6,O_2}}$	=	$4.5\,10^{-2}$	kmol/($\mathrm{m^2_{geo}}$ s)	$E_{\mathrm{C_3H_6,O_2}}/\mathrm{R}$	=	20960	K
$k^{300\,^\circ\mathrm{C,hom}}_{\mathrm{C_3H_8,O_2}}$	=	$1.0\,10^{-4}$	kmol/($\mathrm{m^2_{geo}}$ s)	$E_{\mathrm{C_3H_8,O_2}}/\mathrm{R}$	=	20000	K

Table 5.1: Rate constants, activation energies, adsorption constants and adsorption energies of reactions 4.11 through 4.25, derived from experiments with lean and rich exhaust at temperatures between 100 and 700 °C (sections 5.4.1 and 5.4.2).

Most reported models assume the reaction rate parameters of hydrogen combustion to be equal to carbon monoxide combustion [147, 96, 26, 99, 80, 85, 27, 135, 6]. This may lead to difficulties in predicting catalyst light-off behavior since hydrogen has a significant lower light-off temperature compared to carbon monoxide (see figure 5.1).

Hydrogen and carbon monoxide oxidation are therefore considered independently in the following. The range of adsorption energies in table 5.1 is in agreement with values reported in fundamental literature [170, 123].

Homogeneous-Heterogeneous Coupled Reactions In general, homogeneous mechanisms are neglected when modeling catalytic automotive exhaust aftertreatment[1]. They are believed to be important only at unusually high temperatures [96].

It turns out however that the measured combustion rates of hydrogen, propene and propane at high temperatures (up to 700 °) can not be described with the kinetic expressions evaluated at catalytic light-off temperatures (up to 500 °C). A second combustion mechanism – assumed to be homogeneous-heterogeneous coupled – is therefore introduced for hydrogen and hydrocarbon oxidation. Their activation energies are considerably higher (see table 5.1), supporting the assumption of homogeneous combustion. Interestingly no significant homogeneous-heterogeneous carbon monoxide combustion rate is evident from measurements up to 700 °C. This is in agreement with combustion research, where light-off temperatures in excess of 700 °C have been determined for homogeneous carbon monoxide oxidation [67]. Since such high temperatures are not covered with the kinetic experiments discussed here, the homogeneous-heterogeneous coupled reaction rate constant of carbon monoxide combustion is set to zero in table 5.1.

It should be mentioned that, compared to the values determined for catalytic only combustion in table 5.1, considerably higher hydrocarbon activation temperatures of $E_{C_3H_6,O_2}/R$ = 12600 K, $E_{C_3H_8,O_2}/R$ = 15000 K and $E_{C_3H_6,O_2}/R$ = 11200 K, $E_{C_3H_8,O_2}/R$ = 14400 K are provided elsewhere [98, 99, 80, 85]. These values are believed not to describe the significant difference between rapid propene and rather lazy propane light-off observed here at temperatures below 500 °C (figure 5.2). Moreover activation temperatures well above 10000 K are considered to be indicative of homogeneous mechanisms [39]. The latter holds almost certainly true for activation energies of $E_{C_3H_6,O_2}/R$ = 19250 K and $E_{C_3H_6,O_2}/R$ = 25080 K [26].

5.4 Discussion of Conversion Profiles

5.4.1 Lean Exhaust

Reaction rate experiments under lean conditions are performed with an exhaust base composition (composition G7 in table 5.2) observed 81 seconds after cranking a 2.0l-2V-85kW engine subjected to an FTP75 emission certification driving cycle (figure 2.3).

[1] not so: [159]

	H_2	CO	NO	O_2	C_3H_6	C_3H_8
G7	0.1830	0.5490	0.1050	1.18	0.0500	0.0500
G7.1	**0.0915**	**0.2745**	0.1050	**0.99**	0.0500	0.0500
G7.2	**0.3660**	**1.0980**	0.1050	**1.54**	0.0500	0.0500
G7.3	0.1830	0.5490	0.1050	**1.06**	**0.0250**	0.0500
G7.4	0.1830	0.5490	0.1050	**1.40**	**0.1000**	0.0500
G7.5	0.1830	0.5490	0.1050	**1.05**	0.0500	**0.0250**
G7.6	0.1830	0.5490	0.1050	**1.43**	0.0500	**0.1000**
G7.7	0.1830	0.5490	**0.0525**	**1.20**	0.0500	0.0500
G7.8	0.1830	0.5490	**0.2100**	**1.12**	0.0500	0.0500

Table 5.2: Average lean gas mixture species concentrations in vol%: 11 % H_2O, 12 % CO_2, 14 ppm SO_2, the air to fuel ratio is perturbed around its average value of λ = 1.02 with an amplitude of 3 % at a frequency of 1 Hz.

Base System The base system G7 depicts the original composition. Subsystems G7.1 through G7.8 are derived from the base system by selectively varying a specific exhaust species concentration within its characteristic light-off temperature range. E.g. G7.7 and G7.8 contain half and twice respectively the amount of G7's nitrogen oxide concentration. By adjusting the oxygen partial pressure the average air to fuel ratio is fixed to a lean value of $\lambda = 1.02$.

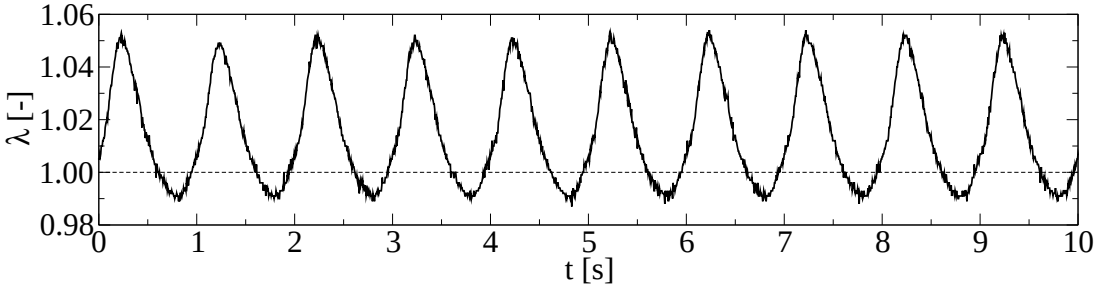

Figure 5.3: Measured exhaust air to fuel ratio upstream of the catalyst during lean-bias conversion experiments ($\lambda = 1.02 \pm 0.03$, $f = 1$ Hz).

Conversion profiles of the base system at $T = 100 \ldots 275\,^{\circ}\mathrm{C}$ and $T = 300 \ldots 600\,^{\circ}\mathrm{C}$ are provided by figures 5.4 and 5.5 respectively: Even at 100 °C measurable hydrogen combustion is observed. Increasing the temperature by 50 °C results in hydrogen conversion greater than 50 %. Significant carbon monoxide oxidation starts at 200 °C. At 225 °C more than 50 % of carbon monoxide is converted accompanied with propene light-off. Hydrogen, carbon monoxide and propene combustion is complete at 275 °C – a temperature obviously to cold for catalytic propane conversion. With that temperature a quite stable nitrogen oxide conversion of approximately 40 % establishes downstream of the catalyst (figures 5.4, 5.5 and 5.1).

At 325 °C hydrogen, carbon monoxide and propene combustion are complete within the first 40 mm of the catalyst and some propane combustion occurs over the entire length of the catalyst (figure 5.5). An overall propane combustion of 50 % is obtained

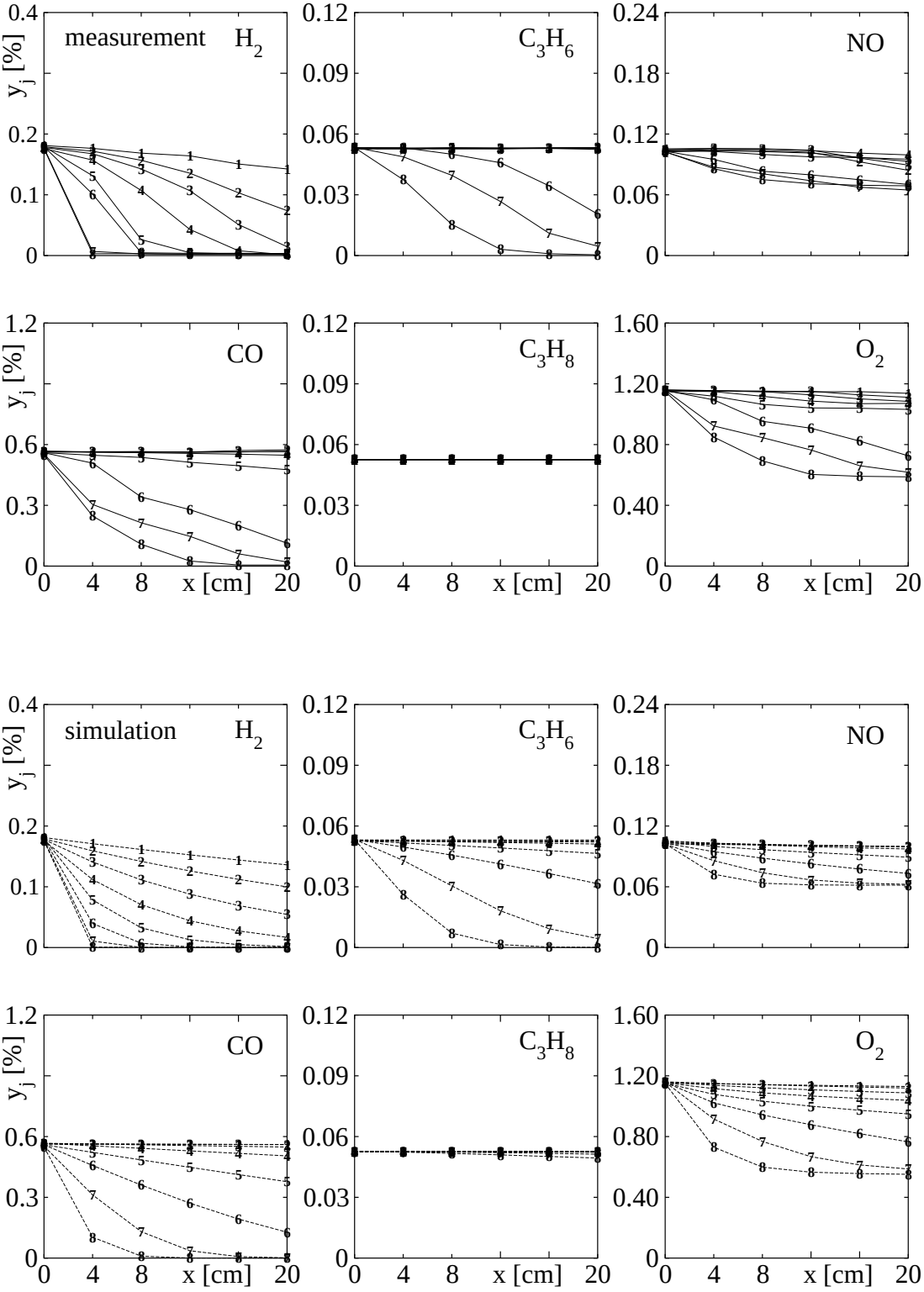

Figure 5.4: Concentration profiles for basic lean conditions (composition **G7** in table 5.2), $SV = 16500$ 1/h at T = 100, 125, 150, 175, 200, 225, 250, 275 °C (numbered 1 – 8). Above: measured in multiple slice reactor; below: simulated with rate equations 4.15 through 4.25 and respective parameters listed in table 5.1.

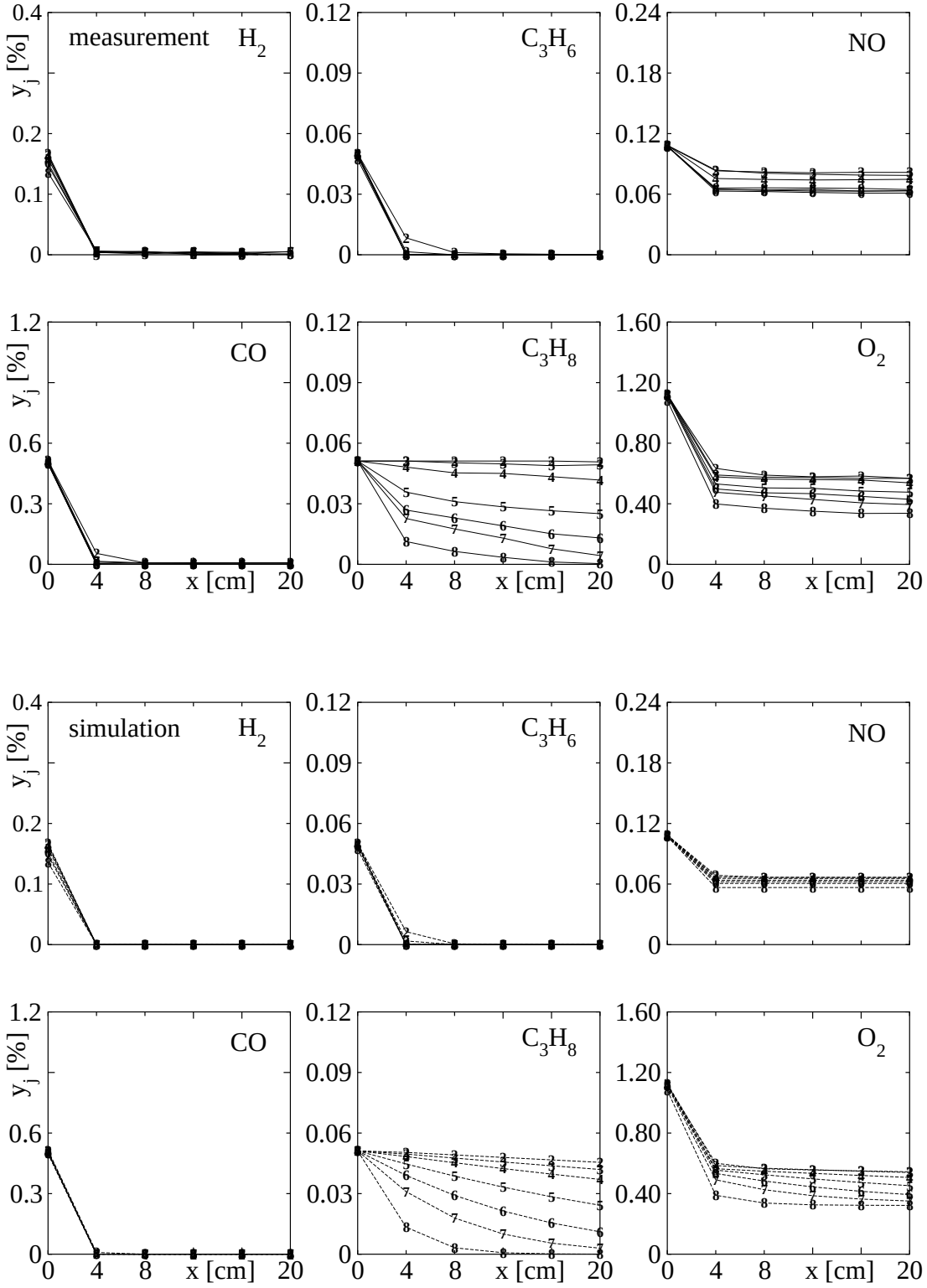

Figure 5.5: Concentration profiles for basic lean conditions (composition **G7** in table 5.2), $SV = 16500$ 1/h at T = 300, 325, 350, 400, 450, 500, 600 °C (numbered 1 – 7). Above: measured in multiple slice reactor; below: simulated with rate equations 4.15 through 4.25 and respective parameters listed in table 5.1.

between 400 and 450 °C. The kinetic competition between nitrogen oxide and oxygen seems to be limited to hydrogen, carbon monoxide and propene combustion within the catalyst entrance region. It is concluded from the flat nitrogen oxide profiles at 4 cm $< x <$ 20 cm that nitrogen oxide does not significantly contribute to propane combustion. The corresponding nitrogen oxide reduction rate is thus set to zero (table 5.1). At 600 °C it still takes the entire catalyst length to yield complete propane combustion. Some homogeneous hydrogen oxidation is evident at higher temperatures from Fig. 5.5: at $x = 0$ the measured catalyst inlet hydrogen concentration drops down with increasing temperature.

Variation of Hydrogen and Carbon Monoxide Since engine out hydrogen and carbon monoxide concentrations are linked to each other (figure 3.3) they are varied simultaneously along with oxygen to keep the air to fuel ratio unchanged at $\lambda = 1.02$ (table 5.1). Elevated concentrations result in a shift of hydrogen, carbon monoxide and propene light-off to higher temperatures by roughly 25 °C (figure 5.6 and 5.7). At 275 °C the carbon monoxide oxidation rate decreases with increasing conversion (rates obey a positive order dependence from reaction species) while propene oxidation seems to suffer from high inlet concentrations. Simulated profiles scope this behavior quite well.

Measured low temperature hydrogen combustion rates increase along the catalyst axis (figure 5.7). Since all other concentrations except the weak adsorbing hydrogen remain at roughly the same concentration level at these low temperatures this behavior is rather considered to be due to a pronounced sensitivity of hydrogen combustion towards traces of sulfur poisoning – which is not observed with the other combustion reactions (such as carbon monoxide combustion) – than a self inhibition of hydrogen species. Since neither of both effects is considered in the reaction model the negative order hydrogen combustion profiles at low temperatures are not reflected by the respective simulation profiles.

In figure 5.7 enhanced nitrogen oxide conversion obtained with increased hydrogen and carbon monoxide concentrations (despite of higher competing oxygen concentrations) illustrates the important contribution of hydrogen and carbon monoxide to nitrogen oxide reduction.

Variation of Propene The influence of propene partial pressure on overall species conversion under lean conditions is investigated in the temperature range $225 < T <$ 350 °C (figures 5.8 and 5.9). Above 300 °C propene seems to take over part of the nitrogen oxide reduction potential from carbon monoxide and hydrogen which is reflected in a lower rate constant at 300 °C but a significantly higher activation temperature (table 5.1). Measurements with high propene concentrations reveal a pronounced self-inhibition of propene oxidation. Whereas the kinetic model covers the overall propene conversion quite well, it fails to provide a sound description of the self-inhibition phenomenon. Furthermore the model provides a poor description of propane conversion between 300 and 350 °C.

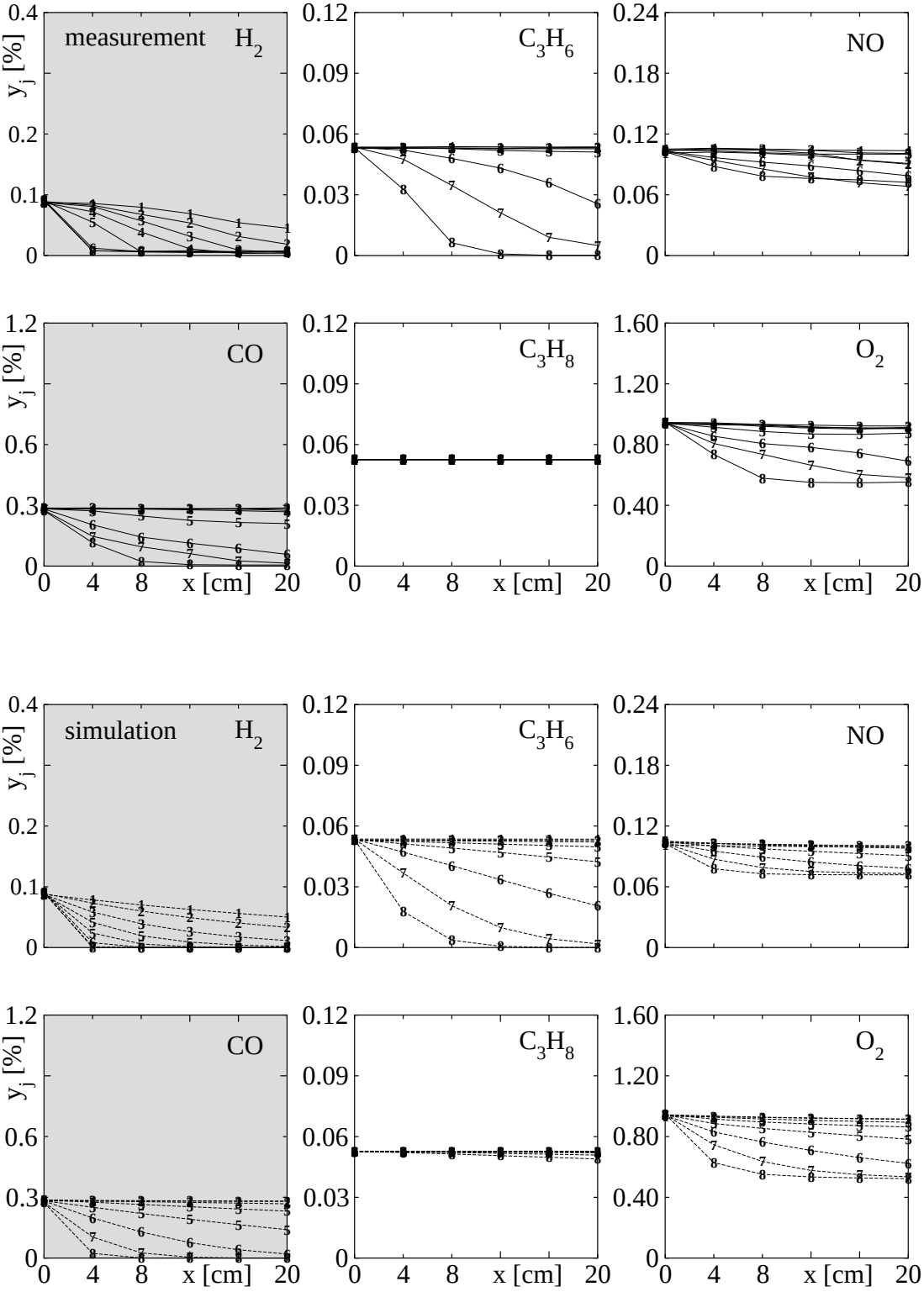

Figure 5.6: Concentration profiles for H_2/CO-reduced lean conditions (composition **G7.1** in table 5.2), $SV = 16500$ 1/h at T = 100, 125, 150, 175, 200, 225, 250, 275 °C (numbered 1 – 8). Above: measured in multiple slice reactor; below: simulated with rate equations 4.15 through 4.25 and respective parameters listed in table 5.1.

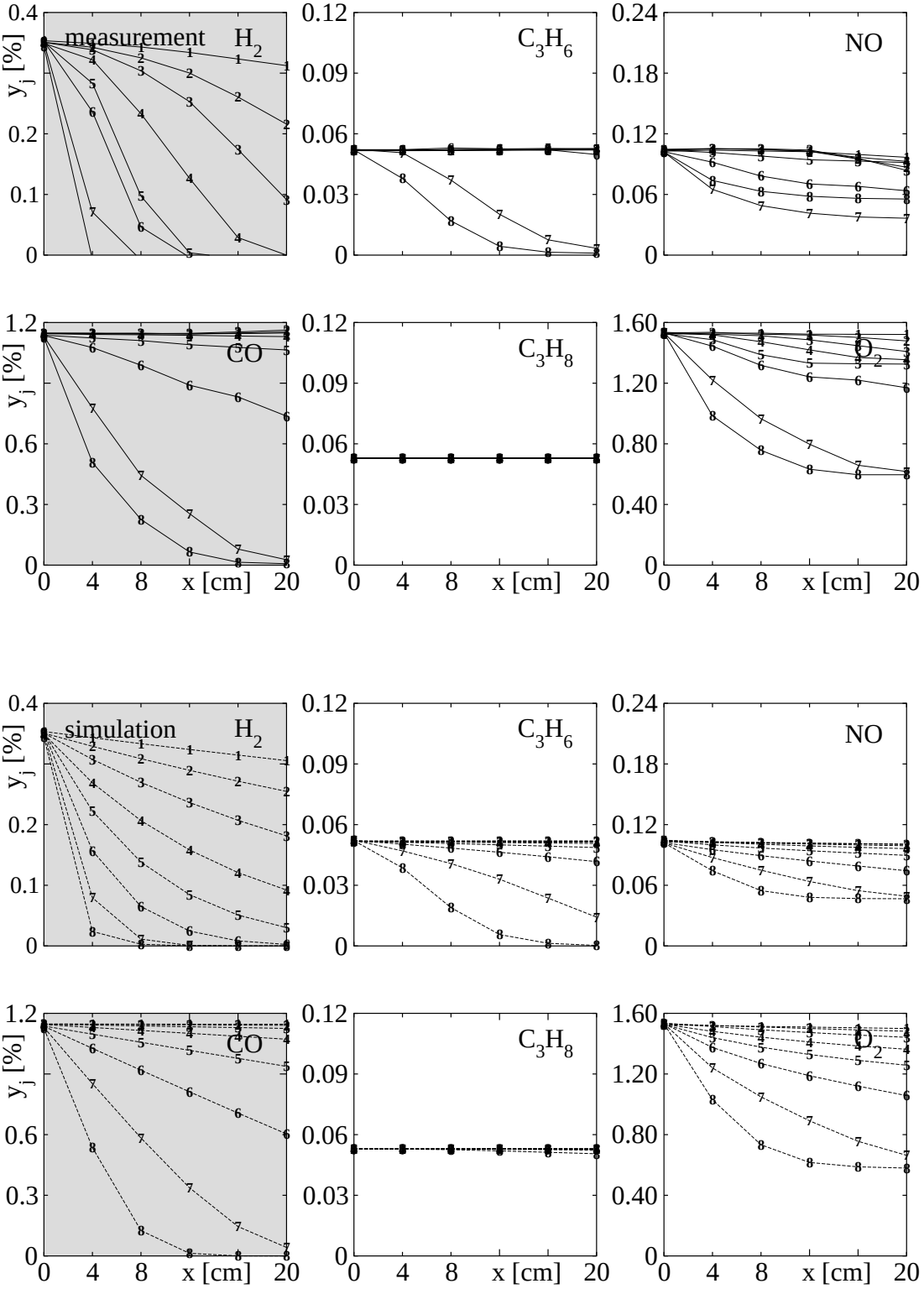

Figure 5.7: Conversion profiles for H_2/CO-increased lean conditions (composition **G7.2** in table 5.2), $SV = 16500$ 1/h at T = 100, 125, 150, 175, 200, 225, 250, 275 °C (numbered 1 – 8). Above: measured in multiple slice reactor; below: simulated with rate equations 4.15 through 4.25 and respective parameters listed in table 5.1.

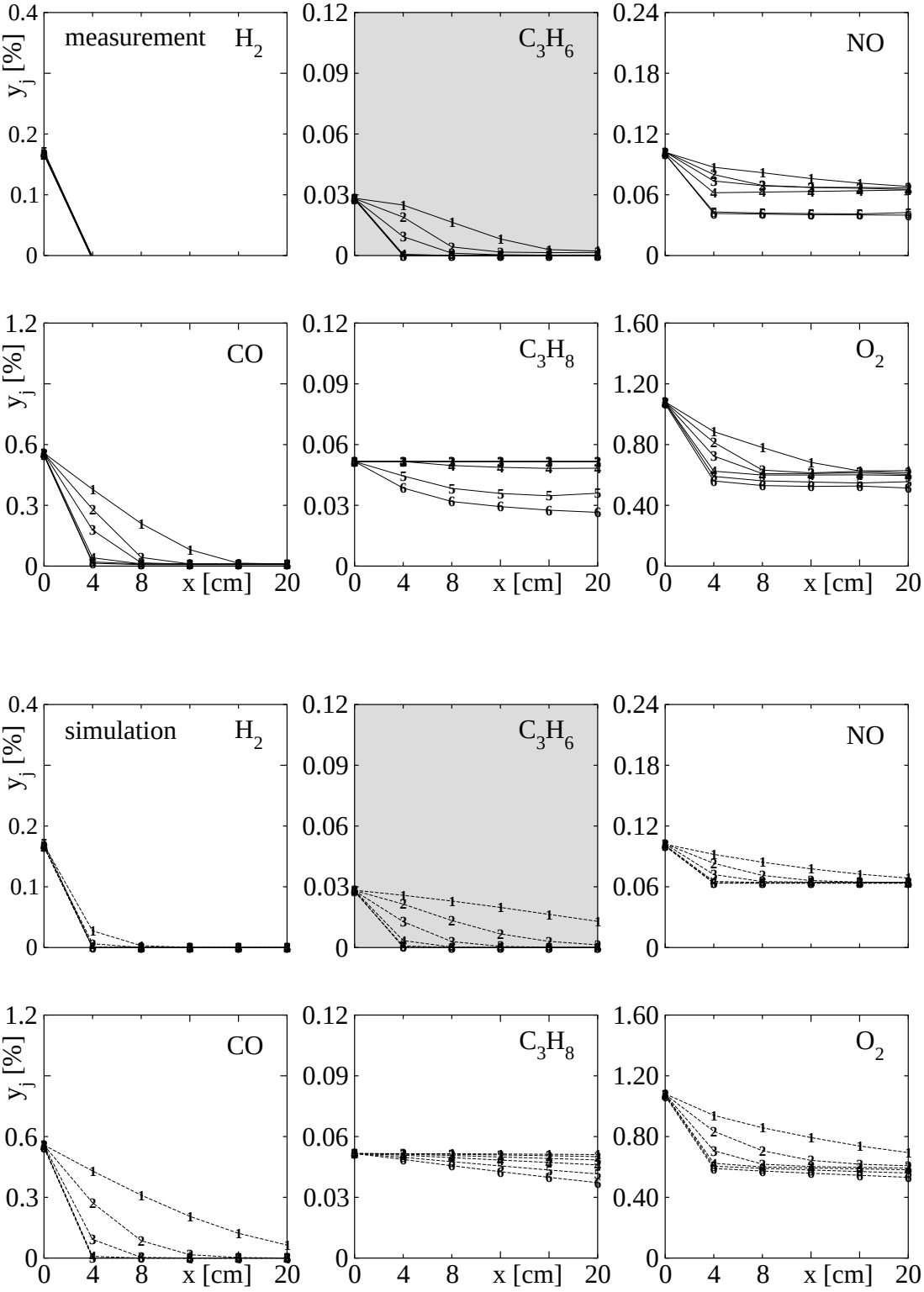

Figure 5.8: Conversion profiles for C_3H_6-reduced lean conditions (composition **G7.3** in table 5.2), $SV = 16500$ 1/h at T = 225, 250, 275, 300, 325, 350 °C (numbered 1 – 6). Above: measured in multiple slice reactor; below: simulated with rate equations 4.15 through 4.25 and respective parameters listed in table 5.1.

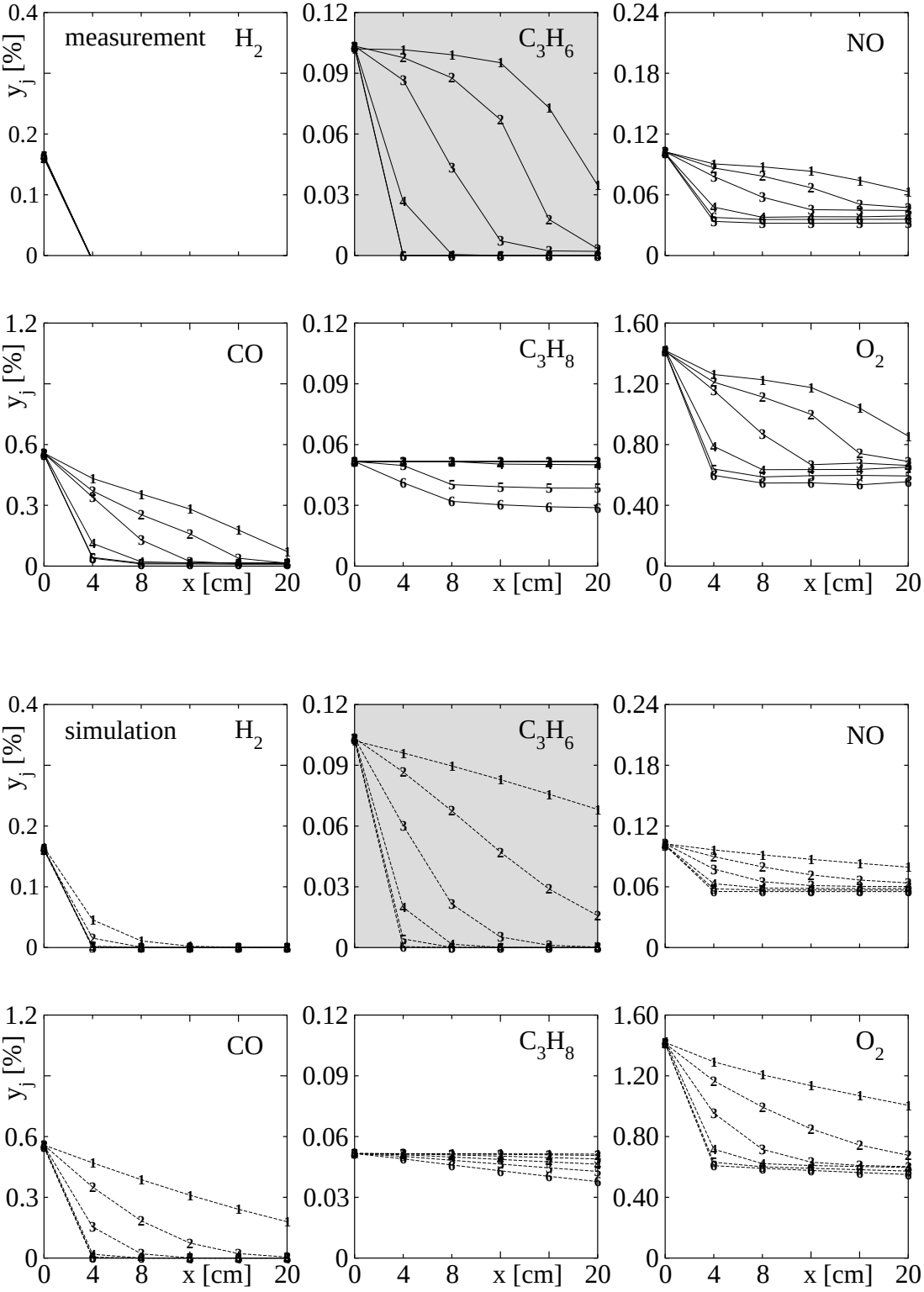

Figure 5.9: Conversion profiles for C_3H_6-increased lean conditions (composition **G7.4** in table 5.2), $SV = 16500$ 1/h at T = 225, 250, 275, 300, 325, 350 °C (numbered 1 – 6). Above: measured in multiple slice reactor; below: simulated with rate equations 4.15 through 4.25 and respective parameters listed in table 5.1.

Variation of Nitrogen Monoxide Nitrogen monoxide concentrations are varied in the temperature range $100 < T < 500\,^{\circ}\mathrm{C}$ since nitrogen oxide conversion under lean conditions is an issue over the full temperature range. Hydrogen, carbon monoxide and hydrocarbon conversion is not significantly altered by increased nitrogen monoxide concentrations (figure 5.10 and 5.11).

Even relative nitrogen monoxide concentrations are quite unaffected: above $300\,^{\circ}\mathrm{C}$ overall conversions seem to obey a "50 %-rule" (figure 5.10, 5.11 and 5.5). Since thermodynamics practically do not impose bounds to lean nitrogen oxide reduction below $600\,^{\circ}\mathrm{C}$ (figure 3.1) this phenomenon is likely to be just a matter of reaction rate competition within the catalyst entry. The kinetic model is believed to provide a sufficiently sound description of nitrogen oxide conversion at all three concentration levels over a the full temperature range. This is crucial since nitrogen oxide emissions are a major issue downstream of a warmed-up catalyst subjected to lean biased exhaust. Again propane does not contribute significantly to nitrogen oxide reduction.

Variation of Propane Propane light-off at different levels of propane concentration is investigated in the temperature range $275 < T < 600\,^{\circ}\mathrm{C}$. With an onset of significant propane combustion at $350\,^{\circ}\mathrm{C}$ 50 % conversion is reached between 400 and $450\,^{\circ}\mathrm{C}$ (figures 5.12 and 5.13). Again a temperature of $600\,^{\circ}\mathrm{C}$ and the full catalyst length of 20 cm are necessary for practically complete propane conversion. Increased oxygen concentrations – which accompany increased propane concentrations – seem to slow down propene and nitrogen oxide conversion. Homogeneous hydrogen combustion within the stainless steal reactor and/or uncoated cordierite slice in front of the coated catalyst slices (experimental setup section A.1) on the other hand is enhanced by higher oxygen partial pressures.

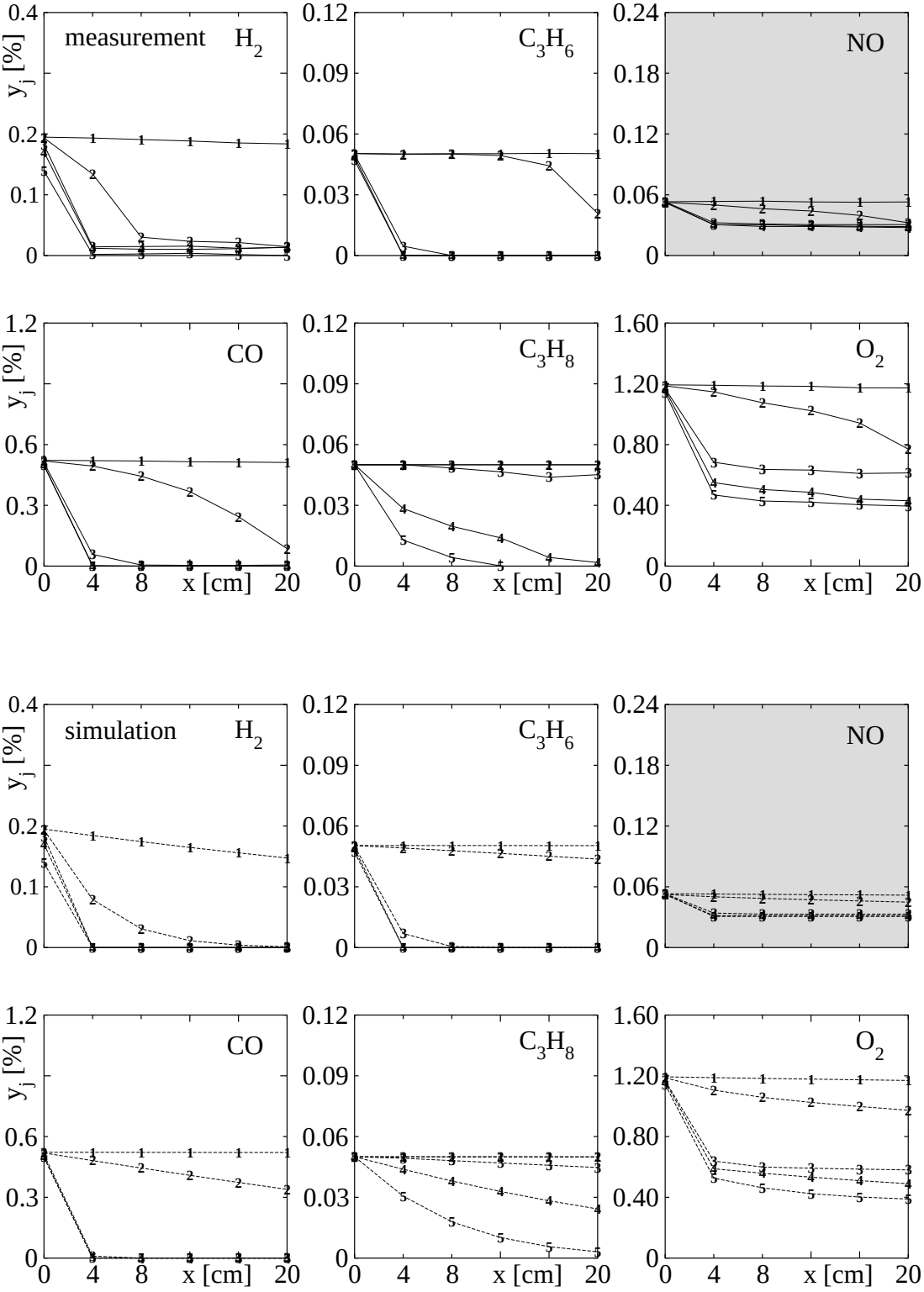

Figure 5.10: Conversion profiles for NO-reduced lean conditions (composition **G7.7** in table 5.2), $SV = 16500$ 1/h at T = 100, 200, 300, 400, 500 °C (numbered 1 – 5). Above: measured in multiple slice reactor; below: simulated with rate equations 4.15 through 4.25 and respective parameters listed in table 5.1.

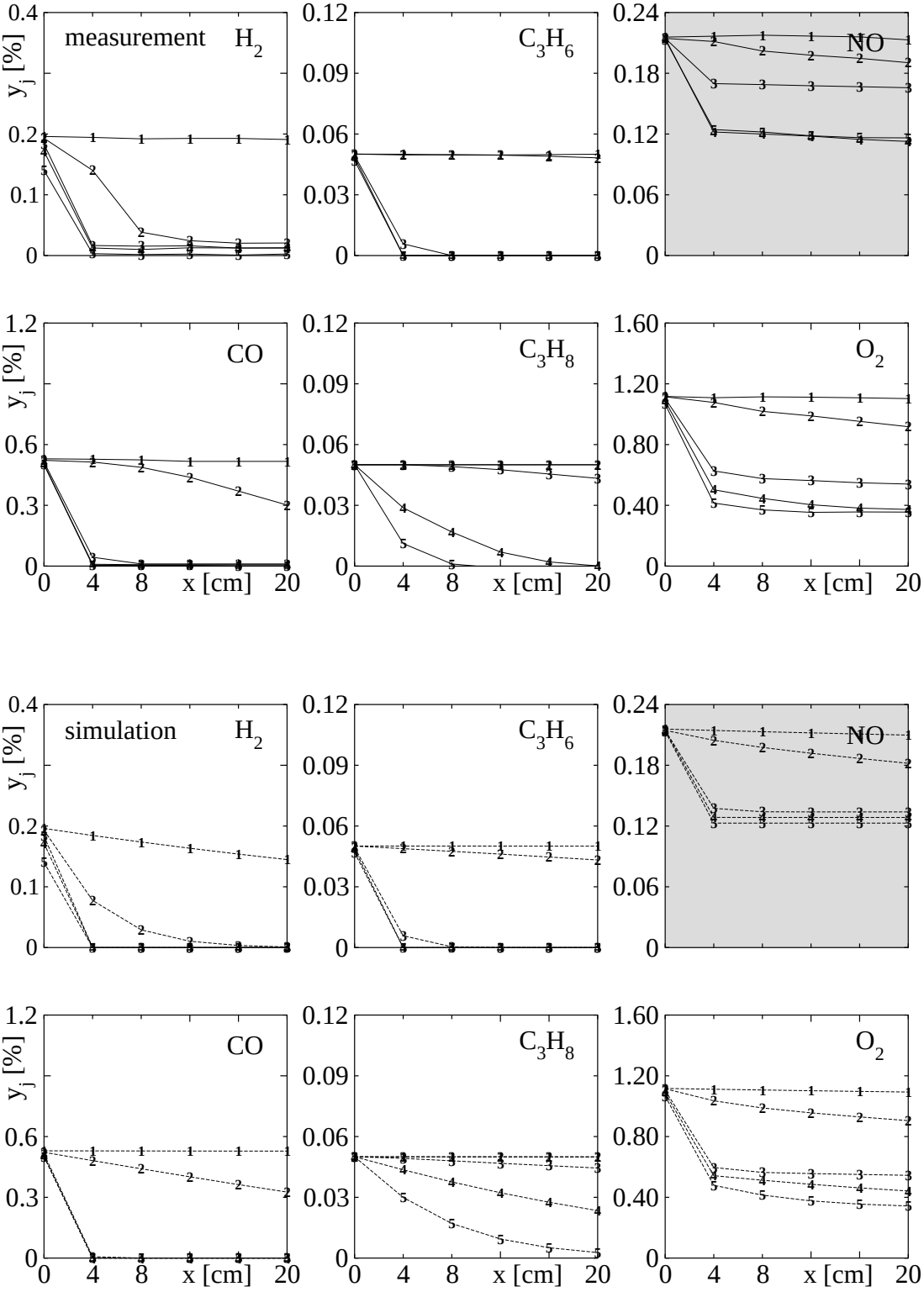

Figure 5.11: Conversion profiles for NO-increased lean conditions (composition **G7.8** in table 5.2), $SV = 16500$ 1/h at T = 100, 200, 300, 400, 500 °C (numbered 1 – 5). Above: measured in multiple slice reactor; below: simulated with rate equations 4.15 through 4.25 and respective parameters listed in table 5.1.

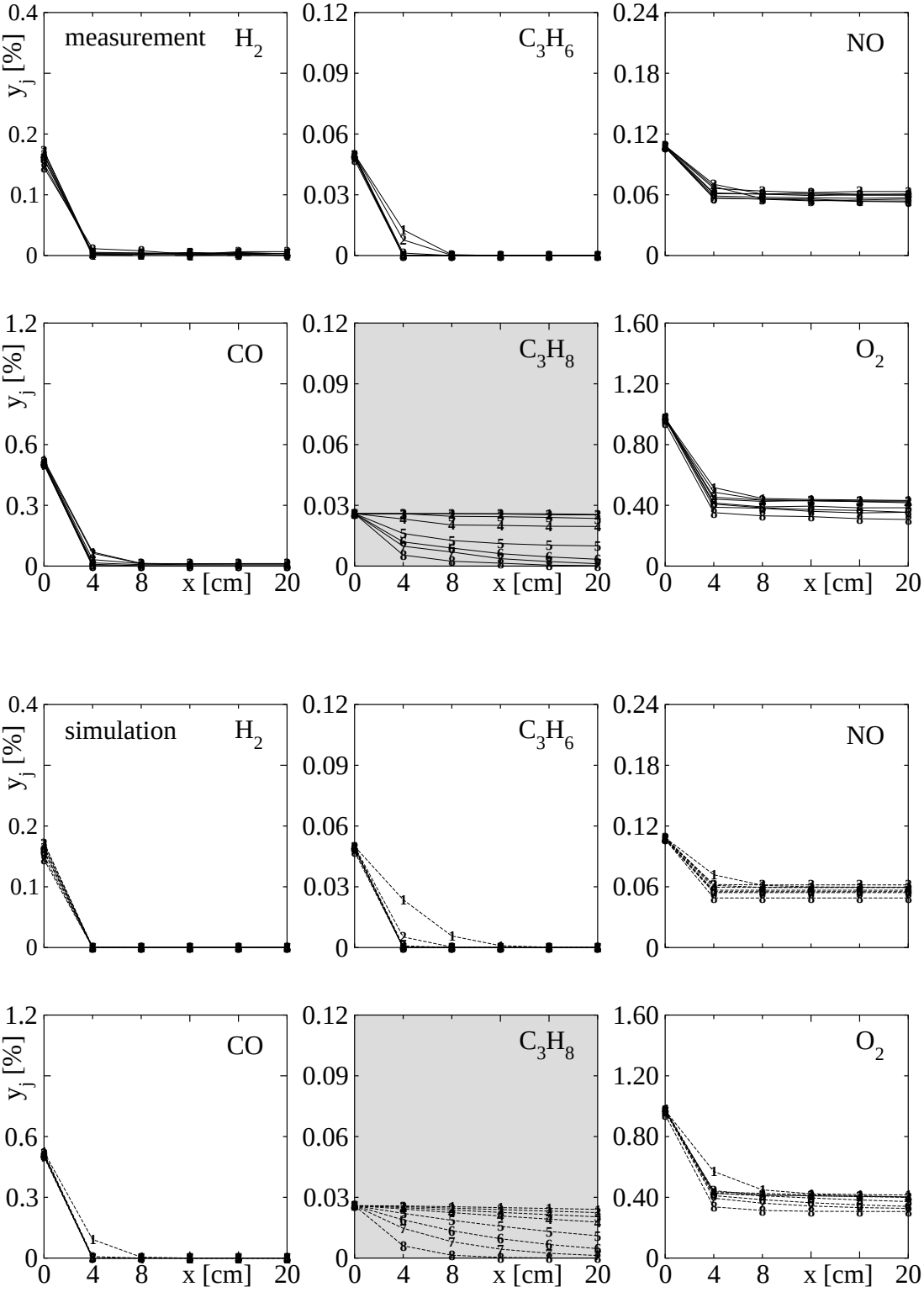

Figure 5.12: Conversion profiles for C_3H_8-reduced lean conditions (composition **G7.5** in table 5.2), SV = 16500 1/h at T = 275, 300, 325, 350, 400, 450, 500, 600 °C (numbered 1 – 8). Above: measured in multiple slice reactor; below: simulated with rate equations 4.15 through 4.25 and respective parameters listed in table 5.1.

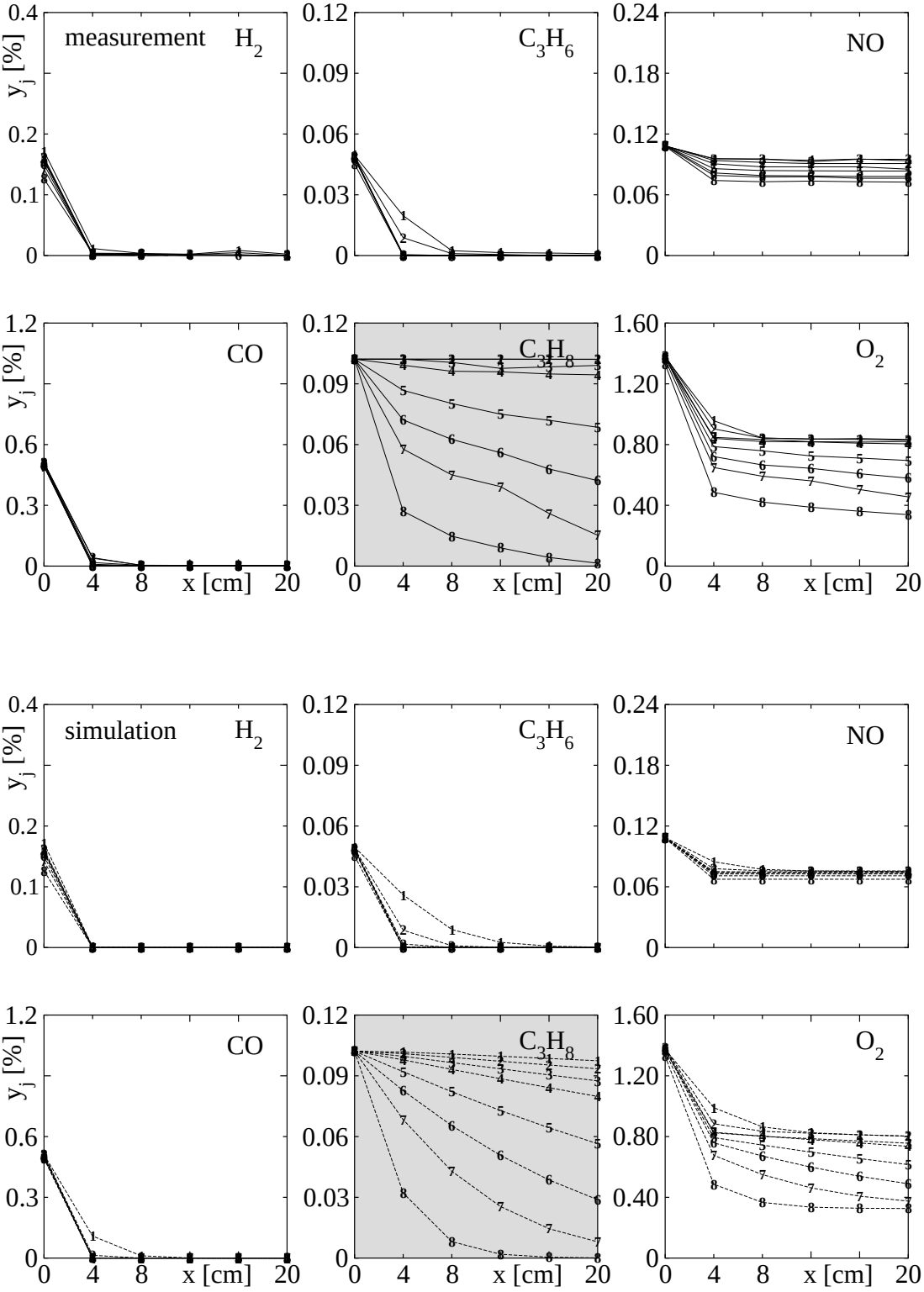

Figure 5.13: Conversion profiles for C_3H_8-increased lean conditions (composition **G7.6** in table 5.2), $SV = 16500$ 1/h at T = 275, 300, 325, 350, 400, 450, 500, 600 °C (numbered 1 – 8). Above: measured in multiple slice reactor; below: simulated with rate equations 4.15 through 4.25 and respective parameters listed in table 5.1.

5.4.2 Rich Exhaust

Again a realistic rich exhaust composition is retrieved from raw emission measurements of a 2.0l-2V-85kW engine subjected to an FTP75 emission certification driving cycle (figure 2.3). The exhaust composition sampled at $t = 251$ s (G8) is taken as basis for a rich exhaust from which certain species are varied selectively (table 5.3). The respective λ-variation is given in figure 5.14.

	H_2	CO	NO	O_2	C_3H_6	C_3H_8	λ
G8	0.300	0.900	0.0450	0.33	0.0185	0.0145	0.98
G8.1	0.300	0.900	**0**	**0**	**0.0330**	**0**	0.96
G8.2	0.300	0.900	**0**	**0**	**0**	**0.0330**	0.96
G8.3	**0.600**	**1.800**	0.0450	**0.94**	0.0185	0.0145	0.98
G8.4	0.300	0.900	0.0450	**0.30**	**0.0093**	0.0145	0.98
G8.5	0.300	0.900	0.0450	**0.42**	**0.0370**	0.0145	0.98
G8.6	0.300	0.900	0.0450	**0.30**	0.0185	**0.0073**	0.98
G8.7	0.300	0.900	0.0450	**0.41**	0.0185	**0.0290**	0.98

Table 5.3: Average rich gas mixture species concentrations in vol%: all mixtures contain nitrogen, 11 % H_2O, 12 % CO_2, 14 ppm SO_2, the air to fuel ratio is perturbed around its average value with an amplitude of $\pm$ 1 % at a frequency of 1 Hz.

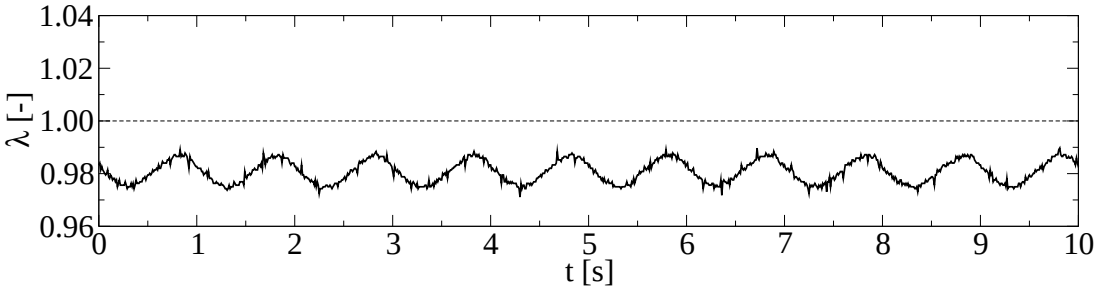

Figure 5.14: Measured exhaust air to fuel ratio upstream of the catalyst during rich bias conversion experiments ($\Delta\lambda = \pm 0.01$, $f = 1$ Hz).

Steam Reforming and Water Gas Shift Since steam reforming and water gas shift turn out to be important reactions under rich conditions and higher temperatures, they are studied in separate experiments in the absence of nitrogen oxide and oxygen (composition G8.1 and G.2 in table 5.3) at high flow rates of $SV = 77\,000\,\mathrm{h}^{-1}$ in the single slice reactor (appendix A.1).

As can be seen from figure 5.15 the reactions start at about 550 °C with propene (top) being converted more easily than propane (bottom). Due to the short residence time ($SV = 77\,000\,\mathrm{h}^{-1}$) even at 800 °C equilibrium of the water gas shift reaction ($y^{eq}_{H_2} : y^{eq}_{CO} \approx 1$ from figure 3.3) is not reached. The experimental results can be well represented by the kinetic model (table 5.1). Propene and propane steam reforming activation temperatures of 19900 K and 22000 K respectively (table 5.1) are indicative of

homogeneous mechanisms, participating in the overall conversion. It should be noted that – as all other experiments – the experiments are performed with 14 ppm SO_2 in the feed. Since catalytic steam reforming is known to be sensitive to small amounts of SO_2 [176], the high activation energies could also result from sulfur poisoning. This will be addressed in some detail in chapter 8.

Base System Composition In agreement with conversion measurements of lean biased exhaust, approximately 50 % hydrogen combustion can be achieved with rich biased exhaust at 150 °C (figure 5.16). Related to their respective inlet concentration nitrogen oxide and oxygen contribute to a quite similar extent. In absolute figures hydrogen combustion with oxygen is much more important since oxygen concentrations are almost one order of magnitude higher than nitrogen oxide concentrations. From 250 °C on both nitrogen oxide and oxygen conversion are complete within $x = 200\,\mathrm{mm}$. However the model somewhat underestimates the rapid increase in nitrogen oxide conversion observed experimentally between 200 and 250 °C. At 250 °C carbon monoxide conversion is higher than 50 % and some propene conversion is observed (figure 5.16). Under oxygen rich (fuel lean) conditions even somewhat higher carbon monoxide and propene conversions are obtained at a colder temperature of 225 °C (figure 5.4).

Above 300 °C combustion is virtually complete within the first slice of the multiple slice reactor. A nitrogen oxide and oxygen free rich exhaust mixture passes catalyst sections located downstream ($40\,\mathrm{mm} < x < 200\,\mathrm{mm}$). Since 300 °C is a temperature too low for significant water gas shift and reforming reactions (water as a reaction partner is available with $y_{H_2O} \approx 12\,\%$, chapter 2) even at high residence times ($SV = 16500\,1/\mathrm{h}$) overall conversion is determined by combustible species' oxidation rate competition within the very first millimeters of the catalyst. This competition is temperature dependent which reflects itself in the increasing activation energies for combustion with oxygen or nitrogen oxide from hydrogen over carbon monoxide to propene (table 5.1). While propene conversion at 300 °C amounts to only 20 % after oxygen and nitrogen oxide is completely consumed it rises to more than 50 % at 400 °C.

Again, homogeneous hydrogen and – to some extent – hydrocarbon combustion upstream of the first catalyst slice are observed at 500 °C. At this temperature also propane oxidation rates start to get competitive enough to participate in oxygen conversion. Starting at about 500 °C water gas shift and steam reforming reactions play an increasing role with increasing temperature. This is reflected in the decrease of carbon monoxide and propene concentration beyond the point of nitrogen oxide/oxygen depletion and in the substantial increase in hydrogen production. Consequently hydrogen concentrations – primarily reduced in the combustion zone – level up towards the catalyst outlet. At 600 °C water gas shift reaction equilibrium ($y_{H_2}^{eq} : y_{CO}^{eq} \approx 2.3$ at 600 °C) is not yet established. At 700 °C the water gas shift reaction equilibrium ($y_{H_2}^{eq} : y_{CO}^{eq} \approx 1.4$ at 700 °C) is reached – also indicated by flattening hydrogen and carbon monoxide concentration profiles.

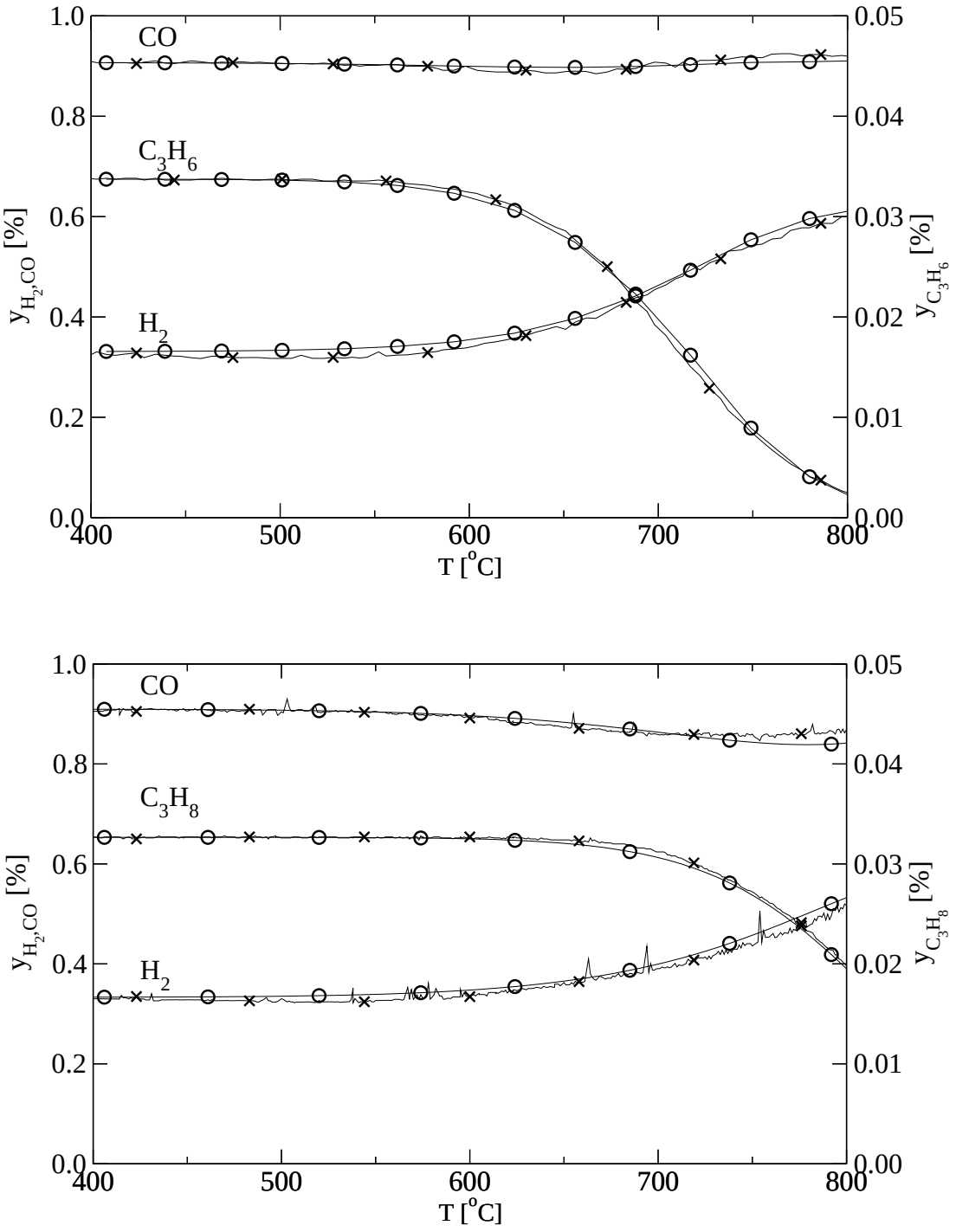

Figure 5.15: Catalyst exit concentrations for water gas shift and steam reforming at $SV = 77000\,1/\mathrm{h}$, composition **G8.1** (top) and **G8.2** (bottom) of table 5.3. Conversion at $T < 800\,^{\circ}\mathrm{C}$ measured ($+$) in single slice reactor and simulated ($\circ$) with rate equations 4.15 through 4.25 and respective parameters listed in table 5.1.

Variation of Hydrogen and Carbon Monoxide Doubled hydrogen and carbon monoxide concentrations along with increased oxygen concentrations to maintain the average air to fuel ratio at $\lambda = 0.98$ results up to 250 °C in slightly smaller relative hydrogen conversion (figure 5.17). Relative carbon monoxide conversion seems unchanged and propene conversion is enhanced. At 400 °C the whole species conversion occurs within the first catalyst section $0\,\text{mm} < x < 40\,\text{mm}$. The remaining combustible species concentrations are similar to the base system since absolute oxygen shortage remains unchanged due to fixed rich-biased air to fuel ratio.

At temperatures above 400 °C increased hydrogen and oxygen concentrations obviously result in increased homogeneous preoxidation of hydrogen leading to a decrease of hydrogen entrance concentrations. However the model somewhat over predicts hydrogen oxidation rates in relation to carbon monoxide oxidation rates in the high temperature range.

As a side-effect, the increased oxygen concentrations accelerate propane oxidation above 500 °C remarkably compared to the base case. Again water gas shift activity is measurable at 500 °C, pronounced at 600 °C and in equilibrium at 700 °C.

Variation of Propene Species conversion is not significantly altered with a variation of propene inlet concentrations (figures 5.18 and 5.19). However it is evident from figure 5.19 that carbon monoxide conversion suffers in the temperature range $300 < T < 500\,°\text{C}$ from increased propene conversion. This might be due to partial propene oxidation which is not considered in the reaction kinetic model outlined in chapter 4. In homogeneous combustion the partial oxidation product carbon monoxide is reported to be an important intermediate even under lean conditions [67].

Variation of Propane Under steady state rich conditions hydrocarbon conversion is not complete even at 700 °C. Little propane conversion is obtained at low levels of propane inlet concentrations (figure 5.20). At elevated propane and associated oxygen concentrations a significantly improved hydrocarbon (partial) oxidation is observed (figure 5.21). Above 300 °C increasing temperatures lead to an enhanced hydrocarbon conversion at a lower carbon monoxide and hydrogen conversion within the first catalyst section $0 < x < 4$ cm. In the absence of oxygen and nitrogen oxide ($4 < x < 20$ cm) carbon monoxide is converted by water gas shift reaction and hydrogen is produced at temperatures above 450 °C.

In an absolutely sulfur free exhaust propane conversion under steady state rich conditions should be much higher. Steam reforming is in particular prone towards sulfur poisoning, which deactivates the catalyst slowly at temperatures up to 500 °C and quickly beyond 600 °C (see chapter 8 and appendix C).

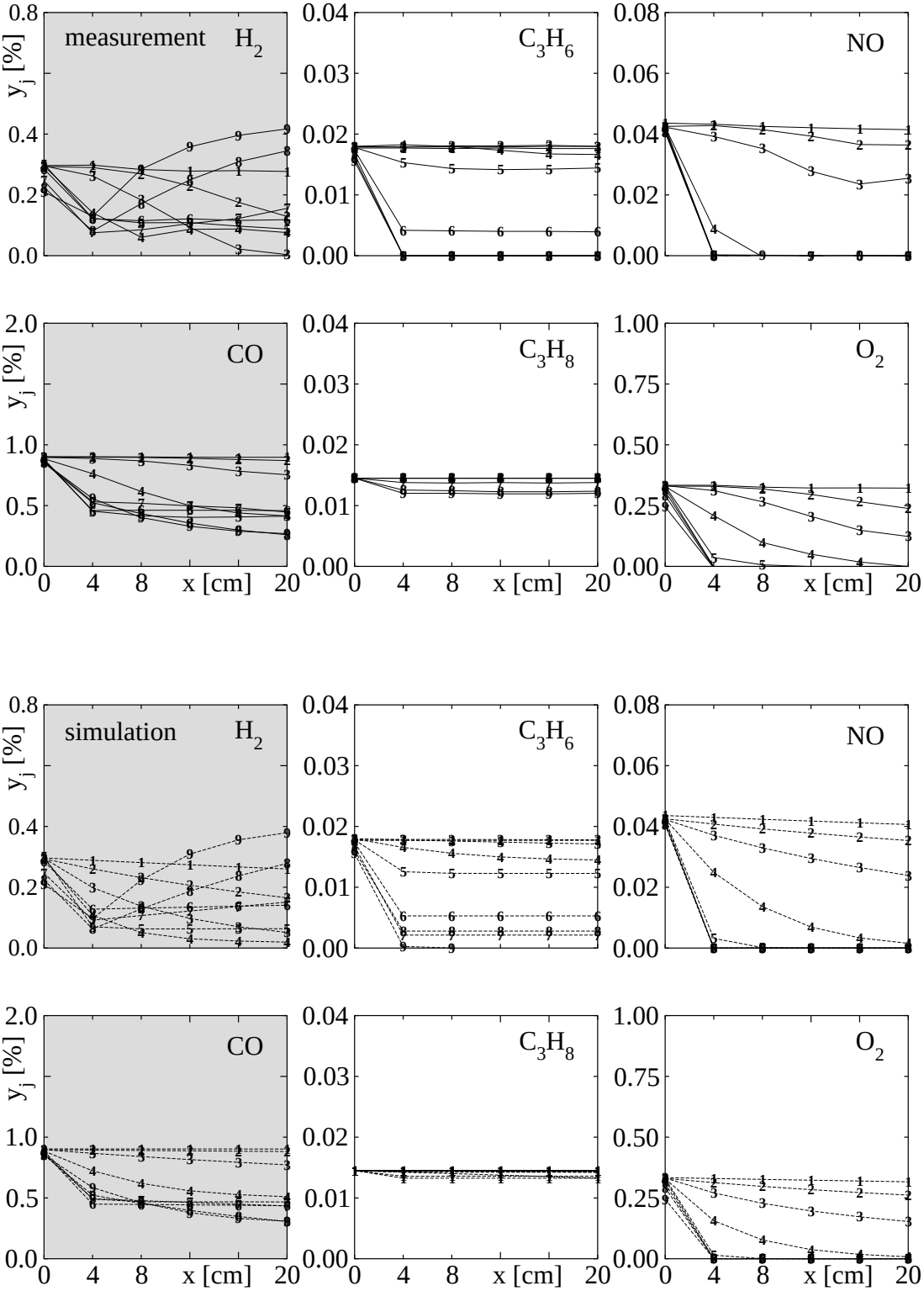

Figure 5.16: Conversion profiles for basic rich conditions (composition G8 in table 5.3), $SV = 16500$ 1/h at T = 100, 150, 200, 250, 300, 400, 500, 600, 700 °C (numbered 1 – 9). Above: measured in multiple slice reactor; below: simulated with rate equations 4.15 through 4.25 and respective parameters listed in table 5.1.

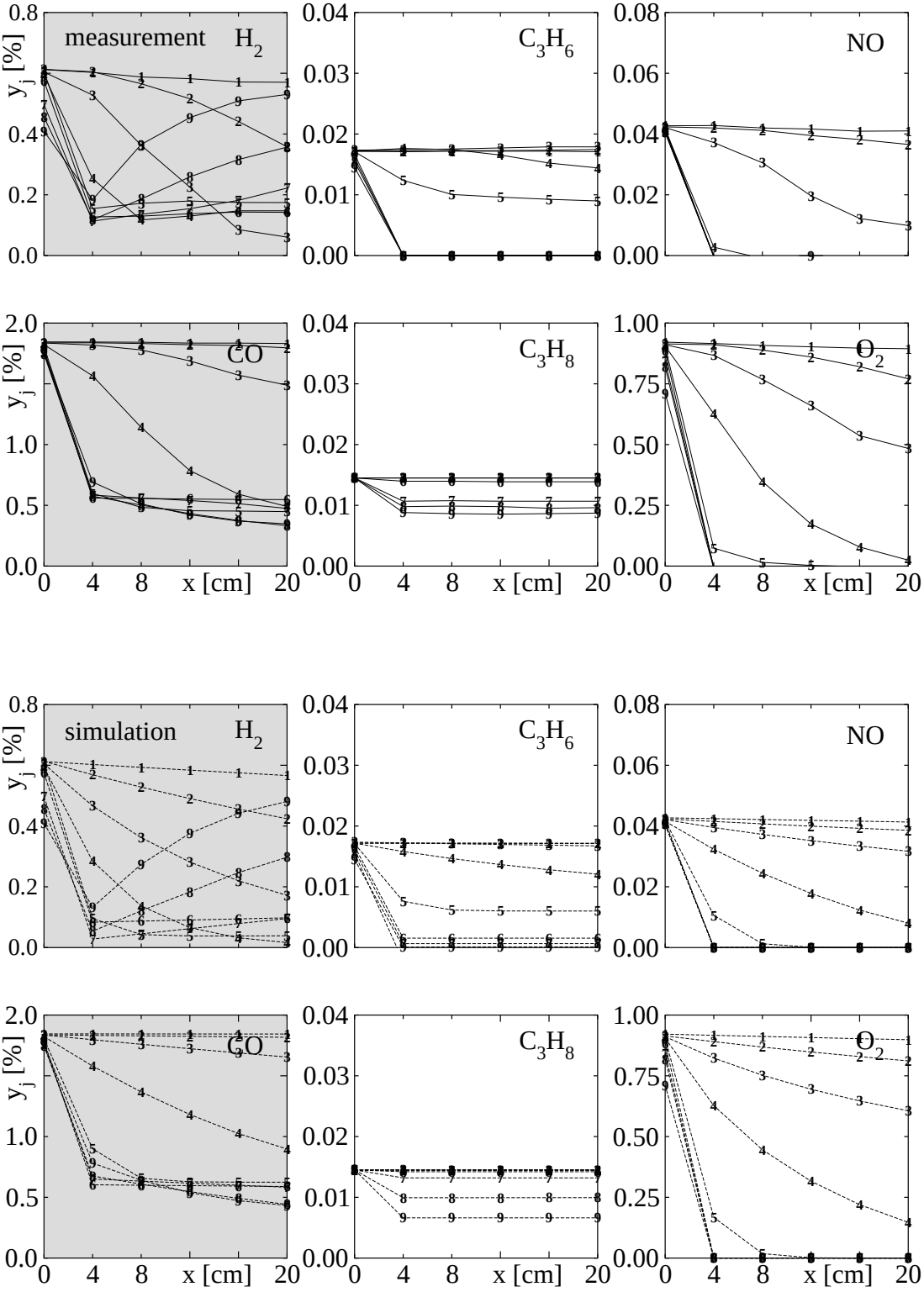

Figure 5.17: Conversion profiles for H_2/CO-increased rich conditions (composition G8.3 in table 5.3), SV = 16500 1/h at T = 100, 150, 200, 250, 300, 400, 500, 600, 700 °C (numbered 1 – 9). Above: measured in multiple slice reactor; below: simulated with rate equations 4.15 through 4.25 and respective parameters listed in table 5.1.

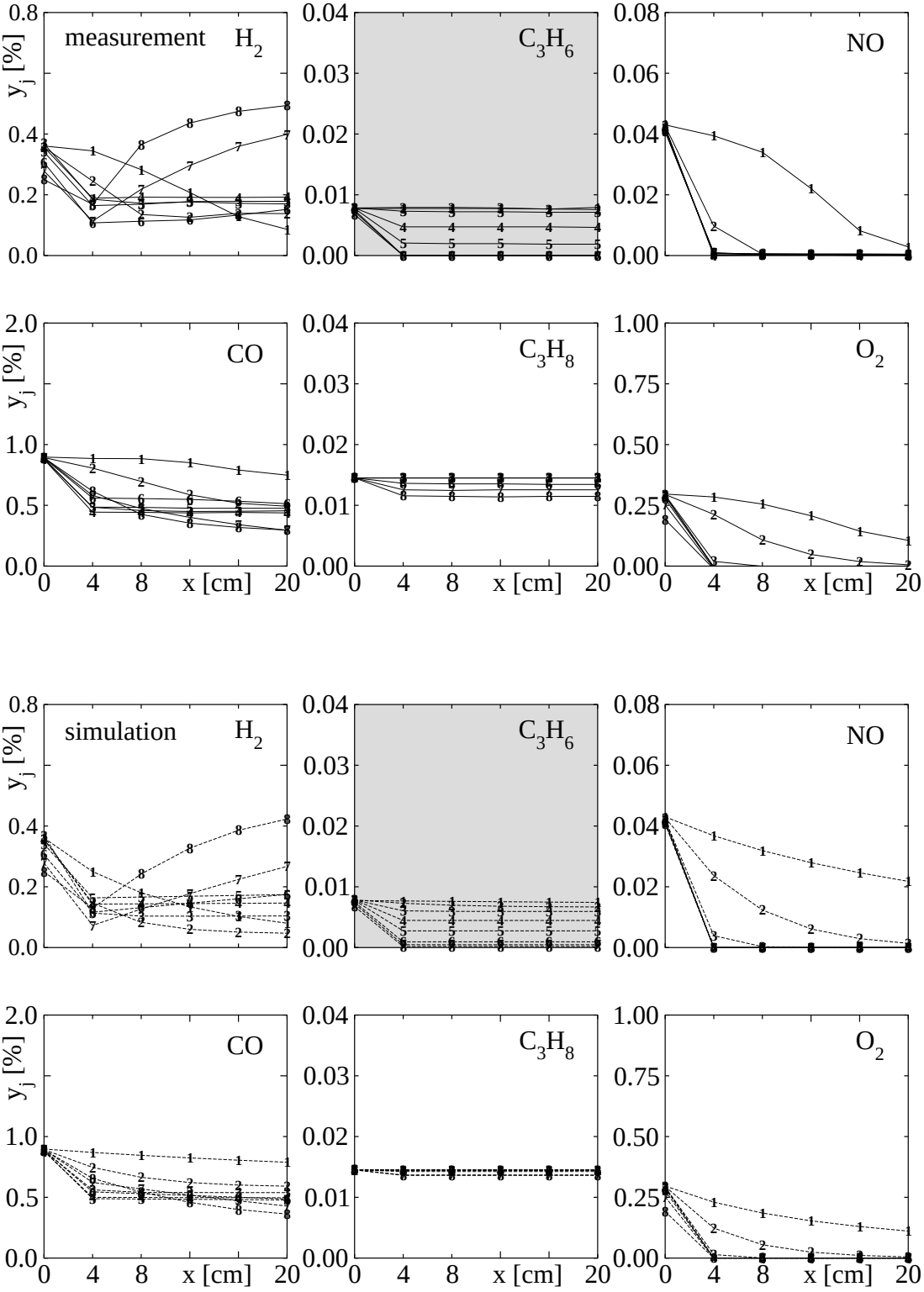

Figure 5.18: Conversion profiles for C_3H_6-reduced rich conditions (composition G8.4 in table 5.3), SV = 16500 1/h at T = 200, 250, 300, 350, 400, 500, 600, 700 °C (numbered 1 – 8). Above: measured in multiple slice reactor; below: simulated with rate equations 4.15 through 4.25 and respective parameters listed in table 5.1.

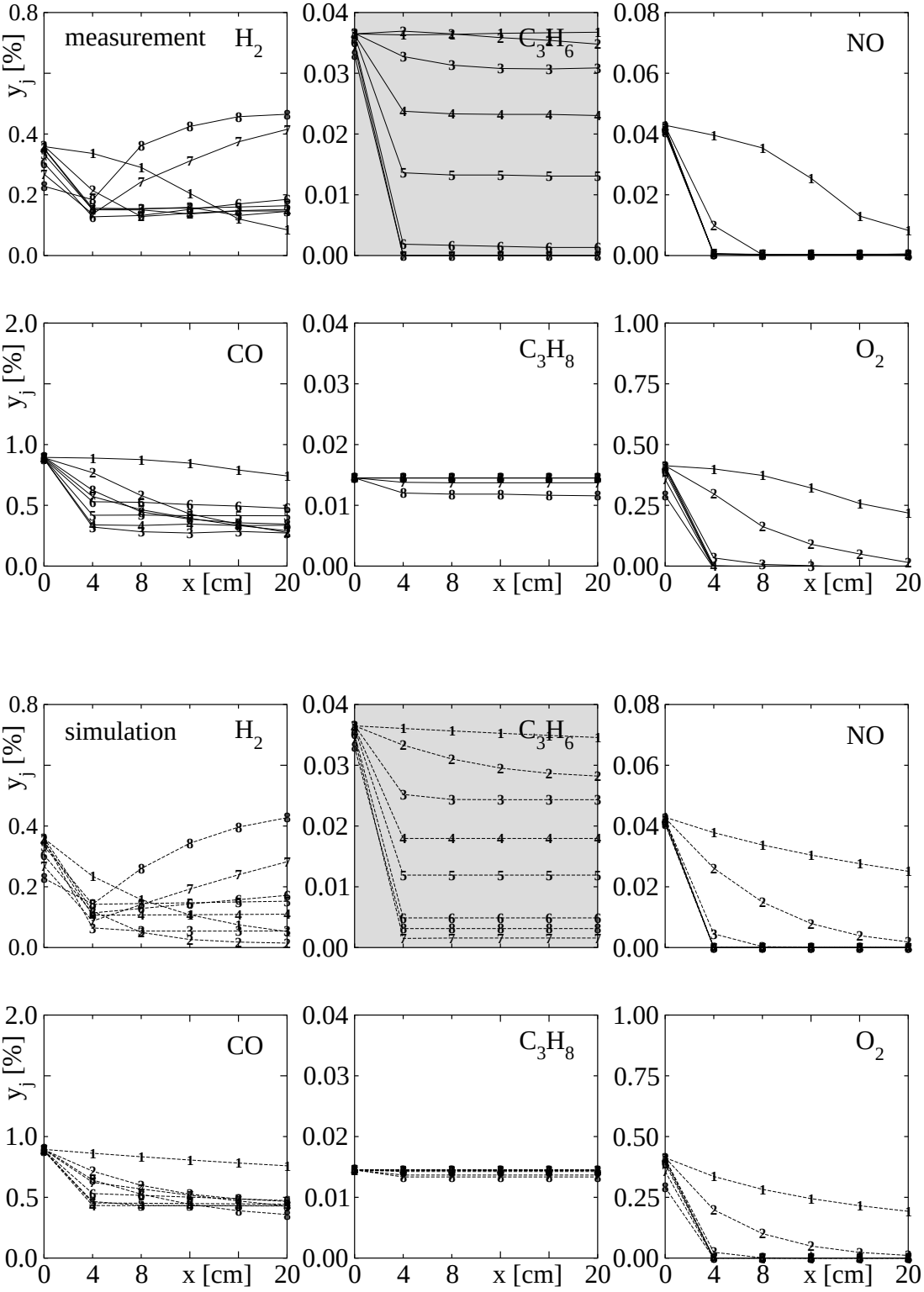

Figure 5.19: Conversion profiles for C_3H_6-increased rich conditions (composition G8.5 in table 5.3), $SV = 16500$ 1/h at T = 200, 250, 300, 350, 400, 500, 600, 700 °C (numbered 1 – 8). Above: measured in multiple slice reactor; below: simulated with rate equations 4.15 through 4.25 and respective parameters listed in table 5.1.

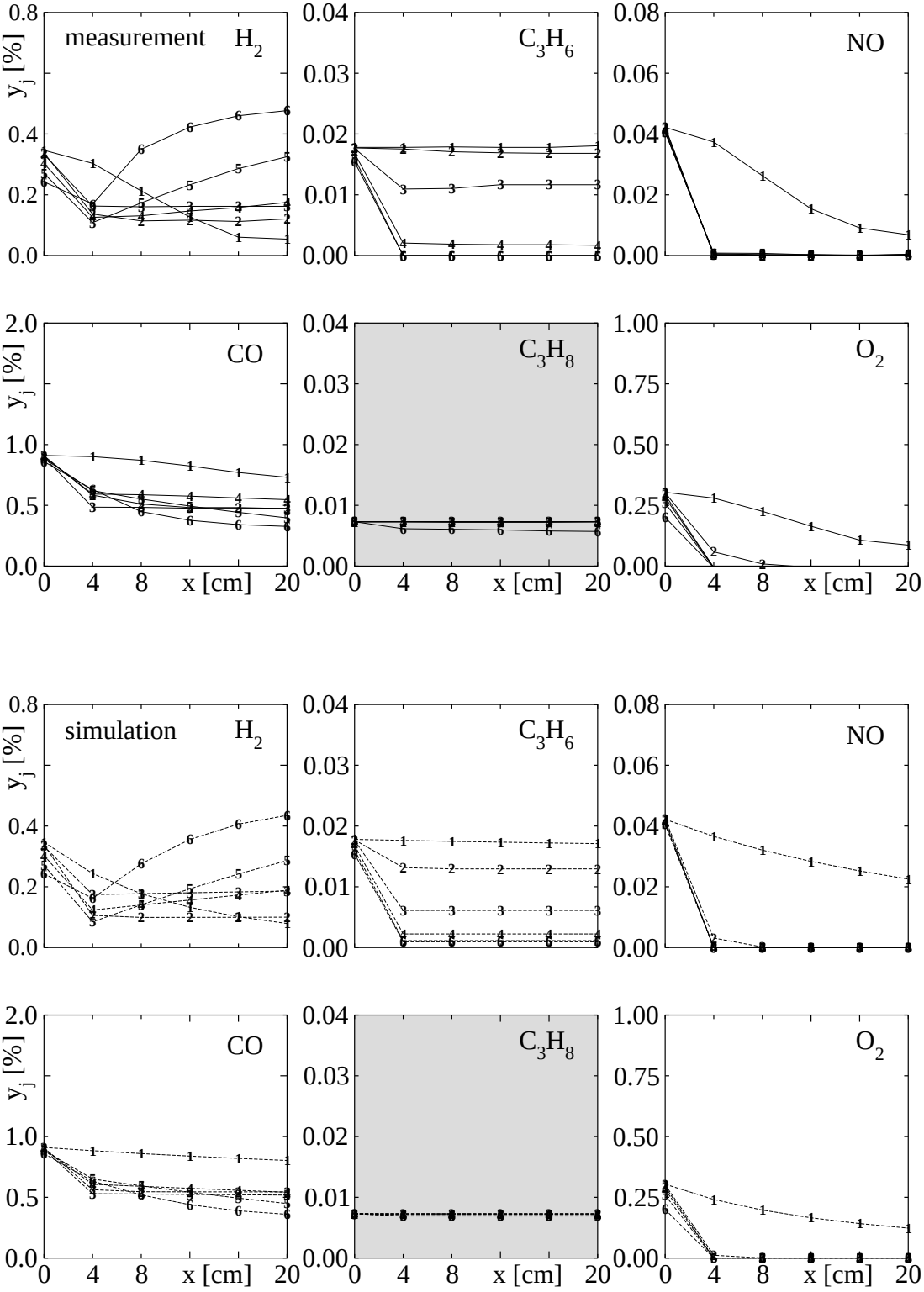

Figure 5.20: Conversion profiles for C_3H_8-reduced rich conditions (composition G8.6 in table 5.3), $SV = 16500$ 1/h at T = 200, 300, 400, 500, 600, 700 °C (numbered 1 – 6). Above: measured in multiple slice reactor; below: simulated with rate equations 4.15 through 4.25 and respective parameters listed in table 5.1.

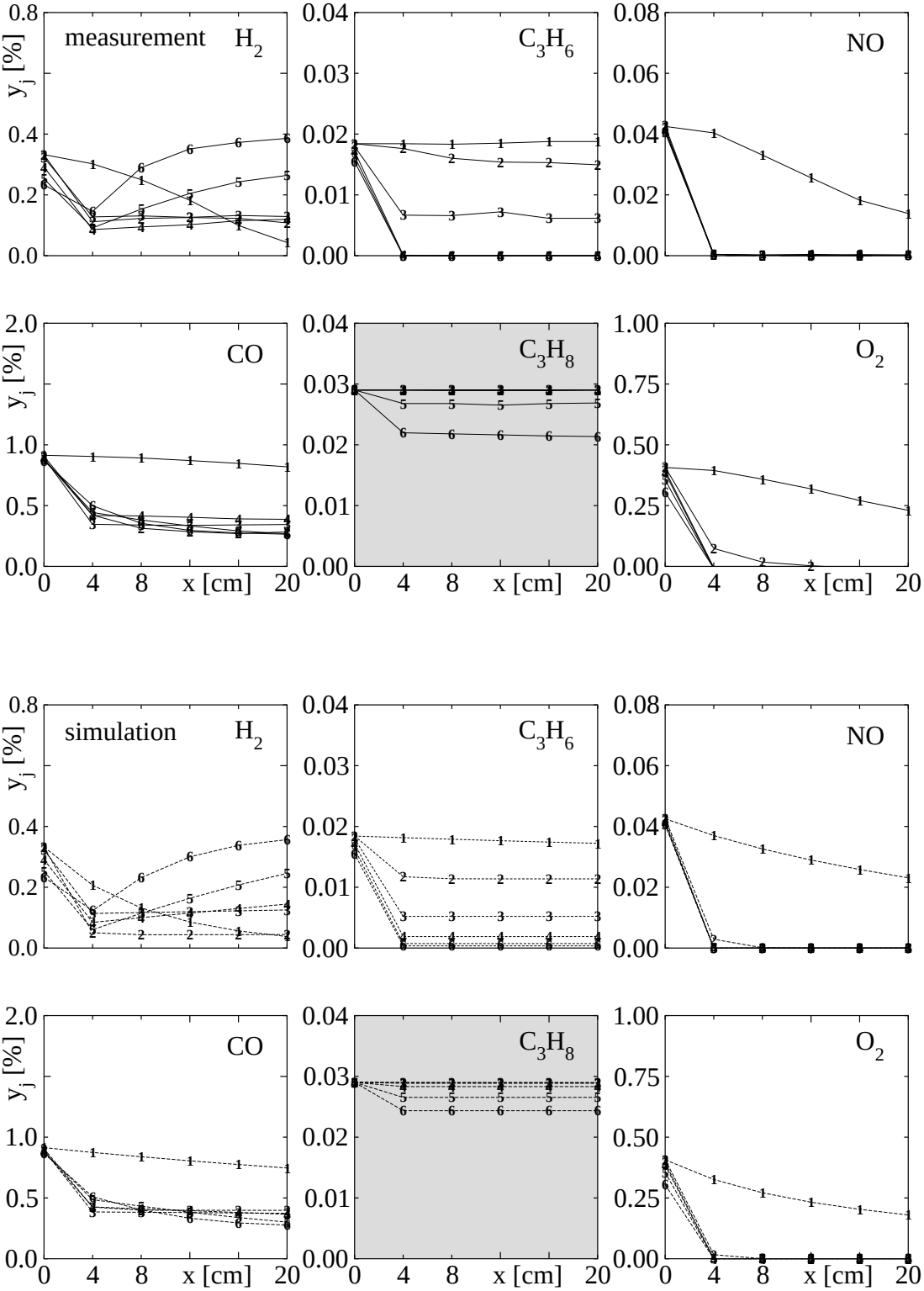

Figure 5.21: Conversion profiles for C_3H_8-increased rich conditions (composition G8.7 in table 5.3), $SV = 16500$ 1/h at T = 200, 300, 400, 500, 600, 700 °C (numbered 1 – 6). Above: measured in multiple slice reactor; below: simulated with rate equations 4.15 through 4.25 and respective parameters listed in table 5.1.

Chapter 6

Oxygen Storage Capacity and Kinetics

After catalyst light-off main dynamic effects are a consequence of air to fuel-ratio control and oxygen storage and release [6]. A common procedure to measure the oxygen storage capacity is to stepwise change the stoichiometry of the feed mixture from e.g. $\lambda = 0.97$ to $\lambda = 1.03$ and reverse [157]. Catalyst inlet concentrations applied in flat bed reactor experiments are listed in table 6.1.

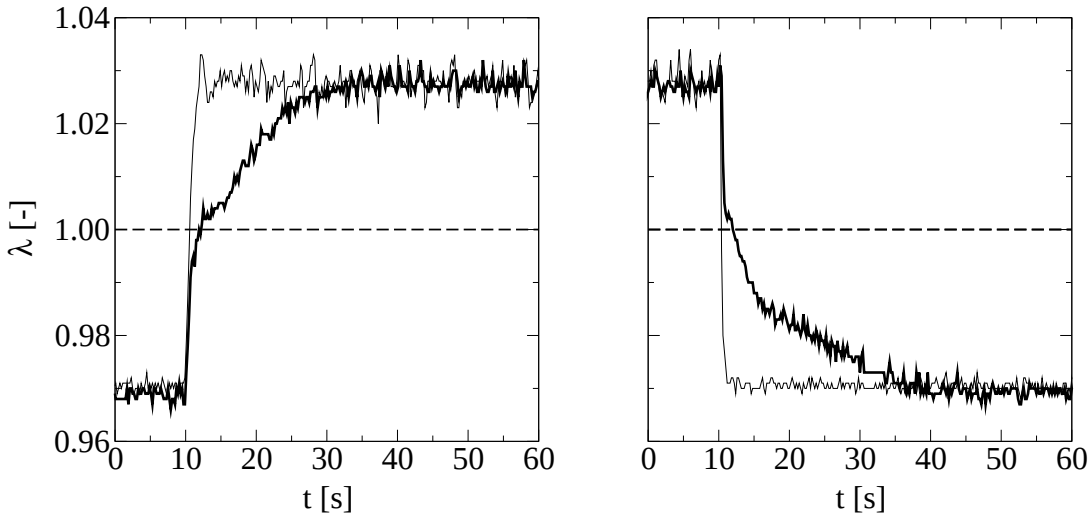

Figure 6.1: Wide range oxygen sensor (Bosch LSU 4.2) responses to rich-lean (left) and lean-rich (right) transitions at $T = 700\,^{\circ}\mathrm{C}$. Signal of sensor mounted upstream (thin line) and downstream (thick line) of a single monolith slice (section A.1) - corrected signals (details see appendix D).

Switching from rich to lean the sensor located upstream of the catalyst follows the step change immediately (figure 6.1). The sensor located downstream of the catalyst also follows until a stoichiometric ratio ($\lambda = 1$) is reached. Then only a delayed increase to the new steady state value of $\lambda = 1.03$ is measured. Stepping back from lean to rich conditions the downstream sensor again follows the exhaust composition step change immediately up to stoichiometric composition. The detection of even richer

λ	H_2	CO	NO	O_2	C_3H_6	C_3H_8
0.97	0.39	1.17	0.108	0.59	0.051	0.051
1.03	0.37	1.11	0.103	1.70	0.048	0.049

Table 6.1: Rich and and lean feed exhaust composition (vol%) during step experiments in single slice reactor ($SV = 77\,000\,1/\mathrm{h}$) and multiple slice reactor ($SV = 16\,500\,1/\mathrm{h}$), background gas concentrations: 11 % H_2O, 12 % CO_2, 14 ppm SO_2 and balance nitrogen, setup see section A.1.

compositions is delayed due to oxygen release. The steady state composition $\lambda = 0.97$ establishes after oxygen storage depletion[1].

Oxygen Sensor Signal Correction The post catalyst oxygen sensor signals shown in figure 6.1 to 6.3 are already corrected signals. Without correction the rich/lean-switch experiments show a certain steady-state deviation between the measured air to fuel ratio readings upstream and downstream of the catalyst as shown in figure D.3. The reason for this deviation is the specific sensor's sensitivity towards each single exhaust constituent (e.g. the sensor's sensitivity towards hydrogen is strong whereas it's sensitivity towards hydrocarbons is poor). In the steady state (when the oxygen storage is either full or empty) the λ-signal before and after the catalyst should be the same but the concentrations of exhaust species (in particular combustibles) are of course different due to catalyst reactions. This requires a λ-signal correction which is explained in more detail in appendix D.

6.1 Oxygen Storage Capacity

At a fixed mass flow the area between the two sensor readings is proportional to the amount of oxygen stored/released. Taking into account the stoichiometry of fuel combustion with air (section 2.1) the temperature dependent, volume based oxygen storage capacity Ω [kg O_2/m^3 cat] can be calculated (see appendix E):

$$\Omega = \frac{p^0 MW_{O_2}}{R\,T^0} \frac{1 + x/4}{1 + \frac{x}{2} + \frac{1+x/4}{y_{O_2,\mathrm{air}}}(1 - y_{O_2,\mathrm{air}})} SV \int_{t_1}^{t_2} (\lambda_{\mathrm{up}} - \lambda_{\mathrm{down}})\, dt \tag{6.1}$$

Step experiments carried out at temperatures between 70 and 750 °C reveal that oxygen storage capacity is immeasurably small below 300 °C. Figures 6.2 and 6.3 depict the

[1]The corrected sensor readings suggest that oxygen release already starts at slightly lean conditions. It is evident from figure 3.8 that oxygen release from cerium-zirconium solid solution can not be expected above $\lambda = 1$. Reduction of palladium oxide (figure 3.5) might be more facile at elevated temperatures. However this phenomenon is most likely due to a shortcoming in static post catalyst sensor correction (see appendix D).

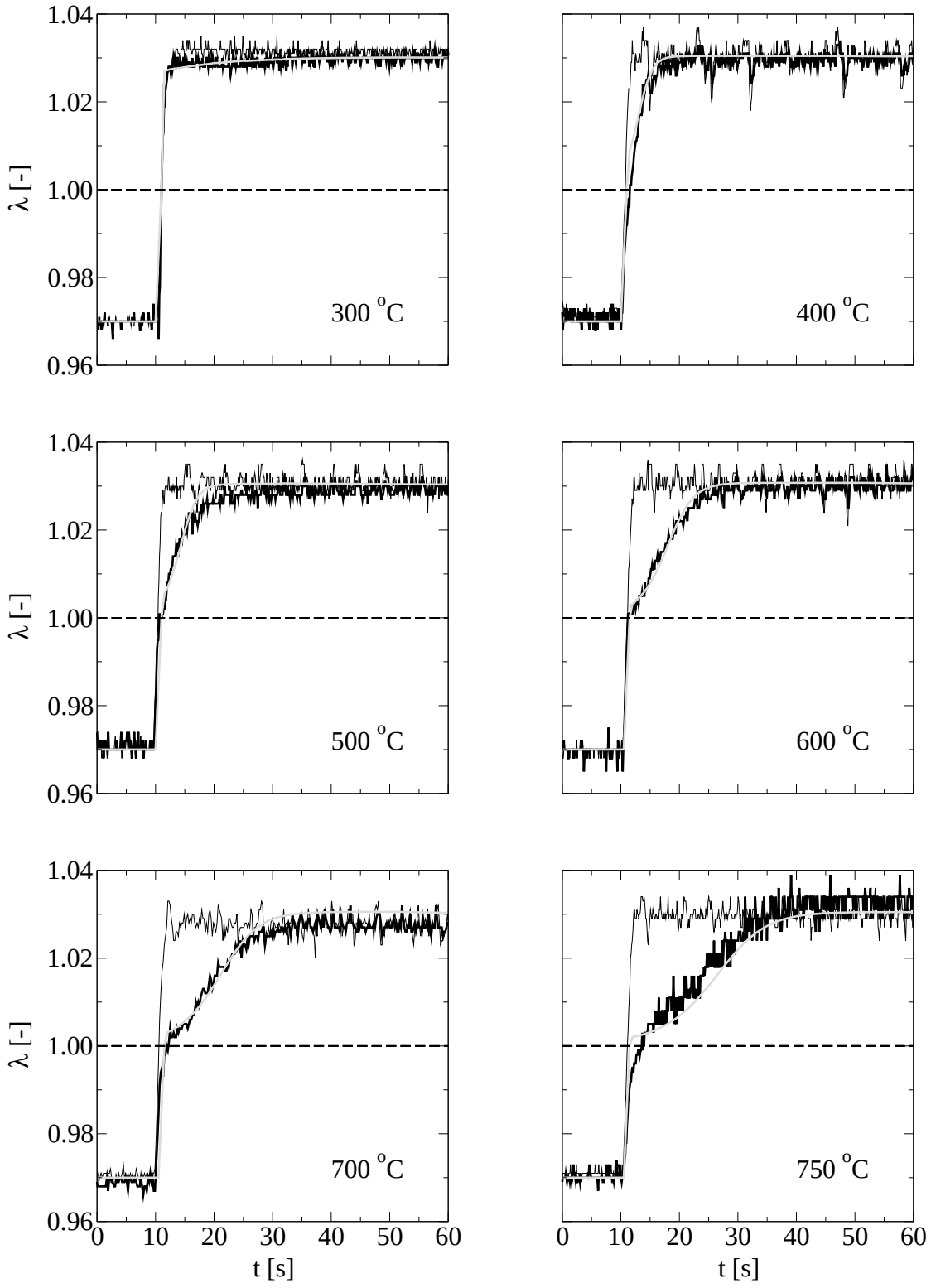

Figure 6.2: Air to fuel ratio upstream and downstream of a catalyst subjected to rich-lean transitions at $SV = 77\,000$ 1/h. Corrected measured wide range oxygen sensor Bosch LSU 4.2 readings (black lines, correction see appendix D) along with simulated post catalyst air to fuel ratio (grey lines).

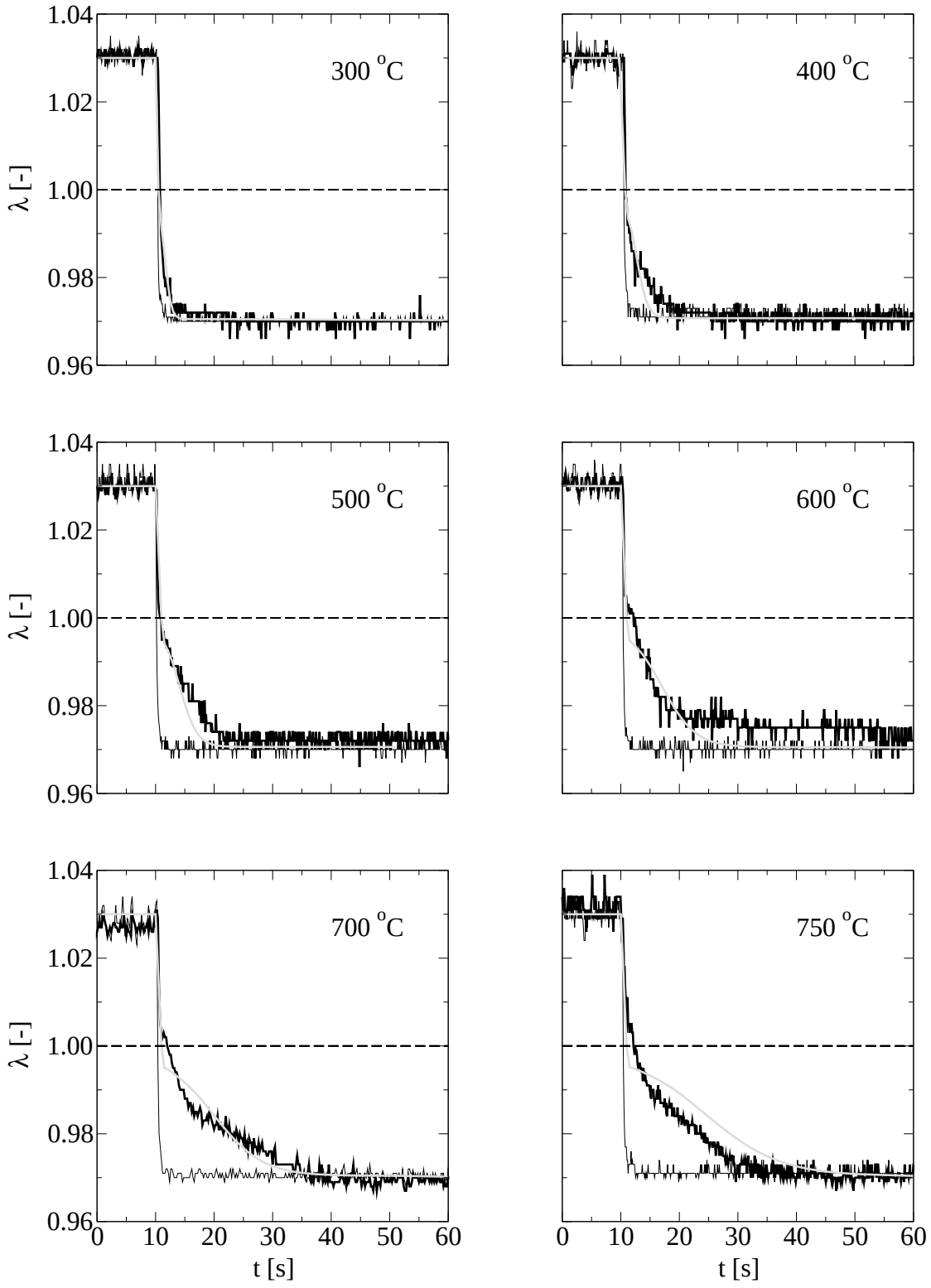

Figure 6.3: Air to fuel ratio upstream and downstream of a catalyst subjected to lean-rich transitions at $SV = 77\,000$ 1/h. Corrected measured wide range oxygen sensor Bosch LSU 4.2 readings (black lines, correction see appendix D) along with simulated post catalyst air to fuel ratio (grey lines).

sensors responses to a step from rich to lean and back at temperatures between 300 and 750 °C.

The integrated complete oxygen storage capacities according to equation 6.1 are plotted against temperature in figure 6.4. It can be clearly seen that the capacity increases with temperature, moderately up to 500 °C and more pronounced with higher temperatures. This phenomenon is qualitatively in good agreement with data on a different washcoat formulation reported elsewhere [10] (figure 6.4) and many other reports [155, 179, 154, 126, 79, 167, 41, 53, 168, 68, 169, 55, 13, 12, 152].

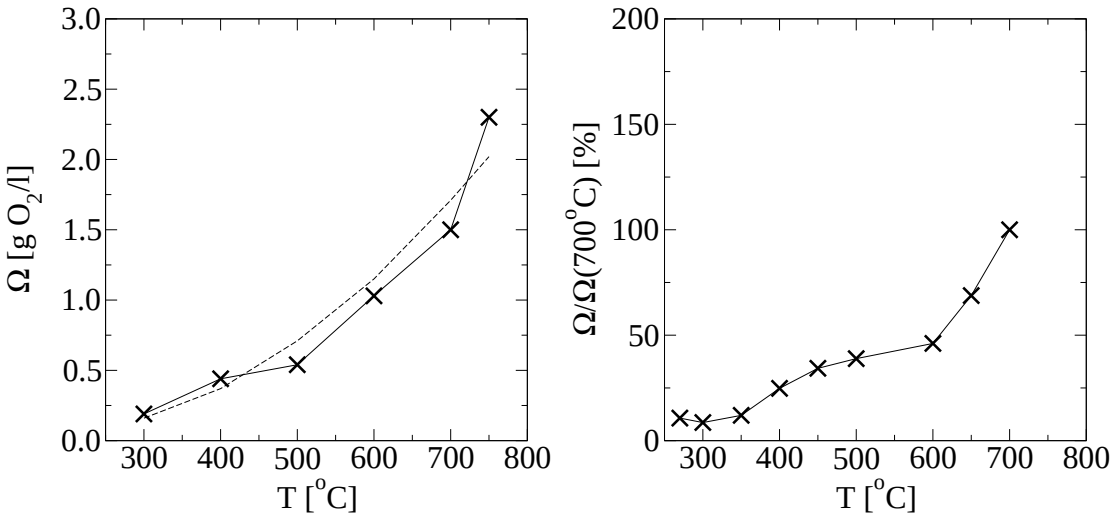

Figure 6.4: Complete oxygen storage capacities (OSCC) at different temperatures: this work (left) compared with data on a different washcoat formulation reported elsewhere (right) [10]; measured (solid lines) and calculated from equation 6.2 (dashed line).

Even though the value $\Omega(750\,^{\circ}\mathrm{C}) = 2.3\,\mathrm{gO_2/l}$ seems to be somewhat overestimated by comparing measured and simulated downstream air to fuel ratios (figure 6.2 and 6.3) this value is still reasonable assuming that the washcoat cerium content is about 30 weight%: with a measured washcoat loading of 280 g/l (section F.2) the theoretical oxygen storage capacity limit based on reaction 3.14 turns out to be roughly $4\,\mathrm{gO_2/l}$. Full oxidation of 100 g/ft^3 metallic palladium adds another $0.5\,\mathrm{gO_2/l}$. Due to the lack of information about washcoat nature and composition and due to a limited number of experiments the oxygen storage model described in chapter 4 does not distinguish between different sources of oxygen storage capacity. To be consistent with the simple one site storage model one single fit is applied – if not otherwise stated – to describe the complete oxygen storage capacity over the full temperature range:

$$\begin{aligned} \Omega(T) &= \Omega^{300\,^{\circ}\mathrm{C}}\,\mathrm{e}^{\left(-\frac{E_\Omega}{\mathrm{R}}\left(\frac{1}{T}-\frac{1}{573.15\,K}\right)\right)} \\ \Omega^{300\,^{\circ}\mathrm{C}} &= 0.158\,\mathrm{g/l} \\ E_\Omega/R &= 3317\,\mathrm{K} \end{aligned} \tag{6.2}$$

6.2 Oxygen Storage and Release Kinetics

The rate of oxygen uptake of the oxygen storage material also increases with temperature. This leads to a relatively flat signal of the post oxygen sensor at the onset of oxygen storage at λ = 1.00 with higher temperatures (figure 6.2). Dynamic simulation based on the measured OSCC values (figure 6.4) is applied to determine the oxygen storage and release rate constants in equation 4.30 and 4.31. The kinetic rate constants that provide a good fit of the experimental data (figures 6.2 and 6.3) are gathered in figure 6.5.

The derived kinetic rate constant for the rate expression of oxygen uptake shows a weak temperature dependence at temperatures above 400 °C (figure 6.5):

$$\begin{aligned} k_{\mathrm{os}}(T) &= k_{\mathrm{os}}^{300\,^{\circ}\mathrm{C}}\,\mathrm{e}^{\left(-\frac{E_{\mathrm{os}}}{\mathrm{R}}\left(\frac{1}{T}-\frac{1}{573.15\,K}\right)\right)}, \quad T \geq 400\,^{\circ}\mathrm{C} \\ k_{\mathrm{os}}^{300\,^{\circ}\mathrm{C}} &= 1.063\cdot 10^{-4}\,\mathrm{kmol}/(\mathrm{m}^2\,\mathrm{s}) \\ E_{\mathrm{os}}/R &= 1360\,\mathrm{K} \end{aligned} \tag{6.3}$$

If the rate constant for the reduction is at all dependent on temperature this dependence is considerably weaker. Thus in this work the rate constant for reduction is regarded as independent of temperature over the full temperature range (figure 6.5).

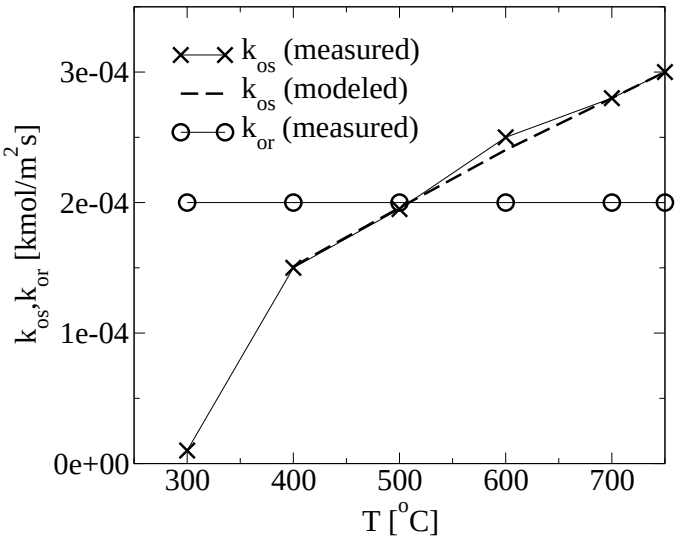

Figure 6.5: Oxygen storage and oxygen release rate constants (k_{os} and k_{or} in equation 4.30 and 4.31) providing the best match of simulated and measured post catalyst λ-values to rich-lean (figure 6.2) and lean-rich (figure 6.3) transitions (solid lines) along with modeled oxygen storage rate constant according to equation 6.3 (dashed line).

Due to intake port wall-applied fuel film dynamics the exhaust composition oscillates around the average air to fuel ratio during closed loop operation (figure 6.6). A common assumption is that the air to fuel ratio oscillates with an amplitude of $\Delta\lambda = \pm 0.03$

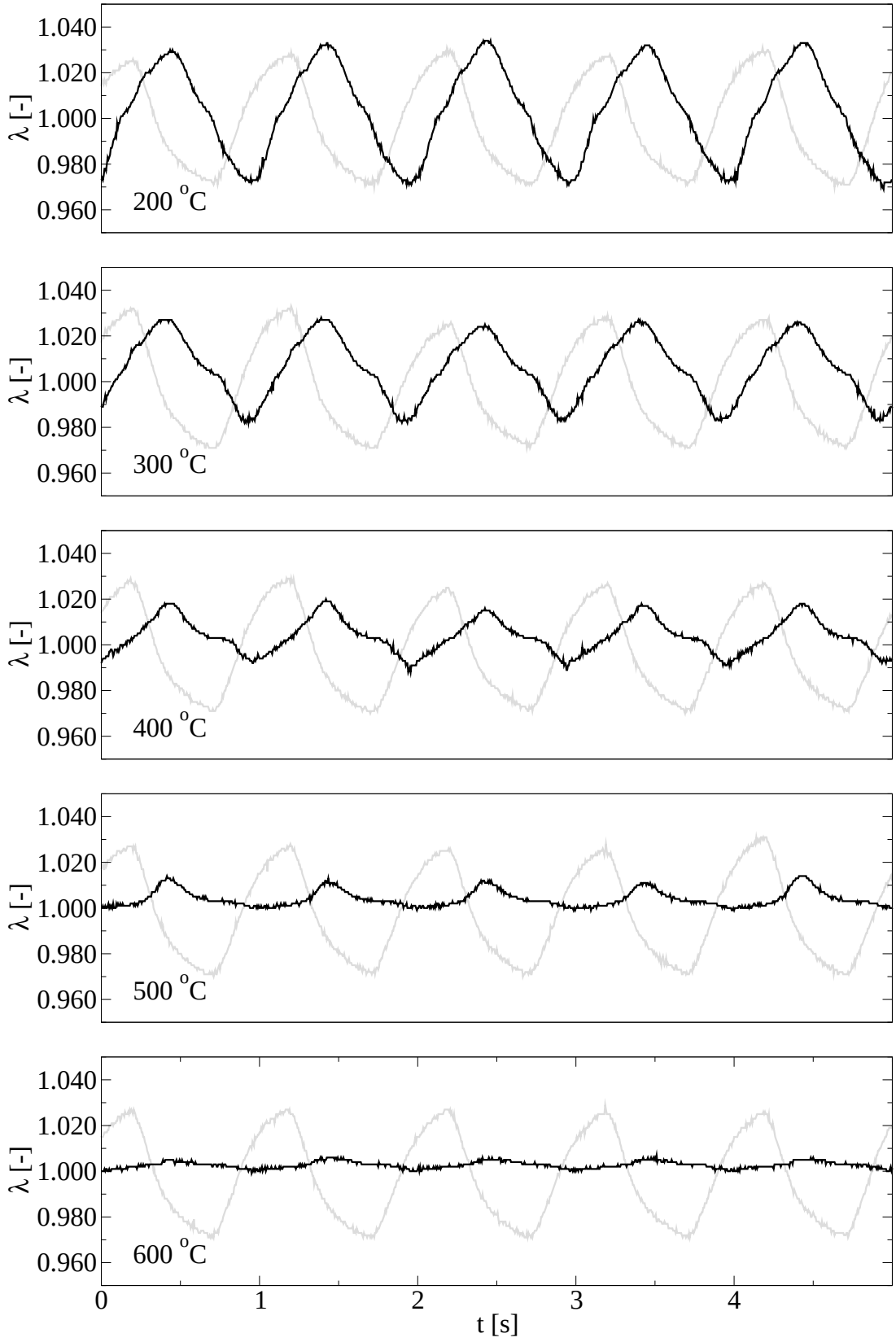

Figure 6.6: Damping of air to fuel ratio oscillations ($\lambda^{\mathrm{up}} = 1.00 \pm 0.03$, $f = 1$ Hz, $SV = 77000\ \mathrm{h}^{-1}$) with temperature (grey: λ^{up}, black: λ^{down}).

at a frequency of $f = 1$ Hz around its respective average value [174]. With an average exhaust composition close to stoichiometry air to fuel ratio perturbations downstream of a three-way catalyst can be significantly damped due to oxygen storage and release.

Some on board catalyst activity diagnostics rely on a so-called oxygen index as defined by equation 6.4:

$$i = \frac{\Delta\lambda_{\text{post}}}{\Delta\lambda_{\text{pre}}} \tag{6.4}$$

Thus an index of 0 would refer to a high oxygen buffering activity and an index of 1 to a poor activity [158, 65]. At 200 °C the oscillation passes the catalyst without damping ($i \approx 1$). The offset of some hundreds of milliseconds is due to the gas travel time between the upstream and downstream lambda sensor. However at 300 °C some damping already occurs. Oxidation kinetics are limiting since the OSCC value of $\Omega(T = 300\,^{\circ}\text{C}) = 0.19\,\text{g}O_2/\text{l}$ is approximately three times the amount necessary for full damping. At 500 °C the amplitude is diminished by a factor $i \approx 0.5$. With even further increased temperature the oscillation is completely damped within the monolith. At 700 °C ($i \approx 0$) just 2 % of the OSCC participates in the dynamic oxidation and reduction process under the chosen dynamic conditions.

Chapter 7

Model Validation

Validation of the three-way catalytic converter model is performed by comparing measured vehicle dynamometer emissions with simulated emissions during the cold transient phase of an FTP75 certification driving cycle. The vehicle chosen for this purpose is a Volkswagen Jetta equipped with the low-end torque Volkswagen 2.0L-2V-85 kW engine (165 Nm at 2600 rpm). A thorough revamp of the engine, its control, the gasoline supply and the exhaust system made this vehicle the first Partial Zero Emission Vehicle (PZEV) of Volkswagen [178]. To ensure ultra-fast catalyst light-off the engine is started in rich mode (λ = 0.6 – 0.75) with secondary air being added into the manifold targeting for exhaust compositions of λ = 1.05 – 1.25.

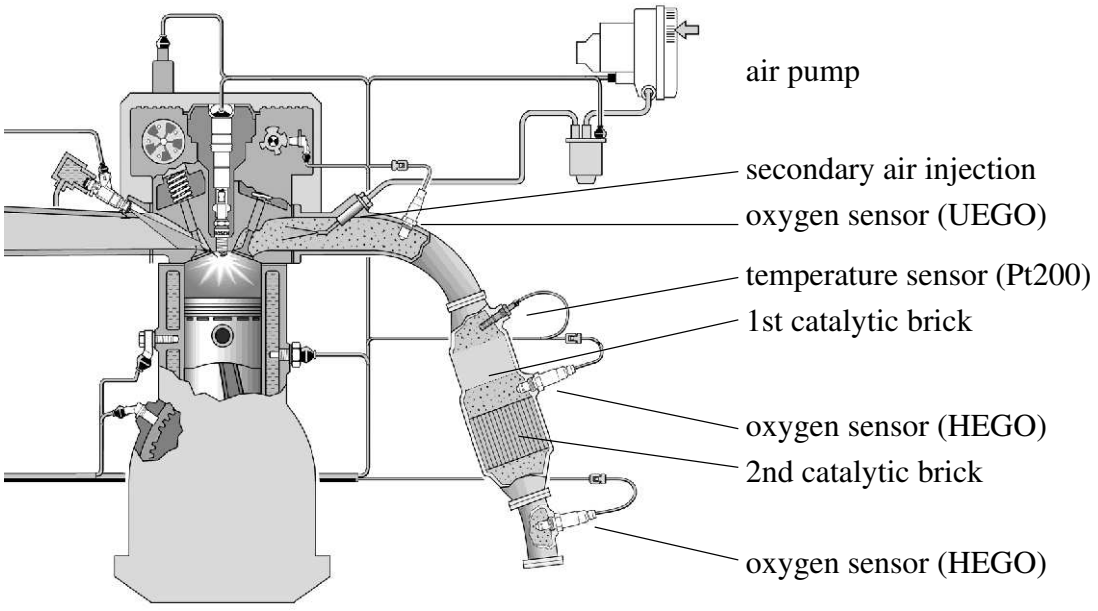

Figure 7.1: Schematic sketch of Bosch Motronic ME7.1.1 system architecture (source: Robert Bosch GmbH, GS/ESK) - incomplete.

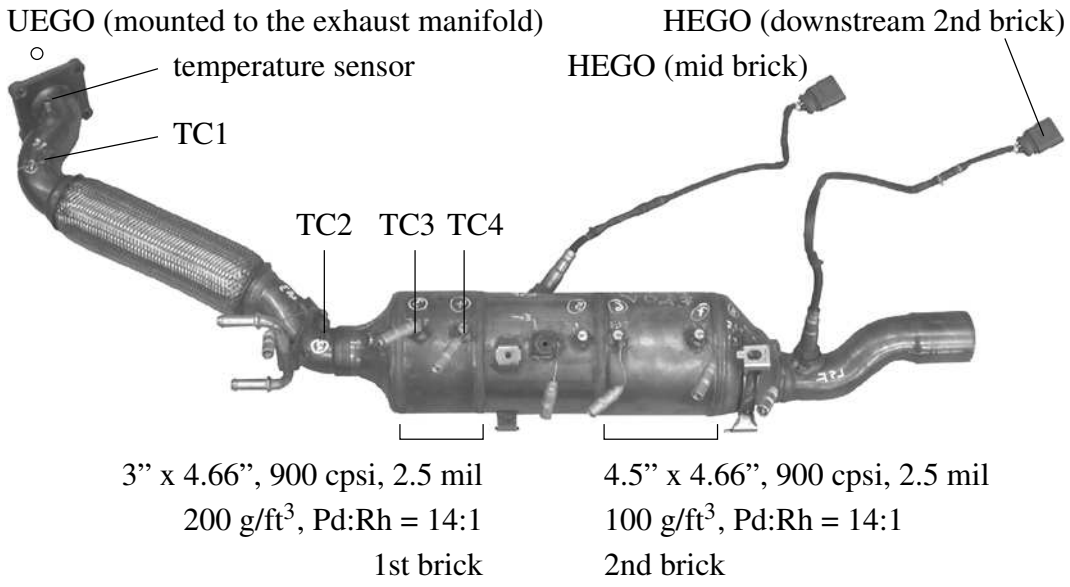

Figure 7.2: Volkswagen's Jetta 2.0l-2V-85 kW SULEV compliant exhaust system equipped with thermocouples (TC1 - TC4).

The air-gap insulated manifold acts during this phase as a so-called thermoreactor, completing the combustion process in a hot flame [178]. The temperature sensor located downstream in the takedown pipe checks for proper operation of thermoreactor and secondary air pump (figure 7.1). Since the SULEV emission thresholds (figure 1.1) have to be fulfilled for mileages of 150 thousand miles without further facilitation, the catalytic converter system is located in the underfloor position to avoid severe aging conditions under full load operation. The system contains two bricks of the same diameter. The first brick is shorter and has twice the precious metal loading of the second brick (figure 7.2). There is one oxygen sensor with step characteristic mounted between the two bricks and another one behind the second brick.

Modal measurements of the raw gas entering the catalytic converter system and of the gas behind the first brick are performed at 1 Hz by means of Fourier-Transformation-Infrared-Spectrometry (FTIR) with Volkswagen's System for Emission Sampling And Measurement (SESAM) [8].

Accumulated mass of carbon monoxide, hydrocarbons and nitrogen oxides behind the first brick during the cold transient phase ($t = 0 \ldots 507$ s) of the FTP75 test procedure are shown in figure 7.3. During cold start – which only needs a couple of seconds for this application – a major fraction of total carbon monoxide and hydrocarbons is emitted. After light-off, the temperatures are high enough for complete combustion under lean conditions. Hydrocarbons are even converted under rich conditions: only a slight and almost constant increase in hydrocarbon mass is registered after the first brick – emphasizing the importance of converter light-off on hydrocarbon emissions. The emissions of carbon monoxide and nitrogen monoxide after the first brick are substantial. Especially nitrogen oxide emissions are significant between $t = 180 \ldots 300$ s and thus due to warmed-up catalyst performance. In general, NO_x control strategies focus on closed-loop, stabilized engine operation [174].

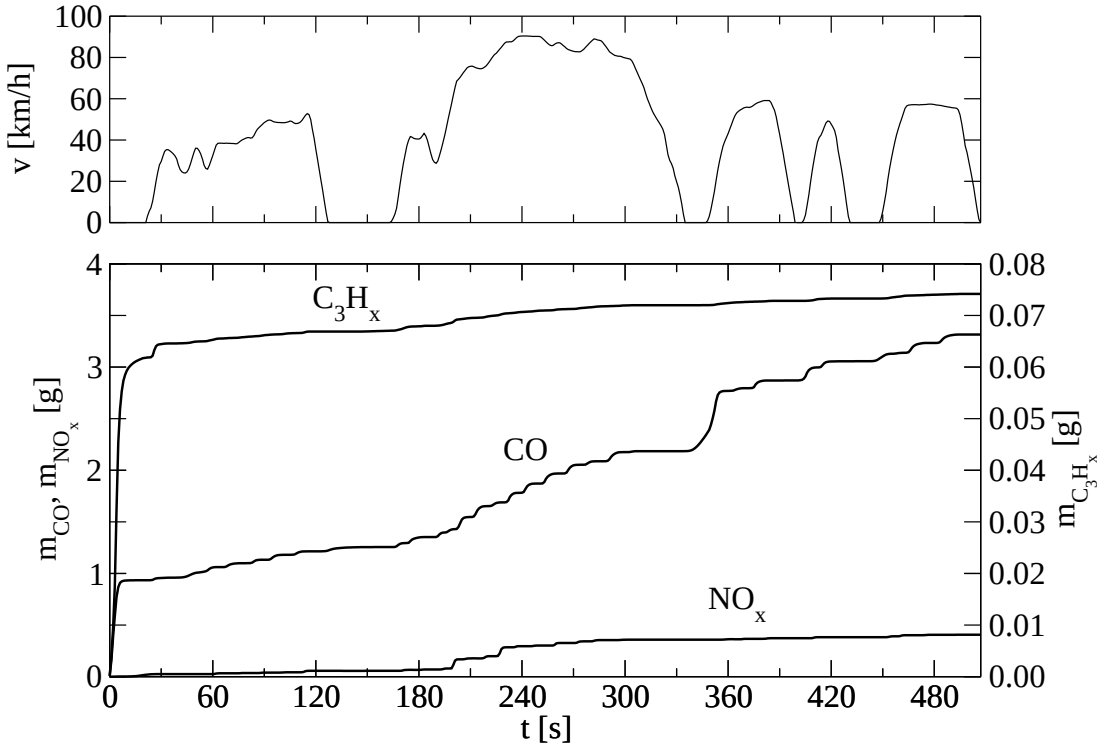

Figure 7.3: Measured accumulated carbon monoxide, nitrogen oxide and hydrocarbon mass behind first brick during the cold transient phase of the FTP75 driving cycle.

The stoichiometry of the catalyst inlet emissions are crucial for three-way catalytic emission control and thus for a sound description of the catalyst behavior modeled in this work (see chapter 4). It is evident from figures 2.2 and 2.3 that the dynamic response of the oxygen concentration signal is significantly slower than the dynamic response of the polar species measured by FTIR technique. The dynamics of all analyzed emission components are damped compared to the relative air to fuel ratio signal provided by the linear oxygen sensor. Thus the oxygen concentration in the feed is calculated from equation 2.17 based on the linear oxygen sensor (UEGO) signal which exhibits a much better dynamic response to changes in gas phase composition (figure 7.4)[1]. The hydrogen concentration is assumed to be one third of the carbon monoxide concentration (see chapter 3).

With the calculated oxygen concentrations the resulting set of engine out emissions still underestimates the dynamics in engine out hydrogen, carbon monoxide, hydrocarbon and nitrogen oxide emissions but obeys the fast dynamics of the measured relative air to fuel ratio.

[1]The relative air to fuel ratio signal is obtained from an extra Bosch LSU sensor not connected to the engine control unit. This sensor is powered up well in advance to cranking the engine – thus providing sound readings from the very first second. The obvious offset of the measured oxygen concentration (not used in this work) is probably caused by a leakage in the vehicle roll exhaust sample piping.

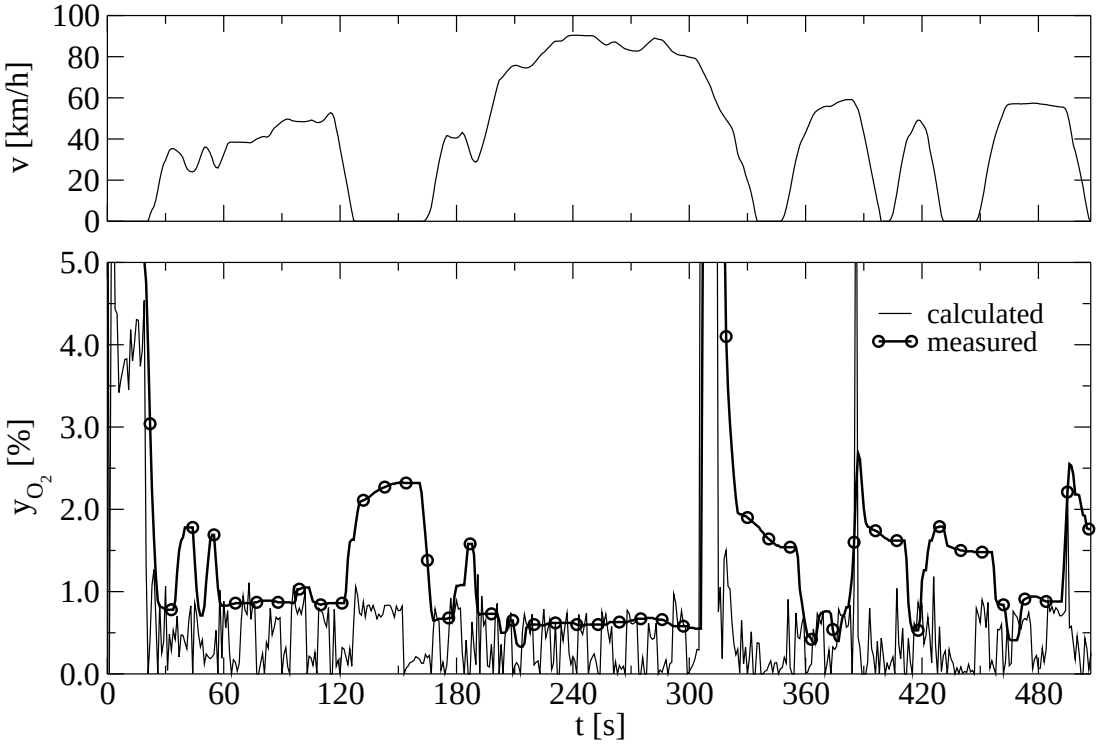

Figure 7.4: Converter inlet oxygen concentrations calculated from equation 2.17 based on the linear oxygen sensor (UEGO) signal compared with the respective oxygen concentration measured by means of a paramagnetic oxygen analyzer.

7.1 Thermal Behavior

Feed temperature estimates Even though temperature readings of thermocouples placed within the tube in front of the first brick are available (thermocouple TC2 in figure 7.2), simulations based on these values result in way too low catalyst bed temperatures: due to radiative heat losses temperature sensors positioned within a hot gas phase surrounded by colder walls do have lower body temperatures (and thus provide lower readings) compared to the gas phase they are positioned in [112, 121]. Thus a feed gas temperature estimate believed to be more realistic is obtained by "interpolation" of the erroneous reading in front of the catalyst (TC2) and a hotter – also erroneous – reading even further upstream (TC1 in figure 7.2). The empirical formula $T_{\mathrm{g,in}} \approx 0.3\,T_{\mathrm{TC1}} + 0.7\,T_{\mathrm{TC2}}$ yields reasonable feed temperature values for the first brick. This can be seen in the following, where start-up measurements of the FTP75 cycle of figure 2.2 are compared to simulations (figure 7.5).

Heat of reaction for oxygen storage and release In order to check the influence of the heat of reaction of oxygen storage and release, several simulation results are compared with temperatures measured at two positions within the first brick. A quite good description of the temperature progression with time at different positions within the catalyst is obtained with the model described in chapter 4 and the parameters obtained

in chapter 5 and 6[2]. The heat of oxygen storage is varied between a value of -760 (equivalent to the heat of reaction 3.14), a value of -200 kJ/(mol O_2) and zero.

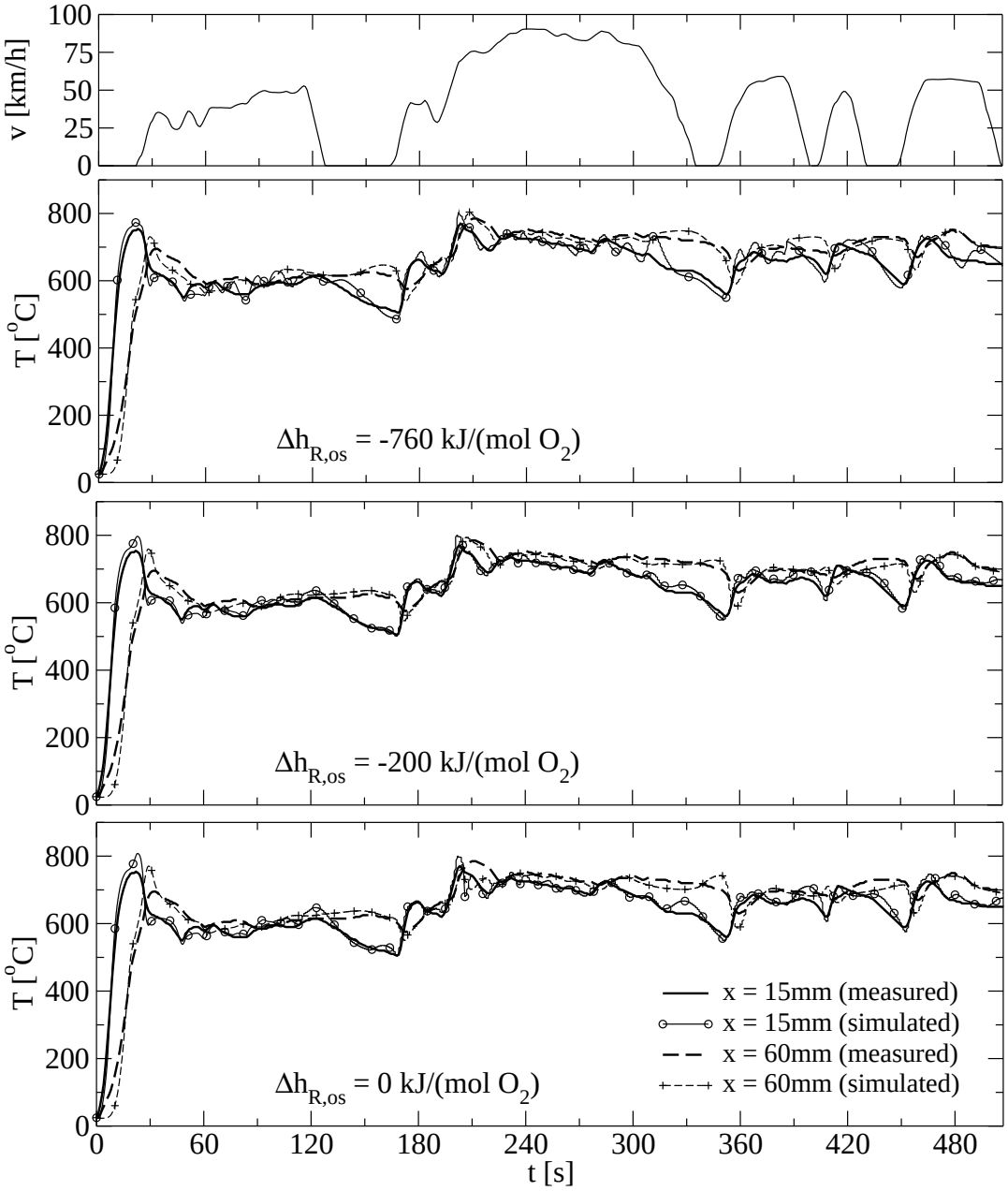

Figure 7.5: Measured and simulated temperatures within the first brick, assuming different values of the enthalpy $\Delta h_{R,os}$ of oxygen storage reaction.

The value of -200 (close to the value of -220 kJ/(mol O_2) associated with palladium oxidation) has been reported for calorimetric properties of ceria and ceria-zirconia based palladium three-way catalysts [180]. The literature value of -200 kJ/(mol O_2) provides the best description of the thermal behavior under warmed-up conditions.

[2]Since the precious metal loading in the first brick is twice the loading of the catalyst the kinetic parameters are obtained for, all kinetic rate constants are assumed to be twice as high.

With both a higher and a lower heat of oxygen storage and release significant deviations between measured and simulated temperatures arise – especially during deceleration associated with fuel cut and subsequent rich purges (figure 7.5, 120 s $< t <$ 360 s).

7.2 Cold Start Conversion

Due to the thermoreactor cold start strategy the first brick experiences temperatures in excess of 700 °C within a couple of seconds after cranking the engine (figure 7.5). The critical cold start phase is passed within less than 20 s just before the first road load is put on the engine. Figure 7.6 allows a comparison of measured and simulated combustible species concentrations during this phase.

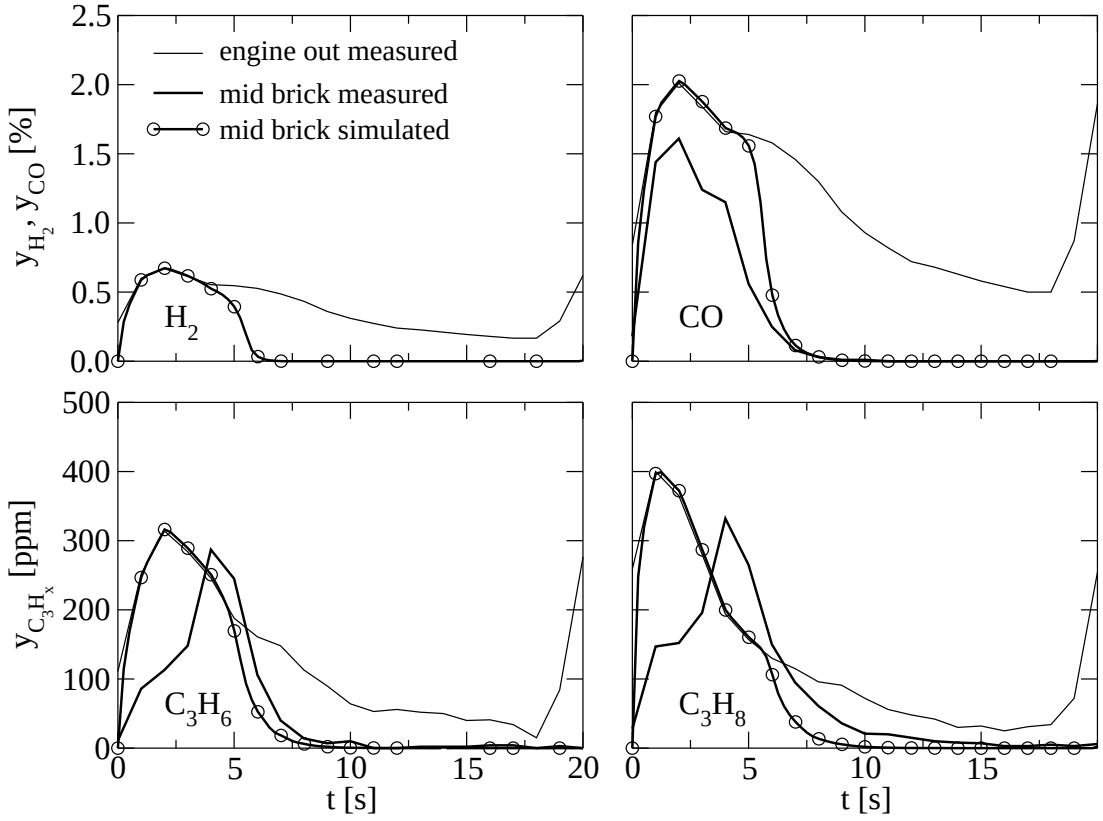

Figure 7.6: Measured and simulated hydrogen, carbon monoxide and hydrocarbon emissions after the first brick (”mid brick”) during cold start.

Hydrocarbons are mainly emitted during the very first seconds of the driving cycle and to a lesser degree during the corresponding seconds of the hot transient phase. More than 10 different hydrocarbon species are measured by SESAM. They are grouped into a fraction with relatively low catalytic ignition temperature represented by propene and another fraction with relatively high catalytic ignition temperature represented by propane.

During light-off propene shows a similar behavior as carbon monoxide with full conversion after approximately 8 s. Propane light-off is somewhat delayed with full conversion after 10 s. The evident time shift between simulated and measured peak hydrocarbon emissions is due to the catalyst's ability to store hydrocarbons in an intermediate temperature range – a phenomenon not covered by the mathematical model. As can be seen, hydrocarbon storage has no substantial influence on total hydrocarbon emissions as long as hydrocarbon desorption occurs well in advance of catalyst light-off.

7.3 Transient Phase Conversion

During light-off the rates of catalytic combustion are limited by the low temperature. In the hot catalyst under rich feed conditions after removal of residual oxygen, combustion rates are limited by the rate of oxygen release from the oxygen storage. Under lean feed conditions the conversion of nitrogen oxide to nitrogen is limited by the rate of oxygen uptake.

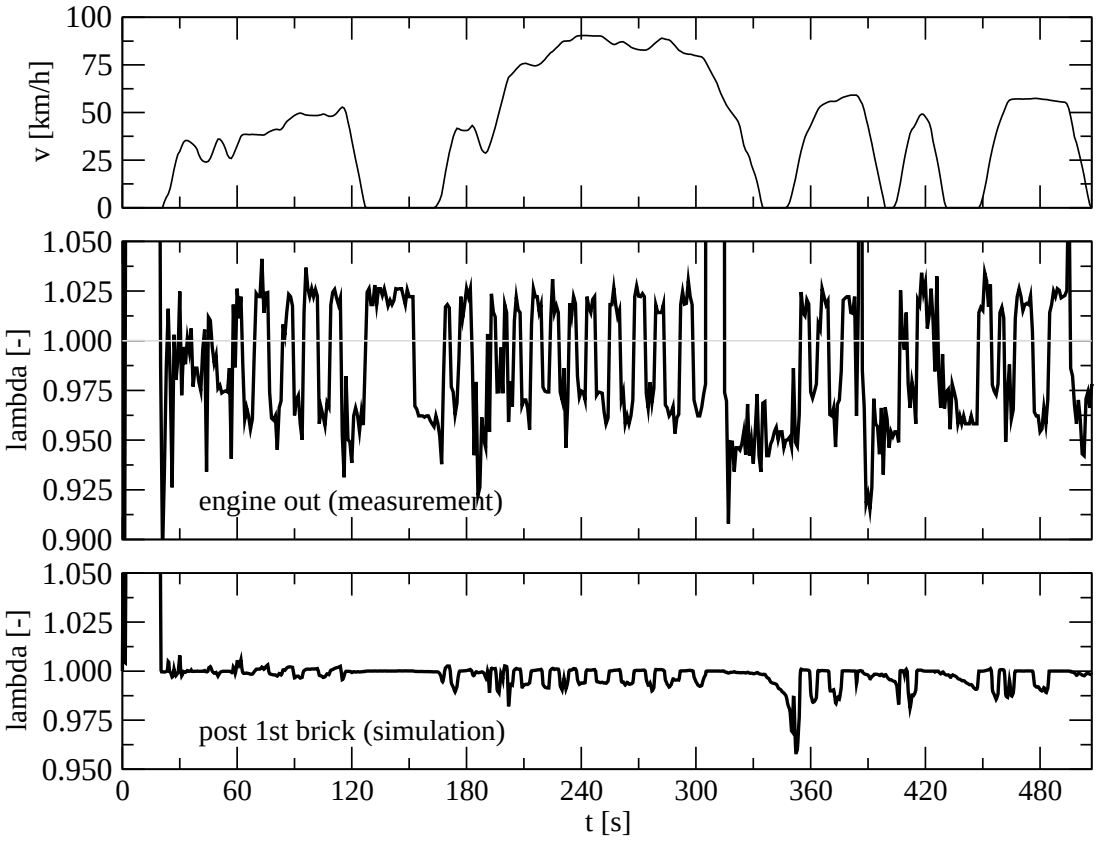

Figure 7.7: Relative Air to Fuel ratio across the first brick.

If oxygen uptake and release were high enough all deviations from stoichiometric composition would be buffered, resulting in a steady $\lambda = 1$ signal behind the catalyst. The simulated exhaust composition after the first brick shows this behavior during idling

with low load after the first cruising period (around $t \approx 150$ s). Higher load operation is accompanied with lean and rich breakthroughs (figure 7.7).

Significant nitrogen oxide breakthrough occurs during the following high speed operation between second 200 and 300 (figure 7.3). It is evident from the time resolved traces in figure 7.8 that these emissions are due to isolated peaks. While overall conversion is well in excess of 80%, oxygen storage during lean engine operation seems to be not sufficiently high to buffer all the oxygen – hindering complete nitrogen oxide reduction.

During acceleration with high engine load the first brick emits significant amounts of carbon monoxide under rich conditions. The accumulated mass of carbon monoxide shows a pronounced increase around $t \approx 350$ s (figure 7.3). These few seconds add approximately 20% to the mass accumulated during the cold transient phase. An explanation will be given by considering the (simulated) change of stored oxygen.

It can be seen from the measured pre-first brick gas composition and the calculated post-first brick gas composition (figure 7.7) that the average engine exhaust is slightly rich. The exhaust composition is controlled such that the oxygen sensor's voltage behind the second brick is always 600-650 mV to ensure further high conversion of nitrogen monoxide in the second brick [178].

With the catalyst storage being initially completely oxidized due to lean cold start with secondary air injection, the slightly rich operation afterwards results in an average decrease of the stored oxygen (figure 7.10). During the second hill ($t \approx 150 \ldots 300$ s) an average oxidation extend of roughly 35% is maintained providing high oxygen uptake rates at still good oxygen release rates. During deceleration with fuel cut ($t \approx 320$ s) the storage material is rapidly oxidized. During the following rich purge ($t \approx 320 \ldots 350$ s) oxygen is released from the storage until the storage is virtually empty. At $t = 350$ s the engine accelerates the vehicle with rich combustion and relatively high load. The carbon monoxide conversion now suffers from a completely reduced storage material, unable to compensate oxygen shortage in the feed. This explains the strong carbon monoxide increase at about 350 s (figures 7.3 and 7.9).

After coldstart the measured hydrocarbon conversion is almost complete (figures 7.3 and 7.11). Using the kinetic data for steam reforming and water gas shift reaction determined separately in section 5.4.2 and given in table 5.1, the simulated propane conversion would have been too low. In other words: measured hydrocarbon conversion under transient rich conditions with the Volkswagen Jetta 2.0l SULEV development application is much better than the one predicted by simulation based on kinetic data retrieved from steady state experiments. It is evident from data discussed in chapter 8 and appendix C that these differences most likely arise from sulfur poisoning: Kinetic measurements discussed in chapter 5 are performed with an exhaust sulfur content of $y_{SO_2} = 14$ ppm, while the certification driving cycle measurements discussed here are performed with a much lower sulfur level. Furthermore in the presence of sulfur the catalyst transforms into a less active state during prolonged steady state rich operation. During real engine operation the catalyst is subjected to rich conditions no longer than 40 sec (see figure 7.7). Sulfur blocking the catalyst's active sites as e.g. hydrogen

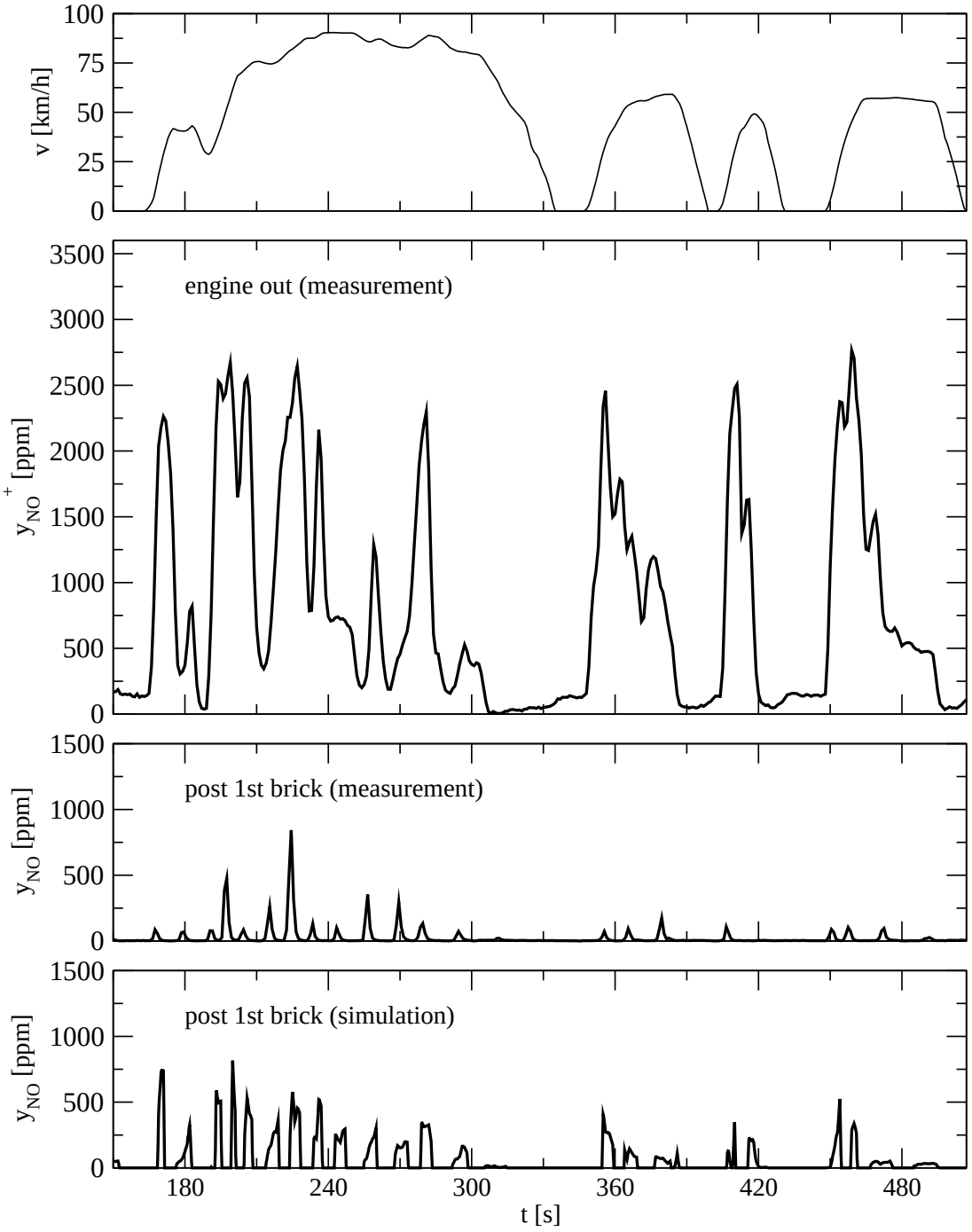

Figure 7.8: Comparison of measured nitrogen monoxide emissions in front and behind the first brick with simulated emissions behind the first brick.

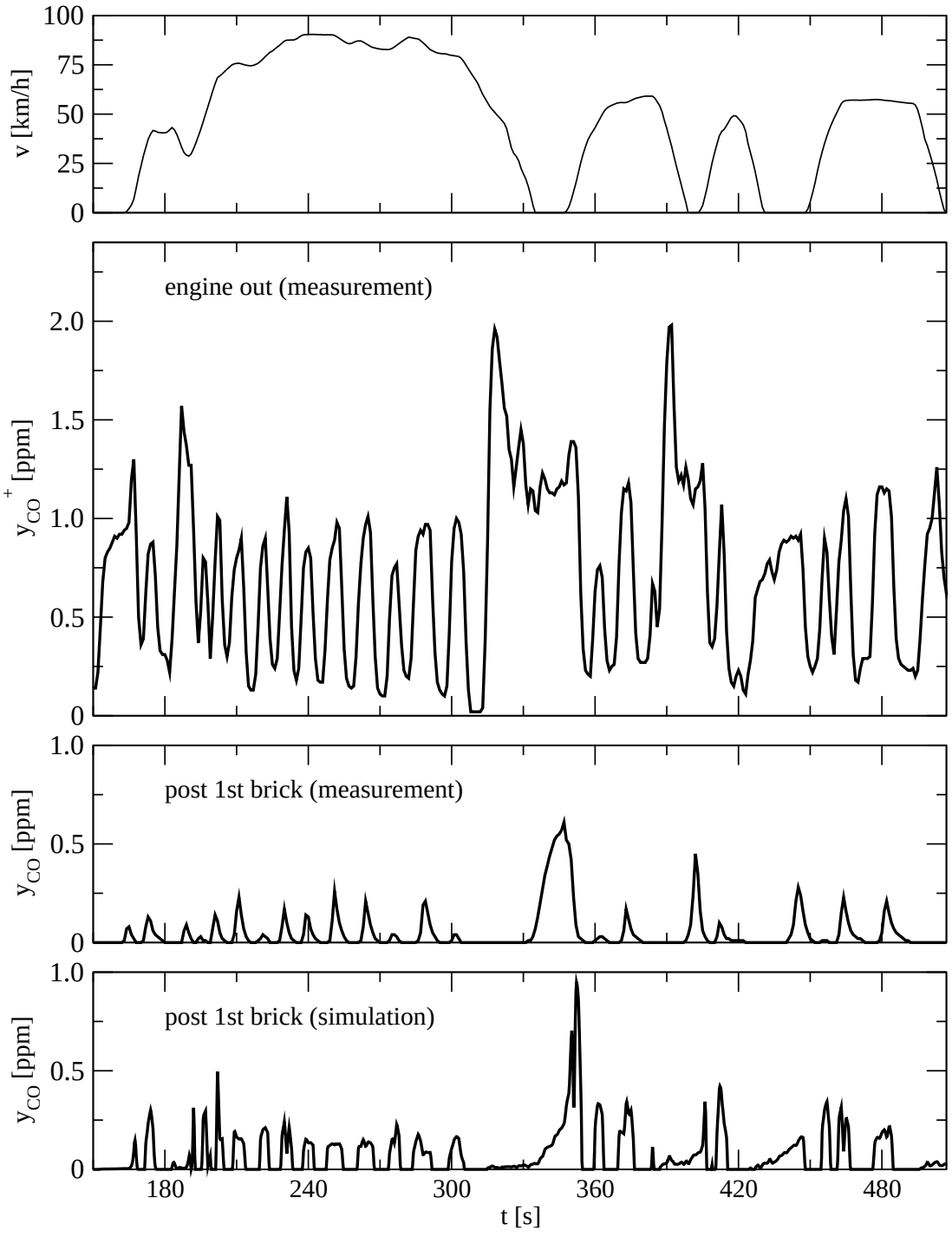

Figure 7.9: Comparison of measured carbon monoxide emissions in front and behind the first brick with simulated emissions behind the first brick.

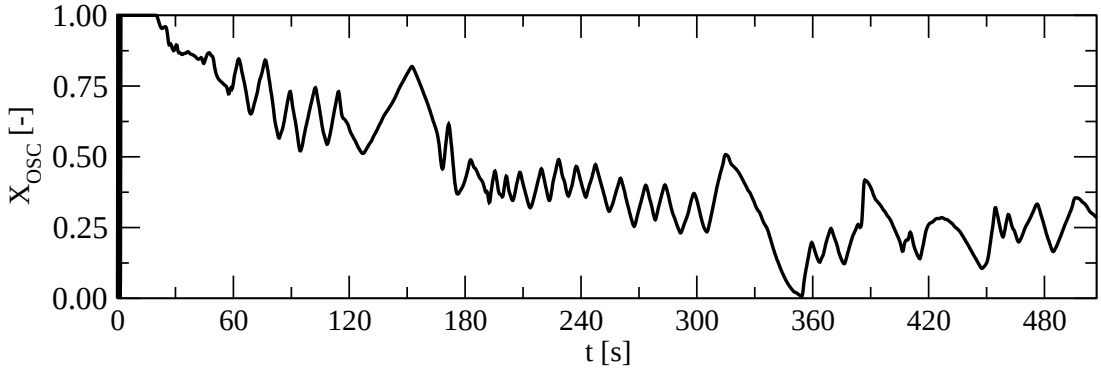

Figure 7.10: Simulated averaged oxidation extent of the storage material.

sulfide are swept away in the subsequent lean phase. Therefore propane conversion was calculated with the same rate parameters as propene in figure 7.11. Nevertheless some break-through of hydrocarbons is simulated during the rich acceleration at about 350 s.

7.4 Discussion

With model parameters and properties obtained from the suppliers (e.g. substrate cell density and wall thickness, washcoat loading, precious metal loading), from literature (e.g. heat capacities, transfer coefficients, oxygen diffusivity within oxygen storage) and kinetic and capacity data from isothermal measurements performed on a sample with half the precious metal loading and a 25 % lower specific geometric surface area the behavior of a full size catalytic converter operated under highly transient thermal and stoichiometric conditions can be described reasonably well. This is in particular remarkable since one single set of species conversion kinetic parameters obtained from both fuel lean (oxygen saturated catalyst) and fuel rich (oxygen depleted catalyst) conditions (table 5.1) is applied. During Volkswagen Jetta 2.0l SULEV FTP drive cycle simulation however the catalyst does change between periods of oxygen release and oxygen uptake. Hence the oxygen storage is usually not completely filled or completely empty but somewhere inbetween ($0 \leq x \leq 1$, see figure 7.10).

While the independently parameterized model provides a good description of the cold start behavior and the thermal behavior throughout the cold transient FTP cycle quantitative differences between measurement and simulation are evident from a comparison of transient carbon monoxide and nitrogen oxide emissions on a peak to peak basis (figure 7.9 and 7.8). With the significantly higher sulfur content applied throughout all kinetic measurements, the scale up by more than two orders of magnitude, poor time resolved emission analysis, lack of hydrogen concentration analysis and a questionable flow distribution within the first brick (see inlet cone geometry figure 7.2) the degree of carbon monoxide and nitrogen oxide conversion prediction is believed to be remarkably good. Drive cycle simulations with similar models reported in literature provide roughly the same accuracy [126, 146, 4].

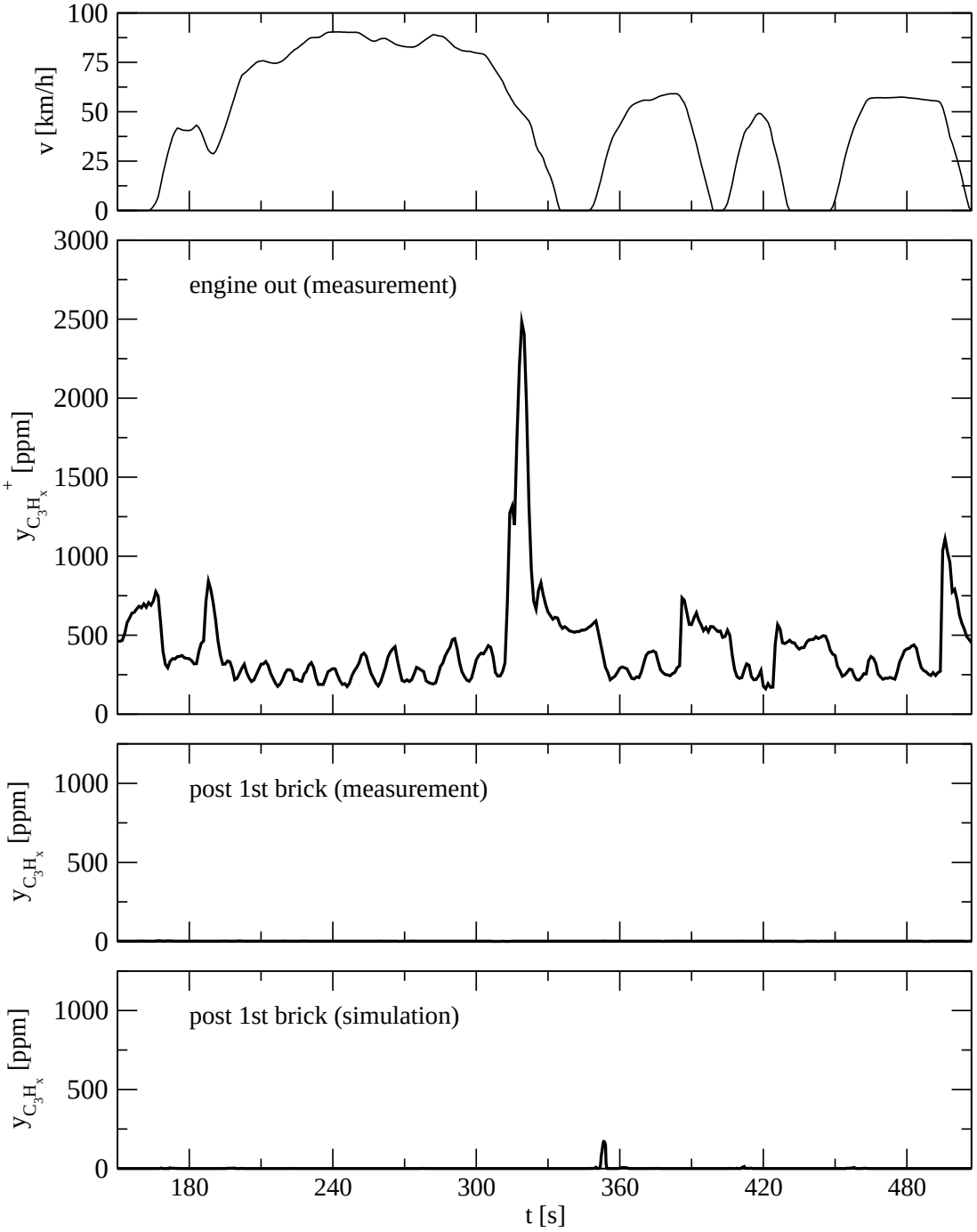

Figure 7.11: Comparison of measured hydrocarbon emissions in front and behind the first brick with simulated emissions behind the first brick. After coldstart engine out hydrocarbons are assumed to be propene only.

The simulations underestimate the warmed-up propane conversion under rich conditions compared to the measured – almost complete – alkane conversion. Similar shortcomings in predicting transient improved hydrocarbon conversion under rich conditions are reported in literature [166]. Steady state experiments with a rich bias to mean air to fuel ratio (e.g. $\lambda = 0.98 \pm 0.01$, $f = 1$ Hz) carried out in this work (section 5.4.2) maintain the catalyst in an oxygen depleted state over its full length. With the Volkswagen Jetta 2.0l SULEV application described before the oxygen storage is controlled at an intermediate oxidation state during transient operation by applying low frequency oxidation and reduction cycles with reasonable amplitude. It has been reported that the overall conversion of a three-way catalytic converter system can be enhanced by prolonged rich/lean phases as long as full system break through is avoided (e.g. [90, 111]). Further experiments towards the understanding of this transient improved rich conversion phenomenon are discussed in chapter 8 and appendix C.

Chapter 8

Deactivation

As discussed in the previous section 7.4 species conversion (especially hydrocarbon conversion) might be temporarily improved upon transition from fuel lean to fuel rich conditions compared to the respective steady state conversion – even subsequently to oxygen storage depletion. This phenomenon – not covered by superposing species conversion kinetics obtained from steady state experiments (chapter 5) and oxygen storage kinetics retrieved from transient experiments (chapter 6) – is discussed in some detail below and in more detail in appendix C.

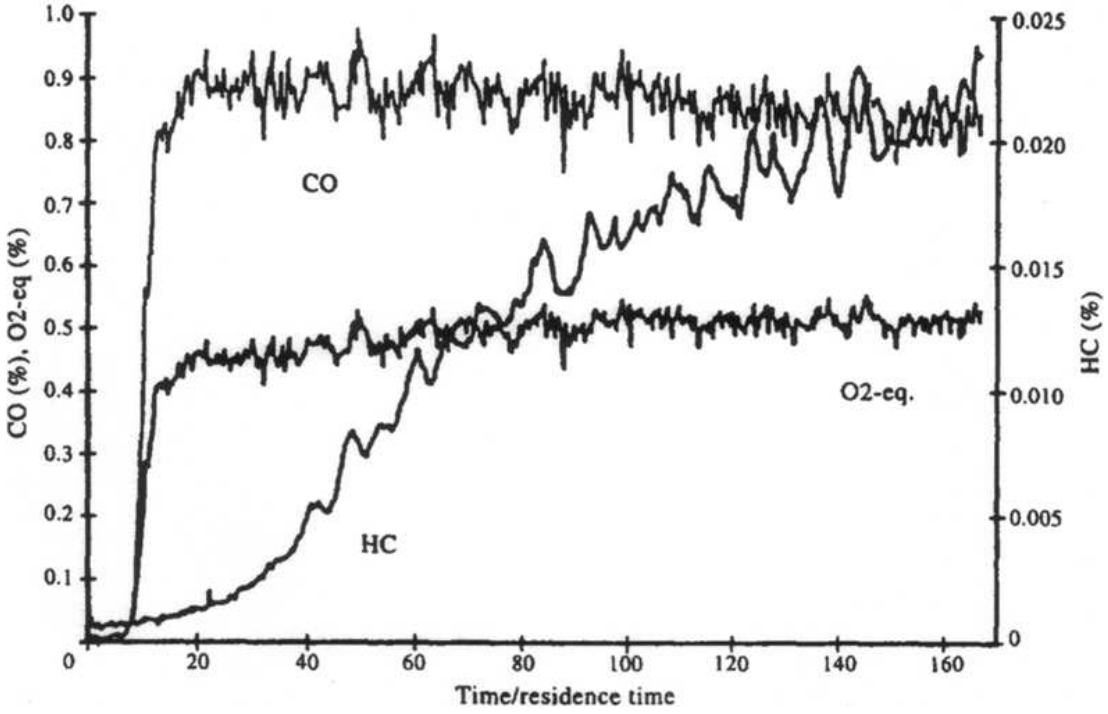

Figure 8.1: Transient hydrocarbon, carbon monoxide and thereof calculated oxygen equivalents of a catalyst subjected to a step increase of carbon monoxide concentration by 1 %. Catalyst operated lean at λ = 1.01 prior to the rich step ($SV = 30\,000\,\mathrm{h}^{-1}$, $T = 773\,\mathrm{K}$) [149].

Engine bench measurements were reported to exhibit a significant loss in both carbon monoxide and hydrocarbon rich conversion due to slow deactivation [45, 3]. The slow decrease in rich hydrocarbon conversion depicted in figure 8.1 – originally interpreted as oxygen storage – is probably an early proof of the rich atmosphere hydrocarbon conversion deactivation phenomenon.

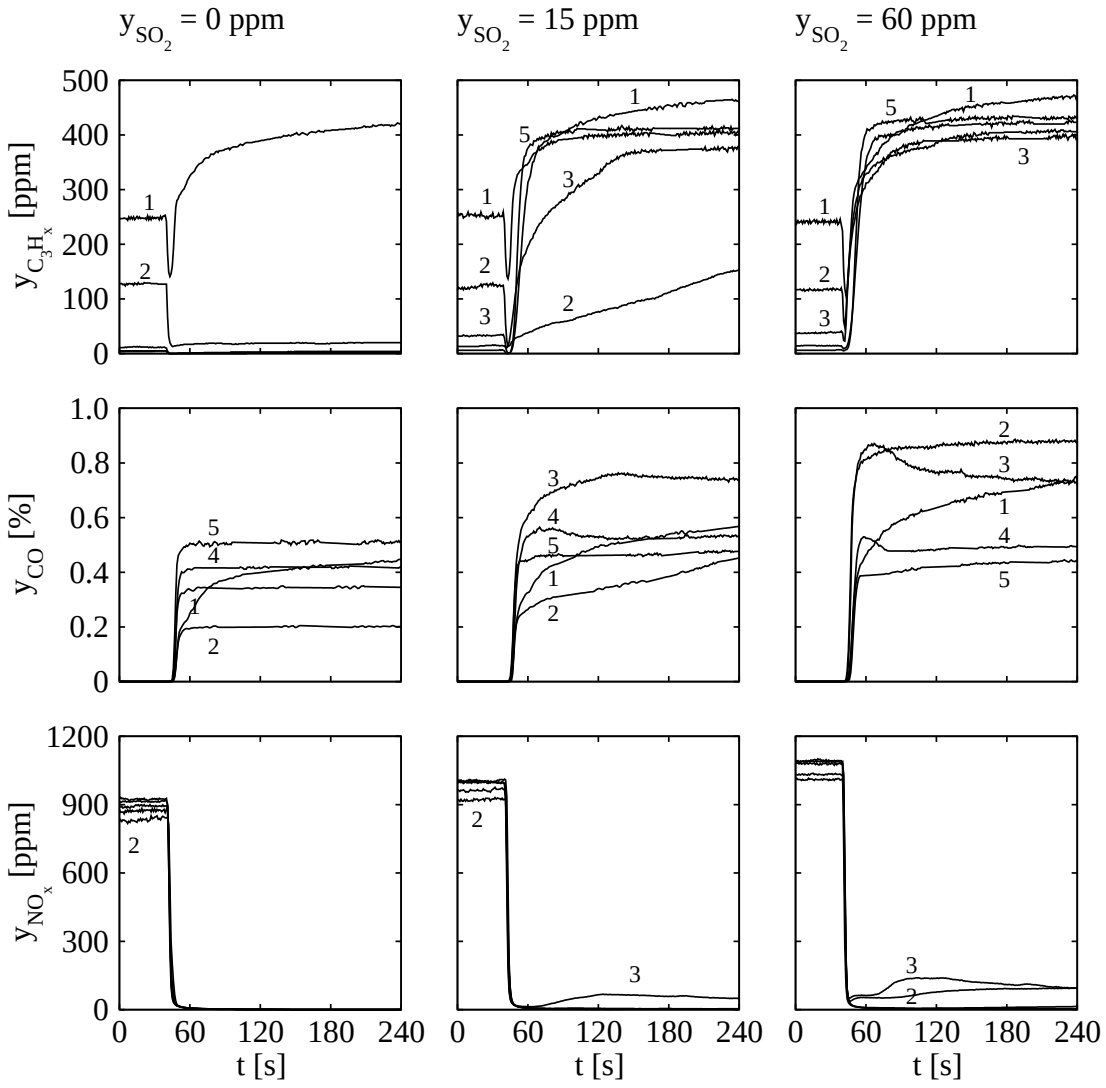

Figure 8.2: Exhaust species responses to a step change from lean ($y^{\mathrm{f}}_{\mathrm{H_2}} = 300$ ppm, $y^{\mathrm{f}}_{\mathrm{CO}} = 900$ ppm, $y^{\mathrm{f}}_{\mathrm{O_2}} = 7100$ ppm) to rich ($y^{\mathrm{f}}_{\mathrm{H_2}} = 3740$ ppm, $y^{\mathrm{f}}_{\mathrm{CO}} = 11200$ ppm, $y^{\mathrm{f}}_{\mathrm{O_2}} = 2690$ ppm) feed composition at $T \approx 330$, 420, 510, 560 and 610 °C (traces 1 through 5); $SV = 74\,600$ h^{-1}, $y^{\mathrm{f}}_{\mathrm{C_3H_6}} = y^{\mathrm{f}}_{\mathrm{C_3H_8}} = 250$ ppm, $y^{\mathrm{f}}_{\mathrm{NO}} = 1000$ ppm, $y^{\mathrm{f}}_{\mathrm{CO_2}} = 14$ %, $y^{\mathrm{f}}_{\mathrm{H_2O}} = 10$ %, $y^{\mathrm{f}}_{\mathrm{SO_2}}$ as indicated.

In this work likely causes of rich-side deactivation are addressed by step response measurements with different exhaust sulfur concentrations: It is evident from figure 8.2 that post catalyst responses of the three legislated exhaust species hydrocarbon, carbon monoxide and nitrogen oxide to lean-rich transitions at temperatures between $T = 330$ and 610 °C are severely affected by the exhaust's sulfur concentration.

Sulfur Poisoning With $y^{f}_{SO_2} = 15$ ppm hydrocarbon conversion at 420 °C deactivates slowly - not reaching steady state within four minutes. At 510 °C – a temperature high enough for virtually complete hydrocarbon conversion with sulfur free exhaust – the catalyst deactivates within approximately two minutes reaching a steady state hydrocarbon conversion of no more than 30 %. With even higher temperatures the deactivated steady state is reached within a shorter period of time. The temperature activated deactivation mechanism is considered to be due to precious metal sites poisoning sulfur species originating both from the instantaneous feed sulfur content and sulfur previously stored under lean conditions in the catalyst's washcoat getting thermodynamically instable and thus desorbing under rich conditions (thermodynamic considerations see section 3.2.3) [163].

With even further increased sulfur content ($y^{f}_{SO_2} = 60$ ppm in figure 8.2) deactivation is consequently much faster resulting in a very poor hydrocarbon conversion under rich conditions at all investigated temperatures. Sulfur worsens also nitrogen oxide conversion under rich conditions at intermediate temperatures (figure 8.2). At temperatures as high as 560 and 610 °C however the strongest deactivating impact of sulfur is on hydrocarbon emissions dropping down from virtually complete conversion to no more than 20 %.

Carbonaceous Deposits However at 330 °C a slight deactivation of hydrocarbon and carbon monoxide conversion over several minutes even with sulfur free feed is observed. Even though this deactivation is slightly enhanced with increasing sulfur content the deactivation at 330 °C is believed to be dominated by the formation of carbonaceous deposits. Carbonaceous deposits on ceria containing catalysts are recognized as a cause for water-gas shift and steam reforming reaction deactivation: Under rich conditions ceria exists in a reduced state and is covered by carbonate species that are removed only by re-oxidation of ceria as carbon dioxide [57, 107, 72, 115, 70, 73, 56, 57, 71, 58, 104, 69, 3]. A clear correlation between the percentage of deactivation and the amount of carbon deposited is reported [48]. Thermodynamics predict, that the formation of carbonaceous deposits under rich automotive exhaust conditions is not favored at higher temperatures (e.g. solid carbon formation not above approximately 330 °C, see section 3.2.1). Indeed no slow deactivation is observed at higher temperatures with sulfur free exhaust: Hydrocarbon conversion exceeds 90 % at 420 °C and is practically complete above 510 °C (figure 8.2). Also carbon monoxide readings are stable within a few tens of seconds above 330 °C.

Air to Fuel Ratio Control Strategies Most state of the art engine control strategies maintain a major section of the three-way catalytic converter at slightly rich conditions – and such in an oxygen depleted state. In the presence of sulfur these sections transform into a less active state. Exhaust aftertreatment efficiency based on precious metal usage drops down to uneconomically low values. Fortunately poisoning sulfur species are easily removed by means of short lean pulses [25]. At present few engine

control strategies (e.g. the Volkswagen's SULEV 2.01 application discussed in chapter 7, which periodically maintains fuel lean conditions for some seconds in closed loop operation) already make extended use of this reactivation mechanism.

Chapter 9

Suggested Directions for Future Work

Bulk Sulfur Storage When operating under steady state lean conditions at intermediate temperatures for a prolonged period of time, sulfur storage results in significant deactivation – primarily of the catalyst inlet section (see section 3.2.3). An object of further research should be the influence of different sulfur loadings on species conversion rates and apparent oxygen storage. To experimentally observe sulfur storage and release, gas analysis of relevant sulfur species (such as sulfur dioxide and hydrogen sulfide) is considered to be a must.

Surface Sulfur Storage Even under slightly rich conditions (e.g. post catalyst oxygen sensor voltage ≈ 650 mV) – considered to be necessary to ensure high nitrogen oxide conversion – the catalyst's ability to convert both nitrogen oxide and hydrocarbons tends to deactivate due to sulfur poisoning of the catalytic sites. Sulfur poisoning depending on fuel sulfur content and air to fuel ratio should be modeled to increase the model's accuracy for warmed-up emission control. Again a suitable gas analysis of sulfur containing gas species is necessary to experimentally monitor this process.

Oxygen Storage Recently thermodynamic models became available describing the temperature and composition dependent equilibrium partial pressure above ceria-zirconia solid solutions [75, 74, 76, 77]. It would be straight forward to model both the oxygen storage capacity and the storage/release rates to be dependent on the actual and equilibrium oxygen partial pressures in the materials vicinity. It might be necessary to account for more than one oxygen storing bulk phase. Even if the material is perfectly homogeneous in its fresh state it will segregate upon aging into separate phases (pure and/or solutions) with no/less[1] oxygen storage capacity.

The contribution of precious metal oxidation/reduction to oxygen storage should be considered as well. A even more complete description of oxygen storage would be obtained by modeling the formation of hydroxyls under lean and – in the presence of sulfur – hydrogen sulfide species under rich conditions.

[1] under certain circumstances the formation of a solution with a higher capacity is possible as well.

Water Condensation The effect of water condensation/evaporation should be included for an improved description of the system's thermal behavior under cold start conditions [26].

Reaction Kinetics Reaction rate parameters might be deduced from transient experiments as well. Gas concentration analyzers with fast response would be helpful in order to identify the occurring fast transient phenomena [45]. Hydrogen analysis is considered to be a must. One set of experiments could include full purges (e.g. rich-lean step experiments as discussed in this work): Another set of experiments would look at partial purges by superimposed higher frequency air to fuel ratio perturbations (e.g. sine waves and square waves) to average slightly lean, stoichiometric and rich biased exhaust [111, 166]. Engine bench experiments (such as lambda-sweep-tests) might be conducted in a similar way to avoid steady state deactivation [23].

Control Oriented Modeling With increasing computational capacities it will be feasible to implement one-dimensional phenomenological models in upcoming engine control units. Thus the effort of building and maintaining such a model will not just result in a better understanding of three-way catalysts containing aftertreatment systems and an efficient engineering simulation tool but also in better engine control models. Less extensive "grey box models" may also be derived from phenomenological one-dimensional models [46]. Models of other major exhaust system devices such as oxygen sensors and their sensitivity towards different exhaust species should be included in engine control units as well to raise the full potential of emission control modeling. Indeed the application engineer should play a major role in this integrated model development process: he observes and describes phenomena important in emission control. His knowledge stems from experience rather than from research and should give a good indication for necessary model refinements.

Appendix A

Experimental Facilities

This chapter describes non-standard experimental facilities applied to examine the behavior of fresh and aged catalysts under both quasi steady state and transient operation.

Flat bed reactors reactors (section A.1) allow to study the conversion and oxygen storage mechanisms under almost isothermal conditions (chapters 5 and 6). Since most of the investigated processes are strongly temperature activated, isothermal conditions significantly reduce the system's complexity and thus facilitate gaining of reliable information. With the current design the maximum catalyst temperature in these reactors is limited to 750 °C – a temperature sufficient for representing emission certification driving cycles' operation conditions (chapter 7) and for catalyst regeneration (sulfur removal).

Even higher temperatures can be achieved in the fired tube reactor (section A.2) where maximum steady state brick temperatures under rather adiabatic conditions can be as high as 1200 °C, causing severe catalyst aging (appendix B). Under transient conditions the catalyst can be exposed to even higher peak temperatures.

A description of the roller dynamometer used for reference measurements (chapter 7) is not included in this work since it is a standard configuration.

A.1 Flat Bed Reactors

Stainless steel reactors incorporating thin slices of precious metal catalyst supported on ceramic monoliths have proven to be a convenient experimental tool for the investigation of catalytic reaction rates [89]. The reactors are constructed in a sandwich type manner (figure A.1): the massive bottom plate contains one or more catalyst slices in line – being just one channel height thick – preceded by a static mixer. The top plate's matching key slips into the bottom plate groove. All parts are sealed with mica paper which is inert even under high temperature lean conditions. The reactors are heated with evenly distributed electrical resistive heaters positioned in the top and bottom plates. The top and bottom plates are also equipped with cooling pockets, cooled

by compressed air, allowing a three-point temperature control and ensuring acceptable cooling rates. Thus the stainless steel reactor itself can be controlled with ± 1°C to quite isothermal conditions.

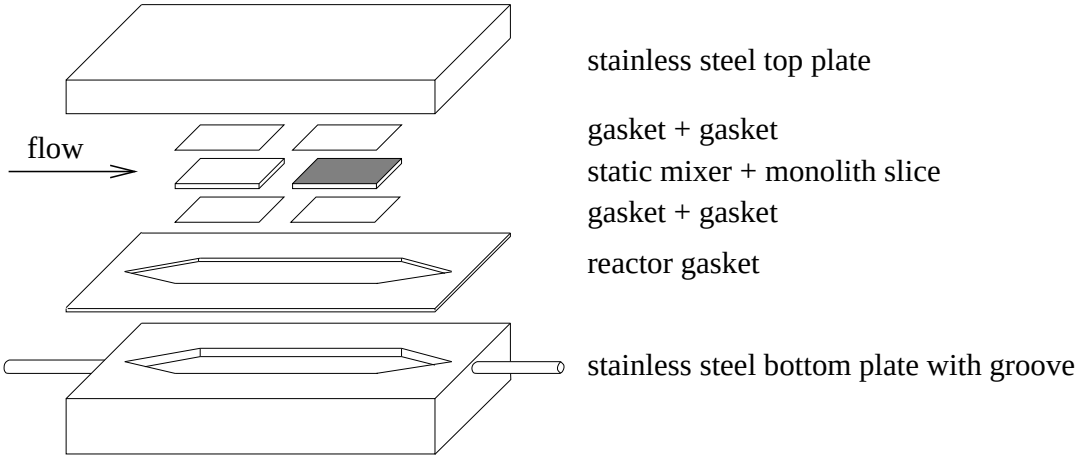

Figure A.1: Sketch of Single Slice Reactor; the catalyst slice is preceded by a static mixer, both parts are sealed against the reactor.

Due to the sample's high ratio of outer geometric surface area to volume (this ratio is roughly 50 times higher compared to a full size monolith) the heat released within the sample can be effectively removed via heat conduction into the reactor plates. Fed with lean mixtures (ΔT_{ad} = 105 ... 150 °C) under conditions which allow practically complete combustion the temperature rise within the reactor (measured with thin thermocouples, inserted into the monolith channels) can be kept well below 10 °C (figure A.2).

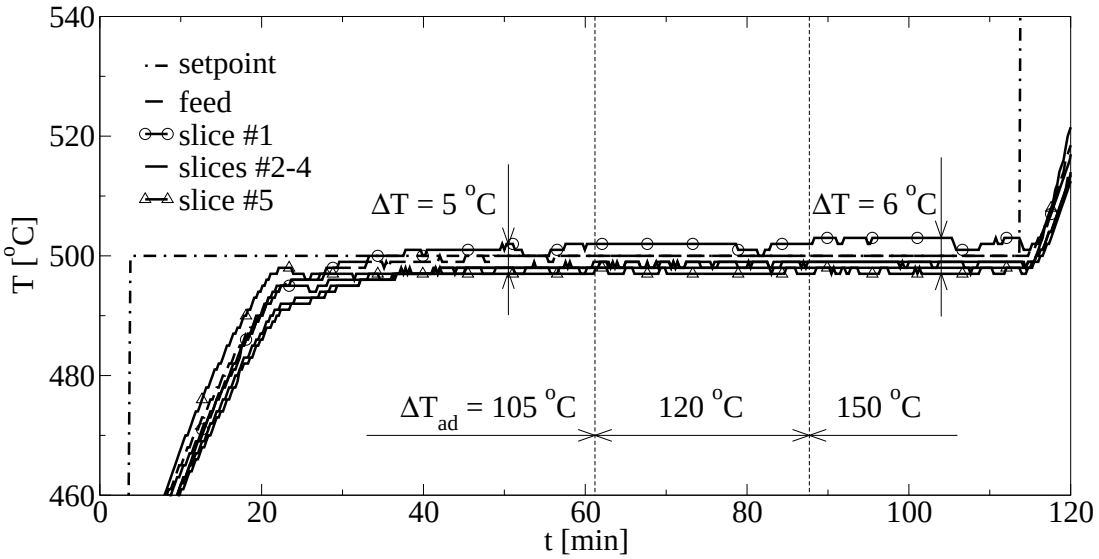

Figure A.2: Measured temperature rise upon practically complete oxidation of mixtures G7, G7.5 and G7.6 (table 5.2) in the multiple slice reactor. The three different feed compositions are characterized by their adiabatic temperature rise.

A.1.1 Setup

Multiple slice and single slice reactors share common infrastructure such as dry gas and water supply, sample conditioning, emission analyzers, pre and post catalyst oxygen sensors, compressed air for cooling purpose and laboratory atmosphere gas warning installation. These functions are assembled to separate units described below.

Standard Gas Supply A realistic exhaust composition is obtained by blending the dry gas species hydrogen, carbon monoxide, propene, propane, oxygen, nitrogen monoxide, sulfur dioxide, carbon dioxide and nitrogen – taken from compressed gas cylinders – with steam (figure A.3). An additional gas line containing pure hydrogen as a catalyst regenerating agent is not shown. Gas flow is adjusted by mass flow controllers (MKS type 1259 and 1179). A twin piston micropump (Hitachi type L-6200) delivers the appropriate amount of water into a capillary evaporator heated to approx. 120 °C. The special evaporator design allows for a pulse-free steam supply [43, 95].

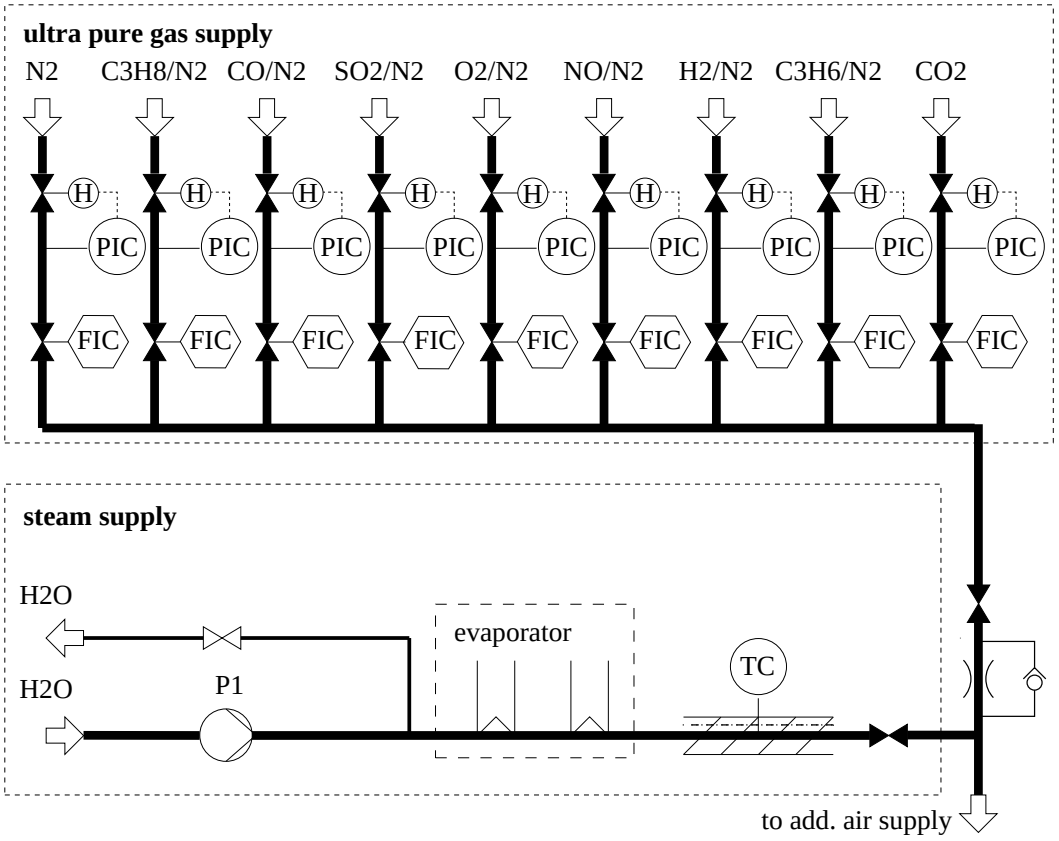

Figure A.3: Flow sheet of standard gas supply for flat bed reactors.

Air to Fuel Ratio Modulation In order to instantaneously increase the feed air to fuel ratio, additional air is injected which is otherwise passed through a hydrostatic

pressure control column (figure A.4). Since the back-pressure of the hydrostatic control column is set to the reactor system back-pressure the secondary air mass flow controller FIC is operated under steady state conditions and the catalyst sample is exposed to an almost ideal step change in air to fuel ratio (figure 6.1) if the flow through the bypass is opened or closed via the magnetic valves EV1 and EV2. The vessel shown in figure A.4 is shut off during λ-step change experiments. This operation mode is utilized for oxygen storage measurements (chapter 6).

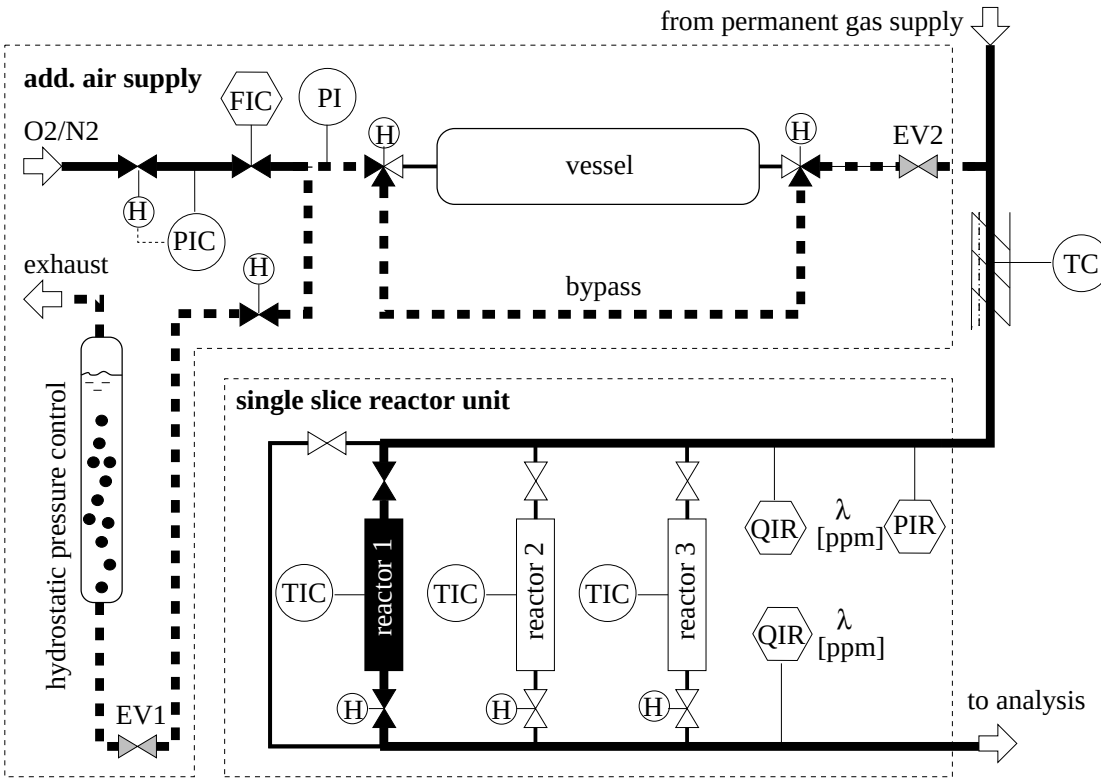

Figure A.4: Flow sheet of additional air supply in step change mode in combination with the single slice reactor unit.

Steady state catalyst conversion is measured with superimposed air to fuel ratio cycling of typically ± 3 % amplitude at a frequency of 1 Hz, simulating closed loop engine operation (chapter 5). This is simply realized by periodically closing and opening the electrical valve EV2 (figure A.5). Since slightly different back-pressures would result in an unequal partitioning of the secondary air flux, the hydrostatic pressure control column is disconnected during these experiments by closing a manual valve. To not confuse the secondary air mass flow controller FIC the air is conducted through a pressure compensating vessel which stores the extra amount of air when the magnetic valve EV2 is closed.

Single Slice Reactor The reactor unit (figure A.4) contains three single slice reactors in parallel with just one of them being on stream. This configuration allows e.g. to have

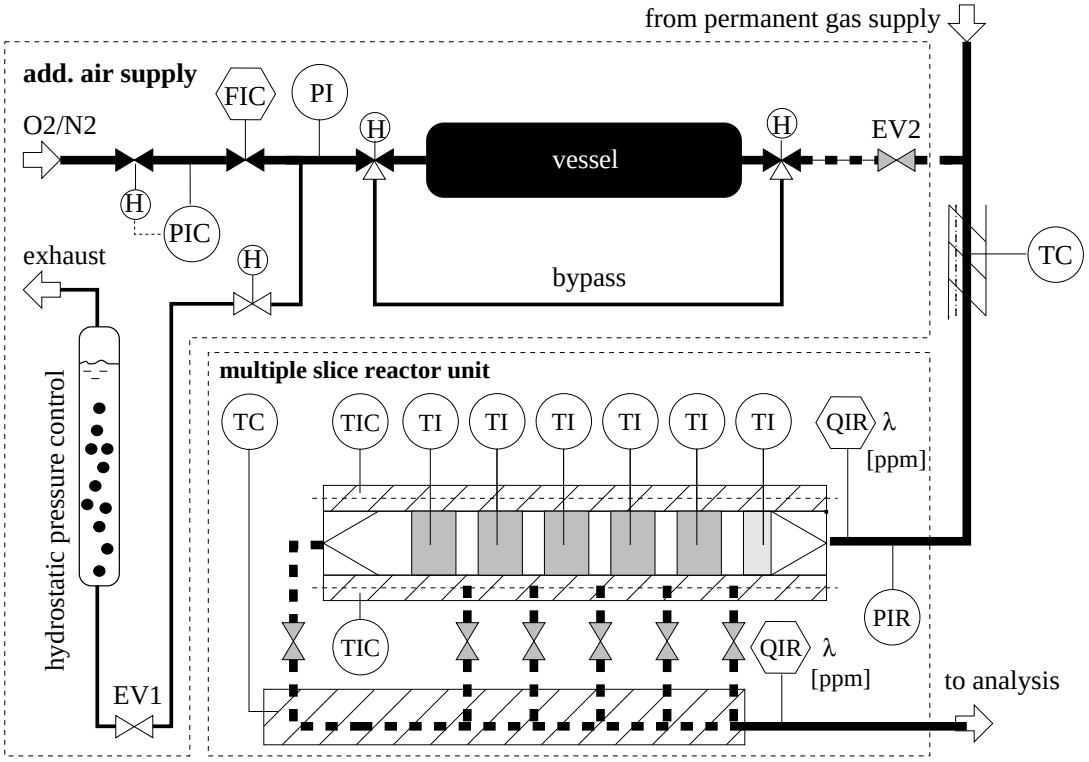

Figure A.5: Flow sheet of additional air supply for air to fuel ratio λ-cycling mode in combination with multiple slice reactor unit.

a fresh catalyst as reference sample when measuring aged samples. The slices are one channel height thick, 30 mm wide and 50 mm long (sample volume 1.56 ml).

The feed gas passes a heated pressure sensor PIR (Haenni type ED 510) and a wide range oxygen sensor QIR (Bosch type LSU 4.2) connected to special operating units (Etas type LA3). Three pneumatically operated valves are positioned in front of each reactor and one valve is positioned in the bypass line. This allows to choose the active line. Manual valves located downstream allow to have one reactor open (e.g. for sample loading) while another one is on-line. Downstream the air to fuel ratio is measured again by means of a wide range oxygen sensor QIR.

Each reactor is heated with six electrical cartridge heaters (Türk und Hillinger type HLPK, 400 W) inserted in the high temperature resistant stainless steel reactor body (steel no. 1.4893, Avesta Sheffield type 253 M). Each cartridge is assigned to a neighboring body temperature. A standard industrial three-point controller (Newport type CN77344-C4) is used to switch the respective cartridge on or off. The third controller position is only used with the mid-reactor temperature to pass compressed air through cooling pockets which spread over the entire length of the reactor. This setup allows heating rates well above 5 °C/min even at temperatures as high as 800 °C. Cooling-down from 800 °C to 100 °C takes one hour. Standard type K thermocouples (outer diameter 0.5 mm) are centered within the monolith slices.

Multiple Slice Reactor Five one channel high, 35 mm wide and 40 mm long catalyst slices (total sample volume 7.26 ml) are positioned in line (figure A.5). Air to fuel ratio readings are obtained from wide range oxygen sensors QIR upstream and downstream of the reactor. The reactor temperature is again controlled by six industrial standard temperature controllers TIC each driving two neighboring heater cartridges (instead of one as with the single slice reactor). Six pneumatically operated valves located downstream determine whether the feed gas is directly transferred to the gas analysis unit or withdrawn behind of one of the catalyst slices.

Gas Analysis Concentrations of the dry gas species are measured online in the gas analysis unit after water condensation (unit A, condenser Bühler type PKE 4-PTS). The effective condenser volume is minimized – and thus the residence time – by means of a close-coupled peristaltic pump P2 which continuously removes a small amount of gas plus condensate.

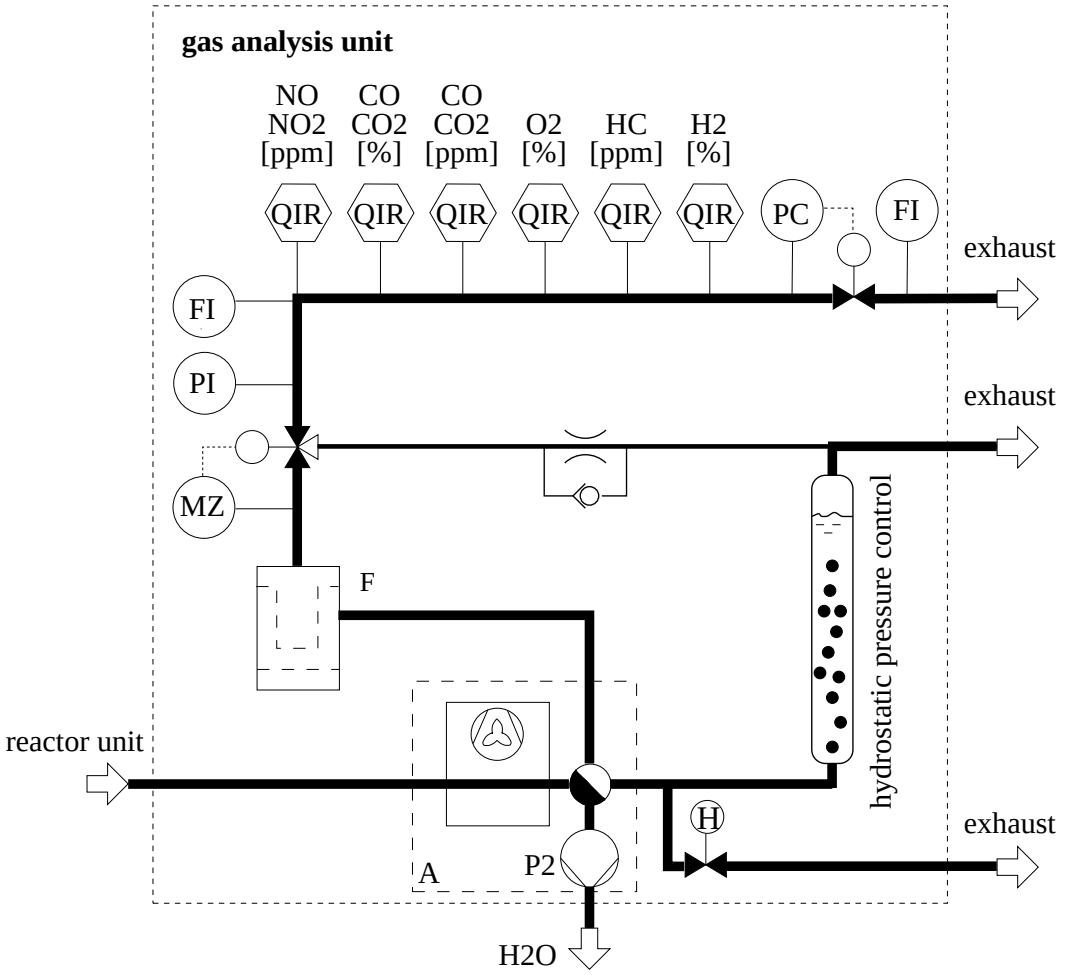

Figure A.6: Flow sheet of gas analysis unit.

Gas flow through the analyzers is adjusted to 1 Nl/min. The residual exhaust is con-

ducted into the building's exhaust system while a small fraction of it is passed through a hydrostatic pressure control column to ensure isobaric conditions within the pressure sensitive analyzers. Before entering the line of analyzers the flow passes through a filter F and a moisture sensor (Bühler type AGF-PV-30-S2 and FF-1-U).

The applied gas analyzers are summarized in table A.1.

type	manufacturer	channel 1	channel 2
Binos 4b.2	Rosemount	3000 ppm NO	500 ppm NO_2
Binos 100	Rosemount	3 % CO	5 % CO_2
Ultramat 22P	Siemens	5000 ppm CO_2	5000 ppm CO
Oxymat 5E	Siemens	100 % O_2	-
RS 55	Ratfisch	1 % C_3H_y	-
Caldos 7G	ABB	4 % H_2	-

Table A.1: Applied gas analyzers: types, manufacturers and maximum concentrations per channel.

Measured oxygen and hydrogen concentrations require cross sensitivity correction. Nitrogen monoxide causes a positive signal of the paramagnetic oxygen analyzer:

$$y_{O_2}^{cross,NO} = 0.37\, y_{NO} \tag{A.1}$$

Hydrogen measurements based on heat conductivity measurements are cross sensitive towards every other exhaust component. The compensations applied are:

$$y_{H_2}^{cross,H_2O} = +0.136\, y_{H_2O} \tag{A.2}$$

$$y_{H_2}^{cross,CO} = -0.010\, y_{CO} \tag{A.3}$$

$$y_{H_2}^{cross,O_2} = +0.018\, y_{O_2} \tag{A.4}$$

$$y_{H_2}^{cross,C_3H_6} = -0.070\, y_{C_3H_6} \tag{A.5}$$

$$y_{H_2}^{cross,C_3H_8} = -0.055\, y_{C_3H_8} \tag{A.6}$$

$$y_{H_2}^{cross,CO_2} = -0.0948\, y_{CO_2} \tag{A.7}$$

Due to its cross sensitivity the hydrogen analyzer is calibrated with a zero gas mixture containing 11 % water, 12 % carbon dioxide and 77 % nitrogen. Across the condenser the water concentration will drop down to approx. 0.75 % (the saturation concentration at system pressure 1250 mbar and controlled condenser temperature 6 °C). Thus the hydrogen analyzer is calibrated to a reactor exhaust containing more than 0.75 % water and a background carbon dioxide concentration of 12 %. Equations A.3 through A.7 allow to compensate cross sensitivities from carbon dioxide concentrations exceeding 12 % and every other exhaust component except water. Carbon dioxide concentrations (around 12 %) are not detected since they are well outside of the respective analyzers's range (table A.1). The carbon dioxide concentration is therefore calculated from carbon balances along the reactor.

A.1.2 Instrumentation, Automation and Safety

Instrumentation and Control A virtual instrumentation is realized with the Microsoft Windows based software TestPoint on an industrial design personal computer. Multiple channel multimeters (Keithley type DMM2000 and DMM2700) take care of the analog to digital conversion within the gas analysis unit and the single slice reactor unit respectively. They communicate with the PC via digital communication line RS232 (Keithley type PCL 849). Analog and digital IO PCI-interface cards (Keithley type DAS-TC, PIO-24) digitize the multiple slice reactor thermocouple signals and indirectly switch solenoid and pneumatic valves. Temperature controllers and mass flow controller operating units (MKS 647B and MKS 247B) are decentralized and communicate with the PC via digital communication line RS485 (RS485/RS232-converter Advantech type ADAM 4520) and GPIB (Keithley type KPCI-488) respectively.

Since Microsoft Windows is not a real-time operating system and to be consistent with the described modular architecture the secondary air supply is controlled with an SPC (Siemens type Simatic S7-200 CPU 212). This allows to simultaneously close the injection valve EV1 (figure A.4) and open EV2 (both Bosch type 0 280 150 706) to induce a rich-lean step. In addition simulated closed loop high frequency air to fuel ratio cycling (e.g. 5 Hz) can be realized.

Up- and downstream air to fuel ratio signals are logged with a sufficiently high scanning rate to a separate personal computer equipped with a multipurpose PCI interface card (Keithley type DAS-1702ST-DA).

Since the duration of most test runs is in the range of 12-24 h a fully automatic process control is realized. In automatic mode the control program is fed with an ASCII control file which contains information subject to change during program execution such as time, temperature, gas routing and exhaust composition.

Safety Considerations Save operation in both manual and automatic mode prevents the setup, the environment and personnel from damage. Whenever possible, the automation is designed to be intrinsically safe. If e.g. moisture is detected upstream of the gas analyzer and/or the condenser temperature fails to be at its setpoint of 7 $\pm$ 3 °C or if the total system's back pressure exceeds 500 mbar the exhaust is directly discharged without passing the analyzers. Since these features are realized within the units "dry gas supply" and "gas analysis" they are active whatever control mode is chosen (manual or automatic).

When power is shut off, the system goes into the save state. In fully automatic mode power is switched through as long as both the PC based automation program and a redundant SPC (Siemens type Simatic S7-200 CPU 212) signal safe operating conditions. Then the reactor temperatures are within a safe region (below 750 °C) and the laboratory atmosphere is well below explosive and toxic limits. Furthermore the SPC expects a periodic watchdog reset provided by the Microsoft Windows based automation routine.

A.2 Fired Tube Reactor

Certain oxygen storage measurements as well as accelerated catalyst aging experiments at temperatures of up to 1200 °C (appendix B) are carried out in a fired tube reactor. It provides a stable and representative exhaust composition at steady state temperatures up to 1200°C. Compared to the Pulse Flame Combustor of Ford [65] it provides an even more stable fuel combustion and yields higher exhaust temperatures.

A.2.1 Setup

Burner A burner (Pierburg 17 kW prototype [127, 89]) equipped with an electric arc generator is mounted to a tube containing the catalyst sample positioned further downstream (figure A.7). The volume of the catalyst sample is 0.146 l (D = 35 mm, L = 118 mm). A mass flow controller FIRC (Bronkhorst Hitec type M1L202-FB-33-P) meters iso-octane which is combusted with dehumidified air dosed by another mass flow controller (MKS type 1259CC, condenser Sabroe type Ultratroc SD0045/303). High-grade iso-octane is chosen as a fuel since this allows to establish a stable clean flame in the combustion chamber, whereas gasoline fuel causes flame pulsation under steady state conditions and diesel fuel tends to form significant amounts of soot. Diesel sooting is likely to result from poor spray atomization. The prototype burner was originally developed to be operated with standard low pressure on-board secondary air to reduce gasoline vehicle cold start emissions. Pressure drop across the nozzle's annular gap is below 200 mbar. Flame pulsation is believed to result from evaporation of low boiling point gasoline fractions and can be avoided by fueling with iso-octane (see table A.2). Even with iso-octane external cooling of the burner nozzle with compressed air is necessary if the burner is operated at less than 9 kW to ensure stable combustion.

	boiling temperature T_b [°C]	density ρ [kg/l]	molar H/C-ratio x [-]
gasoline	25 ... 215	0.715 ... 0.765	$\sim$ 1.85
diesel	180 ... 360	0.815 ... 0.855	$\sim$ 1.85
iso-octane	99	0.690	2.25

Table A.2: Basic properties of gasoline, diesel and iso-octane [9].

Under steady state operation (7 kW, $0.97 < \lambda < 1.03$) the burner exhaust contains low levels of nitrogen oxides (100 ppm $< y_{NO_x} <$ 130 ppm) and hydrocarbon concentrations below 1 ppm. Due to the higher molar H/C-ratio, water concentrations are somewhat higher and carbon dioxide concentrations somewhat lower (complete stoichiometric iso-octane combustion: $y_{H_2O} = 14\%$ and $y_{CO_2} = 12.5\%$) compared to gasoline combustion (chapter 2).

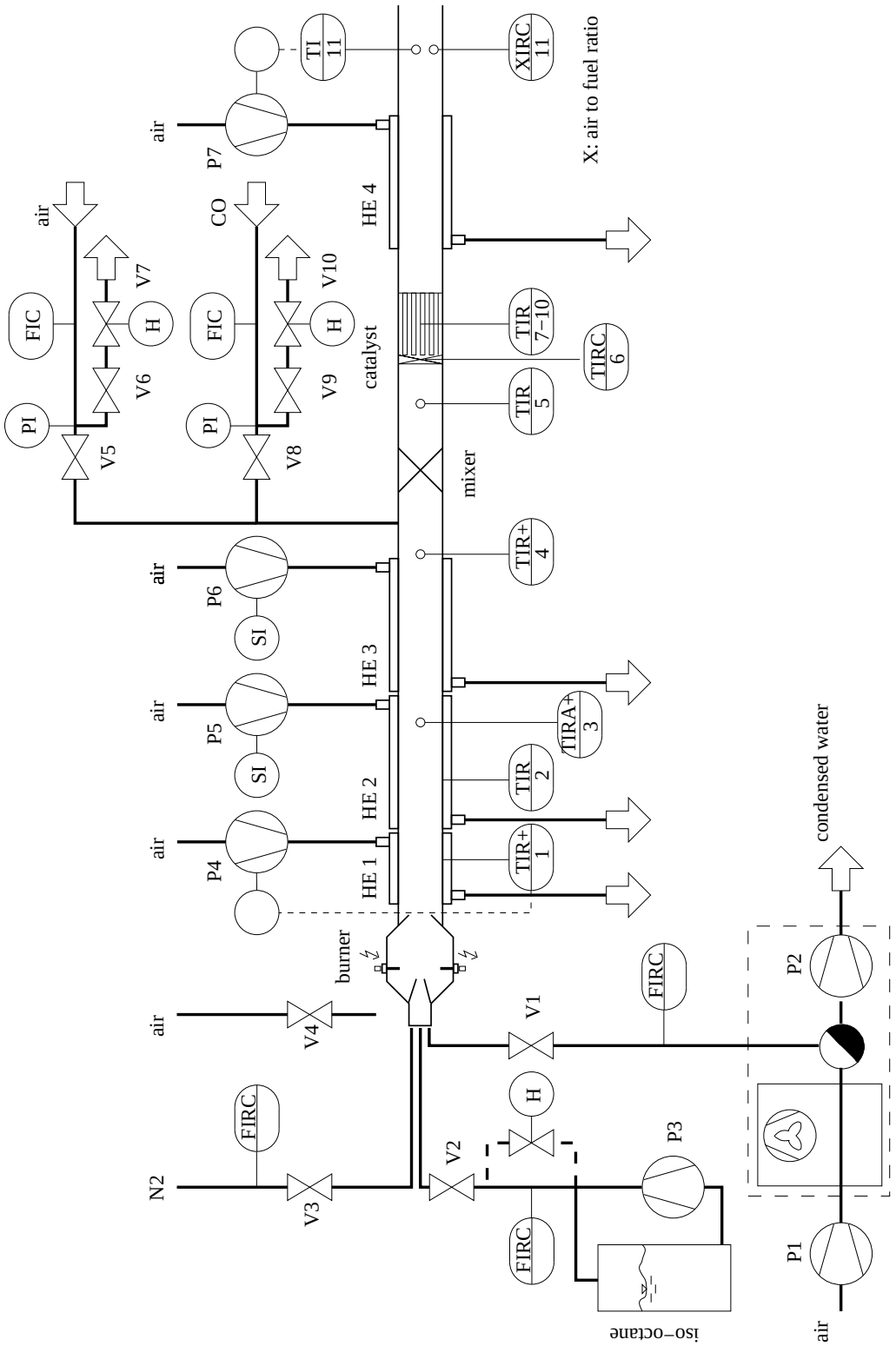

Figure A.7: Fired tube - schematic sketch combined with flow sheet.

Tube Several subsequent gas-gas heat exchanger sections provide exhaust cooling. Each heat exchanger is fed with air by a separate side-channel blower (Siemens types 2BH1 510, 2BH1 810, 2CH6 002, P_{total} = 22 kW). When cooling air is shut off they serve as air-gap insulation. All other sections are air-gap insulated as well. Furthermore the tube is insulated against the environment with several layers of ceramic mat. The inner tube is made of steel no. 1.4893 (Avesta type 253M) with a solidification range of 1350 to 1430 °C. Due to even higher flame temperatures (ΔT_{ad} = 1700 °C) an α-Al_2O_3 liner protects the first 0.5 m of the 2.2m long tube.

Secondary Gas Injection Additional gas species such as carbon monoxide, gaseous hydrocarbons and air can be injected in front of the catalyst to e.g. impose fuel cut deceleration conditions on the catalyst for aging purpose or to switch between rich and lean conditions in order to measure the catalysts oxygen storage capacity.

Gas Analysis The post catalyst air to fuel ratio is monitored by means of a wide range lambda sensor XIRC (Bosch type LSU 4.2). A fraction of the exhaust is filtered, passed through a condenser (Bühler type PKE4) and both hydrocarbon and oxygen concentrations (Ratfisch type RS 53 and Servomex type Xentra 4100) are measured.

A.2.2 Instrumentation, Automation and Safety

Instrumentation and Control A virtual instrumentation is build with the software TestPoint running under Microsoft Windows. Several computer plug in boards (Keithley type DAS-TC, DAS-1601, DDA-08, PIO-24) convert thermocouple and mass flow controller readings, open and close valves, switch on the fuel pump, spark ignition and set the frequency of the frequency converters (Siemens type Simovert Mircomaster and Midimaster Vector) which control the side channel pumps' speeds. Several software PID-controllers are applied for temperature control.

Safety Considerations Due to the high level of acoustic noise caused by the side channel pumps, the duration of aging experiments and to ensure repeatability, the setup can be operated in automatic mode.

The gas analysis unit is generally designed as described in section A.1.2. In addition to a threshold check by the PC based automation routine, a SPC (Siemens type Simatic S7 CPU 215-2) provides redundant check of critical states. The SPC expects a periodic watchdog signal from the PC, checks temperature thresholds based on separate temperature readings (Jumo type MDA1-48/1), if the burner is still in the ignited state, the cooling water circuit is not leaking and whether the ambient atmosphere is well below toxic and explosive limits.

Appendix B

Aging

Full load engine operation – accompanied with high engine out temperatures – causes severe catalyst aging. In the following section oxygen storage capacity and catalytic activity of catalysts aged at three different temperatures is compared to the respective properties of a fresh reference sample. Furthermore the correlation of oxygen storage and activity degradation with catalyst aging is discussed since mandatory state of the art on-board catalyst diagnosis (OBD) relies on this correlation.

B.1 Influence on Oxygen Storage and Combustion

Catalysts subjected to four hours of lean hydrothermal oven-aging ($\lambda = 1.1$) at 1050, 1200 and 1300 °C have a significantly deteriorated light-off behavior compared to their fresh state (figure B.1). Lower catalytic activity under lean conditions is probably related to a lower precious metal surface area. Initially highly dispersed precious metal tends to agglomerate at elevated temperatures – turning into particles with a lower volume specific surface. Another cause of accessible precious metal surface loss is encapsulation: support migrates onto the precious metal particles - encapsulating them in a few monolayers thick washcoat decoration [14, 49, 54].

The complete oxygen storage capacities of these catalysts are also influenced by the aging procedure (figure B.3). While the fresh OSCC at 700 °C is as high as 1.5 gO_2/l, the respective value of the catalyst aged at 1300 °C is diminished by more than 95 % ($\approx$ 0.05 gO_2/l). Oxygen storage capacity is reported to be not related to surface area [133, 162, 106, 114]. A recent review concludes that the OSC of ceria-based materials depends on the formed phase rather than its surface area [2]. Surface and bulk reduction can not be separated [42, 162].

Thus OSCC values of ceria-zirconia solid solutions should be dominated by the composition of the material. Highly ordered solutions provide a higher oxygen storage capacity compared to relatively irregular distributed materials [114, 152]. Phase segregation of ceria-zirconia occurs in the region of 1000 to 1100 °C and the solid solution

is partially divided into stable CeO_2 and ZrO_2 [86, 78, 114]. Both pure materials have (almost) no oxygen storage capacity under automotive exhaust conditions (see section 3.2).

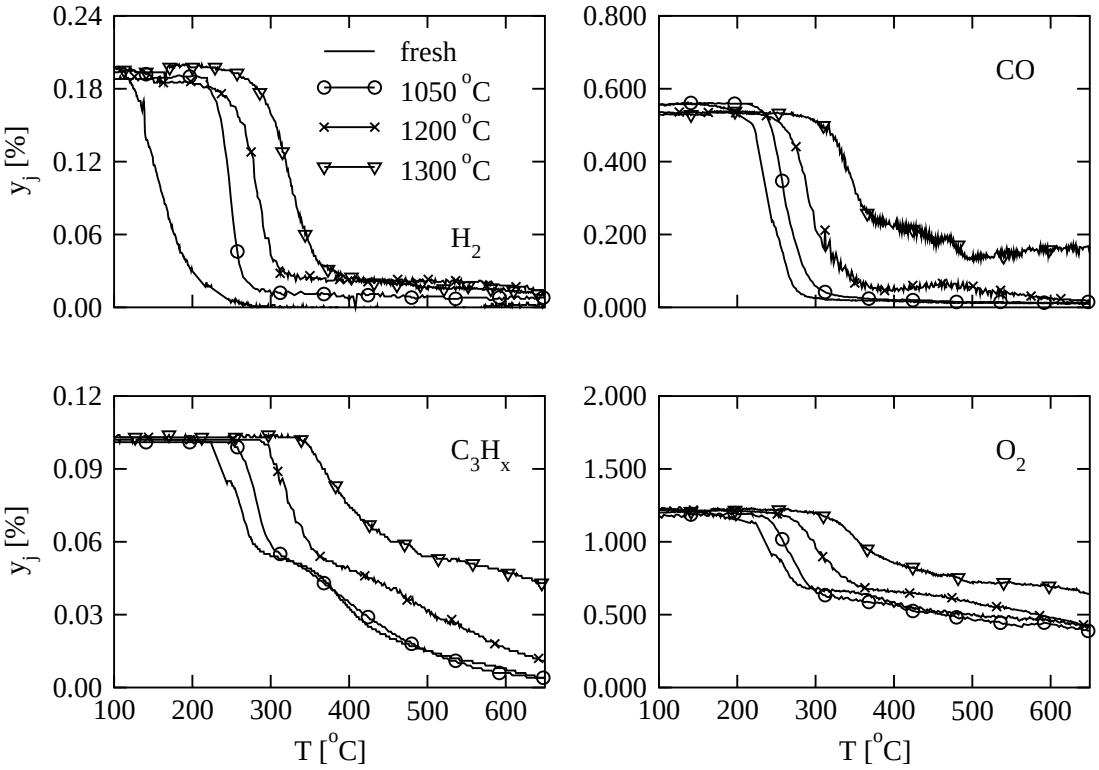

Figure B.1: Combustible species conversion of aged catalysts (aging temperature $T = 1050$, 1200 and 1300 °C, $\lambda = 1.1$, 4 h) compared to a fresh reference sample; exhaust composition G7 in table 5.2, $SV = 77000\ \mathrm{h}^{-1}$, average air to fuel ratio $\lambda = 1.02$ perturbed with ± 0.03 at a frequency of $f = 1$ Hz.

Since reliable commercial analyzers for legislated exhaust species are not yet available at reasonable costs, on-board diagnosis of catalytic activity is based on oxygen storage capacity measurements. Deterioration of catalytic activity and oxygen storage capacity correlate to some extent (figure B.2). It depends on the specific situation how well this correlation suits to meet legal OBD requirements.

B.2 Simulated Deceleration with Fuel Cut

Upon open throttle operation with reasonable air mass flow and intake manifold pressures close to ambient pressures higher boiling fuel fractions (see table A.2) tend to condense in the intake manifold, building-up a wall-applied fuel film.

Subsequent decelerations with trailing throttle fuel cut-off are generally agreed to subject the catalyst to harsh transient conditions: Partially burned and unburned hydrocarbons stemming from the intake port wall-applied fuel film during full load operation

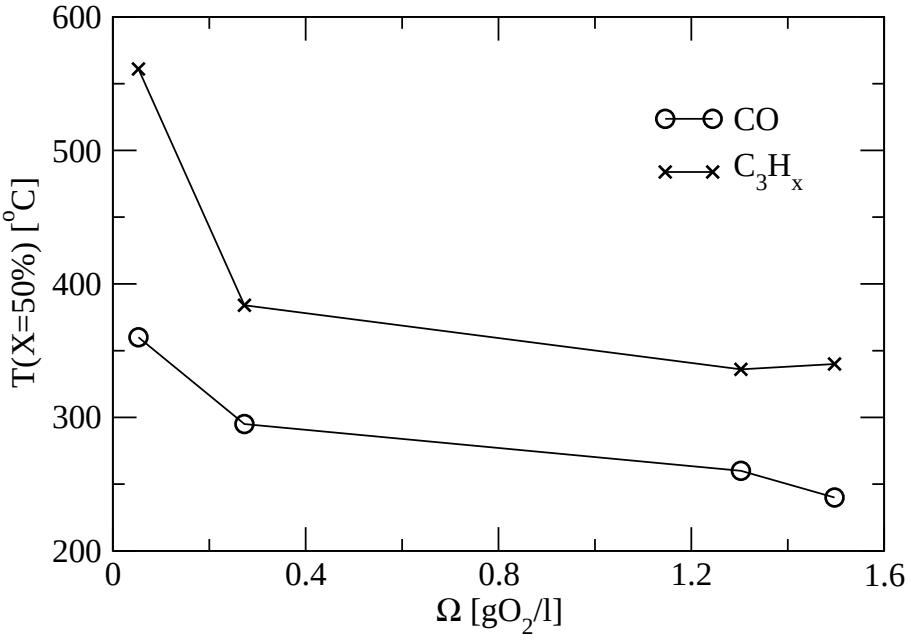

Figure B.2: Correlation of catalytic activity (represented by temperatures necessary for 50 % conversion of the respective legislated exhaust species, figure B.1) and complete oxygen storage capacity (measured at 700 °C, figure B.3).

and partial load crankcase ventilation enter the exhaust system along with excess air. Thus the catalyst experiences high transient peak temperatures (figure B.4).

The first 38 mm section is subjected to the highest temperatures – no matter whether the combustion occurs within the catalyst (figure B.4, left column) or in front of the catalyst (figure B.4, right column). However the first catalyst section subjected to the reaction load turns out to be less aged than the corresponding section the already reacted hot gas is admitted to. This finding emphases the dominant influence of temperature on catalyst aging.

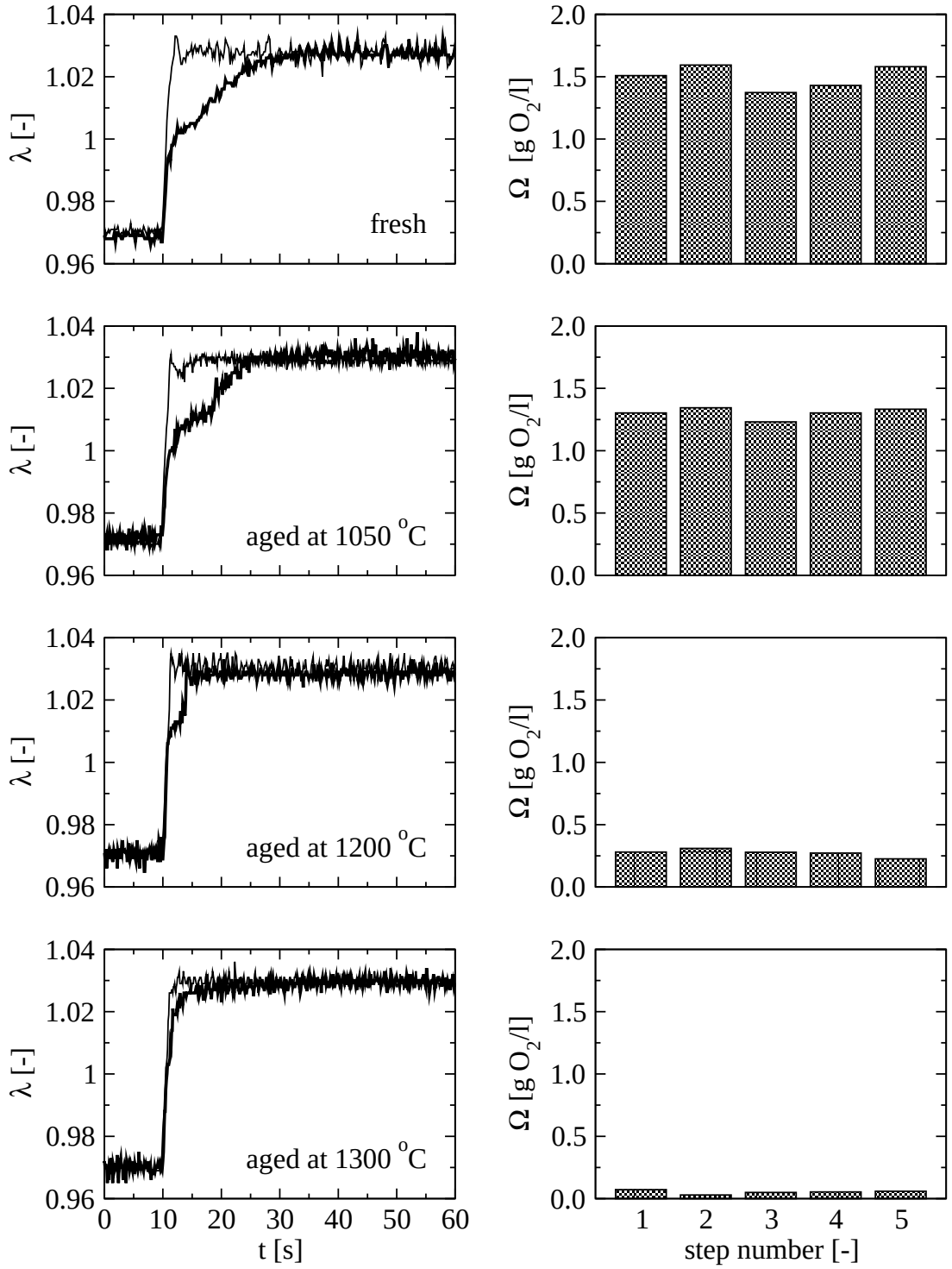

Figure B.3: Air to fuel ratio responses to step changes in feed stoichiometry (conditions see table 6.1, signal correction see appendix D) measured at 700 °C upstream and downstream of different catalyst samples (fresh and four hours hydrothermal lean aged at 1050, 1200 and 1300 °C) along with the respective OSCC values of five consecutive rich-lean steps.

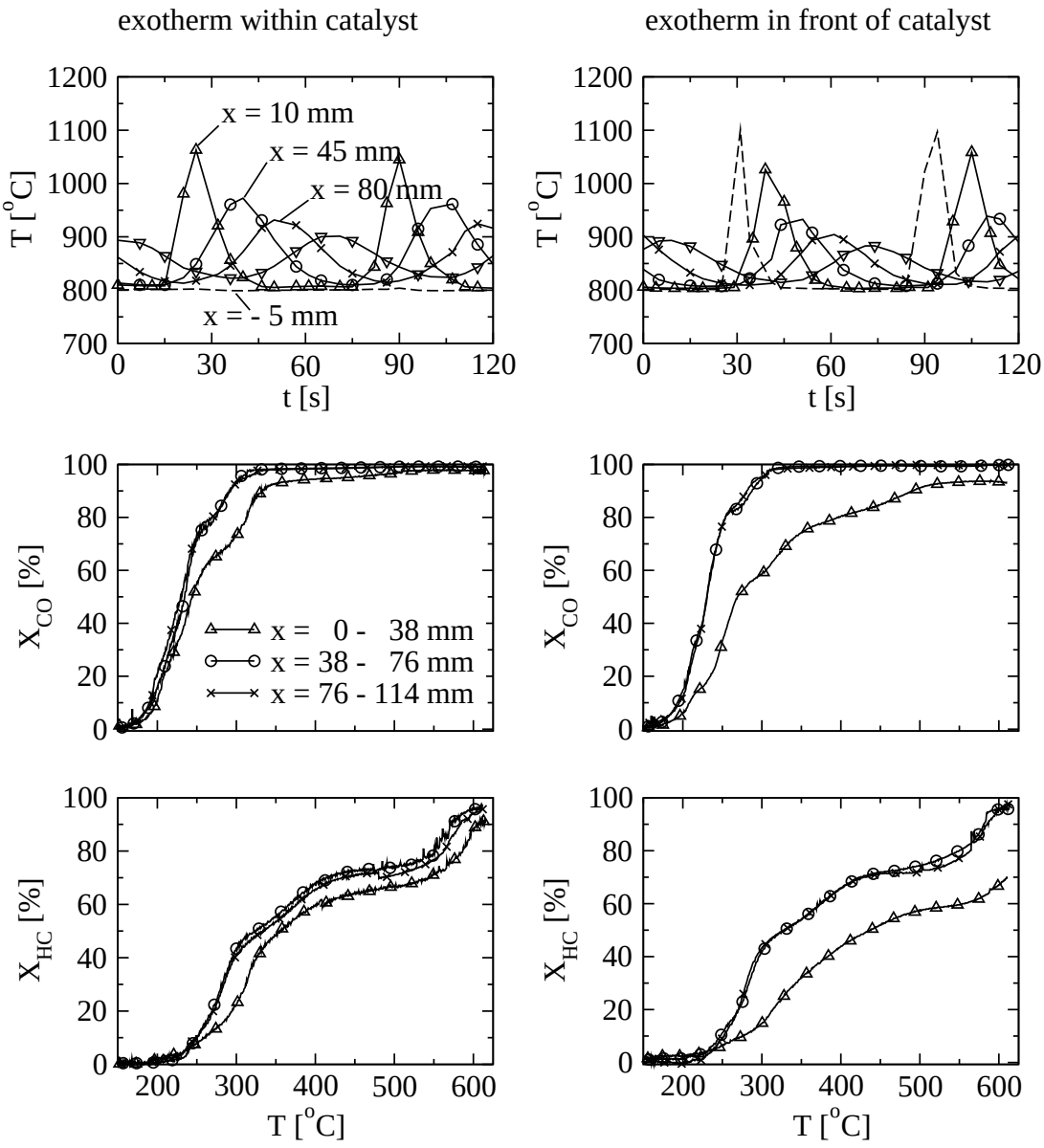

Figure B.4: Catalyst deactivation due to simulated fuel cut aging in the fired tube reactor (see section A.2). Top: Temperature traces at different positions within the monolith catalyst. Middle and bottom: Carbon monoxide and hydrocarbon light-off conversion of aged catalyst sections. Aging conditions: Burner is operated at $\lambda = 1$ for four hours. Every 60 sec pure propane and oxygen are added simultaneously downstream of the burner (propane valve opening duration: 5 sec, oxygen valve opening duration: 15 sec). Amount of secondary oxygen injection adjusted such that the measured air to fuel ratio during propane injection is stoichiometric (left) and lean (right column).

Appendix C

Deactivation - Additional Data

The transient improved conversion under fuel rich conditions discussed in chapter 8 may be further analyzed by step change experiments conducted in the multiple slice reactor. Transient responses of hydrogen, carbon monoxide, propene, propane, nitrogen oxide, oxygen and a post catalyst linear oxygen sensor to step changes in stoichiometric composition at different temperatures are gathered in figures C.1 through C.5. As outlined in section A.1 the thermal conductivity based hydrogen analyzer's cross sensitivity towards carbon dioxide is calculated under the assumption that carbon atoms are not stored within the catalyst – which is probably not valid under transient conditions as discussed below. Hydrogen concentration measurements within the catalyst are therefore considered as qualitative rather than quantitative.

An undershoot of the post catalyst linear oxygen sensor upon lean-rich transition similar to the one depicted in figure C.3 has been reported elsewhere [32, 111, 83].

Under lean conditions at 700 °C subsequent to apparent filling of the oxygen storage, combustible species conversion is complete within $x = 0 \ldots 80\,\text{mm}$ (upper part of figure C.5). However a gradual drop of the oxygen concentration is registered further downstream ($x = 80 \ldots 200\,\text{mm}$). Since removal of sulfuric or carbonaceous deposits is reported to be a rather spontaneous process this phenomenon might be due to hydroxyl formation. During lean operation hydroxyls build up on the ceria surface and become unstable on reduced ceria or in the presence of carbonates [72, 73, 116, 104].

The conversion of all combustible species at 300 °C is dominated by oxidation with oxygen and nitrogen oxide. Upon transition to rich conditions and stored oxygen depletion, oxygen and nitrogen oxide are converted within $x = 0 \ldots 80$ mm (lower part of figure C.1). High conversion of hydrogen and carbon monoxide along with little hydrocarbon conversion leads to a significant lean shift of the linear oxygen sensor located downstream (details on the oxygen sensor's sensitivity towards different exhaust species see appendix D).

After apparent oxygen storage depletion at 400 °C, oxidation under rich conditions is complete within $x = 0 \ldots 40$ mm (lower part of figure C.2). Hydrocarbon and carbon monoxide conversion continues – at a slower rate – in the nitrogen oxide and oxygen

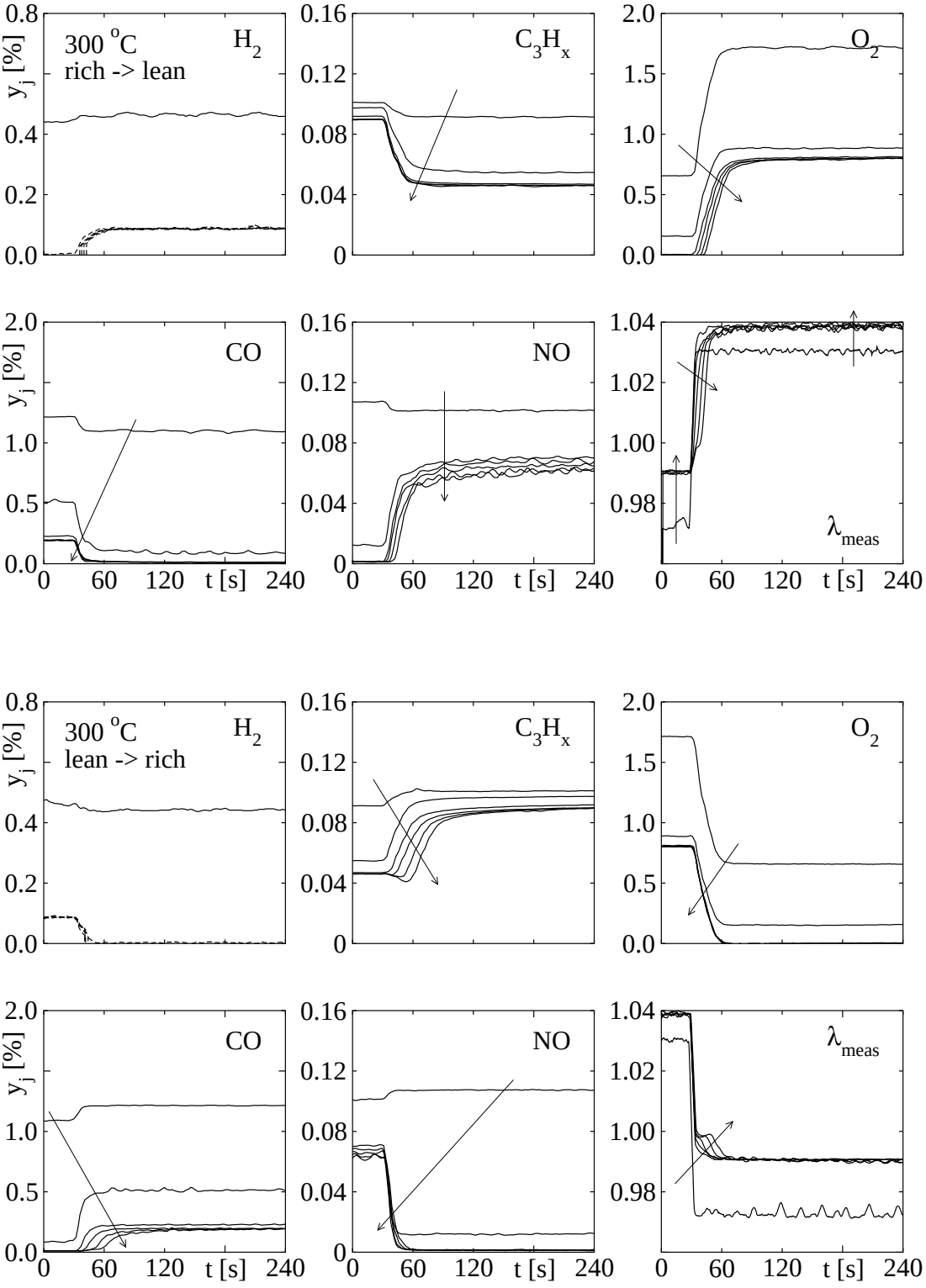

Figure C.1: Exhaust species and linear oxygen sensor responses to step changes in feed composition (table 6.1) at x = 0, 4, 8, 12, 20 cm within the catalyst at 300 °C.

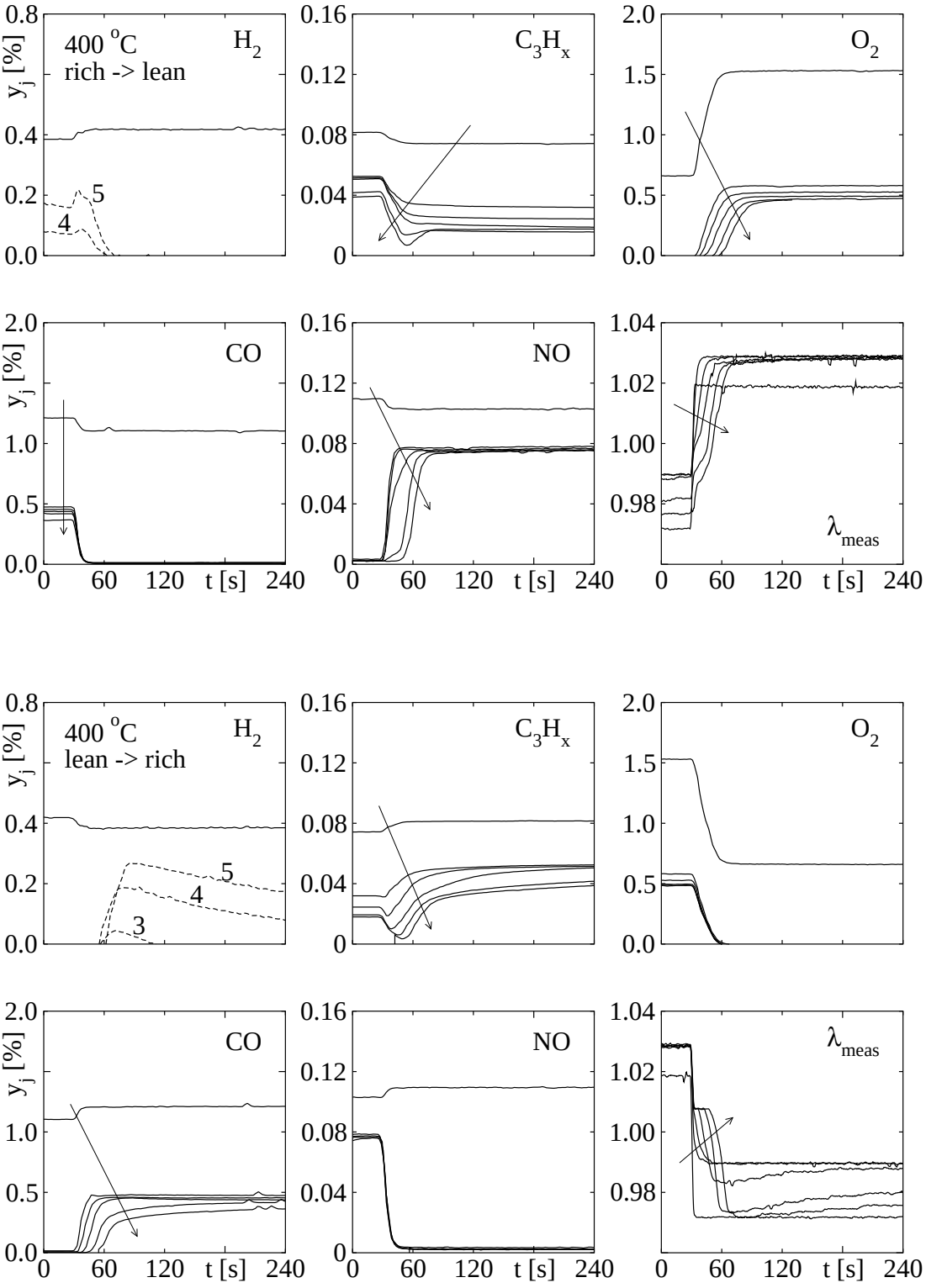

Figure C.2: Exhaust species and linear oxygen sensor responses to step changes in feed composition (table 6.1) at x = 0, 4, 8, 12, 20 cm within the catalyst at 400 °C.

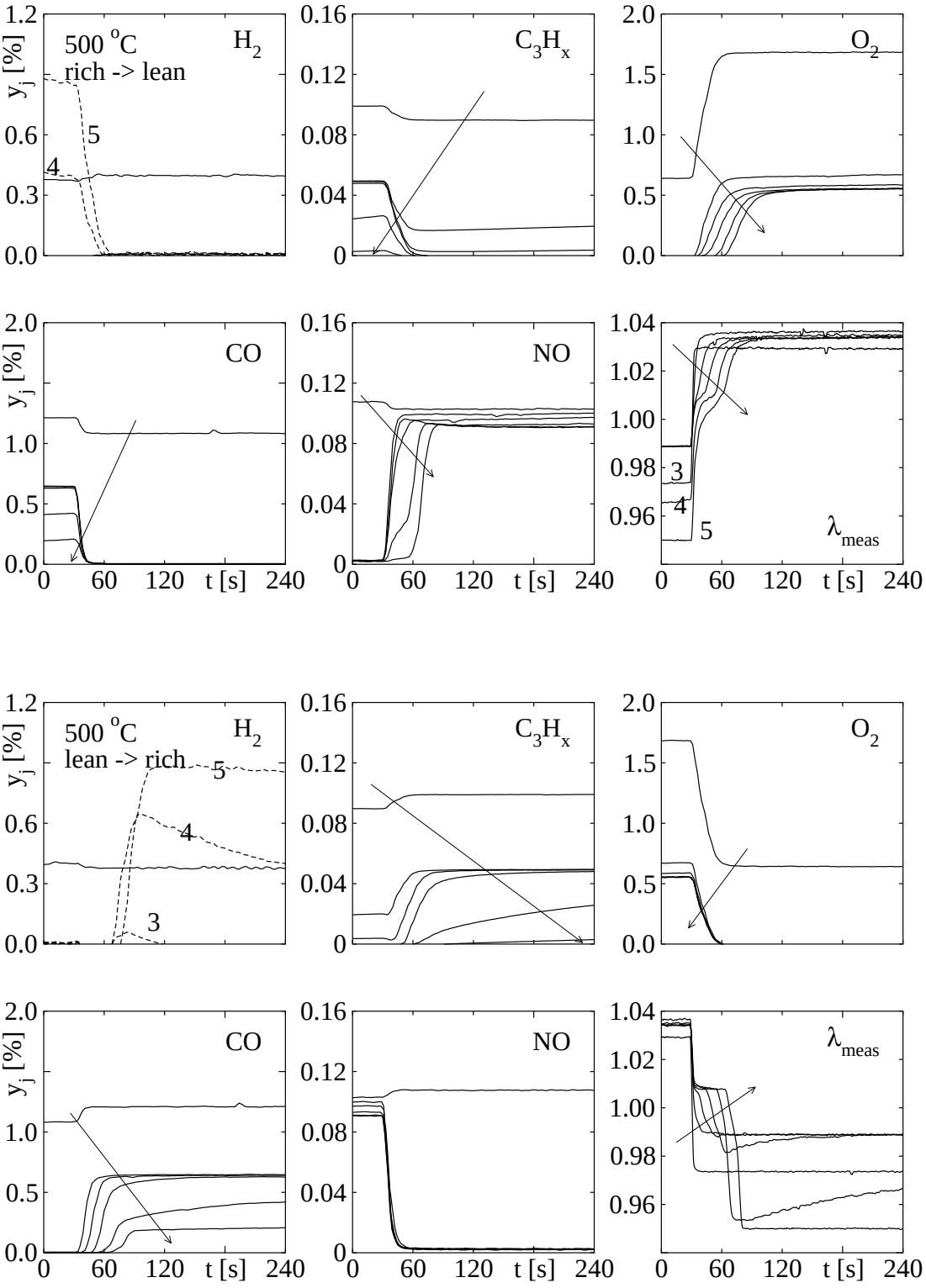

Figure C.3: Exhaust species and linear oxygen sensor responses to step changes in feed composition (table 6.1) at x = 0, 4, 8, 12, 20 cm within the catalyst at 500 °C.

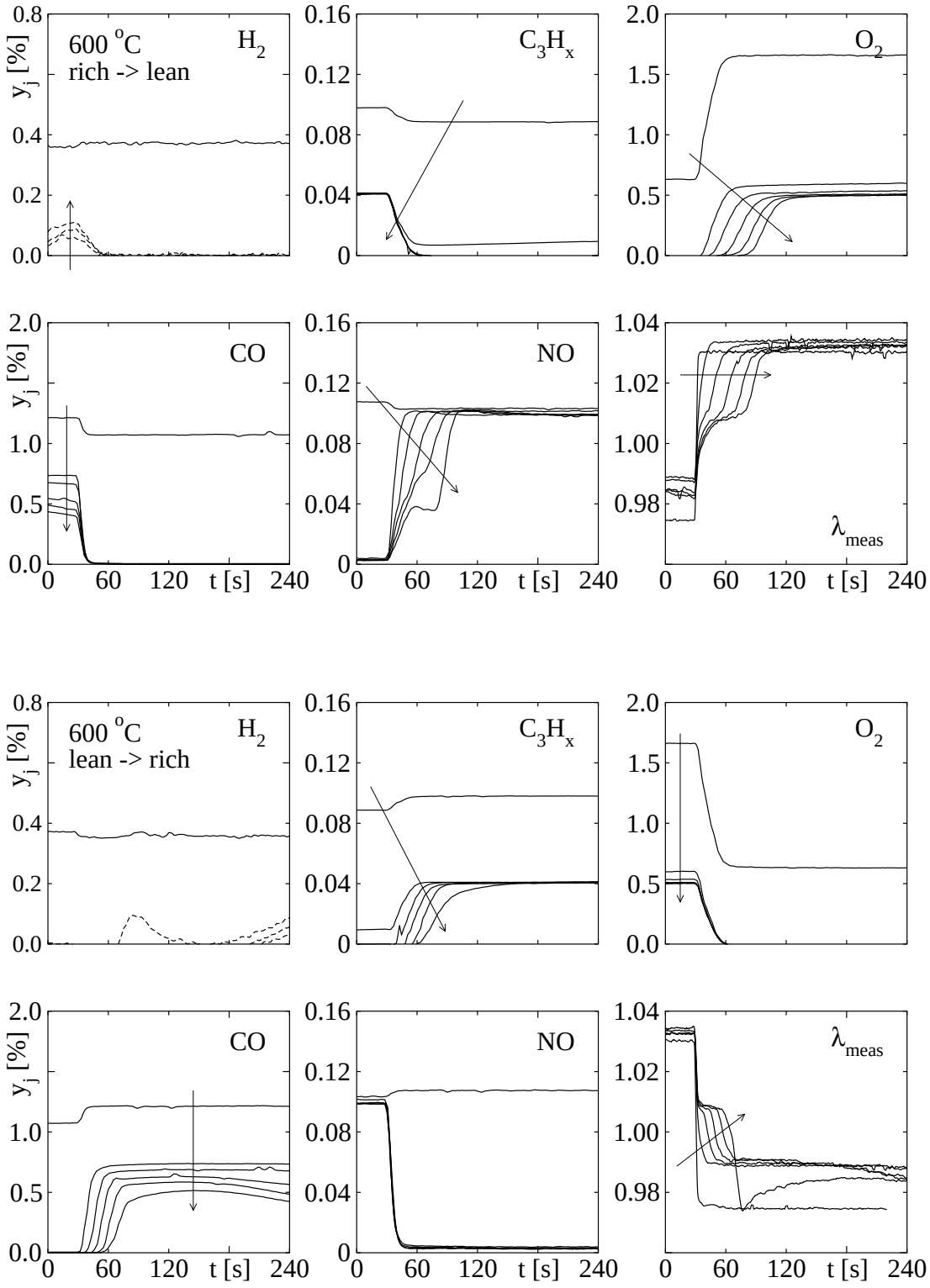

Figure C.4: Exhaust species and linear oxygen sensor responses to step changes in feed composition (table 6.1) at x = 0, 4, 8, 12, 20 cm within the catalyst at 600 °C.

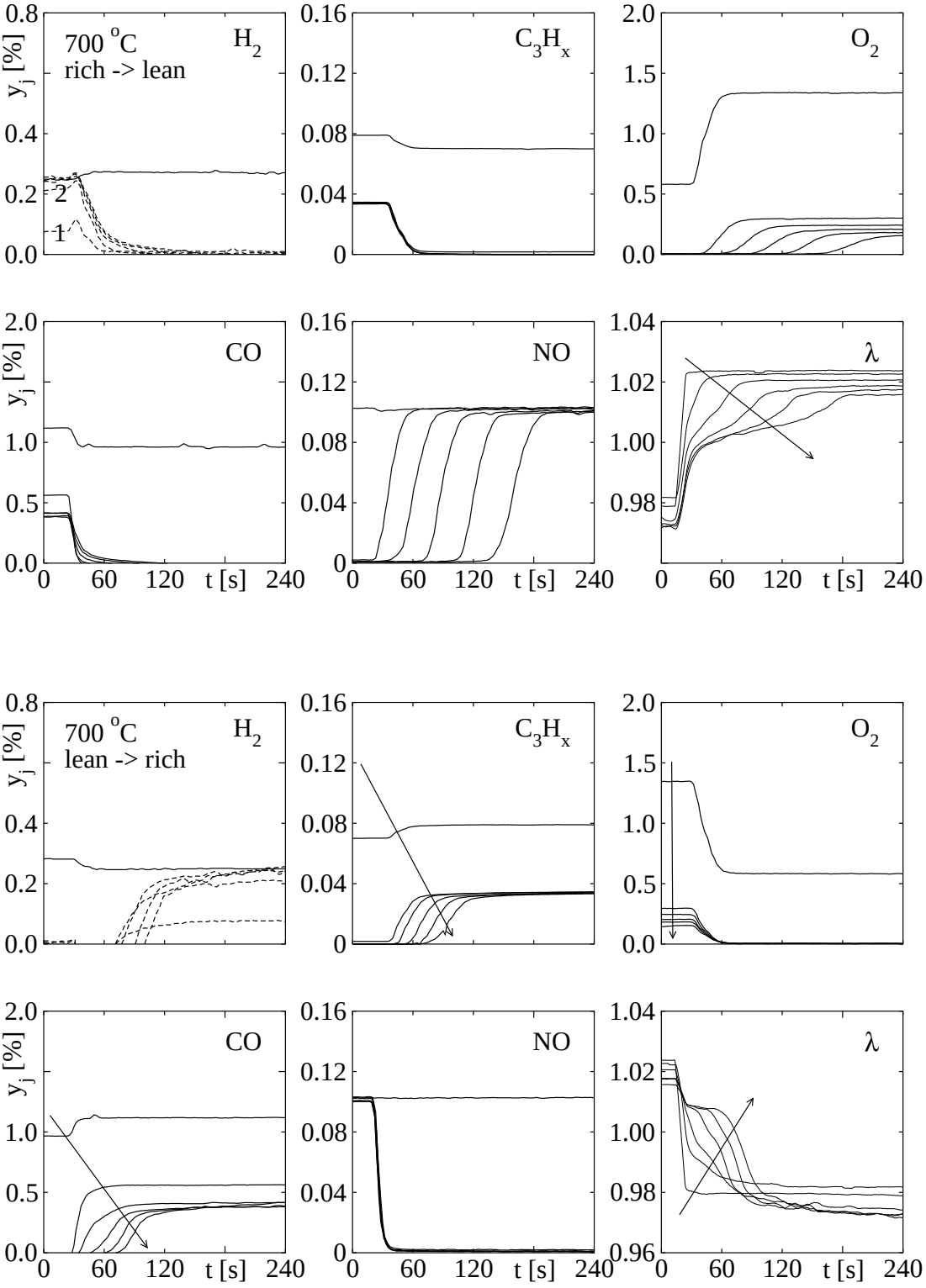

Figure C.5: Exhaust species and linear oxygen sensor responses to step changes in feed composition (table 6.1) at x = 0, 4, 8, 12, 20 cm within the catalyst at 700 °C.

free sections of the catalyst located further downstream ($x = 40 \ldots 200$ mm). Carbon monoxide and hydrocarbon conversion is accompanied with significant hydrogen production – somewhat compensating the oxygen sensors lean shift due to still significant hydrocarbon concentrations. However due to a slow deactivation of both hydrocarbon and carbon monoxide conversion the catalytic converter transforms into a less active state within minutes.

At 500 °C hydrocarbon rich side conversion following apparent oxygen storage depletion is almost complete at $x = 200$ mm (lower part of figure C.3). The huge amount of hydrogen produced due to steam reforming and water gas shift reaction leads to a severe rich shift of the linear oxygen sensor located downstream. Again a slow deactivation of water gas shift and steam reforming reactions can be observed. With even higher temperatures the almost complete transient hydrocarbon conversion is no longer observed (figures C.4 and C.5). Deactivation seems to be significantly accelerated. Whereas carbon monoxide is converted at 600 °C between $x = 40$ and 200 mm by means of water gas shift reaction, equilibrium conversion is reached at 700 °C within $x = 40 \ldots 80$ mm.

Appendix D

Lambda Sensor Characteristics

Commercial lambda sensors are based on yttrium doped zirconium dioxide solid electrolytes which are placed between the exhaust gas and a suitable reference gas atmosphere (usually ambient air). Both sides are coated with platinum which catalyzes further exhaust gas equilibration and the electrode reactions [177]. The equilibration voltage across a potentiometric sensor (such as Bosch type LSF 4.2) can be calculated from the Nernst equation:

$$U = \frac{\mathrm{R}\,T}{4\,\mathrm{F}} \ln \frac{p_{\mathrm{O_2,ref}}}{p_{\mathrm{O_2}}} \tag{D.1}$$

Sensors based on solely potentiometric operation are often referred to as HEGO's (heated exhaust gas oxygen sensors) and are applied both upstream and downstream of catalytic converters with air providing the reference oxygen partial pressure.

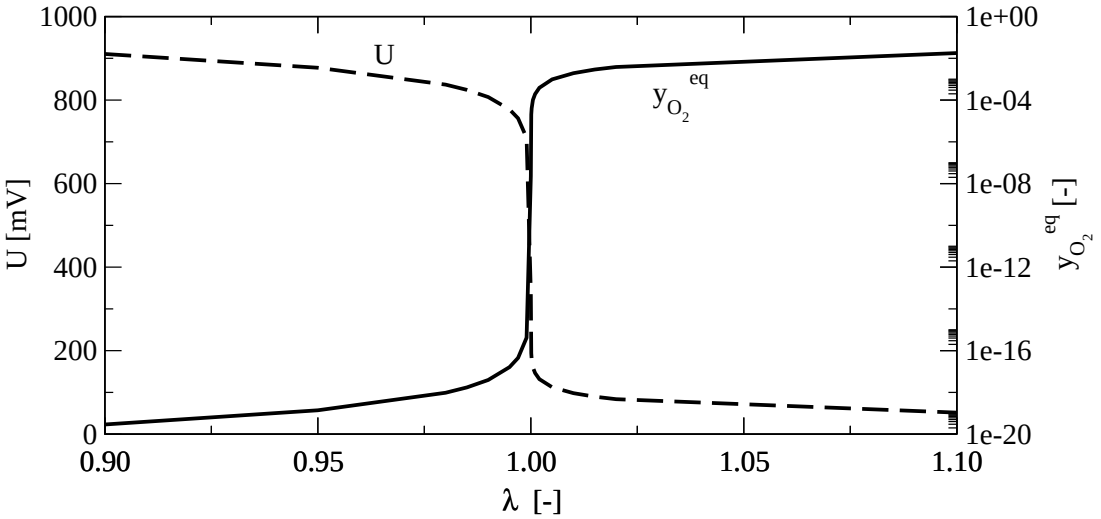

Figure D.1: Theoretical HEGO voltage dependent on exhaust gas oxygen potential and equilibrium oxygen potential as a function of air to fuel ratio at T = 700 °C.

The voltage signal of such a sensor has a rather step function characteristic due to the change of equilibrium oxygen partial pressure by several orders of magnitude when

crossing the stoichiometric composition (figure D.1). A continuous control of engine out air to fuel ratio can only be approximated by a two-point controller based on the HEGO information “rich” and “lean”.

It can be seen from Nernst equation D.1 that the so called lambda sensor is indeed not a lambda but an oxygen sensor of the residual oxygen at the sensor electrode after oxidation of the combustibles. In order to ensure the equilibrium oxygen partial pressure to establish, the platinum electrodes are separated from the exhaust atmosphere by diffusion barriers. Thus the atmosphere in the vicinity of the solid oxide surface does not necessarily represent the air to fuel ratio in the exhaust bulk but is biased by the different diffusivities of the exhaust components, the HEGO voltage transition (e.g. $U = 650$ mV) is shifted towards leaner compositions if the hydrogen content in the exhaust increases [65]. This diffusion barrier effect on sensor reading is discussed in more detail with the wide range oxygen sensor in the following paragraph.

Wide Range Oxygen Sensors such as Bosch type LSU 4.2 are applied in state of the art aftertreatment systems as part of the engine air to fuel control positioned in front of the first catalytic converter [178]. Through a hole the exhaust diffuses to electrodes at the end of the diffusion barrier (see figure D.2). The sensor maintains a stoichiometric mixture in the exhaust cavity (potentiometric voltage between exhaust cavity and reference air cavity $U \approx 450$ mV) by imposing voltage on the oxygen pump electrodes. Under lean conditions oxygen is removed, under rich conditions oxygen ions are provided by water and carbon dioxide dissociation at the outer electrodes. Since the oxygen pump current is proportional to the oxygen abundance/deficiency an unambiguous good resolution sensor reading I_p is provided over a wide operating range ($0.7 < \lambda < 4$) [177]. This allows continuous control of – even non-stoichiometric – air to fuel ratios (see chapter 7).

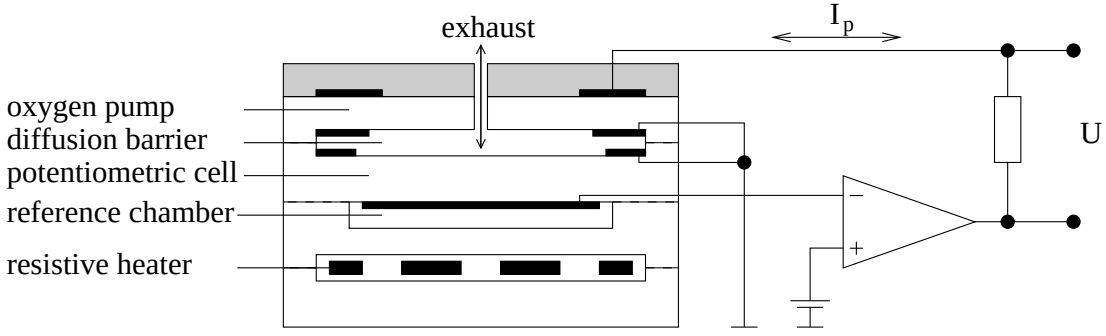

Figure D.2: Sketch of a planar universal exhaust gas oxygen sensor [177].

Due to different diffusive mobilities of the exhaust gas species the air to fuel ratio within the exhaust cavity however does not necessarily represent the gas bulk composition. Lambda readings of a universal exhaust gas oxygen sensor (UEGO) located downstream of a three-way catalyst have been reported to deviate significantly from their respective true values under rich conditions to either the lean side [82] or the rich side [44].

Since the characteristic of each sensor is somewhat specific the combination of wide range lambda sensor (Bosch LSU 4.7) and measuring device (Etas LA3) can be calibrated [87]. Steady state UEGO readings obtained from an oxygen sensor used in this work after calibration with a stoichiometric and lean gas mixture (mixtures A and B in table D.1) is listed in the table as well. If the the same leanness $\lambda = 1.03$ is maintained by replacing oxygen with nitrogen monoxide (mixture C) the sensor returns a perfect reading. Under rich conditions however the sensor reading very much depends on the mixture composition: CO and C_3H_y give a much weaker signal at equivalent air to fuel ratios as H_2 due to their smaller diffusivities.

	H_2	CO	NO	O_2	C_3H_6	C_3H_8	SO_2	λ	λ_{meas}	I_p^{rel}
	vol%	vol%	vol%	vol%	vol%	vol%	vol%	-	-	%
A*	0	0	0	0	0	0	0	1.00	1.000	-
B*	0	0	0	0.575	0	0	0	1.03	1.031	103
C	0	0	1.150	0	0	0	0	1.03	1.031	103
D	0	1.20	0	0	0	0	0	0.97	0.981	63
E	1.20	0	0	0	0	0	0	0.97	0.928	240
F	0.30	0.90	0	0	0	0	0	0.97	0.967	110
G	0	0	0	0	0	0.121	0	0.97	0.988	40
H	0	0	0	0	0.135	0	0	0.97	0.988	40
I	0.38	1.14	0.105	0.577	0.050	0.050	0.0014	0.97	0.969	103
J	0.38	1.14	0.105	1.164	0.050	0.050	0.0014	1.00	0.998	-
K	0.38	1.14	0.105	1.750	0.050	0.050	0.0014	1.03	1.030	100

Table D.1: Exhaust gas mixture concentrations applied to check for Bosch Lambda Sensor type LSU 4.2 sensitivity towards different gas species (all mixtures contain nitrogen, 11 % H_2O and 12 % CO_2) along with measured values (λ_{meas}) and relative sensor signal readings calculated from $I_p^{rel} = (\lambda_{meas} - 1)/(\lambda - 1)$. The compositions I and K are close to those applied for oxygen storage measurements (table 6.1).
$\star$: Mixtures applied for initial calibration.

In the exhaust cavity all λ-relevant exhaust species are fully oxidized by the oxygen contained in the exhaust and the oxygen provided or removed by the oxygen pump electrodes. Hence the oxidizable species concentration and the concentration of oxygen can be assumed to be zero. This allows to calculate the species flux into the exhaust cavity assuming binary diffusion in the diffusion barrier (diffusion coefficients see appendix I.4). According to Faraday's law the electrochemical current of the oxygen pump is proportional to the oxygen ion flux which can be calculated from the stoichiometry of the combustible component fluxes. This leads to the equation for the electrical sensor current [82]:

$$\begin{aligned} I_p &= \frac{4 F A_{db} p}{R T L_{db}} (-0.5 D_{H_2} y_{H_2} - 0.5 D_{CO} y_{CO} + 0.5 D_{NO} y_{NO} + \\ &+ D_{O_2} y_{O_2} - 4.5 D_{C_3H_6} y_{C_3H_6} - 5 D_{C_3H_8} y_{C_3H_8}) \end{aligned} \tag{D.2}$$

The sensor's signal sensitivity towards different exhaust species can be thus be approx-

imated with the binary diffusion coefficients in an inert carrier gas given in table I.4:

$$\frac{\frac{\partial I_\mathrm{p}}{\partial y_{\mathrm{H_2}}}}{\frac{\partial I_\mathrm{p}}{\partial y_{\mathrm{CO}}}} = \frac{0.5\,D_{\mathrm{H_2}}}{0.5\,D_{\mathrm{CO}}} = \frac{0.5\cdot 7.61}{0.5\cdot 2.05} = 3.7$$

$$\text{or} \quad \frac{\frac{\partial I_\mathrm{p}}{\partial y_{\mathrm{H_2}}}}{\frac{\partial I_\mathrm{p}}{\partial y_{\mathrm{C_3H_6}}}} = \frac{0.5\,D_{\mathrm{H_2}}}{4.5\,D_{\mathrm{C_3H_6}}} = \frac{0.5\cdot 7.61}{4.5\cdot 1.21} = 0.70$$

The validity of such an approximation is checked by comparison with the true λ-values calculated from the compositions of table D.1, using equation 2.14 with $x = 1.85$ and $y_{\mathrm{O_2,air}} = 0.2093$. The measured air to fuel ratio readings are given in table D.1 as λ_{meas}. Composition D shows that for 1.2 % of carbon monoxide the relative signal $I_\mathrm{p}^{\mathrm{rel}} = (\lambda_{\mathrm{meas}} - 1)/(\lambda - 1)$ equals 63 %. The respective signal for 1.2 % hydrogen is 240 %.

Hence the sensor signals' sensitivity based upon measured values is:

$$\frac{\frac{\partial I_\mathrm{p}}{\partial y_{\mathrm{H_2}}}}{\frac{\partial I_\mathrm{p}}{\partial y_{\mathrm{CO}}}} = \frac{\frac{240}{1.2}}{\frac{63}{1.2}} = 3.8$$

$$\text{similarly} \quad \frac{\frac{\partial I_\mathrm{p}}{\partial y_{\mathrm{H_2}}}}{\frac{\partial I_\mathrm{p}}{\partial y_{\mathrm{C_3H_6}}}} = \frac{\frac{240}{1.2}}{\frac{40}{0.135}} = 0.69$$

The measured sensitivities are therefore sufficiently close to the ones predicted by equation D.2.

Oxygen Sensor Signal Correction The determination of oxygen storage capacity by rich/lean step experiments described in chapter 6 requires a precise measurement of the difference between the λ-signals obtained before and behind the catalyst. In steady state (when the oxygen storage is either saturated or depleted) this difference should be zero. As can be seen from figure D.3 the actual readings may show substantial differences. They are caused by differences in combustibles concentrations before and behind the catalyst due to catalytic reactions, as explained above.

To compensate for these differences, a simplified correction procedure is applied. It is based upon the fact that the deviations between the two λ-sensor readings under lean conditions, δ_l and under rich conditions δ_r should be zero. Such a simple correction however could result in different storage capacities for rich to lean and the respective

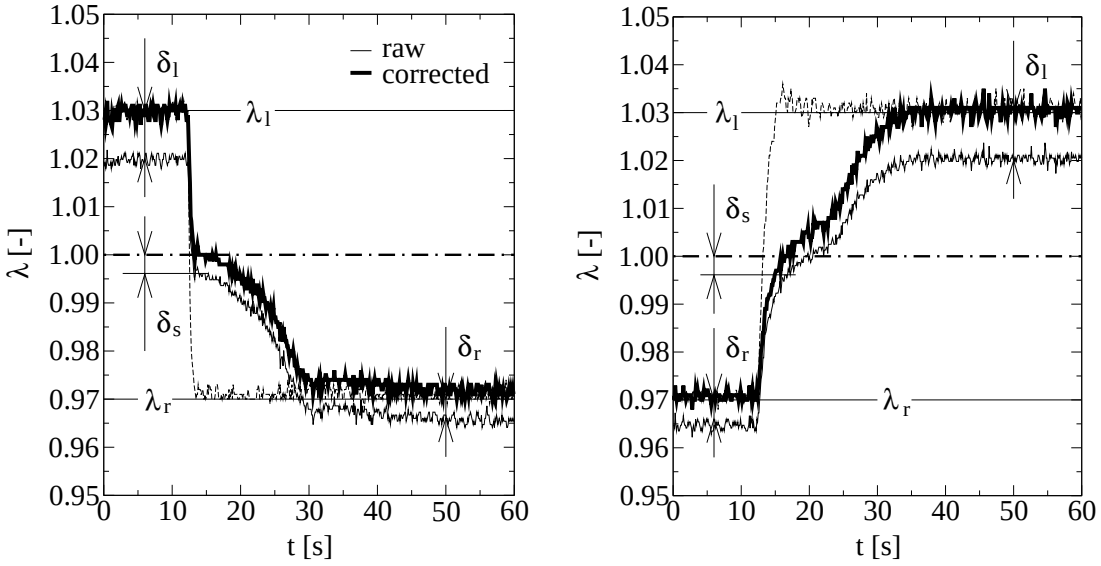

Figure D.3: Post catalyst UEGO sensor (here Bosch type LSU 4.2) signal correction during rich (λ_r)/lean (λ_l) switch experiments with a fresh catalyst at 700 °C: dashed line: λ-reference signal of sensor mounted in front of catalyst; thin solid line: λ-signal measured downstream of catalyst; thick solid line: corrected λ-signal downstream of catalyst; δ_l: lean bias, δ_r: rich bias, δ_s: stoichiometric bias.

lean to rich back switch. A third correction parameter, δ_s is therefore introduced which corrects the post catalyst λ-reading with respect to the value λ=1. This results in the following correction procedure (equations D.3 and D.4):

$$\lambda_{raw}(t) < (1+\delta_s) : \lambda_{cor}(t) = 1 + \frac{\lambda_r - 1}{(\lambda_r + \delta_r) - (1+\delta_s)} (\lambda_{raw}(t) - (1+\delta_s)) \quad \text{(D.3)}$$

$$\lambda_{raw}(t) \geq (1+\delta_s) : \lambda_{cor}(t) = 1 + \frac{\lambda_l - 1}{(\lambda_l + \delta_l) - (1+\delta_s)} (\lambda_{raw}(t) - (1+\delta_s)) \quad \text{(D.4)}$$

In a first step, δ_s is assumed to be zero. Next the OSCC (see chapter 6) is calculated for both transitions. If the system has reached cyclic steady state the amount of oxygen stored upon rich to lean transition has to be the same as the amount of oxygen released in the subsequent lean to rich transition. If the calculated OSCC values do not fulfill this condition the stoichiometric signal deviation δ_s is adjusted until they do. It turns out that this method of UEGO signal correction provides reasonable lambda progressions (e.g. no significant oxygen release above stoichiometry) under the conditions studied in this work. However the linear interpolation described above assumes the ratio of exhaust species with high and low diffusion coefficients (e.g. y_{H_2}/y_{CO}) to be fixed to either a rich side or a lean side value, which is not necessarily an appropriate assumption as further discussed in chapter 7. The same logic has been applied by a different group to calculate the post-catalyst air to fuel ratio from standard engine test bench exhaust emission measurement equipment (no hydrogen sensor): well after the ceria reduction process is over the corresponding hydrogen concentration is calculated

such that the calculated air to fuel ratio equals the rich feed fuel ratio. Now the resulting hydrogen to carbon monoxide ratio is assumed to be fixed over the entire rich phase and the time resolved hydrogen concentrations are calculated from the carbon monoxide concentrations. With this information the time resolved air to fuel ratio response downstream of the catalyst is calculated [157]. Again with information provided in chapter 8 this procedure seems to be inaccurate.

Appendix E

Oxygen Storage Capacity Calculation

According to section 2.1, λ represents the ratio of air provided for fuel combustion to the amount of air necessary for stoichiometric combustion. The respective oxygen mass flux for stoichiometric fuel combustion is represented by $\dot{m}_{O_2}^{+,s}$. The catalyst volume (V_{cat}) based oxygen storage capacity Ω [kg O_2/m^3 cat] can be calculated from the relative air to fuel ratio upstream and downstream of an oxygen storing/releasing catalyst:

$$\Omega = \frac{\dot{m}_{O_2}^{+,s}}{V_{cat}} \int_{t_1}^{t_2} (\lambda_{up} - \lambda_{down})\, dt = \frac{\dot{N}_{O_2}^{+,s} MW_{O_2}}{V_{cat}} \int_{t_1}^{t_2} (\lambda_{up} - \lambda_{down})\, dt \tag{E.1}$$

Upon ideal stoichiometric combustion the amount of oxygen consumed is related to the amount of exhaust, which is made up from carbon dioxide and water (both combustion products) and inert nitrogen passed through the engine (see reaction 2.1).

$$\frac{\dot{N}_{O_2}^{+,s}}{\dot{N}_{exh}^{s}} = \frac{\dot{N}_{O_2}^{+,s}}{\dot{N}_{CO_2}^{s} + \dot{N}_{H_2O}^{s} + \dot{N}_{N_2}^{+}} = \frac{\left(1 + \frac{x}{4}\right)}{1 + \frac{x}{2} + \left(1 + \frac{x}{4}\right) \frac{1 - y_{O_2,air}}{y_{O_2,air}}} \tag{E.2}$$

The molar exhaust flux can be calculated from the volumetric exhaust flux at standard conditions (ideal gas) or the space velocity $SV = \dot{V}_{exh}/V_{cat}$:

$$\dot{N}_{exh} = \frac{p^0}{R\, T^0} \dot{V}_{exh} = \frac{p^0}{R\, T^0} SV \cdot V_{cat} \tag{E.3}$$

Equations E.2 and E.3 in E.1 give:

$$\Omega = \frac{p^0 MW_{O_2}}{R\, T^0} \frac{1 + x/4}{1 + \frac{x}{2} + \frac{1 + x/4}{y_{O_2,air}} (1 - y_{O_2,air})} SV \int_{t_1}^{t_2} (\lambda_{up} - \lambda_{down})\, dt \tag{E.4}$$

Appendix F

Converter - Additional Data

Modeling of the transient thermal behavior is based on solid phase properties such as density, heat capacity and thermal conductivity. The solid phase is made up from the substrate and at least one layer of catalytic washcoat. Reliable geometric and thermal property data are believed to be crucial for a sound description of the three-way catalyst. Automotive three-way catalysts' washcoat densities reported in literature range from $\rho_s = 1000$ kg/m^3 [98, 85] to 2160 kg/m^3 [147] which is not that surprising due to most likely different washcoat formulations. Representative solid phase densities are reported to have values between $\rho_{subs} = 2280$ [173] and 2500 kg/m^3 [123, 107, 3] – significant higher than solid phase densities derived below. However the higher specific masses might be somehow compensated by washcoat thicknesses that are considered to range from $s_{wc} = 0.018$ [89] to 0.039 mm [70] with 0.025 mm being most popular [147, 107, 85] – clearly lower than the thicknesses measured in this work (table F.2).

For two different series production catalytic converters the attempt of gaining a consistent set of solid phase geometric and thermal property data based on weighing, microscopic images and pure substances property data is outlined in section F.1 and F.2.

F.1 Bare Substrate

Ceramic honeycomb substrates with square cell shapes are investigated in this work (table 3.1, figure F.4). The total geometric surface area of the bare substrate is

$$A_{geo,subs} = N\,4\,(h-s)\,L \tag{F.1}$$

$$\text{its volume} \quad V = \frac{\pi D^2}{4} L \tag{F.2}$$

$$\text{the specific surface area} \quad a_{geo,subs} = \frac{A_{geo,subs}}{V} \tag{F.3}$$

$$\text{and the void fraction of the bare substrate} \quad \varepsilon_{subs} = \frac{(h-s)^2}{h^2} \tag{F.4}$$

Corning specifies the porosity of 400 cpsi/8 mil monoliths as $\gamma_{\text{subs}} = 31\,\%$ and the porosity of the 600 cpsi/4.3 mil products as $\gamma_{\text{subs}} = 34\,\%$. Thus the substrate density ρ_{subs} and the overall substrate loading ψ_{subs} can be calculated with the density of dense cordierite of $\rho_{\text{cordierite}} = 2508\,\text{kg/m}^3$ [142]:

$$\rho_{\text{subs}} = (1-\gamma_{\text{subs}})\,\rho_{\text{cordierite}} \tag{F.5}$$

and

$$\psi_{\text{subs}} = (1-\varepsilon_{\text{subs}})\,\rho_{\text{subs}} \tag{F.6}$$

These densities along with other geometric data of the bare substrates are summarized in table F.2.

F.2 Coated Substrate

Void Fraction Due to the coating process the washcoat thickness may vary along the channel axis as can be seen from figures F.1 and F.2.

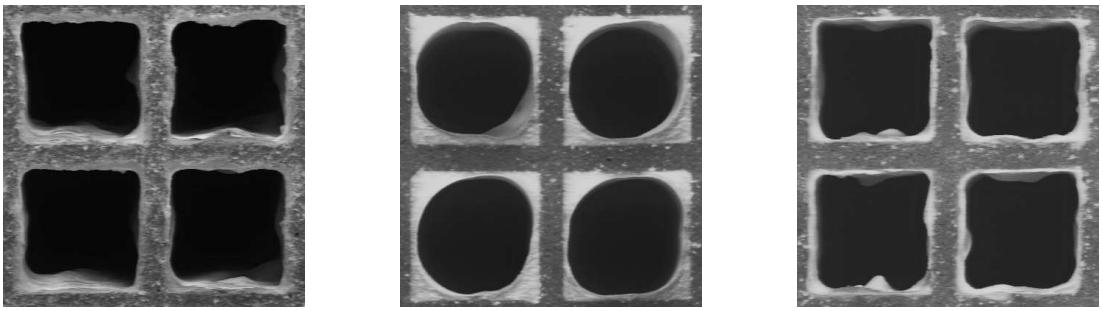

Figure F.1: Low resolution REM images of four neighboring monolith channels: entrance, center, exit (converter B).

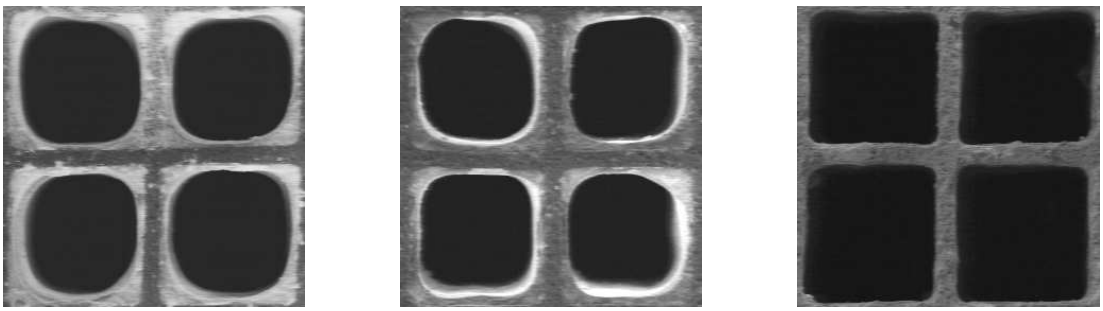

Figure F.2: Low resolution REM images of four neighboring monolith channels: entrance, center, exit (converter A).

Converter B's void fraction decreases within some 10 mm from approximately 60 % to less than 50 % (figure F.3). The average void fraction is 48 %. At both ends the cross-section of the gas channels is square shaped, whereas it tends to be circle shaped within the brick.

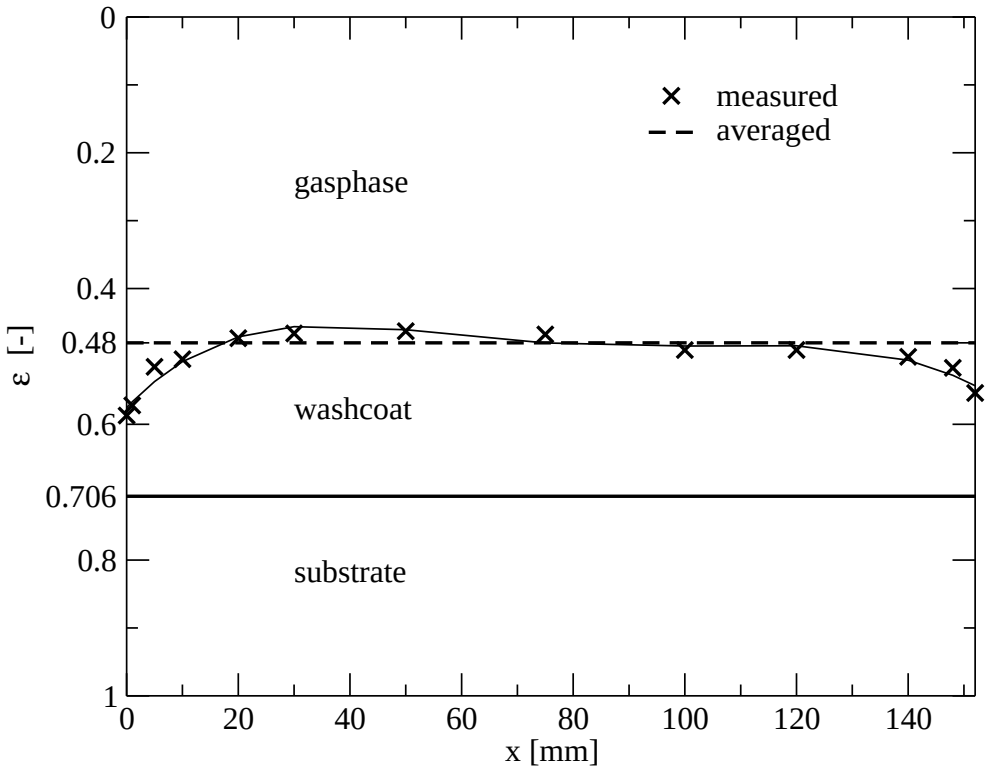

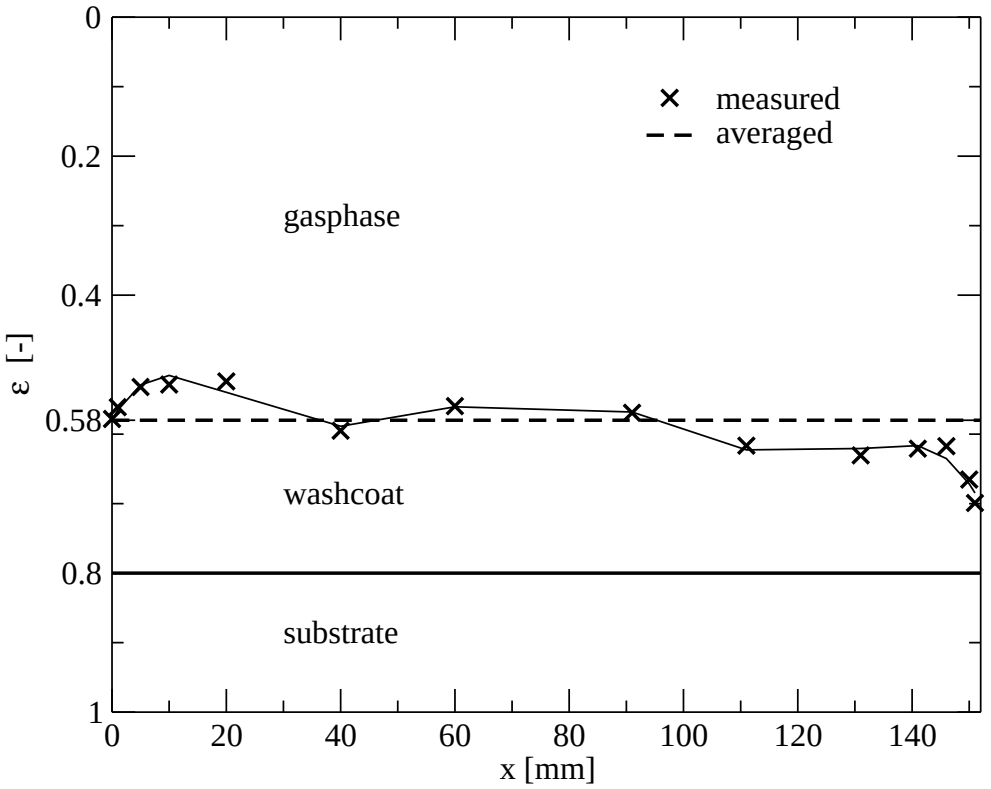

Figure F.3: Axial profile of void fraction after washcoating - converter B (top) and converter A (bottom).

Converter A's profile of washcoat thickness is less uniform (figures F.3). At one end the void fraction is again well above – at the other end below the average value of 58 %. Washcoat accumulation with the substrate's corners is not as pronounced as with the 400 cpsi substrate.

Washcoat Thickness For the sake of simplicity the gas channel cross section can be considered as square or circle shaped (figure F.4). Based on the averaged measured void fractions and information provided by the manufacturer (table 3.1, F.2) the washcoat thickness and specific geometric surface area are calculated for the respective cross section assumed.

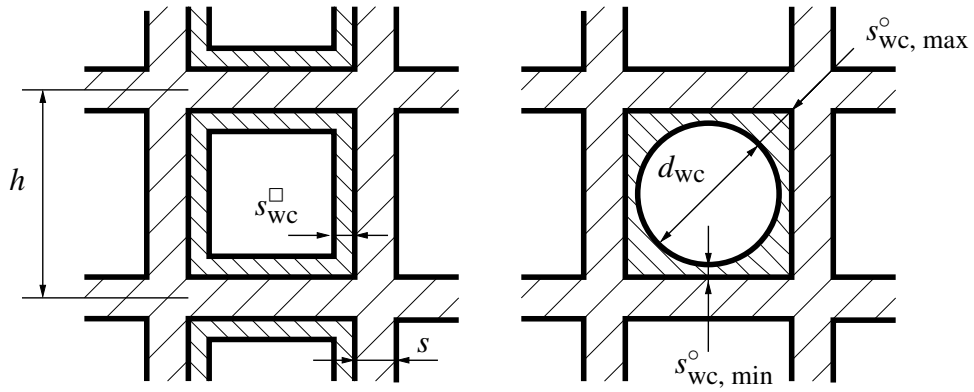

Figure F.4: Sketch of simplified gas channel shapes: square and circle

In case of square shaped averaged cross section the washcoat thickness and specific surface area can be calculated from:

$$\varepsilon = \frac{(h - s - 2\,s^{\square}_{wc})^2}{h^2}$$

$$\text{or} \quad s^{\square}_{wc} = \frac{h\,(1-\sqrt{\varepsilon}) - s}{2} \tag{F.7}$$

$$a^{\square}_{geo} = \frac{4\,(h - s - 2\,s^{\square}_{wc})}{h^2} \tag{F.8}$$

If the averaged cross section is assumed to be circle shaped the washcoat thickness varies between a maximum value (washcoat deposited in the substrate's corners) and a minimum value:

$$\varepsilon = \frac{\pi\, d^2_{wc}}{4\,h^2}$$

$$\text{or} \quad d_{wc} = 2\,h\sqrt{\frac{\varepsilon}{\pi}} \tag{F.9}$$

$$\text{and} \quad s^{\circ}_{wc,min} = \frac{h - s - d_{wc}}{2} \tag{F.10}$$

$$s^{\circ}_{\mathrm{wc,max}} = \frac{\sqrt{2}\,(h-s) - d_{\mathrm{wc}}}{2} \tag{F.11}$$

$$a^{\circ}_{\mathrm{geo}} = \frac{\pi\, d_{\mathrm{wc}}}{h^2} \tag{F.12}$$

Washcoat Density In order to obtain a consistent set of parameters for the catalytic converter the washcoat density is calculated based on data described above and measured weights of representative samples. Sizes and weights of these samples are listed in table F.1.

		converter A	converter B	
h_{smp}	mm	50.8	53.7	
N_{smp}	-	2500	1600	
m_{smp}	g	85.2	111.4	
$m_{\mathrm{smp,subs}}$	g	46.2	72.5	eqn. F.14
$m_{\mathrm{smp,wc}}$	g	38.9	38.4	eqn. F.13
$m_{\mathrm{smp,pm}}$	g	0.49	0.49	eqn. F.15

Table F.1: Sizes and weights of representative converter samples.

The sample's washcoat weight $m_{\mathrm{smp,wc}}$ can now be calculated from the total weight $m_{\mathrm{smp,tot}}$, the substrate weight $m_{\mathrm{smp,subs}}$ and the precious metal mass deposited on the sample $m_{\mathrm{smp,pm}}$:

$$m_{\mathrm{smp,wc}} = m_{\mathrm{smp,tot}} - m_{\mathrm{smp,subs}} - m_{\mathrm{smp,pm}} \tag{F.13}$$

$$\text{with} \quad m_{\mathrm{smp,subs}} = h_{\mathrm{smp}} \left[N_{\mathrm{smp}} h^2 (1-\varepsilon_{\mathrm{subs}}) + \right.$$
$$\left. +2\sqrt{N_{\mathrm{smp}}}\, h\, s \right] (1-\gamma_{\mathrm{subs}}) \rho_{\mathrm{cordierite}} \tag{F.14}$$

$$\text{and} \quad m_{\mathrm{smp,pm}} = \psi_{\mathrm{pm}} N_{\mathrm{smp}} h^2 h_{\mathrm{smp}} \tag{F.15}$$

The overall washcoat loading can thus be calculated based on the specified substrate data from:

$$\psi_{\mathrm{wc}} = \frac{m_{\mathrm{smp,wc}}}{N_{\mathrm{smp}} h^2 h_{\mathrm{smp}}} \tag{F.16}$$

Thus the porous washcoat's density is

$$\rho_{\mathrm{wc}} = \frac{\psi_{\mathrm{wc}}}{\varepsilon_{\mathrm{subs}} - \varepsilon} \tag{F.17}$$

Calculated washcoat densities $\rho_{\mathrm{wc}} \approx 1250$ kg/m^3 (table F.2) agree with certain literature values of $\rho_{\mathrm{wc}} = 1300$ kg/m^3 [124, 18].

Solid Phase Properties Since the coated monolith is treated in the energy balance of the mathematical model described in chapter 4 as a seeming continuum, representative solid densities ρ_{s}, heat capacities $c_{p,\mathrm{s}}$ and thermal conductivities λ_{s} have to be derived.

Obviously the solid density can be calculated from the washcoat and the substrate density and their respective occupied frontal area fractions:

$$\rho_{\mathrm{s}} = \frac{f_{\mathrm{sub}}\,\rho_{\mathrm{subs}} + f_{\mathrm{wc}}\,\rho_{\mathrm{wc}}}{f_{\mathrm{subs}} + f_{\mathrm{wc}}} \tag{F.18}$$

The representative solid phase heat capacity is calculated from:

$$c_{p,\mathrm{s}} = \frac{\psi_{\mathrm{subs}}}{\psi_{\mathrm{s}}}\,c_{p,\mathrm{subs}} + \frac{\psi_{\mathrm{wc}}}{\psi_{\mathrm{s}}}\,c_{p,\mathrm{wc}} \tag{F.19}$$

Again the washcoat is an inhomogeneous mixture of materials such as aluminum oxide, cerium-zirconium mixed oxides and additional materials. Considering aluminum, cerium and zirconium oxides to be the major constituents washcoated on a cordierite substrate the solid phase heat capacity equation reads:

$$\begin{aligned} c_{p,\mathrm{s}} &= \frac{\psi_{\mathrm{subs}}}{\psi_{\mathrm{s}}}\,c_{p,\mathrm{cordierite}} + \frac{\psi_{\mathrm{wc}}}{\psi_{\mathrm{s}}}\left[x_{\mathrm{CeO_2}}\,c_{p,\mathrm{CeO_2}} + \right. \\ &+ \left. x_{\mathrm{ZrO_2}}\,c_{p,\mathrm{ZrO_2}} + \left(1 - x_{\mathrm{CeO_2}} - x_{\mathrm{ZrO_2}}\right) c_{p,\mathrm{Al_2O_3}}\right] \end{aligned} \tag{F.20}$$

Table J.1 supplies the respective heat capacity correlations. Due to the lack of information about washcoat constituents and moreover quantitative composition the washcoat's cerium oxide mass fraction is assumed to be $x_{\mathrm{CeO_2}} = 0.3$ [96, 115, 166]. If only the heat capacity of cordierite would be chosen to represent the whole solid phase [123, 124, 147] the heat capacity would be somewhat overestimated (figure J.1). The same is believed to apply to temperature averaged values of $c_{p,\mathrm{s}} = 0.975 \ldots 1.1$ kJ/(kg K) [173, 98, 107, 85, 3] – at least under cold start conditions.

Since the dynamic converter behavior is reported to be rather insensitive towards minor changes of the substrate's thermal conductivity [124] a quite common value of $\lambda_{\mathrm{c,s}} = 1.675$ W/(m K) is adopted from literature [123, 140, 107, 3].

bare substrate		converter A	converter B	
s	mm	0.110	0.203	
$A_{\text{geo,subs}}$	m^2	5.787	4.436	eqn. F.1
$a_{\text{geo,subs}}$	m^2/m^3	3450	2645	eqn. F.3
$\varepsilon_{\text{subs}}$	-	0.800	0.706	eqn. F.4
f_{subs}	-	0.200	0.294	
γ_{subs}	-	0.34	0.31	
ρ_{subs}	kg/m^3	1655	1730	eqn. F.5
ψ_{subs}	kg/m^3	330	510	eqn. F.6
washcoat				
f_{wc}	-	0.22	0.226	
ρ_{wc}	kg/m^3	1286	1226	eqn. F.17
ψ_{wc}	kg/m^3	283	277	eqn. F.16
square shaped gas channels				
$s^{\square}_{\text{wc}}$	mm	**0.069**	0.093	eqn. F.7
circle shaped gas channels				
d_{wc}	mm	0.891	**0.993**	eqn. F.9
$s^{\circ}_{\text{wc,min}}$	mm	0.018	**0.037**	eqn. F.10
$s^{\circ}_{\text{wc,max}}$	mm	0.211	**0.258**	eqn. F.11
coated substrate				
h	mm	1.04	1.27	
N		10230	6820	
V	l	1.677	1.677	eqn. F.2
ε	-	0.58	0.48	
ρ_{s}	kg/m^3	1460	1510	eqn. F.18
ψ_{s}	kg/m^3	613	787	
$\lambda_{\text{c,s}}$	W/(m K)	1.675	1.675	[123, 140, 107, 101, 3]
$c_{p,\text{s}}(T)$	kJ/(kg K)	$\rightarrow$	$\rightarrow$	eqn. F.20
square shaped gas channels				
$a^{\square}_{\text{geo}}$	m^2/m^3	**2938**	2184	eqn. F.8
circle shaped gas channels				
a°_{geo}	m^2/m^3	2603	**1934**	eqn. F.12

Table F.2: Summary of geometric and thermal three-way catalytic converter property data. Bold values mark the ones chosen if data depend on geometric assumption – such as square or circle shape gas passage.

Appendix G

Heats of Formation, Entropies and Gibbs Enthalpies of Reaction

	a_j [J/mol]	b_j [J/(mol K)]	temperature range [K]
Pd + 0.5 O_2 ⇌ PdO	$-114.1\,10^3$	99.9	298 . . . 1143
2 Rh + 1.5 O_2 ⇌ Rh_2O_3	$-377.0\,10^3$	266.0	298 . . . 1273

Table G.1: Gibbs enthalpies of palladium and rhodium oxide formation reactions at 1 atm to be calculated from $\Delta g_{\mathrm{R},i}^{0,T} = a_j + b_j T\,[\mathrm{K}]$, [102].

	a_j [J/mol]	b_j [J/(mol K)]	temperature range [K]
Pd + H_2S ⇌ PdS + H_2	-42.6 10^3	40.5	298 . . . 1825
2 Rh + 3 H_2S ⇌ Rh_2S_3 + 3 H_2	-182.4 10^3	118.6	298 . . . 2000

Table G.2: Gibbs enthalpies of palladium and rhodium sulfide formation reactions at 1 atm to be calculated from $\Delta g_{\mathrm{R},i}^{0,T} = a_j + b_j T + c_j T^2$, $[T]$ = K, [5].

	a_j [J/mol]	b_j [J/(mol K)]	temperature range [K]
0.5 κ-$Ce_2Zr_2O_7$ + 0.25 O_2 $\rightleftharpoons$ $CeZrO_2$	$-114.5\,10^3$	60.05	873 ... 1073
0.5 t-$Ce_2Zr_2O_7$ + 0.25 O_2 $\rightleftharpoons$ $CeZrO_2$	$-136.8\,10^3$	62.52	873 ... 1073

Table G.3: Gibbs enthalpies of metastable tetragonal (t-) and cubic (κ-) phase $CeZrO_4$ formation from oxygen deficient pyrochlore $Ce_2Zr_2O_7$ (according to the electrical charge transferred during coulometric titrations; data are based on pyrochlore with the composition $Ce_2Zr_2O_{7+x}$, x = 0.065) at 1 atm to be calculated from $\Delta G_i^{0,T} = a_j + b_j T$[K], [128].

	Δh_j^0 [kJ/mol]	s_j^0 [J/(mol K)]	data source
gaseous species			
H_2	0.0	130.7	[17]
H_2O(g)	-241.8	188.8	[17]
NO	90.3	210.8	[17]
CO	-110.5	197.7	[17]
N_2	0.0	191.6	[17]
O_2	0.0	205.1	[17]
H_2S	-20.5	205.8	[17]
C_3H_6	20.4	267.0	[17]
C_3H_8	-103.8	270.0	[17]
CO_2	-393.5	213.8	[17]
N_2O	82.1	220.0	[17]
NO_2	33.1	240.0	[17]
SO_2	-296.8	248.2	[17]
solid species			
C	1.9	93.1	[17]
Al_2O_3	-1675.7	51.0	[17]
$Al_2(SO_4)_3$	-3440.8	239.3	[17]
$CeO_{1.5}$	-899.9	74.1	[17]
$CeO_{1.72}$	-995.8	69.0	[144]
$CeO_{1.83}$	-1033.4	67.8	[144]
CeO_2	-1088.7	62.3	[17]
$Ce_2(SO_4)_3$	-3955.1	287.4	[17]

Table G.4: Heats of formation and entropies at standard conditions (1 atm, 298 K).

Appendix H

Heat and Mass Transfer

Both heat and mass transfer between the gas phase and the catalyst's solid phase are expressed in a linear driving force manner. Heat transfer coefficients α and mass transfer coefficients β_j are obtained from semi-empirical literature correlations.

The choice of a suitable correlation is based upon the system's geometry and the state of flow condition (laminar or turbulent) within the converter's channels.

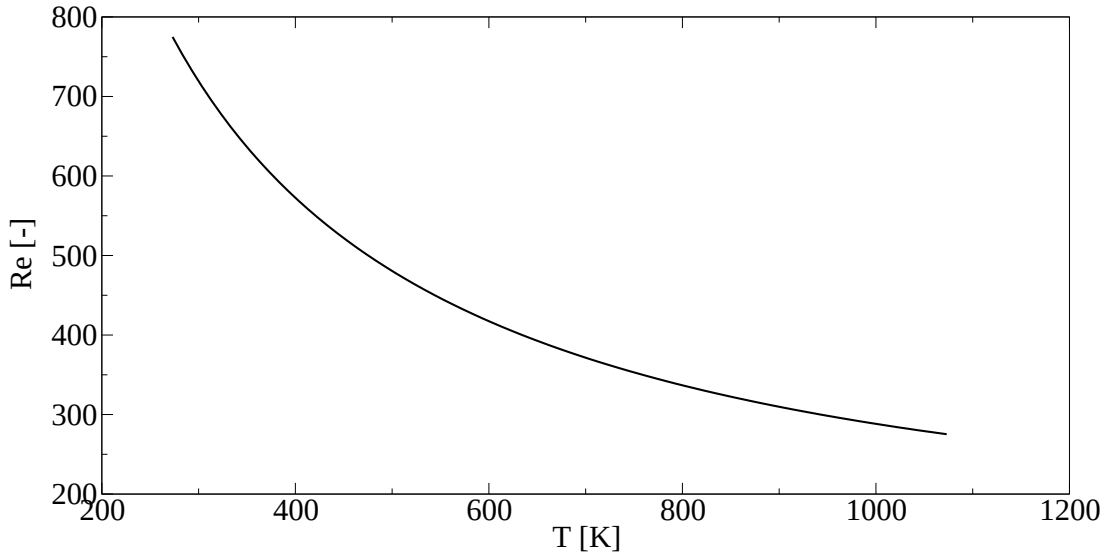

Figure H.1: Reynolds number change at $\dot{m}_{\text{exh}} = 230$ kg/h within a standard ceramic converter ($D = 4.66$ inch, 400 cpsi, $\varepsilon = 0.45$).

Due to the narrow channel diameters flow is even at relatively high exhaust mass flow rates within regular size catalytic converters well within the laminar regime (figure H.1). This is even more pronounced at higher temperatures due to increased sheer forces induced by higher viscosities (see section I.2).

H.1 Heat Transfer

A linear driving force approach is chosen to describe the heat transfer between the gas phase and the catalyst's solid phase due to forced convection (chapter 4).

A variety of correlations describe forced-convection heat transfer in terms of the dimensionless Nusselt number [134, 139]:

$$Nu = \frac{\alpha\, d_\mathrm{h}}{\lambda_\mathrm{c}}$$

The local Nusselt number at each position within a tube taking thermal and hydrodynamic boundary layer buildup into account is described by [47]:

$$\begin{aligned} & Nu &=& \left(Nu_1^3 + 0.7^3 + (Nu_2 - 0.7)^3 + Nu_3^3\right)^{1/3} \\ \text{with:} \quad & Nu_1 &=& 3.66 \\ & Nu_2 &=& 1.077\,(Re\,Pr\,d_\mathrm{h}/z)^{1/3} \\ & Nu_3 &=& \frac{1}{2}\left(\frac{2}{1+22\,Pr}\right)^{1/6}\sqrt{Re\,Pr\,d_\mathrm{h}/z} \end{aligned} \tag{H.1}$$

The asymptotic Nusselt number is in good agreement with the corresponding values reported in literature [107, 18, 101, 11]. Heat transfer is enhanced in the catalyst inlet and decreases within the catalyst:

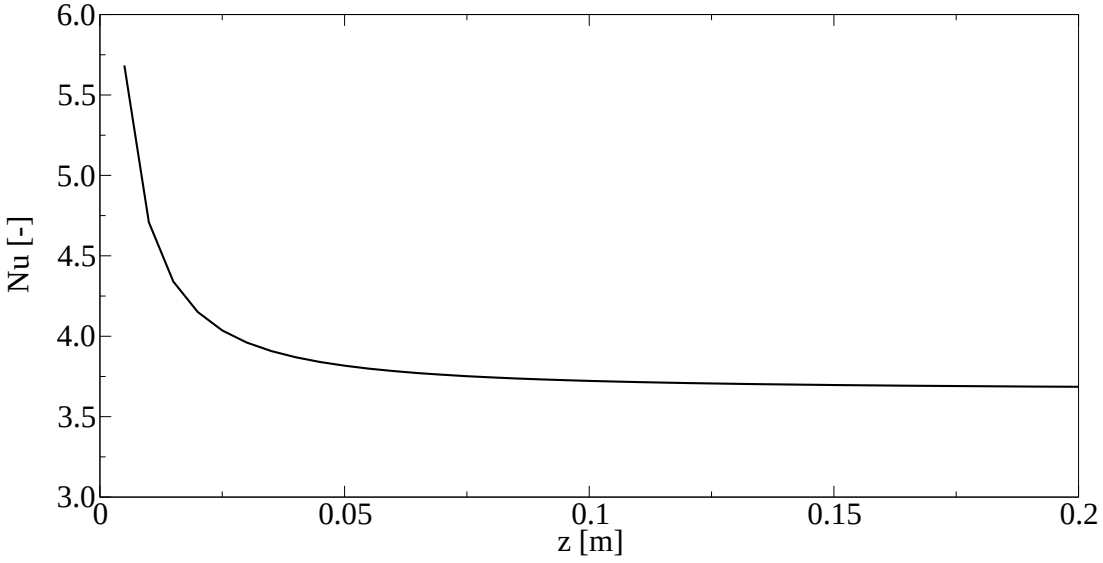

Figure H.2: Local Nusselt number along catalyst axis at $\dot{m}_\mathrm{exh} = 230$ kg/h, T = 25 °C within a standard ceramic converter ($D = 4.66$ inch, 400 cpsi, $\varepsilon = 0.45$).

Furthermore the heat transfer in the catalyst inlet decreases with increasing temperature at a fixed mass flow rate (figure H.3).

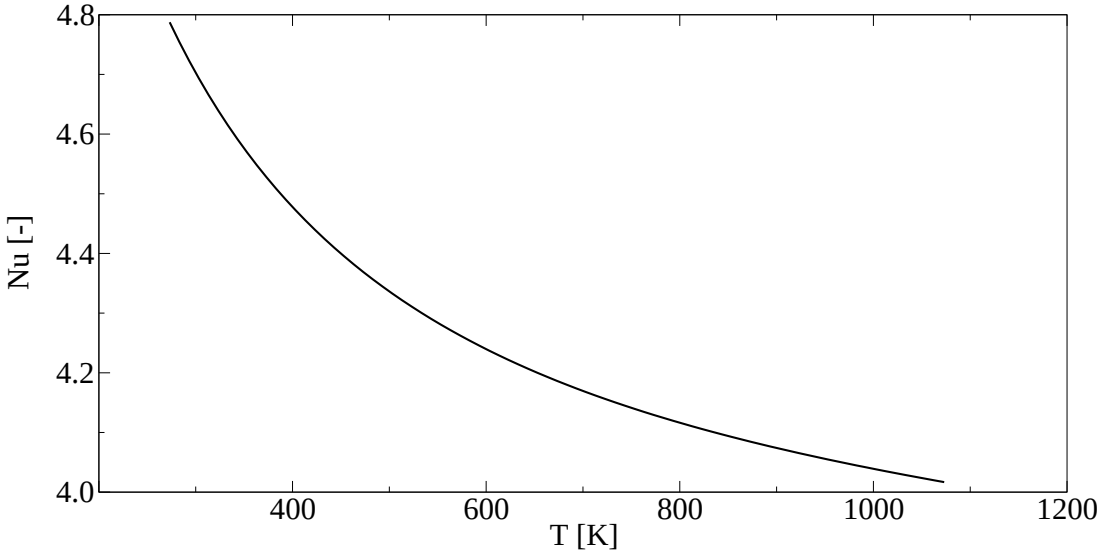

Figure H.3: Variation of local Nusselt number (z = 0.01 m) with temperature at $\dot{m}_{\text{exh}} = 230$ kg/h (y_{N_2} = 77 %, y_{CO_2} = 12 %, y_{H_2O} = 11 %) within a standard ceramic converter ($D = 4.66$ inch, 400 cpsi, $\varepsilon = 0.45$).

H.2 Mass Transfer

Again a linear driving force approach is applied for modeling of the mass transfer rate between the gas bulk phase and the catalytic surface (chapter 4).

The mass transfer coefficient is obtained by making use of the analogy between heat and mass transfer as recommended in literature [134]. Thus by replacing the Prandtl number (section I.5) with the respective species's Schmidt number the dimensionless Sherwood number

$$Sh = \frac{\beta_j d_{\text{h}}}{D_j}$$

is obtained from equation H.1:

$$\begin{aligned} Sh_j &= \left(Sh_1^3 + 0.7^3 + (Sh_{2,j} - 0.7)^3 + Sh_{3,j}^3\right)^{1/3} \\ Sh_1 &= 3.66 \\ Sh_{2,j} &= 1.077 \left(Re\, Sc_j\, d_h/z\right)^{1/3} \\ Sh_{3,j} &= \frac{1}{2}\left(\frac{2}{1+22\,Sc_j}\right)^{1/6} \sqrt{Re\, Sc_j\, d_h/z} \end{aligned} \tag{H.2}$$

The mass transfer coefficient β_j increases with increasing temperature (figure H.4). The mass transfer coefficient ratio of two species j and k is proportional to the ratio of the respective diffusivities (section I.4).

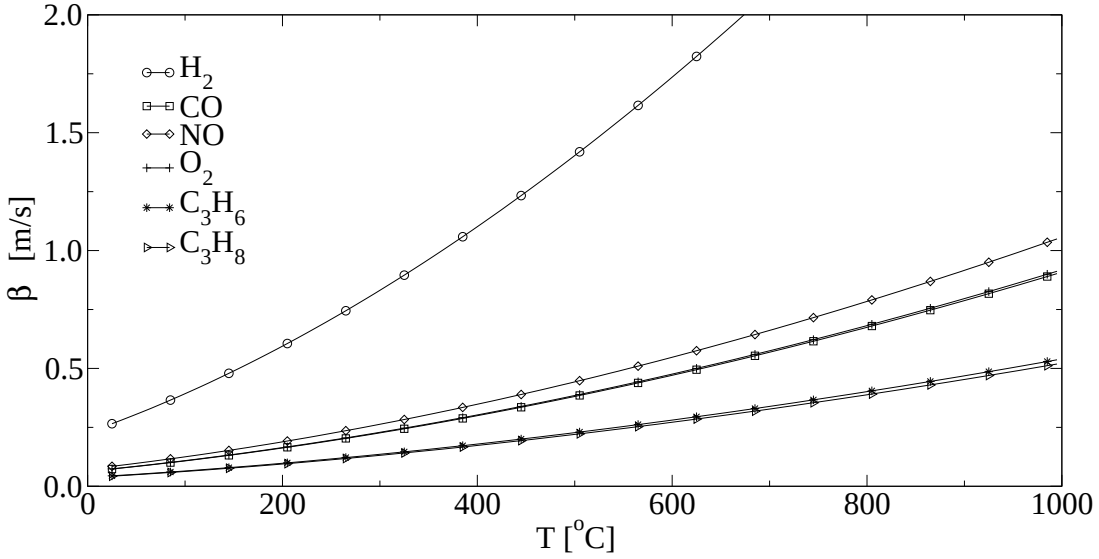

Figure H.4: Temperature dependence of the mass transfer coefficient β_j 5 mm within the catalytic converter (space velocity $SV = 17000\ \mathrm{h}^{-1}$ at $p = 1.2$ bar.)

At a fixed temperature the mass transfer coefficient drops down within a very short distance from the converter inlet to its stable value (figure H.5). Over the full range of reasonable space velocities the mass transfer coefficient at a fixed position and temperature does change very little (figure H.6). As the heat transfer coefficient it is virtually independent of the gas flow rate [123].

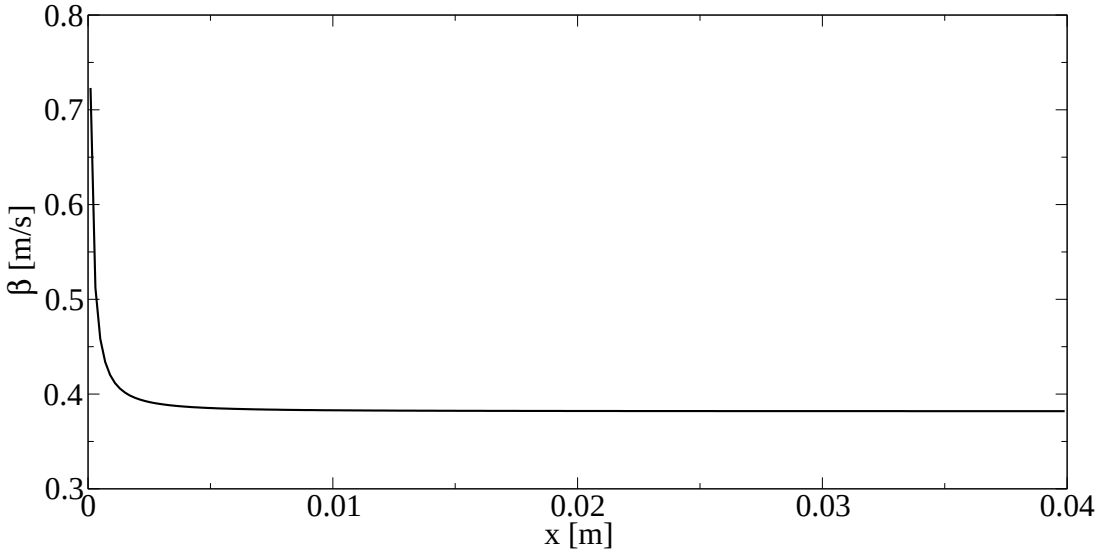

Figure H.5: Mass transfer coefficient β_{O_2} along the catalytic converter's axis (space velocity $SV = 17000$ h^{-1}, $p = 1.2$ bar and $T = 500\ ^{o}$C.)

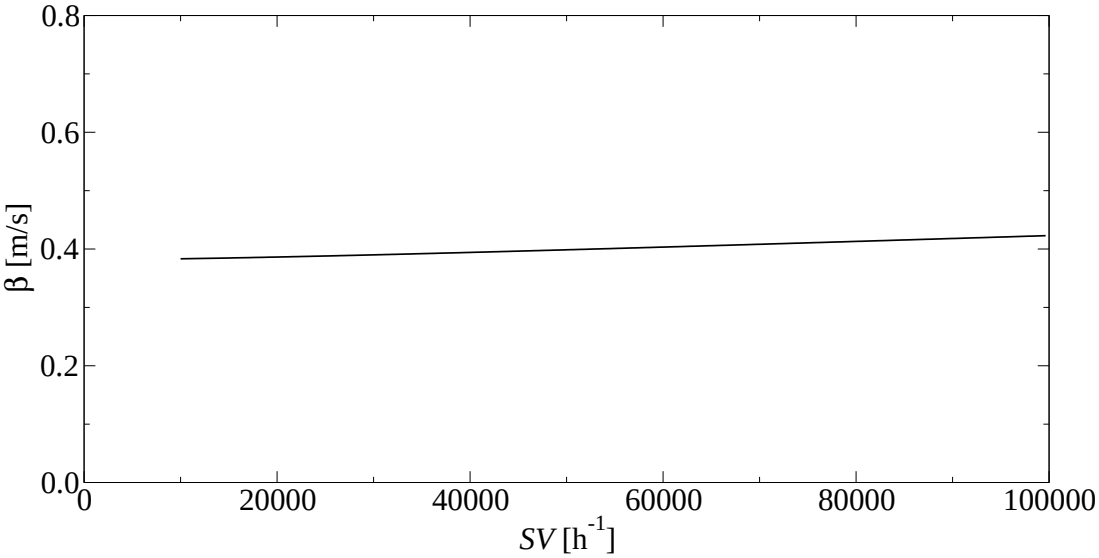

Figure H.6: Space velocity dependence of the mass transfer coefficient β_{O_2} 5 mm within the catalytic converter ($T = 500$ °C and $p = 1.2$ bar.)

Appendix I

Properties of Gases

Neglecting minor components, stoichiometric gasoline engine exhaust is basically made up from 77% N_2, 12% CO_2 and 11% H_2O (chapter 2). Since most correlations provide pure species data mixture properties need to be calculated from appropriate mixing formulas. The mixing formulas depend on the respective gas property [103].

Correlations applied in this work to describe the temperature (and pressure) dependent gas properties heat capacity, viscosity, thermal conductivity and diffusivity are discussed below. The relative error made when treating the exhaust as pure nitrogen flow instead of the mixture mentioned above is checked as well. All properties – except the dimensionless groups Prandtl and Schmidt number derived from these (sections I.5 and I.6) – exhibit a temperature dependence which can not be neglected.

I.1 Heat Capacity

Heat capacities of the exhaust constituents considered in this work are calculated from the correlation and its respective parameters listed in table I.1. Whereas just the heat capacities of the major exhaust components are used to calculate the exhaust gas heat capacity the remaining correlations are applied to calculate thermodynamic reaction equilibria in chapter 3.

Assuming that the stoichiometric exhaust is a mixture made up from the ideal gases nitrogen, carbon dioxide and water the exact mixing formula applies [103]:

$$c_{p,\mathrm{exh}} = \sum_{j=1}^{J} c_{p,j} \overset{\lambda=1}{=} 0.77\, c_{p,\mathrm{N_2}} + 0.12\, c_{p,\mathrm{CO_2}} + 0.11\, c_{p,\mathrm{H_2O}} \tag{I.1}$$

If the exhaust is considered as pure nitrogen the heat capacity is underestimated – most pronounced at higher temperatures (figure I.1).

	a	b	c	d	valid	data
	[J/(mol K)]	[J/(mol K^2)]	[(J K)/mol]	[J/(mol K^3)]	[K]	source
H_2	26.88	$3.59\,10^{-3}$	$0.11\,10^{6}$	-	298 ... 3000	[17]
$H_2O(g)$	34.38	$7.84\,10^{-3}$	$-0.42\,10^{6}$	-	298 ... 3000	[17]
NO	29.41	$3.85\,10^{-3}$	$-0.06\,10^{6}$	-	298 ... 2000	[17]
CO	30.95	$2.44\,10^{-3}$	$-0.28\,10^{6}$	-	298 ... 3000	[17]
N_2	30.42	$2.54\,10^{-3}$	$-0.24\,10^{6}$	-	298 ... 3000	[17]
O_2	29.15	$6.48\,10^{-3}$	$-0.18\,10^{6}$	-	298 ... 3200	[17]
H_2S	34.91	$10.69\,10^{-3}$	$-0.45\,10^{6}$	-	298 ... 2000	[17]
C_3H_6	25.85	$167.82\,10^{-3}$	$-0.68\,10^{6}$	$-48.66\,10^{-6}$	n.a.	[139]
C_3H_8	19.01	$224.48\,10^{-3}$	$-0.58\,10^{6}$	$-66.47\,10^{-6}$	298 ... 1000	[17]
CO_2	51.13	$4.37\,10^{-3}$	$-1.47\,10^{6}$	-	298 ... 3000	[17]
N_2O	38.10	$23.17\,10^{-3}$	$-0.55\,10^{6}$	$-6.16\,10^{-6}$	298 ... 2000	[17]
NO_2	34.53	$24.67\,10^{-3}$	$-0.42\,10^{6}$	$-6.87\,10^{-6}$	298 ... 3000	[17]
SO_2	49.94	$4.77\,10^{-3}$	$-1.05\,10^{6}$	-	298 ... 2000	[17]

Table I.1: Correlation $c_p = a + bT + cT^{-2} + dT^2$, $[T]$ = K, returns c_p in J/(mol K).

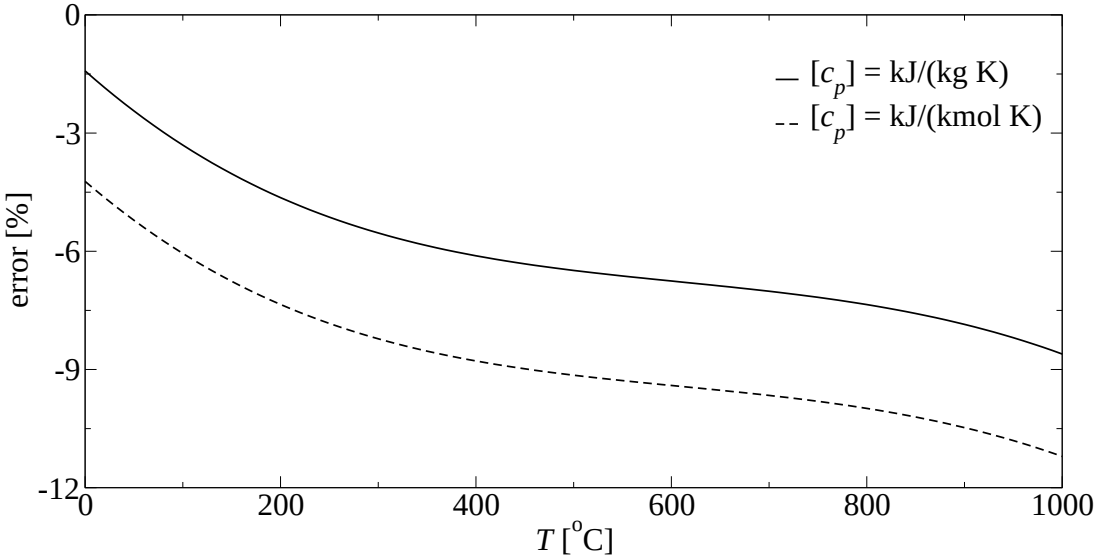

Figure I.1: Heat capacity error made if a mixture containing 77% N_2, 12% CO_2 and 11% H_2O is considered to consist of pure nitrogen.

I.2 Viscosity

The Lucas method of corresponding states [103] predicts the viscosity of polar and non polar gases at low pressure (equation I.2). Predicted values of e.g. CO_2 and N_2 match very well with tabulated values (figure I.2). Minor discrepancies exist however between predicted and tabulated values of the polar molecule water at higher temperatures.

$$
\begin{aligned}
\eta &= (\eta\,\xi)^{\mathrm{r}}\, f_{\mathrm{P}}\, f_{\mathrm{Q}}\, \frac{1}{\xi} \quad \text{with:} \qquad \text{(I.2)}\\
(\eta\,\xi)^{\mathrm{r}} &= 0.807\, T_{\mathrm{r}}^{0.618} - 0.357\, e^{-0.449\, T_{\mathrm{r}}} + 0.340\, e^{-4.058\, T_{\mathrm{r}}} + 0.018\\
\xi &= \frac{T_{\mathrm{c}}^{1/6}\, \mathrm{R}^{1/6}\, \mathrm{N_A}^{1/3}}{MW^{1/2}\, p_{\mathrm{c}}^{2/3}}\\
f_{\mathrm{P}} &= 1, \quad 0 \leq \mu_{\mathrm{r}} < 0.022\\
f_{\mathrm{P}} &= 1 + 30.55(0.292 - Z_{\mathrm{c}})^{1.72}, \quad 0.022 \leq \mu_{\mathrm{r}} < 0.075\\
f_{\mathrm{P}} &= 1 + 30.55(0.292 - Z_{\mathrm{c}})^{1.72}(0.96 + 0.1(T_r - 0.7)), \quad 0.075 \leq \mu_{\mathrm{r}}\\
\mu_{\mathrm{r}} &= \frac{\mu^2\, {p_{\mathrm{c}}}^2}{k\, T_{\mathrm{c}}}, \quad f_{\mathrm{Q}} = 1 \quad \text{all gases except He, } H_2 \text{ and } D_2.
\end{aligned}
$$

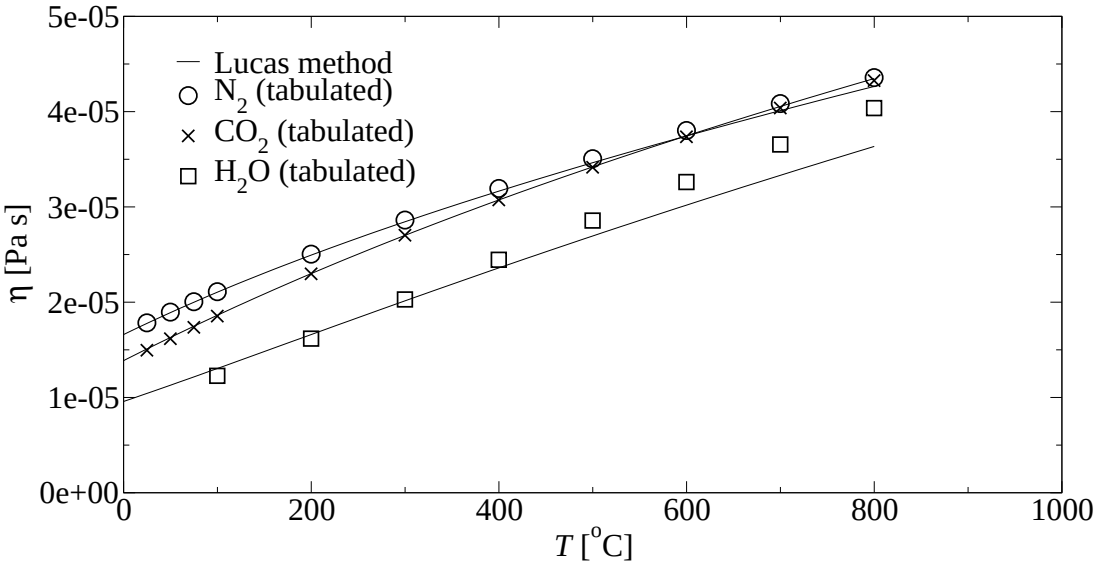

Figure I.2: Pure component viscosities using the Lucas method [139, 103] compared to tabulated values for pure nitrogen, carbon dioxide and water [100].

A fit of the tabulated pure component viscosities with the correlation and parameters listed in table I.2 should supply a sound description of the temperature dependent pure component viscosities.

In contrast to the heat capacity a mixture's viscosity is almost never a linear function of its composition. Moreover the mixture's viscosity can be greater than each of its

	a	b	c	$\eta(25\ ^\circ\mathrm{C})$	$\eta(500\ ^\circ\mathrm{C})$
				$10^{-6}\frac{\mathrm{kg}}{\mathrm{m\ s}}$	$10^{-6}\frac{\mathrm{kg}}{\mathrm{m\ s}}$
CO_2	-0.1924	0.05529	-1.39e-5	14.96	34.16
N_2	4.666	0.04796	-1.10e-5	17.83	35.06
H_2O_g	-3.546	0.04266	-1.542e-6	-	28.57

Table I.2: Dynamic Viscosities at ambient pressure: correlation $\eta_j = \mathrm{a} + \mathrm{b}\,T + \mathrm{c}\,T^2$, returns $[\eta] = 10^{-6}$Pa s with $[T]$ = K, validity range: 25 ... 800 °C - H_2O not below 100 °C [100].

constituents viscosities - a behavior frequently observed when polar and non polar gases are mixed within each other [139]. The Bromley and Wilke mixing formula I.3 is recommended at low pressure [139, 134]. The predicted exhaust viscosity matches quite well with the viscosity of pure nitrogen (figure I.3). In this work the correlation describing the temperature dependent viscosity of pure nitrogen (table I.2) is applied to calculate the exhaust viscosity.

$$\eta_{\mathrm{exh}} = \sum_{k=1}^{J} \frac{\eta_k}{1 + \sum_{k=1, j\neq k}^{J} \left(Q_{kj} \frac{x_j}{x_k} \right)}, \quad \text{with } Q_{kj} = \frac{\left[1 + \left(\frac{\eta_k}{\eta_j} \right)^{1/2} \left(\frac{MW_j}{MW_k} \right)^{1/4} \right]^2}{\sqrt{8} \left[1 + \frac{MW_k}{MW_j} \right]^{1/2}} \tag{I.3}$$

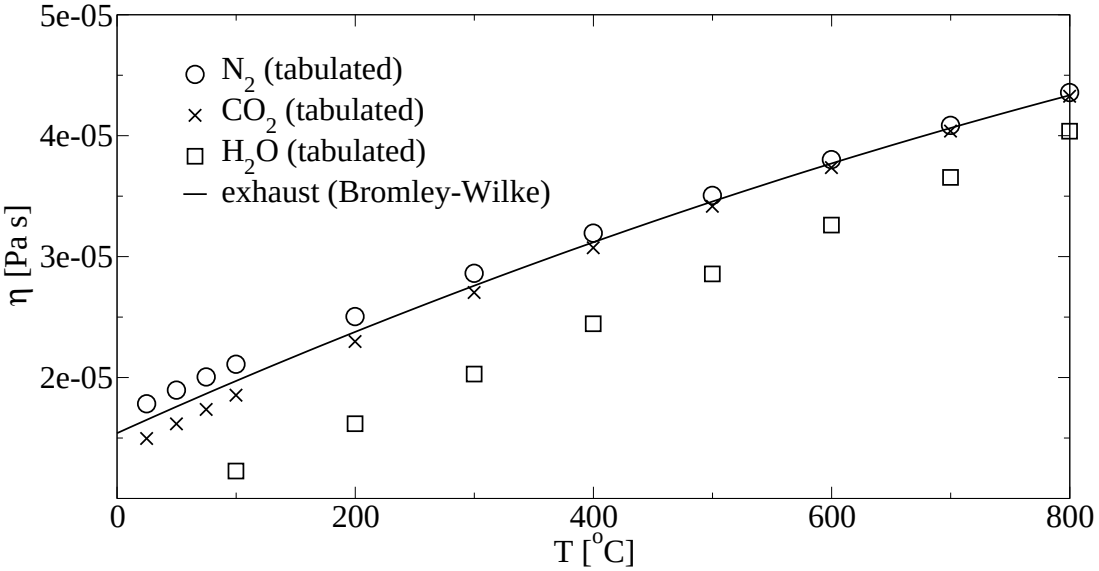

Figure I.3: Exhaust viscosity calculated from Bromley-Wilke mixing formula [134] compared to tabulated values for pure nitrogen, carbon dioxide and water [100].

I.3 Thermal Conductivity

Thermal conductivity correlations for the major exhaust constituents nitrogen, carbon dioxide and water are given in table I.3. In general the thermal conductivity of a gaseous mixture under low pressure is not a linear function of its composition [139].

	a	b	c	λ(25°C)	λ(500°C)
				10^{-3} W/(m K)	10^{-3} W/(m K)
CO_2	-10.02	0.09226	-1.358e-5	16.55	53.42
N_2	7.151	0.06557	-6.871e-6	25.94	53.68
H_2O_g	-1.94	0.05444	4.448e-5	-	66.97

Table I.3: Thermal conductivities of major pure exhaust constituents at ambient pressure: correlation $\lambda_c = a + b\,T + c\,T^2$, returns $[\lambda_c] = 10^{-3}$ W/(m K) with $[T]$ = K, validity range: 25 ... 800 °C - H_2O not below 100 °C [100].

The exhaust mixture's thermal conductivity can be calculated with the Mason-Saxena equation which is quite similar to equation I.3 [139]. It can be seen from figure I.4 that the exhaust mixture's thermal conductivity can again be approximated by pure nitrogen's thermal conductivity [123, 101].

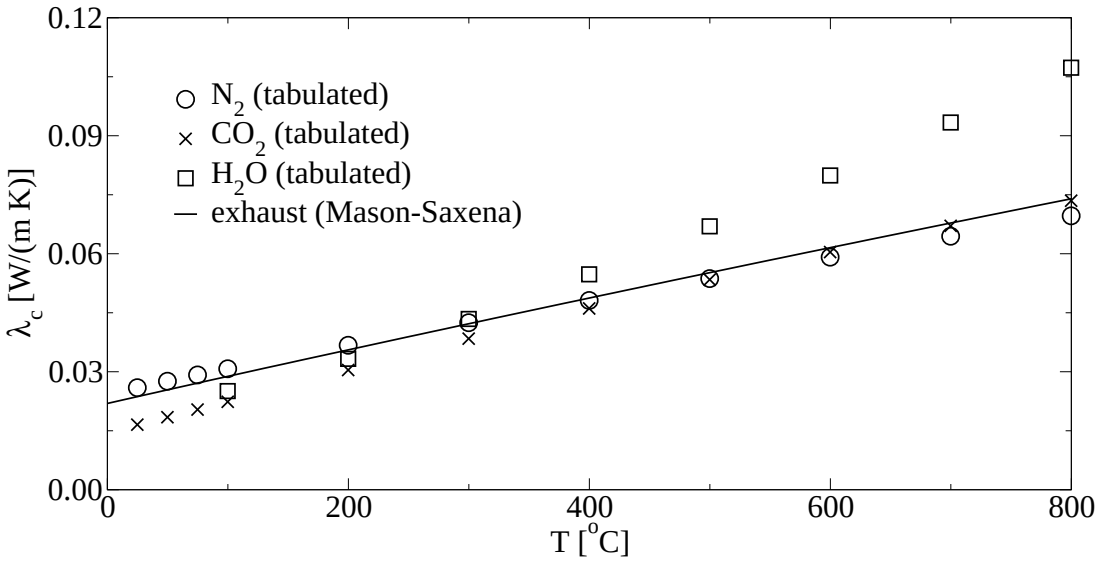

Figure I.4: Exhaust mixture's thermal conductivity calculated from Mason-Saxena mixing formula [139] compared to tabulated values for pure nitrogen, carbon dioxide and water [100].

I.4 Diffusivity

Diffusion coefficient D_{AB} of a gaseous species A diffusing in a carrier gas B can be described by the Fuller-Schettler-Giddings correlation [134]. It is recommended for binary gas mixtures under low pressure [139]:

$$D_{\mathrm{AB}}\left[\frac{\mathrm{m}^2}{\mathrm{s}}\right] = 1.013\,10^{-2}\,\frac{\sqrt{\frac{M_{\mathrm{A}}+M_{\mathrm{B}}}{M_{\mathrm{A}}M_{\mathrm{B}}}}}{\left(\sqrt[3]{v_{\mathrm{A}}}+\sqrt[3]{v_{\mathrm{B}}}\right)^2}\,\frac{T[\mathrm{K}]^{1.75}}{p[\mathrm{N/m}^2]} \tag{I.4}$$

	H_2	H_2O	CO	N_2	NO	O_2	C_3H_6	C_3H_8	CO_2
MW_j [kg/kmol]	2	18	28	28	30	32	42	44	44
v_j [cm^3/mol]	7.07	12.7	18.9	17.9	11.2*	16.6	61.4*	65.34*	26.9

Table I.4: Diffusion volumina of various exhaust gas components to be used with equation (I.4); *diffusion coefficients obtained by summation of atomic increments [134].

Neglecting concentrations smaller than 5 % gasoline engine exhaust contains during stoichiometric operation approximately 77 % nitrogen, approximately 12 % carbon dioxide, 11 % H_2O. Diffusion coefficients of the remaining gas species in this mixture of carrier gas can be calculated from the Blanc-equation [134, 139]:

$$D_{j,\mathrm{mix}} = \left(\sum_{k=1,k\neq j}^{K}\frac{x_k}{D_{j,k}}\right)^{-1} \tag{I.5}$$

The binary diffusion coefficients of several exhaust gas species in the pure major exhaust constituents nitrogen, carbon dioxide and water $D^0_{j,k}$ are compared to the respective diffusion coefficients in a mixture of the pre-mentioned gases representative for stoichiometric exhaust.

		H_2	CO	NO	O_2	C_3H_6	C_3H_8
$D^0_{j,\mathrm{N_2}}$	[10^{-5} m^2/s]	**7.61**	**2.05**	**2.39**	**2.07**	**1.21**	**1.17**
$D^0_{j,\mathrm{CO_2}}$	[10^{-5} m^2/s]	6.40	1.61	1.85	1.61	0.96	0.92
$D^0_{j,\mathrm{H_2O}}$	[10^{-5} m^2/s]	8.81	2.59	3.05	2.64	1.53	1.48
$D^0_{j,\mathrm{mix}}$	[10^{-5} m^2/s]	7.55	2.03	2.36	2.05	1.20	1.16

Table I.5: Binary diffusion coefficients at standard conditions (p^0 = 1 bar, T^0 = 298 K) of different exhaust gas components in pure nitrogen (chosen for this work), carbon dioxide, water and a mixture of the pre-mentioned representative for stoichiometric exhaust calculated from equation I.4 and I.5.

Applying equations I.4 and I.5 and the parameter values given in table I.4 it can be seen that the relative error when regarding pure nitrogen as the carrier gas is less than 1.5 % compared to the value obtained considering the full background mixture. The property estimation I.4 itself is reported to have an error of 5 %, thus the binary diffusion coefficients in pure nitrogen are used in this work [134].

At a given pressure and temperature the diffusion coefficients can be calculated from their standard state values:

$$D_{j,\mathrm{N_2}} \left[\frac{\mathrm{m}^2}{\mathrm{s}}\right] = D^0_{j,\mathrm{N_2}} \frac{p^0}{p} \left(\frac{T}{T^0}\right)^{1.75} \tag{I.6}$$

I.5 Prandtl Number

The Prandtl number is needed for calculation of the heat transfer coefficient in equation H.1. Even so the properties viscosity, heat capacity and thermal conductivity are strongly temperature dependent the Prandtl number does practically not change with temperature (figure I.5). In this work the Prandtl number is fixed at $Pr = 0.74$ over the full temperature range.

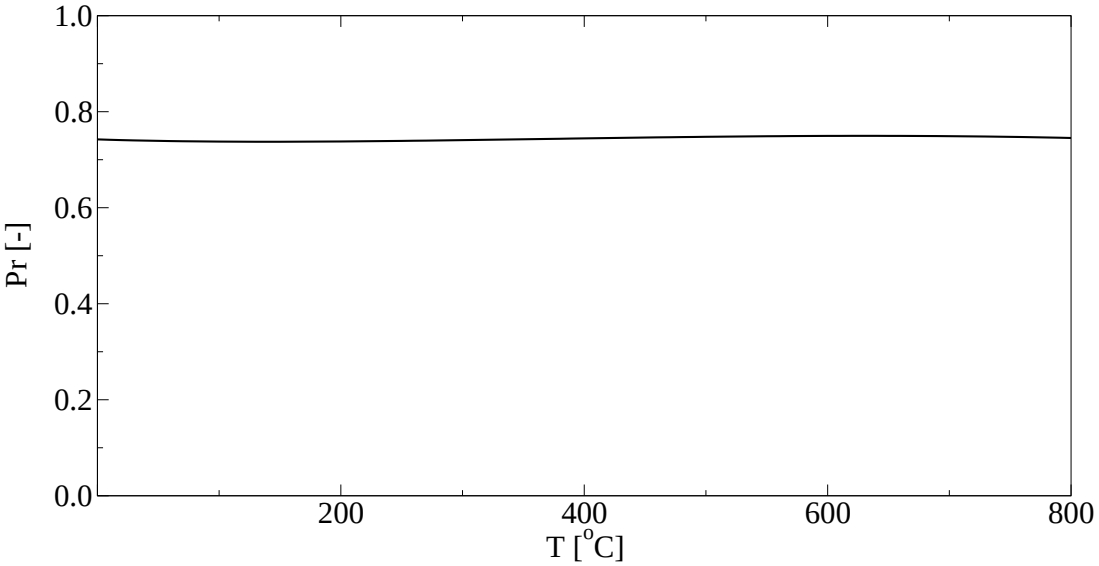

Figure I.5: Prandtl number with temperature ($y_{\mathrm{N_2}}$ = 77 %, $y_{\mathrm{CO_2}}$ = 12 %, $y_{\mathrm{H_2O}}$ = 11 %).

I.6 Schmidt Number

The calculation of the mass transfer coefficient relates to the respective species Schmidt number Sc_j. As with the Prandtl number the Schmidt number is almost temperature independent I.6. Temperature averaged Schmidt numbers listed in table I.6 are applied

in this work. The error due to this simplification is below 4 % within the temperature range 25 °C $< T <$ 1000 °C.

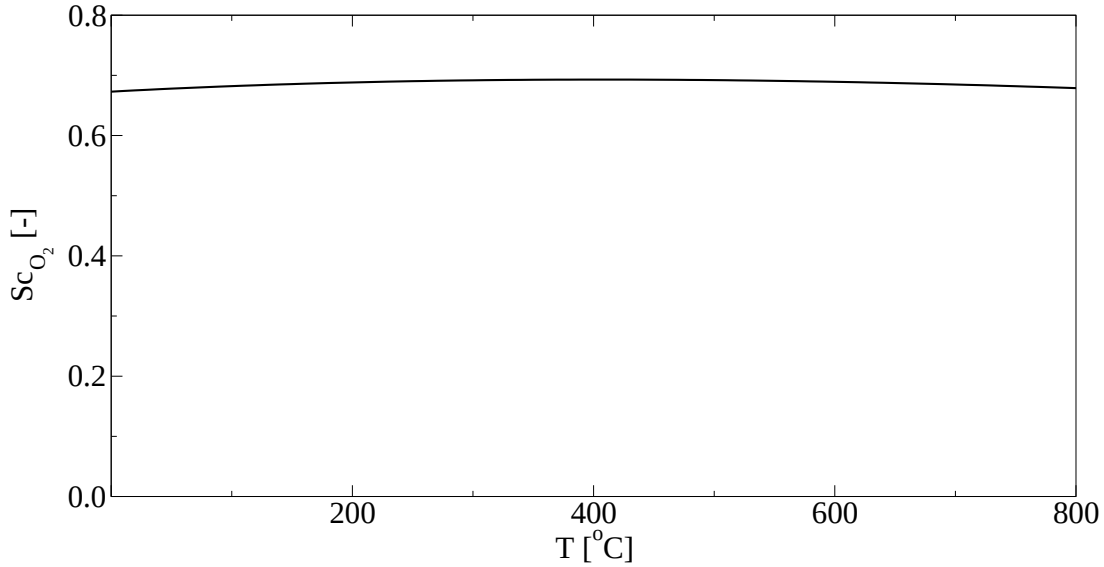

Figure I.6: Oxygen Schmidt number with temperature at a constant pressure of 1.2 bar.

H_2	CO	NO	O_2	C_3H_6	C_3H_8
0.185	0.69	0.59	0.68	1.17	1.24

Table I.6: Temperature averaged Schmidt numbers at a constant pressure of 1.2 bar.

Appendix J

Properties of Solids

Heat Capacity The heat capacity correlations of various washcoat constituents provided by table J.1 are applied in thermodynamic equilibrium calculations performed in section 3.2. Furthermore the converter's solid phase heat capacity is calculated from these correlations according to equation F.20.

	a_j J/(mol K)	b_j J/(mol K^2)	c_j (J K)/mol	d_j J/(mol K^3)	valid K	data source
C	9.12	$13.22\,10^{-3}$	$-0.62\,10^{6}$	-	1400	[17]
Al_2O_3	117.49	$10.38\,10^{-3}$	$-3.71\,10^{6}$	-	2327	[17]
$Al_2(SO_4)_3$	366.31	$62.59\,10^{-3}$	$-11.16\,10^{6}$	-	989	[17]
$CeO_{1.5}$	65.40	$6.89\,10^{-3}$	$-0.80\,10^{6}$	-	2450	[17]
$CeO_{1.72}$	58.37	$19.87\,10^{-3}$	$-0.75\,10^{6}$	-	1200	[144]
$CeO_{1.83}$	60.75	$18.91\,10^{-3}$	$-0.64\,10^{6}$	-	1200	[144]
CeO_2	64.81	$17.70\,10^{-3}$	$-0.76\,10^{6}$	-	2450	[17]
$Ce_2(SO_4)_3$	221.75	$198.74\,10^{-3}$	-	-	1106	[17]
$Mg_2Al_4Si_5O_{18}$	602.92	$95.74\,10^{-3}$	$-10.99\,10^{6}$	$-26.81\,10^{-6}$	2000	[142]
ZrO_2	68.33	$9.08\,10^{-3}$	$-1.34\,10^{6}$	-	1445	[144]

Table J.1: Molar heat capacities of cordierite and major washcoat constituents. Correlation $c_p = a + bT + cT^{-2} + dT^2$, $[T]$ = K, returns $[c_p]$ = J/(mol K); values adopted from literature or fitted to tabulated values therein.

Mass based heat capacities of the cordierite substrate and components that are believed to be the major washcoat constituents – aluminum oxide, cerium oxide and zirconium oxide – are plotted against temperature in figure J.1. Even in the low temperature region the heat capacity of cordierite is relatively high compared the respective value $c_{p,\mathrm{s}} = 0.5$ kJ/(kg K) of stainless steal [9]. However the much higher density of steel will overcompensate this effect in terms of light-off performance.

Oxygen Mobility Impurities in the cerium oxide crystal such as dissolved zirconium oxide are necessary to exploit the oxygen storage and – even more precise – oxygen

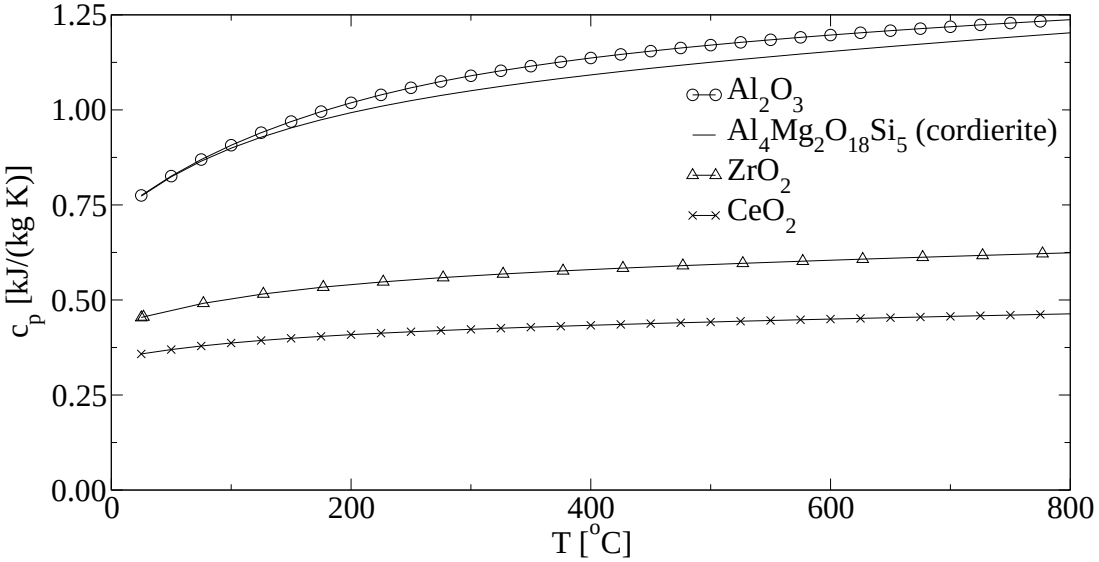

Figure J.1: Mass based heat capacities of ceramic substrate (cordierite) and major washcoat constituents.

reduction potential under real automotive exhaust conditions. These materials provide increased equilibrium oxygen partial pressures compared to pure cerium oxide and are thus more facile to reduce to some reasonable oxygen deficiency under rich conditions (section 3.2.2).

It is also reported that ceria-zirconia solid solution oxides provide better oxygen ion mobilities compared to pure cerium oxide [161, 171]. Especially at lower temperatures replacing every second cerium cation with a zirconium cation increases the oxygen diffusivity within the crystal by two orders of magnitude compared to pure cerium oxide. With increasing temperature oxygen diffusivities increase rapidly over the whole composition range. At 900 °C the cerium-zirconium oxide solid solution provides a still one order of magnitude higher oxygen mobility (figure J.2).

The temperature dependence of oxygen diffusivity with an equimolar cerium-zirconium oxide solution is represented by the Arrhenius type equation J.1.

$$
\begin{aligned}
D_{\mathrm{O_2,s}} &= D^{\infty}_{\mathrm{O_2,s}}\, e^{-\frac{E_{\mathrm{O_2,s}}}{\mathrm{R}\,T}} \\
\text{with} \quad D^{\infty}_{\mathrm{O_2,s}} &= 4.54\,10^{-9}\,\mathrm{m^2/s} \\
\text{and} \quad E_{\mathrm{O_2,s}} &= 0.135 \cdot 10^5\,\mathrm{K}
\end{aligned}
\tag{J.1}
$$

Equation J.1 describes the temperature dependent oxygen diffusivity of $Ce_{0.5}Zr_{0.5}O_2$ quite well in the temperature range $T = 200 \ldots 900$ °C (figure J.3).

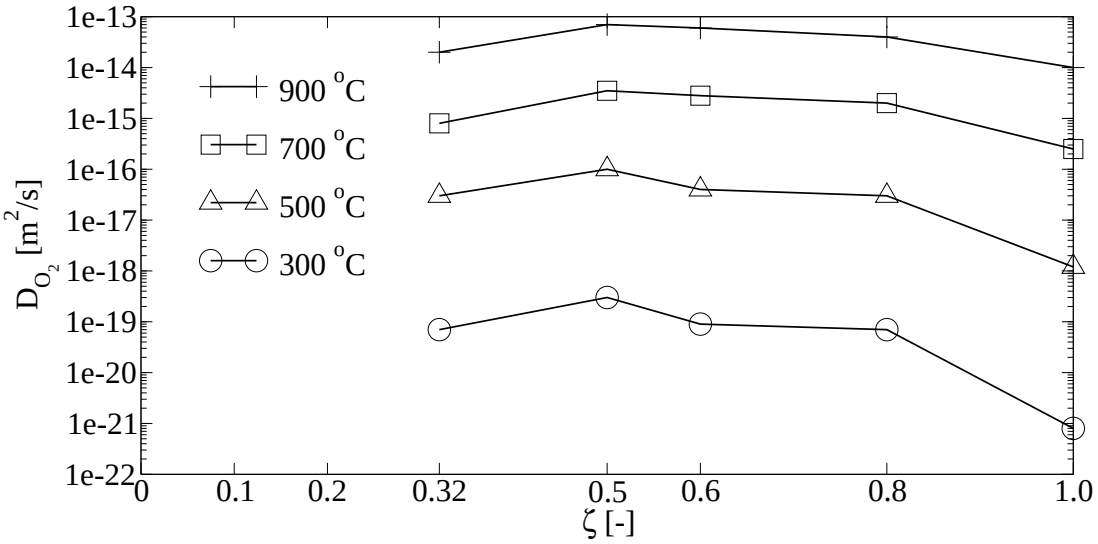

Figure J.2: Oxygen diffusion coefficients of cerium zirconium solid solution oxides $Ce_{\zeta}Zr_{(1-\zeta)}O_2$ versus cerium cation content at various temperatures [19, 161].

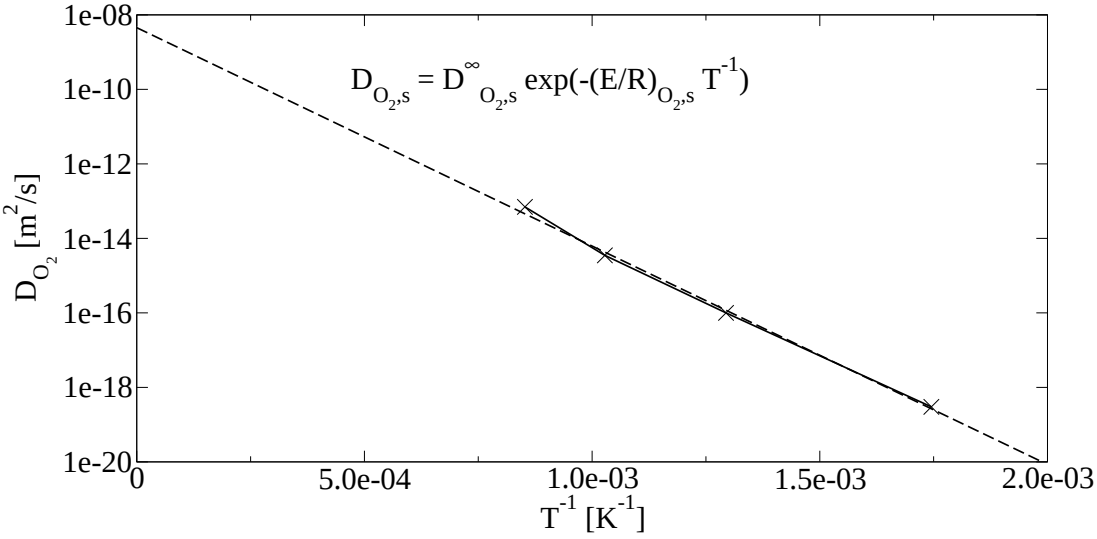

Figure J.3: Arrhenius type temperature dependence of oxygen diffusion within equimolar cerium-zirconium oxide solid solution $Ce_{0.5}Zr_{0.5}O_2$ (equation J.1).

Bibliography

[1] G. Abate, L. Glielmo, P. Rinaldi, M. Milano, S. Santini, and G. Serra. Numerical Simulation and Analysis of the Dynamic Behavior of Three Way Catalytic Converters. In *Proceedings of the International Conference on Internal Combustion Engines, Capri, Italy, 17. - 20. September 1997*, pages 409 – 412, 1997.

[2] G.-Y. Adachi and T. Masui. Synthesis and Modification of Ceria-Based Materials. In A. Trovarelli, editor, *Catalysis by Ceria and Related Materials*, chapter 3, pages 51–83. Imperial College Press, 2002.

[3] Th.S. Auckenthaler, Ch.H. Onder, H.P. Geering, and J. Frauhammer. Modelling of a Three-Way Catalytic Converter with Respect to Fast Transients of Lambda-Sensor Relevant Exhaust Gas Components. *Industrial & Engineering Chemistry Research*, 43(16):4780 – 4788, 2004.

[4] N. Baba, K. Yokata, Sh. Matsunaga, Sh. Kojima, K. Ohsawa, T. Ito, and H. Domyo. Numerical Simulation of Deactivation Process of Three-Way Catalytic Converters. *SAE Technical Paper Series*, 2000-01-0214, 2000.

[5] C.W. Bale, P. Chartrand, S.A. Degterov, G. Eriksson, K. Hack, R. Ben Mahfoud, J. Melançon, A.D. Pelton, and S. Petersen. FactSage Thermochemical Software and Databases. *Calphad*, 26(2):189–228, 2002.

[6] M. Balenovic, A.C.P.M. Backx, and J.H.B.J. Hoebink. On a Model-Based Control of Three-Way Catalytic Converter. *SAE Technical Paper Series*, 2001-01-0937, 2001.

[7] M. Balenovic, J.H.B.J. Hoebink, A.C.P.M. Backx, and A.J.L. Nievergeld. Modeling of an Automotive Exhaust Gas Converter at Low Temperatures, Aiming at Control Application. *SAE Technical Paper Series*, 1999-01-3623, 1999.

[8] J. Baronick, B. Heller, G. Lach, and H. Luf. Modal Measurement of Raw Exhaust Volume and Mass Emissions by SESAM. *SAE Technical Paper Series*, 980047, 1998.

[9] H. Bauer, editor. *Kraftfahrtechnisches Taschenbuch*. Robert Bosch GmbH, Stuttgart, 22nd edition, 1995.

[10] D.D. Beck, J.W. Sommers, and C.L. DiMaggio. Axial Characterization of Oxygen Storage Capacity in Close-Coupled Lightoff and Underfloor Catalytic Converters and Impact of Sulfur. *Applied Catalysis B: Environmental*, 11(3-4):273–290, 1997.

[11] E.R. Becker, R. Watson, M. Brayer, C. Vogt, and M. Makino. Prediction of Catalytic Performance During Light-Off Phase with Different Wall Thickness, Cell Density and Cell Shape. *SAE Technical Paper Series*, 2001-01-0930, 2001.

[12] S. Bedrane, C. Descorme, and D. Duprez. Investigation of the Oxygen Storage Process on Ceria- and Ceria-Zirconia-Supported Catalysts. *Catalysis Today*, 2743:1–5, 2002.

[13] S. Bedrane, C. Descorme, and D. Duprez. Towards the Comprehension of Oxygen Storage Processes on Model Three-Way Catalysts. *Catalysis Today*, 73:233–238, 2002.

[14] S. Bernal, G. Blanco, J.J. Calvino, G.A. Cifredo, J.A. Perez-Omil, J.M. Pintado, and A. Varo. HRTEM and TPO Study of the Behaviour under Oxidizing Conditions of some Rh/CeO_2 Catalysts. *Studies in Surface Science and Catalysis*, 82:507–514, 1994.

[15] S. Bernal, J.J. Calvino, J.M. Gatica, C.L. Cartes, and J.M. Pintado. Chemical and Nanostructural Aspects of the Preparation and Characterisation of Ceria and Ceria-Based Mixed Oxide-Supported Metal Catalysts. In A. Trovarelli, editor, *Catalysis by Ceria and Related Materials*, chapter 4, pages 85–168. Imperial College Press, 2002.

[16] D.J.M. Bevan and J. Kordis. Mixed Oxides of the Type MO_2 (Fluorite)-M_2O_3 — Oxygen Dissociation Pressures and Phase Relationships in the System CeO_2-Ce_2O_3 at high temperatures. *Journal of Inorganic and Nuclear Chemistry*, 26:1509–1523, 1964.

[17] M. Binnewies and E. Milke. *Thermochemical Data of Elements and Compounds*. Wiley-VCH, 1999.

[18] E.J. Bissett and S.H. Oh. Electrically Heated Converters for Automotive Emission Control: Determination of the Best Size Regime for the Heated Element. *Chemical Engineering Science*, 54:3957–3966, 1999.

[19] M. Boaro, C. de Leitenburg, G. Docetti, and A. Trovarelli. The Dynamics of Oxygen Storage in Ceria-Zirconia Model Catalysts Measured by CO Oxidation under Stationary and Cycling Feedstream Compositions. *Journal of Catalysis*, 193:338, 2000.

[20] A.L. Boehmann and S. Niksa. Conversion of Various Hydrocarbons over Supported Pd during Simulated Cold-Start Conditions. *Applied Catalysis B: Environmental*, 8:41–56, 1996.

[21] J. Braun, Th. Hauber, H. Többen, P. Zacke, D. Chatterjee, O. Deutschmann, and J. Warnatz. Influence of Physical and Chemical Parameters on the Conversion Rate of a Catalytic Converter: A Numerical Simulation Study. *SAE Technical Paper Series*, 2000-01-0211, 2000.

[22] C. Brinkmeier, G. Eigenberger, S. Büchner, and A. Donnerstag. Transient Emissions of a SULEV Catalytic Converter System - Dynamic Simulation vs. Dynamometer Measurements. *SAE Technical Paper*, 2003-01-1001, 2003.

[23] R.J. Brisley, G.R. Chandler, H.R. Jones, P.J. Anderson, and P.J. Shady. The Use of Palladium in Advanced Catalysts. *SAE Technical Paper Series*, 950259, 1995.

[24] S. Büchner, S. Santos Lardies, A. Degen, A. Donnerstag, and W. Held. A Modular Numerical Simulation Tool Predicting Catalytic Converter Light-Off by Improved Modeling of Thermal Management and Conversion Characteristics. *SAE Technical Paper Series*, 2001-01-0940, 2001.

[25] B. Campbell, R. Farrington, G. Inman, S. Dinsdale, D. Gregory, D. Eade, and J. Kisenyi. Improved Three-Way Catalyst Performance Using an Active Bias Control Regeneration System. *SAE Technical Paper Series*, 2000-01-0499:125–131, 2000.

[26] S.H. Chan and D.L. Hoang. Modeling of Catalytic Conversion of CO/HC in Gasoline Exhaust at Engine Cold-Start. *SAE Technical Paper Series*, 1999-01-0452, 1999.

[27] S.H. Chan, D.L. Hoang, and P.L. Zhou. Heat Transfer and Chemical Kinetics in the Exhaust System of a Cold-Start Engine Fitted with a Three-Way Catalytic Converter. *Proceedings of the Institution of Mechanical Engineers - Part D: Journal of Automobile Engineering*, 214(7):765–777, 2000.

[28] D. Chatterjee, O. Deutschmann, and J. Warnatz. Detailed Surface Reaction Mechanism in a Three-Way Catalyst. *Faraday Discussions*, 119:371–384, 2001.

[29] D.K.S. Chen, S.H. Oh, E.J. Bissett, and D.L. Van Ostrom. A Three-Dimensional Model for the Analysis of Transient Thermal and Conversion Characteristics of Monolitic Catalytic Converters. *SAE Technical Paper Series*, 880282, 1988.

[30] Y.-M. Chiang, E.B. Lavik, I. Kosacki, H.L. Tuller, and J.Y. Ying. Defect and Transport Properties of Nanocrystalline CeO_{2-x}. *Applied Physics Letters*, 59(2):185–187, 1996.

[31] H. Cordatos, D. Ford, and R.J. Gorte. Simulated Annealing Study of the Structure and Reducibility in Ceria Clusters. *Journal of Physical Chemistry*, 100(46):18128–18132, 1996.

[32] S.J. Cornelius. *Modelling and Control of Automotive Catalysts*. PhD thesis, Sidney Sussex College - University of Cambridge, 2001.

[33] J.-P. Cuif, S. Deutsch, M. Marczi, H.-W. Jen, G.W. Graham, W. Chun, and R.W. McCabe. High Temperature Stability of Ceria-Zirconia Supported Pd Model Catalysts. *SAE Technical Paper Series*, 980668, 1998.

[34] J.P. Cuif, G. Blanchard, O. Touret, A. Seigneurin, M. Marczi, and E. Quéméré. (Ce,Zr)O_2 Solid Solutions for Three-Way Catalysts. *SAE Technical Paper Series*, 970463, 1997.

[35] K. Denbigh. *The Principles of Chemical Equilibrium*. Cambridge University Press, 4th edition, 1981.

[36] A.F. Diwell, Ch. Hallett, and J.R. Taylor. The Impact of Sulphur Storage on Emissions from Three-Way Catalysts. *SAE Technical Paper Series*, 872163, 1987.

[37] D. Duprez and C. Descorme. Oxygen Storage/Redox Capacity and Related Phenomena on Ceria-Based Catalysts. In A. Trovarelli, editor, *Catalysis by Ceria and Related Materials*, pages 243–280. Imperial College Press, 2002.

[38] P. Eastwood. *Critical Topics in Exhaust Aftertreatment*. Research Studies Press Ltd., 2000.

[39] G. Eigenberger. Chemische Reaktionstechnik I. Vorlesungsumdruck Universität Stuttgart, 2004.

[40] J. Hepburn et Al. A Review of the Dual EGO Sensor Method for OBD-II Catalyst Efficiency Monitoring. *SAE Technical Paper Series*, 942057, 1994.

[41] F. Fally, V. Perrichon, H. Vidal, J. Kaspar, G. Blanco, J.M. Pintado, S. Bernal, G. Colon, M. Daturi, and J.C. Lavalley. Modification of the Oxygen Storage Capacity of CeO_2–ZrO_2 Mixed Oxides after Redox Cycling Aging. *Catalysis Today*, 59:373–386, 2000.

[42] P. Fornasiero, G. Balducci, J. Kaspar, S. Meriani, R. Di Monte, and M. Graziani. Metal-Loaded CeO_2-ZrO_2 Solid Solutions as Innovative Catalysts for Automotive Catalytic Converters. *Catalysis Today*, 29(1-4):47–52, 1996.

[43] G. Friedrich, G. Kolios, and G. Eigenberger. Direktverdampfer für kleine Flüssigkeitsströme. *German Patent*, DE 19723680 B4, 2004.

[44] H. Germann, S. Tagliaferri, and H.P. Geering. Differences in Pre- and Post-Converter Lambda Sensor Characteristics. *SAE Technical Paper Series*, 960335, 1996.

[45] H.J. Germann, C.H. Onder, and H.P. Geering. Fast Gas Concentration Measurements for Model Validation of Catalytic Converters. *SAE Technical Paper Series*, 950477, 1995.

[46] L. Glielmo, P. Rinaldi, S. Santini, and G. Serra. Modelling and Numerical Simulation of the Dynamic Behavior of Three Way Catalytic Converters. In *Proceedings of the 1998 IEEE International Converence on Control Applications*, volume 2, pages 731–735, 1998.

[47] V. Gnielinski. Wärmeübergang bei der Strömung durch Rohre. In *VDI-Wärmeatlas*, chapter Gb1-Gb8. Verein Deutscher Ingenieure, 6th edition, 1991.

[48] A. Goguet, F. Meunier, J.P. Breen, R. Burch, M.I. Petch, and A. Faur Ghenciu. Study of the Origin of the Deactivation of a Pt/CeO_2 Catalyst during Reverse Water Gas Shift (RWGS) Reaction. *Journal of Catalysis*, 226(2):382–392, 2004.

[49] S.E. Golunski, H.A. Hatcher, R.R. Rajaram, and T.J. Truex. Origins of Low-Temperature Three-Way Activity in Pt/CeO_2. *Applied Catalysis B: Environmental*, 5:367–376, 1995.

[50] C.T. Goralski and W.F. Schneider. Analysis of the Thermodynamic Feasibility of NO_x Decomposition Catalysis to Meet Next Generation Vehicle NO_x Emissions Standards. *Applied Catalysis B: Environmental*, 37:263–277, 2002.

[51] S. Gordon and B.J. McBride. Computer Program for Calculation of Complex Chemical Equilibrium Compositions and Applications, Volume I: Analysis. Technical Report NASA Reference Publication 1311, National Aeronautics and Space Administration, Lewis Research Center, 1994.

[52] S. Gordon and B.J. McBride. Computer Program for Calculation of Complex Chemical Equilibrium Compositions and Applications, Volume II: Users Manual and Program Description. Technical Report NASA Reference Publication 1311, National Aeronautics and Space Administration, Lewis Research Center, 1996.

[53] G.W. Graham, H.-W. Jen, R.W. McCabe, A.M. Straccia, and L.P. Haack. Characterization of Model Automotive Exhaust Catalysts: Pd on Zr-rich Ceria–Zirconia Supports. *Catalysis Letters*, 67:99–105, 2000.

[54] G.W. Graham, A.E. O'Neill, and A.E. Chen. Pd Encapsulation in Automotive Exhaust-Gas Catalysts. *Applied Catalysis A: General*, 252(2):437–445, 2003.

[55] G.W. Graham, H. Sun, H.-W. Jen, X.Q. Pan, and R.W. McCabe. Aging-Induced Metal Redistribution in Bimetallic Catalysts. *Catalysis Letters*, 81(1):1–7, 2002.

[56] J. M. A. Harmsen, J. H. B. J. Hoebink, and J.C. Schouten. Transient Kinetic Modeling of the Ethylene and Carbon Monoxide Oxidation over a Commercial Automotive Exhaust Gas Catalyst. *Industrial & Engineering Chemistry Research*, 3(39):599–609, 2000.

[57] J.M.A. Harmsen, J.H.B.J. Hoebink, and J.C. Schouten. Acetylen and Carbon Monoxide Oxidation over a $Pt/Rh/CeO_2/\gamma\text{-}Al_2O_3$ Automotive Exhaust Gas Catalyst: Kinetic Modelling of Transient Experiments. *Chemical Engineering Science*, 56:2019–2035, 2001.

[58] J.M.A. Harmsen, J.H.B.J. Hoebink, and J.C. Schouten. Kinetics of the Steady-State Acetylene Oxidation by Oxygen over a Pt/Rh/CeO_2/γ-Al_2O_3 Three-Way Catalyst. *Topics in Catalysis*, 16/17(1-4):297–403, 2001.

[59] B. Harrison, A.F. Diwell, and C. Hallett. Promoting Platinum Metals by Ceria; Metal-Support Interactions in Autocatalysts. *Platinium Metals Review*, 32(2):73–83, 1988.

[60] R.E. Hayes and S.T. Koaczkowsi. Mass and Heat Transfer Effects in Catalytic Monolith Reactors. *Chemical Engineering Science*, 49(21):3587–3599, 1994.

[61] R.E. Hayes, L.S. Mukadi, M. Votsmeier, and J. Gieshoff. Three-Way Catalytic Converter Modelling with Detailed Kinetics and Washcoat Diffusion. *Topics in Catalysis*, 30/31:411–415, 2004.

[62] R.H. Heck, J. Wei, and J.R. Katzer. Mathematical Modeling of Monolithic Catalysts. *American Institute of Chemical Engineers Journal Journal*, 22(3):477–484, 1976.

[63] R.M. Heck and R.J. Farrauto. Automobile Exhaust Catalysts. *Applied Catalysis A: General*, 221:443–457, 2001.

[64] M.G. Henk, J.J. White, and G.W. Denison. Sulfur Storage and Release from Automotive Catalysts. *SAE Technical Paper Series*, 872134, 1987.

[65] J.S. Hepburn, D.A. Dobson, C.P. Hubbard, and K. Otto. The Pulse Flame Combustor Revisited. *SAE Technical Paper Series*, 962118, 1996.

[66] R.K. Herz and S.P. Marin. Surface Chemistry Models of Carbon Monoxide Oxidation on Supported Platinum catalysts. *Journal of Catalysis*, 65:281–296, 1980.

[67] J.B. Heywood. *Internal Combustion Engine Fundamentals*. McGraw-Hill, 1988.

[68] N. Hickey, P. Fornasiero, J. Kaspar, J.M. Gatica, and S. Bernal. Effects of the Nature of the Reducing Agent on the Transient Redox Behavior of NM/$Ce_{0.68}Zr_{0.32}O_2$ (NM=Pt, Pd and Rh). *Journal of Catalysis*, 200:181–193, 2001.

[69] S. Hilaire, X. Wang, T. Luo, R.J. Gorte, and J. Wagner. A Comparative Study of Water-Gas-Shift Reaction over Ceria-Supported Metallic Catalysts. *Applied Catalysis A: General.*, 258(2):271–276, 2004.

[70] J. Hoebink, R. Germert, J. van den Tillaart, and G. Martin. Competing Reactions in Three-Way Catalytic Converters: Modelling of the NO_x Conversion Maximum in the Light-off Curves under net Oxidizing Conditions. *Chemical Engineering Science*, 55:1573–1581, 2000.

[71] J.H.B.J. Hoebink, J.M.A. Harmsen, M. Balenovic, A.C.P.M. Backx, and J.C. Schouten. Automotive Exhaust Gas Conversion: From Elementary Step Kinetics to Prediction of Emission Dynamics. *Topics in Catalysis*, 16/17(1-4):319–327, 2001.

[72] A. Holmgren and B. Andersson. Oxygen Storage Dynamics in $Pt/CeO_2/Al_2O_3$ Catalysts. *Journal of Catalysis*, 178:14–25, 1998.

[73] A. Holmgren, B. Andersson, and D. Duprez. Interactions of CO with Pt/Ceria Catalysts. *Applied Catalysis B: Environmental*, 22:215–230, 1999.

[74] S. Huang, L. Li, O. Van der Biest, J. Vleugels, and P. Wang. Study of Thermodynamic Properties of Nonstoichiometry Phase $Zr_{1-z}Ce_zO_{2-x}$ with Compound Energy Model. *Journal of Materials Science & Technology*, 18(5):422–426, 2002.

[75] S. Huang, L. Li, O. Van der Biest, J. Vleugels, and P. Wang. Thermodynamic Assessment of the ZrO_2-CeO_2 and ZrO_2-$CeO_{1.5}$ Binary System. *Journal of Materials Science & Technology*, 18(4):325 –327, 2002.

[76] S. Huang, L. Li, O. Van der Biest, J. Vleugels, and P. Wang. Thermodynamic Prediction of the Nonstoichiometry Phase $Zr_{1-z}Ce_zO_{2-x}$ in the ZrO_2-$CeO_{1.5}$-CeO_2 System. *Journal of The European Ceramic Society*, 23(1):99–106, 2003.

[77] Sh. Huang, L. Li, O. Van der Biest, and J. Vleugels. Influence of the Oxygen Partial Pressure on the Reduction of CeO_2 and CeO_2-ZrO_2 Ceramics. *Solid State Sciences*, 7:539–544, 2005.

[78] A. Iglesias-Juez, A. Martinez-Arias, and M. Fernandez-Garcia. Metal-Promotor Interface in $Pd/(Ce,Zr)O_x/Al_2O_3$ Catalysts: Effect of Thermal Aging. *Journal of Catalysis*, 221(1):148–161, 2003.

[79] H.W. Jen, G.W. Graham, W. Chun, R.W. McCabe, J.-P. Cuif, S.E. Deutsch, and O. Touret. Characterization of Model Automotive Exhaust Catalysts: Pd on Ceria and Ceria-Zirconia Supports. *Catalysis Today*, 50:309–328, 1999.

[80] J. Jirat, M. Kubicek, and M. Marek. Mathematical Modelling of Catalytic Monolithic Reactors with Storage of Reaction Components on the Catalytic Surface. *Catalysis Today*, 53:583–596, 1999.

[81] J. Jirat, F. Stepanek, M. Kubicek, and M. Marek. Nonstationary Operation of a System of Catalytic Monolithic Reactors for Selective NO_x Reduction. *Chemical Engineering Science*, 1999.

[82] J.C. Peyton Jones and R.A. Jackson. Potential and Pitfalls in the Use of Dual Lambda Sensors for Catalyst Control and OBD. *Proceedings of the Institution of Mechanical Engineers - Part D: Journal of Automobile Engineering*, 6:475–488, 2003.

[83] J.C. Peyton Jones and K.R. Muske. Model-Based OBD for Three-Way Catalyst Systems. *SAE Technical Paper Series*, 2004-01-0639, 2004.

[84] M.W. Chase Jr. NIST-JANAF Thermochemical Tables. *Journal of Physical and Chemical Reference Data*, 9:1–1951, 1998.

[85] I.P. Kandylas and A.M. Stamatelos. Zyklus-Emissionsverhalten eines gealterten Dreiwege-Katalysators. *MTZ Motortechnische Zeitschrift*, 61, 2000.

[86] J. Kaspar, P. Fornasiero, and M. Graziani. Use of CeO2-Based Oxides in the Three-Way Catalysis. *Catalysis Today*, 50:285–298, 1999.

[87] ETAS GmbH & Co. KG. Lambda Meter LA3 - Benutzerhandbuch. Technical Report AM711101 R2.3.1 DE, Etas, 2000.

[88] T. Kirchner and G. Eigenberger. Optimization of the Cold-Start Behaviour of Automotive Catalysts Using an Electrically Heated Pre-Catalyst. *Chemical Engineering Science*, 51(10):2409–2418, 1996.

[89] Th . Kirchner. *Experimentelle Untersuchungen und dynamische Simulation der Autoabgaskatalyse zur Verbesserung des Kaltstartverhaltens*. PhD thesis, Universität Stuttgart, 1997.

[90] N. Kishi, S. Kikuchi, N. Susuki, and T. Hayashi. Technology for Reducing Exhaust Gas Emission in Zero Level Emission Vehicles (ZLEV). *SAE Technical Paper Series*, 1999-01-0772, 1999.

[91] P. Koci, M. Kubicek, and M. Marek. Modeling of Three-Way-Catalyst Monolith Converters with Microkinetics and Diffusion in the Washcoat. *Industrial & Engineering Chemistry Research*, 43(16):4503–4510, 2004.

[92] P. Koci, M. Kubicek, and M. Marek. Multifunctional Aspects of Three-Way Catalyst: Effects of Complex Washcoat Composition. *Chemical Engineering Research and Design*, 82(A2):284–292, 2004.

[93] P. Koci, M. Kubicek, and M. Marek. Periodic Forcing of Three-Way Catalyst with Diffusion in the Washcoat. *Catalysis Today*, 98(3):345–355, 2004.

[94] P. Koci, V. Nevoral, M. Zahrubsky, M. Kubicek, and M. Marek. Nonlinear Dynamics of Automobile Exhaust Gas Converters: The Role of Instationary Kinetics. *Chemical Engineering Science*, 59:5597–5605, 2004.

[95] G. Kolios. *Zur Autothermen Führung der Styrolsynthese mit Periodischem Wechsel der Strömungsrichtung*. PhD thesis, Universität Stuttgart, 1997.

[96] G.C. Koltsakis, P.A. Konstantinidis, and A.M. Stamatelos. Development and Application Range of Mathematical Models for 3-Way Catalytic Converters. *Applied Catalysis B: Environmental*, 12:161–191, 1997.

[97] G.C. Koltsakis and A.M. Stamatelos. Catalytic Automotive Exhaust After-Treatment. *Progress in Energy and Combustion Science*, 23:1–39, 1997.

[98] G.C. Koltsakis and A.M. Stamatelos. Konzept zur Katalysatorüberwachung durch Reaktionswärmeermittlung. *MTZ Motortechnische Zeitschrift*, 58, 1997.

[99] G.C. Koltsakis and A.M. Stamatelos. Dynamic Behavior Issues in Three-Way Catalyst Modeling. *American Institute of Chemical Engineers Journal Journal*, 45(3):603–614, 1999.

[100] R. Krauss. Stoffwerte von Luft. In *VDI-Wärmeatlas*, chapter Db16-Db71. Verein Deutscher Ingenieure, 6th edition, 1991.

[101] F. Lacin and M. Zhuang. Modeling and Simulation of Transient Thermal and Conversion Characteristics for Catalytic Converters. *SAE Technical Paper Series*, 2000-01-0209, 2000.

[102] H.-G. Lee. *Chemical Thermodynamics for Metals and Materials*. Imperial College Press and World Scientific Publishing Co. Ptc. Ltd., 1999.

[103] K. Lucas. Berechnungsmethoden für Stoffeigenschaften. In *VDI-Wärmeatlas*, chapter Da1-Da36. Verein Deutscher Ingenieure, 6th edition, 1991.

[104] T. Luo and R.J. Gorte. A Mechanistic Study of Sulfur Poisoning of the Water-Gas-Shift Reaction over Pd/Ceria. *Catalysis Letters*, 85(3-4):139–146, 2003.

[105] C.H.P. Lupis. *Chemical Thermodynamics of Materials*. Elsevier Science Publishing Co., Inc., 1983.

[106] E. Mamontov, R. Brezny, M. Koranne, and T. Egami. Nanoscale Heterogeneities and Oxygen Storage Capacity of $Ce_{0.5}Zr_{0.5}O_2$. *Journal of Physical Chemistry B*, 107(47):13007–13014, 2003.

[107] G.B. Marin and J.H.B.J. Hoebink. Kinetic Modeling of Automotive Exhaust Catalysis. *Cattech*, 12, 1997.

[108] E. Massing, J.F. Brilhac, A. Brillard, P. Gilot, and G. Prado. Modelling of the Behaviour of a Three Way Catalytic Converter at Steady State – Influence of the Propene Diffusion inside the Catalytic Layer. *Chemical Engineering Science*, 55:1707–1716, 2000.

[109] R.W. McCabe and R.K. Usmen. Chracterization of Pd-Based Automotive Catalysts. In J.W. Hightower, W.N. Delgass, E. Iglesia, and A.T. Bell, editors, *11th International Congress on Catalysis - 40th Anniversary*, volume 101, pages 355–368. Elsevier, 1996.

[110] S. Missy, J. Thams, M. Bollig, R. Tatschl, R. Wanker, G. Bachler, A. Ennemoser, and H. Grantner. Computergestützte Optimierung des Abgasnachbehandlungssystems für den neuen 1.8-l-Valvetronic-Motor von BMW. *MTZ Motortechnische Zeitschrift*, 63:18–29, 2002.

[111] K. Miyamoto, H. Takebayashi, T. Ishihara, H. Kido, and K. Hatamura. Measurement of Oxygen Storage Capacity of Three-Way Catalyst and Optimization of A/F Perturbation Control to its Characteristics. *SAE Technical Paper Series*, 2002-01-1094, 2002.

[112] Ch.R. Morgan, D.W. Carlson, and S.E. Voltz. Thermal Response and Emission Breakthrough of Platinum Monolithic Catalytic Converters. *SAE Technical Paper Series*, 730569, 1973.

[113] L. Mußmann, D. Lindner, E.S. Lox, R. van Yperen, T. Kreuzer, I. Mitsushima, S. Taniguchi, and G. Garr. The Role of Zirconium in Novel Three-Way Catalysts. *SAE Technical Paper Series*, 970465, 1997.

[114] Y. Nagai, T. Nonaka, A. Suda, and M. Sugiura. Structure Analysis of CeO_2-ZrO_2 Mixed Oxides as Oxygen Storage Promoters in Automotive Catalysts. *Technical Journal R&D Review (Toyota Central R&D Labs., Inc.) - Special Issue: Oxygen Storage Materials for Automotive Catalysts - Ceria-Zirconia Solid Solutions*, 37(4):20–27, 2002.

[115] R.H. Nibbelke, A.J.L. Nievergeld, J.H.B.J. Hoebink, and G.B. Marin. Development of a Transient Kinetic Model for the CO Oxidation by O_2 over a Pt/Rh/CeO_2/γ-Al_2O_3 Three-Way Catalyst. *Applied Catalysis B: Environmental*, 19:245–259, 1998.

[116] A. Norman, V. Perrichon, A. Bensaddik, S. Lemaux, H. Bitter, and D. Koningsberger. Study of the Reducibility of Pt or Pd on Ceria-Zirconia Catalysts by XANES Measured at the Ce L_{III} Edge and Magnetic Susceptibility Measurements. *Topics in Catalysis*, 16/17(1-4):363–368, 2001.

[117] C.J. Norman. Zirconium Oxide Products in Automotive Systems. *SAE Technical Paper Series*, 970460, 1997.

[118] F.B. Noronha, E.C. Fendley, R.R. Soares, W.E. Alvarez, and D.E. Resasco. Correlation between Catalytic Activity and Support Reducibility in the CO_2 Reforming of Methane over Pt/$Ce_xZr_{1-x}O_2$ Catalysts. *Chemical Engineering Journal*, 82:21–31, 2001.

[119] U. Nowak, J. Frauhammer, and U. Nieken. A Fully Adaptive Algorithm for Parabolic Partial Differential Equations in One Space Dimension. *Computers & Chemical Engineering*, 20(5):547–561, 1996.

[120] J.G. Nunan, H.J. Robota, M.J. Cohn, and S.A. Bradley. Physicochemical Properties of Ce-Containing Three-Way Catalysts and the Effect of Ce on Catalyst Activity. *Journal of Catalyis*, 133:309–324, 1992.

[121] B. Odendall. Fehlerbetrachtung bei der Messung von Gastemperaturen. *MTZ Motortechnische Zeitschrift*, 03, 2003.

[122] Association of European Automobile Manufacturers (ACEA). ACEA Data of the Sulphur Effect on Advanced Emission Control Technologies, 2000.

[123] H.S. Oh and J.C. Cavendish. Transients of Monolithic Catalytic Converters: Response to Step Changes in Feedstream Temperature as Related to Controlling Automobile Emissions. *Industrial & Engineering Chemistry Product Research and Development*, 21:29–36, 1982.

[124] S.H. Oh and E.J. Bissett. Mathematical Modeling of Monolith Warmup Behavior in Variable-Fuel Vehicle Exhaust. *SAE Technical Paper Series*, 932721, 1993.

[125] S.H. Oh, E.J. Bissett, and P.A. Battiston. Mathematical Modeling of Electrically Heated Monolith Converters: Model Formulation, Numerical Methods and Experimental Verification. *Industrial & Engineering Chemistry Research*, 32:1560–1567, 1993.

[126] K. Ohsawa, N. Baba, S. Kojima, and S. Matsunaga. Numerical Prediction of Transient Conversion Characteristics in a Three-Way Catalytic Converter. *SAE Technical Paper Series*, 982556, 1998.

[127] P. Öser, E. Müller, G.R. Härtel, and A.O. Schürfeld. Novel Emission Technologies with Emphasis on Catalyst Cold Start Improvements — Status Report on VW-Pierburg Burner/Catalyst Systems. *SAE Technical Paper Series*, 940474, 1994.

[128] S. Otsuka-Yao-Matsuo, N. Izu, T. Omata, and K. Ikeda. Thermodynamic Behavior of Various Phases Appearing in the $CeZrO_4$-$CeZrO_{3.5}$ System and the Formation of Metastable Solid Solutions. *Journal of the Electrochemical Society*, 145(4):1406, 1998.

[129] C. Padeste, N.W. Cant, and D.L. Trimm. The Influence of Water on the Reduction and Reoxidation of Ceria. *Catalysis Letters*, 18:305–316, 1993.

[130] R.J. Panlener, R.N. Blumenthal, and J.E. Garnier. A Thermodynamic Study of Nonstoichiometric Cerium Dioxide. *The Journal of Physics and Chemistry of Solids*, 36:1213–1222, 1975.

[131] The European Parliament and the Council of the European Union. Directive 98/70/EC of the European Parliament and of the Council of 13 October 1998 Relating to the Quality of Petrol and Diesel Fuels and Amending Council Directive 93/12/EEC. *Official Journal of the European Communities*, 350(L):58–68, 1998.

[132] K.N. Pattas, A.M. Stamatelos, P.K. Pistikopoulos, G.C. Koltsakis, P.A. Konstandinidis, E. Volpi, and E. Leveroni. Transient Modeling of 3-Way Catalytic Converters. *SAE Technical Paper Series*, 940934, 1994.

[133] H. Permana, D.N. Belton, K.M. Rahmoeller, S.J. Schmieg, C.E. Hori, A. Brenner, and K.Y.S. Ng. Reactor Evaluation of Ceria-Zirconia as an Oxygen Storage Material for Automotive Catalysts. *SAE Technical Paper Series*, 970462, 1997.

[134] R.H. Perry, D.W. Green, and J.O. Maloney, editors. *Perry's Chemical Engineers' Handbook*. McGraw-Hill International Editions, seventh edition, 1997.

[135] G. Pontikakis and A. Stamatelos. Mathematical Modelling of Catalytic Exhaust Systems for EURO-3 and EURO-4 Emissions Standards. *Proceedings of the Institution of Mechanical Engineers - Part D: Journal of Automobile Engineering*, 215(9):1005–1015, 2001.

[136] M. Primet and E. Garbowski. Fundamentals and Applications of Ceria in Combustion Reactions. In A. Trovarelli, editor, *Catalysis by Ceria and Related Materials*, pages 407–429. Imperial College Press, 2002.

[137] J.H.B.J. Hoebink R. Rajasree and J.C. Schouten. Transient Kinetics of Carbon Monoxide Oxidation by Oxygen over Supported Palladium/Ceria/Zirconia Three-Way Catalysts in the Absence and Presence of Water and Carbon Dioxide. *Journal of Catalysis*, 223(1):36–43, 2004.

[138] H.N. Rabinowitz, S.J. Tauster, and R.M. Heck. The Effects of Sulfur & Ceria on the Activity of Automotive Pd/Rh Catalysts. *Applied Catalysis A: General*, 212:215–222, 2001.

[139] R.C. Reid, J.M. Prausnitz, and B.E. Poling. *The Properties of Gases & Liquids*. McGraw-Hill Book Company, 4th edition, 1987.

[140] M.J. Ryan, E.R. Becker, and K. Zygourakis. Light-Off Performance of Catalytic Converters: The Effect of Heat/Mass Transfer Characteristics. *SAE Technical Paper Series*, 910610, 1991.

[141] G.V. Samsonov, editor. *The Oxide Handbook*. IFI/Plenum Data Company, 1982.

[142] S.K. Saxena, N. Chatterjee, Y. Fei, and G. Shen. *Thermodynamic Data on Oxides and Silicates - An Assessed Data Set Based on Thermochemistry and High Pressure Phase Equilibrium*. Springer-Verlag, 1993.

[143] J.C. Schlatter, R.M. Sinkevitch, and P.J. Mitchell. Laboratory Reactor System for Three-Way Automotive Catalyst Evaluation. *Industrial & Engineering Chemistry Product Research and Development*, 22:51–56, 1983.

[144] Scientific Group Thermodata Europe (SGTE). Thermodynamic properties of inorganic materials. In RWTH Aachen W. Martienssen, Lehrstuhl für Theoretische Hüttenkunde, editor, *Landolt-Börnstein, Numerical Data and Functional Relationships in Science and Technology, Group IV: Physical Chemistry*, chapter Subvolume A, Pure Substances, Heat Capacities, Enthalpies, Entropies and Gibbs Energies, Phase Transition Data, Part 2: Compounds from BeBr(g) to $ZrCl_2$(g). Springer, 1999.

[145] M. Shelef and R.W. McCabe. Twenty-Five Years after Introduction of Automotive Catalysts: What Next? *Catalysis Today*, 62:35–50, 2000.

[146] H. Shen, T. Shamim, and S. Sengupta. An Investigation of Catalytic Converter Performances during Cold Starts. *SAE Technical Paper Series*, 1999-01-3473, 1999.

[147] S. Siemund, J.P. Leclerc, D. Schweich, M. Prigent, and F. Castagna. Three-Way Monolithic Converter: Simulations versus Experiments. *Chemical Engineering Science*, 51(15):3709–3720, 1996.

[148] S. Siemund, D. Schweich, J.P. Leclerc, and J. Villermaux. Modeling Three-Way Monolithic Catalytic Converter: Comparison between Simulation and Experimental Data. *Studies in Surface Science and Catalysis*, 96:887–895, 1995.

[149] G. Smedler, S. Eriksson, M. Lindblad, H. Bernler, S. Lundgren, and E. Jobson. Deterioration of Three-Way Automotive Catalysts, Part II — Oxygen Storage Capacity at Exhaust Conditions. *SAE Technical Paper Series*, 930944, 1993.

[150] H. Sobukawa. Development of Ceria-Zirconia Solid Solutions and Future Trends. *Technical Journal R&D Review (Toyota Central R&D Labs., Inc.) - Special Issue: Oxygen Storage Materials for Automotive Catalysts - Ceria-Zirconia Solid Solutions*, 37(4):1–5, 2002.

[151] S. Sriramulu, P.D. Moore, J.P. Mello, and R.S. Weber. Microkinetics Modeling of Catalytic Converters. *SAE Technical Paper Series*, 2001-01-0936, 2001.

[152] M. Sugiura. Oxygen Storage Materials for Automotive Catalysts: Ceria-Zirconia Solid Solutions. *Catalysis Surveys from Asia*, 7(1):77–87, 2003.

[153] S. Tagliaferri, R.A. Koeppel, and A. Baiker. Behavior of Non-Promoted and Ceria-Promoted Pt/Rh and Pd/Rh Three-Way Catalysts under Steady State and Dynamic Operation of Hybrid Vehicles. *Industrial & Engineering Chemistry Research*, 38:108–117, 1999.

[154] R. Taha, D. Duprez, N. Mouaddib-Moral, and C. Gauthier. Oxygen Storage Capacity of Three-Way Catalysts: A Global Test for Catalyst Deactivation. *Studies in Surface Science and Catalysis*, 116:549, 1998.

[155] H. Tanaka and M. Yamamoto. Improvement in Oxygen Storage Capacity. *SAE Technical Paper Series*, 960794, 1996.

[156] E. Tani, M. Yoshimura, and S. Somiya. Revised Phase Diagram of the System ZrO_2-CeO_2 below 1400 °C. *Journal of the American Ceramic Society*, 66(7):506–510, 1983.

[157] J.R. Theis. An Engine Test to Measure the Oxygen Storage Capacity of a Catalyst. *SAE Technical Paper Series*, 961900, 1996.

[158] J.R. Theis, W.J. LaBarge, and G.B. Fisher. The Effects of Catalyst Volume and Ceria Content on the Emission Performance and Oxygen Storage Capacity of Automotive Catalysts. *SAE Technical Paper Series*, 932666, 1993.

[159] J.M. Thomas and W.J. Thomas. *Principles and Practice of Heterogeneous Catalysis*. VCH Verlag, Weinheim, 1997.

[160] A. Trovarelli. Structural Properties and Nonstoichiometric Behavior of CeO_2. In *Catalysis by Ceria and Related Materials*, chapter 2, pages 15–50. Imperial College Press, 2002.

[161] A. Trovarelli, M. Boaro, E. Rocchini, C. de Leitenburg, and G. Dolcetti. Some Recent Developments in the Characterization of Ceria-Based Catalysts. *Journal of Alloys and Compounds*, 323-324:584–591, 2001.

[162] A. Trovarelli, F. Zamar, J. Llorac, C. de Leitenburg, G. Dolcetti, and J.T. Kiss. Nanophase Fluorite-Structured CeO_2-ZrO_2 Catalysts Prepared by High-Energy Mechanical Milling. *Journal of Catalysis*, 169:490–502, 1997.

[163] T.J. Truex. Interaction of Sulfur with Automotive Catalysts and the Impact on Vehicle Emissions - A Review. *SAE Technical Paper Series*, 1999-01-1543, 1999.

[164] A. Tschöpe and R. Birringer. Oxyreduction Studies on Nanostructured Cerium Oxide. *Nanostructured Materials*, 9:591–594, 1997.

[165] D.N. Tsinoglou and G.C. Koltsakis. Effect of Perturbations in the Exhaust Gas Composition on Three-Way Catalyst Light-off. *Chemical Engineering Science*, 58:179–192, 2003.

[166] D.N. Tsinoglou, G.C. Koltsakis, and J.C. Peyton Jones. Oxygen Storage Modeling in Three-Way Catalytic Converters. *Industrial & Engineering Chemistry Research*, 41(5):1152–1165, 2002.

[167] H. Vidal, S. Bernal, J. Kaspar, M. Pijolat, V. Perrichon, B. Blanco, J.M Pintado, R.T. Baker, G. Colon, and F. Fally. Influence of High Temperature Treatments under Net Oxidizing and Reducing Conditions on the Oxygen Storage and Buffering Properties of a $Ce_{0.68}Zr_{0.32}O_2$ Mixed Oxide. *Catalysis Today*, 54:93–100, 1999.

[168] H. Vidal, J. Kaspar, M. Pijolat, G. Colon, S. Bernal, A. Cordon, V. Perrichon, and F. Fally. Redox Behavior of CeO_2–ZrO_2 Mixed Oxides: I. Influence of Redox Treatments on High Surface Area Catalysts. *Applied Catalysis B: Environmental*, 27:49–63, 2000.

[169] H. Vidal, J. Kaspar, M. Pijolat, G. Colon, S. Bernal, A. Cordon, V. Perrichon, and F. Fally. Redox Behavior of CeO_2–ZrO_2 Mixed Oxides: II. Influence of Redox Treatments on Low Surface Area Catalysts. *Applied Catalyis B: Environmental*, 30:75–85, 2001.

[170] S.E. Voltz, C.R. Morgan, D. Liederman, and S.M. Jacob. Kinetic Study of Carbon Monoxide and Propylene Oxidation on Platinum Catalysts. *Industrial & Engineering Chemistry Product Research and Development*, 12(4):294 – 301, 1973.

[171] M. Votsmeier, J. Gieshoff, E.S. Lox, and T. Kreuzer. Computersimulation unter Einbeziehung detaillierter Reaktionsmechnismen als Werkzeug zur Optimierung von Abgasnachbehandlungssystemen. In *Tagungsband Emission Control 10. & 11.06.2002, Dresden*, 2002.

[172] R. Wanker, H. Raupenstrauch, and G. Staudinger. Numerische Simulation eines monolithischen Katalysators zur Abgasreinigung mit einem heterogenen Modell. *Chemie Ingenieur Technik*, 71:1186–1191, 1999.

[173] Y. Watanabe. Numerical Optimization of HC Supply for HC-DeNO$_x$ System, 1: Numerical Modeling of HC-DeNO$_x$ Catalyst. *Technical Journal R&D Review (Toyota Central R&D Labs., Inc.) - Special Issue: Challenges in Realizing Clean High-Performance Diesel Engines*, 37(3):32–39, 2002.

[174] C.C. Webb, W.D. DiSilverio, Ph.A. Weber, B.B. Bykowski, and D.L. McKinnon. Phased Air/Fuel Ratio Perturbation - a Fuel Control Technique for Improved Catalyst Efficiency. *SAE Technical Paper Series*, 2000-01-0891, 2000.

[175] J. Wei. Catalysis for Motor Vehicle Emissions. *Advances in Catalysis*, 24:57–129, 1975.

[176] B.I. Whittington, C.J. Jiang, and D.L. Trimm. Vehicle Exhaust Catalysis; II: The Effect of Traces of Sulphur Dioxide on the Performance of Three-Way Vehicle Emission Catalysts. *Catalysis Today*, 26:47–51, 1995.

[177] H.-M. Wiedenmann, G. Hötzel, H. Neumann, J. Riegel, and H. Weyl. *Sensoranwendungen*, chapter ZrO_2-Lambda-Sonden für die Gemischregelung im Kraftfahrzeug. Hanno Schaumburg, 1995.

[178] M. Wiedmann, M. Friese, M. Ganzer, and F.-M. Wittig. The Volkswagen Group's Super-ULEV Concept for the North American Market. *23rd International Vienna Motor Symposium, VDI Research Report*, 12(490), 2002.

[179] K. Yamada, H. Tanaka, and M. Yamamoto. Oxygen Storage Capacity on Cerium Oxide - Precious Metal System. *SAE Technical Paper Series*, 970464, 1997.

[180] L. Yang, O. Kresnawahjuesa, and R.J. Gorte. A Calorimetric Study of Oxygen-Storage in Pd/Ceria and Pd/Ceria-Zirconia Catalysts. *Catalysis Letters*, 72(1-2):33–37, 2001.

[181] H.C. Yao and Y.F. Yu Yao. Ceria in Automotive Exhaust Catalysts: I. Oxygen Storage. *Journal of Catalysis*, 86(2):254–265, 1984.

[182] Y.F. Yu Yao. Oxidation of Alkanes over Noble Metal Catalysts. *Industrial & Engineering Chemistry Product Research and Development*, 19:293–298, 1980.